DC Distribution Grid and the Associated Advanced DC/DC Converter

Mahmoud Swaisi MSc, BSc

Submitted to the University of Nottingham for the degree of Doctor of Philosophy,

March 2017.



Abstract:

AC or DC has been in the centre of debate since the early days of the electrical system. DC is already proven to be more economical than AC in transmission at elevated power and voltages. Thus, expanding the use of DC to the distribution grids seems promising as most of the distributed generation such as PV generates initial DC voltages and many of the modern loads are using internal DC buses. Still, in order to extend the use of DC to the distribution level a suitable DC distribution grid architecture and a suitable DC/DC converter to serve it should be explored, which is the focus of this Ph.D.

A study based on the Libyan grid and loads was carried out to investigate the most suitable DC distribution grid layout. The results showed that DC grid arrangement utilising two port converters have lower total converter losses and smaller converter installed power when compared with arrangements using three ports converter.

A multi-cell multi–snubbered three phase dual active bridge (DAB) converter was proposed to serve the chosen DC distribution grid layout. The modular multi-cell multi–snubbered 3 phase DAB converter offered low losses over a wide range of loading profiles. Furthermore, the converter performance can be easily modified to be able to serve a specific DC/DC grid loading profile by altering the snubbers attached to the cells and the power management's algorithm between the cells while keeping the core cells the same. Extra cells can be added if higher power rating is required, reducing

the total cost of expanding the proposed DC distribution system.

This thesis is an ambition step on deciding the structure of the futuristic DC grid and the required DC/DC converters to link it is different voltage levels.

Acknowledgements

All praise is to Allah, Lord of the worlds

I would like to express my sincere gratitude and thanks to my supervisors Prof Jon Clare, Prof Mark Johnson and Dr Edward Christopher for their prised suggestions and encouragement through the duration of my study. Also, I would like to thank Prof. Richard McMahon and Dr. Christian Klumpner for their time and valuable input during the thesis assessment.

Moreover, I would like to thank my fellow students and researchers at the PEMC group of the University of Nottingham, for being a good company and their support during the duration of my study. Additionally, I would like to thank all the staff of the PEMC group and the electrical engineering departments at the University of Nottingham, for their help and support during the duration of my study.

I would like to show my dearest respect and graduate and love to my parent, my brothers and sisters and my friend back home, in the UK and around the world.

Moreover I would like to thank the ones who shared the journey with me, my wife and my kids for providing me with the support to curry out this work.

Mahmoud Swaisi

Nottingham, 2017

Table of Contents

1 Chapter 1 1

Introduction 1

1.1 Introduction 1

1.2 Project aims and objectives 4

1.3 Thesis outlines 6

Chapter 2 8

2 The generation, distribution, and consumption of electrical power in Libya 8

2.1 Introduction 8

2.2 Libyan electrical generation 9

2.3 Libyan transmission and distribution lines 11

2.4 Libyan loads 14

2.5 Libyan standalone grids 19

2.5.1 Standalone PV system for Almarhan Well Village [10] 20

2.5.2 Hybrid diesel/solar system for Misread Valley village: 22

2.6 Conclusion of the Libyan Grid 24

Chapter 3 26

3 Current DC usages in electrical systems 26

3.1 Introduction. 26

3.2 DC applications in electrical systems. 27

3.3.1 The International Space Station (ISS). 27

3.3.2 Shipboard power systems. 28
3.3.3 Data centres. 30
3.3.4 Railway systems 31
3.3.5 LED lighting. 32
3.3 The current used DC voltage levels 34
3.3.1 Extra-low voltage: 34
3.3.2 Low voltage: 35
3.3.3 High voltage: 36
3.4 The technical aspects impacting the distribution grid hosting capacity: 37
3.4.1 Voltage deviations. 39
3.4.2 Distribution grid current, power losses, and thermal limits. 41
3.4.3 Voltage unbalance and frequency deviation 42
3.4.4 Harmonics and distortion level. 43
3.5 AC systems hosting capacity improvement techniques. 45
3.6 Conclusions: 46
Chapter 4 47
4 DC Grid layout and DC/DC converter configuration assessment 47
4.1 Introduction 47
4.2 Grid arrangements under test. 49
4.3 The system design. 52
4.3.1 Load estimation. 53

4.3.2 PV estimation. 58
4.3.3 The battery rating. 60
4.3.4 Converter rating 61
4.4 Modelling of converter losses. 63
4.4.1 Low power converters (less 10kW). 65
4.4.2 Medium power converters (between 10 kW to 100kW). 66
4.4.3 High power converter (more than 100kW). 67
4.5 Power managements. 69
4.5.1 Modes of operation 70
4.5.1.1 Mode (1) The PV is equal to zero: 70
4.5.1.2 Mode (2) the PV output is higher than the load: 71
4.5.1.3 Mode (3) the PV output is less than the load: ... 72
4.5.2 Arrangement TWO and FOUR power management: 73
4.5.2.1 Without grid: 73
4.5.2.2 With grid: 76
4.6 MATLAB coding and equations executions..... 79
4.7 Results and findings. 85
4.7.1 Converter and battery installed power. 85
4.7.2 Converter losses: 88
4.7.2.1 Investigating converter CS1 energy losses: 89
4.7.2.2 Investigating Converter CS2 energy losses. 91
4.7.2.2 Investigating converter CS3 energy losses. 94
4.7.2.3 Battery converter energy losses. 94
4.7.2.4 Total converter losses. 95
4.8 Summary. 97

Chapter 5 99

5 Three-Phase Dual-Active Bridge DAB's, theory and analysis..... 99

5.1 Introduction. 99

5.2 Three-Phase Dual-Active Bridge. 101

5.2.1 Analysis of the 3ϕ DAB converter. 103

5.2.2 Three phase DAB converter soft-switching region boundaries. 106

5.3 3ϕ DAB power loss estimation 109

5.3.1 IGBT and Diode conduction losses estimation. 112

5.3.2 IGBT and diode RMS and average current derivation..... 115

5.3.2.1 The crossover time 115

5.3.2.2 Calculating (I_{rms}) and (I_{av}) for the sending bridge IGBTs and the diodes. 116

5.3.2.3 Calculating (I_{rms}) and (I_{av}) for the receiving bridge IGBTs and diodes..... 117

5.3.3 The conduction losses at the sending bridge .. 121

5.3.4 The conduction losses at the receiving bridge. 121

5.3.5 Conduction losses simulation and analytical model comparison..... 122

5.4 The switching losses of the converter and the effect of snubber capacitors on the switching losses 125

5.4.1 IGBT turn-off losses estimation 126

5.4.1.1 Estimating the IGBT turn-off losses without a snubber capacitor 126

5.4.1.2 Estimating the IGBT turn-off losses with a snubber capacitor 128
5.4.2 Minimum current requirement for ZVS with snubber capacitor 131
5.4.3 Switching losses comparison between snubbered and un-snubbered situations 137
5.5 Multi-cell multi-snubbered 3ϕ DAB converter 139
5.6 Summary: 142
Chapter 6 143
6 Hardware Implementation. 143
6.1 Introduction 143
6.2 The experimental rig 144
6.3 The high frequency high power transformer. 145
6.3.1 Transformer rating and specifications: 145
6.3.2 Transformer design. 149
6.4 High- frequency high-power inductor. 157
6.4.1 Inductor rating and specifications. 157
6.4.2 Inductor design: 159
6.5 IGBT selection 164
6.6 Snubber capacitors design 166
6.7 DC link capacitors, power planes, and heat sinks 168
6.8 The gate driver design 171
6.9 Measurement board design 173
6.10 Control unit DSP and FPGA 174
6.10.1 The DSP processing unit TMS320C6713 175

6.10.2 The FPGA Field programmable gate array 175
6.11 Summary 177
Chapter 7 178
7 Experimental Results. 178
7.1 Introduction 178
7.2 Equipment used and test procedures 179
7.2.1 Turn off losses: 184
7.2.2 Turn on losses..... 185
7.2.3 The conduction losses: 186
7.3 Test set up. 187
7.4 Practical Results..... 189
7.4.1 Test without snubber 189
7.4.2 Test with snubbers at both bridges 200
7.4.3 Test with the snubber capacitor connected only at the low voltage side..... 204
7.5 Comparison between the snubbered and the un-snubbered situations..... 213
7.5.1 IGBT turn-off losses..... 213
7.5.2 IGBT turn-on losses 215
7.5.3 Total losses and efficiency. 218
7.6 Evaluation of multi-cell multi-snubbered 3ϕ DAB converter..... 222
7.7 Summary 229
8 Chapter 8 230
Conclusion..... 230

8.1 Thesis Summary 230

8.2 Thesis achievements: 234

8.3 Further work..... 235

9 References: 237

10 Appendices 250

Appendix (A) 6 the percentage of ownership and consumption of the Libyan household electrical equipment's and their consumption: 250

Appendix (B) The inductor current at the different zones of operation..... 253

Appendix (C) Calculating the (I_{rms}) and the (I_{av}) for the sending bridge's IGBTs and the diodes 254

Appendix D Analysis of three ϕ DAB converter using Thevenin's theory to estimate the turn off critical current: 262

List of figures

Figure 1.1 The concept of complete DC distribution grid 5

Figure 2.1 Libyan electrical transmission grid (reprinted from [13]). 12

Figure 2.2 The daily load curves in Libya for the week with highest loading in 2012 [15]. 14

Figure 2.3 The daily load curves in Libya for the week with the lowest loading [15]. 15

Figure 2.4 The daily load curves in Libya for the week with medium loading [15]. 15

Figure 2.5 The consumer types within the Libyan grid (reprinted from [14]). 16

Figure 2.6 One of the solar systems in the Almarhan Well Village (reprinted from [10]). 21

Figure 2.7 The layout of the islanded electrical network in the Misread Valley village [11] 23

Figure 2.8 The solar panels in the Misread Valley Village reprinted from [11] 24

Figure 3.1 Shipboard DC zonal electrical distribution system [23] 29

Figure 3.2 Structure of DC grid for data centres [27]. 31

Figure 3.3 Proposed arrangement for low LVDC for LED lighting [31]. 33

Figure 3.4 The hosting capacity concept [41]. 38

Figure 3.5 Diagram of the generation and load 40

Figure 4.1 Arrangement ONE, three port converter with the battery connected to three port converter. 50

Figure 4.2 Arrangement TWO, two port converters with the battery connected through separate converter and centralized PV. 50

Figure 4.3 Arrangement THREE, two port converter with the battery connected through separate converter and distributed PV. 51

Figure 4.4 Arrangement FOUR, three port converter with two buses: a generation bus and a load bus. 51

Figure 4.5 The daily load profile for a Libyan house as generated using CREST model. 54

Figure 4.6 The solar radiation design data for a day in June. 59

Figure 4.7 Comparison between the original efficiency curve and the efficiency curve obtained from the losses equation for the SUNNY BOY 3000HF. 66

Figure 4.8 Comparison between the original efficiency curve and the efficiency curve obtained from the loss equation for the SUNNY TRIPOWER 17000TL 67

Figure 4.9 Comparison between the original efficiency curve and the efficiency curve obtained from the loss equation for the SUNNY CENTRAL 800CP. 68

Figure 4.10 Power transfers in mode (1) where the PV output is equal to zero. 71

Figure 4.11 Power transfers in mode (2) the PV output is higher than the load. 72

Figure 4.12 Power transfers in mode (3) the PV output is less than the load 72

Figure 4.13 Arrangement TWO working isolated from the grid in mode 1. 73

Figure 4.14 Arrangement FOUR working isolated from the grid in mode 1. 74

Figure 4.15 Arrangement TWO working isolated from the grid in mode 2. 74

Figure 4.16 Arrangement FOUR working isolated from the grid in mode 2. 75

Figure 4.17 Arrangement TWO working isolated from the grid in mode 3. 75

Figure 4.18 Arrangement FOUR working isolated from the grid in mode 3. 76

Figure 4.19 Arrangement TWO connected with the grid in mode 1. 76

Figure 4.20 Arrangement FOUR connected with the grid in mode 1. 77

Figure 4.21 Arrangement TWO connected with the grid in mode 2. 77

Figure 4.22 Arrangement FOUR connected to the grid in mode 2. 78

Figure 4.23 Arrangement TWO connected to the grid in mode 3. 78

Figure 4.24 Arrangement FOUR connected to the grid in mode 3. 79

Figure 4.25 Flow-chart of the MATLAB code used in the grid arrangements comparison study. 81

Figure 4.26 The battery energy for arrangement TWO with 20 houses. 83

Figure 4.27 Power of the PV converter, the grid converter, the battery converter over a day. The load consists of 20 houses and the cluster is grid connected. 83

Figure 4.28 Power of the PV converter, the grid converter, the battery converter over a day. The load consists of 20 houses and the cluster is not grid connected. 84

Figure 4.29: Relation between the total connected converter installed power and the number of houses for different grid arrangements (red curve superposed arrangements, ONE, TWO, and THREE) 86

Figure 4.30 Relation between grid side converter CS1 installed power and the number of houses. 87

Figure 4.31 The required battery size for all grid arrangements. 87

Figure 4.32 Total energy transferred through arrangement Two for a day..... 88

Figure 4.33 Comparison between the converter CS1 energy losses over one day with the number of houses. a with grid .b. without grid. 90

Figure 4.34, Comparison between the converter CS2 losses, the number of houses for different grid arrangements. a. with grid b. without grid (arrangements THREE, TWO in red). 92

Figure 4.35 Comparison between the converter CS3 losses, with the number of houses for different grid arrangements. a. with grid b. without grid. 93

Figure 4.36 Comparison between the battery converter energy losses, the number of houses for different grid arrangements. a. with grid, b. without grid. 95

Figure 4.37 Comparison between the converters energy losses, the number of houses for different grid arrangements. a. with grid, b. without grid. 96

Figure 5.1 3ϕ DAB converter. 102

Figure 5.2 Simplified 3ϕ DAB converter circuit referred to the sending bridge [68]. 103

Figure 5.3, 3ϕ DAB voltage and current waveforms..... 104

Figure 5.4 Soft switching region of the 3ϕ DAB converter [68]. 108

Figure 5.5 3ϕ DAB converter one leg circuit 109

Figure 5.6, IGBT and diode voltage and current waveforms for the upper devices of leg one of the 3ϕ DAB..... 111

Figure 5.7 Extracting V_{CE0} and r_C from an Infineon-FS100R17KE3-B17 IGBT data sheet..... 114

Figure 5.8 Extracting V_{D0} and r_D from an Infineon-FS100R17KE3-B17 diode data sheet 114

Figure 5.9 A comparison between switched based simulation and the analytical device currents for the sending (high voltage) bridge a. The D1 average current, b. The D1 RMS

current, c. The IGBT1 average current, d. The IGBT1 RMS current..... 120

Figure 5.10 High voltage bridge IGBT conduction losses comparison between analytical and simulation. 123

Figure 5.11 High voltage bridge diode conduction losses comparison between analytical and simulation. 123

Figure 5.12 Low voltage bridge IGBT conduction losses comparison between analytical and simulation. 124

Figure 5.13 Low voltage bridge diode conduction losses comparison between analytical and simulation. 124

Figure 5.14 Simplified voltage and current the waveform of IGBT at the turn off without a snubber [75]. 127

Figure 5.15 The simplified voltage and current waveform of IGBT at the turn off with a snubber [75]. 128

Figure 5.16 Current path and conducting devices at snubber commutation 132

Figure 5.17 The snubber capacitor voltage and current at commutation 133

Figure 5.18 Snubber voltage and current at three different turn off current levels [74]. 134

Figure 5.19 The multi-cell multi-snubbered 3ϕ DAB converter concept..... 141

Figure 6.1 The star/star connection of the transformer..... 146

Figure 6.2 The three phase dab transformer current and voltages, a. The high and low voltage side current, b. The high and low voltage phase voltages, c. The high and low voltage lone to line voltages..... 147

Figure 6.3 Flow chart showing the transformer design steps. 150

Figures 6.4 The Nanocrystalline NANOPERM core M-142 specifications a. Hysteresis loop of core M-142 (reprinted from [78]) b. Specific Losses of core M-142 [78]. 153

Figure 6.5 The completed fabricated single phase transformer 157

Figure 6.6 Design flow chart of the inductor design..... 159

Figure 6.7 Relation between core losses and flux density for the Metglas® amorphous alloy 2605SA1 (reprinted from [79]). 160

Figure 6.8 The fabricated high-frequency inductor 164

Figure 6.9 The completed high voltage bridge being tested (at the front). 170

Figure 6.10 The completed low voltage bridge being tested. 171

Figure 6.11 Gate driver for the high voltage bridge..... 173

Figure 6.12 Gate driver for the low voltage bridge 173

Figure 6.13 The measurements board. 174

Figure 6.14 The complete control unit stack..... 175

Figure 7.2 Low voltage switch current and voltage waveforms for a load of 14.8% of the rated power, f=20 kHz, and no snubber. 190

Figure 7.3 Low voltage switch current, voltage waveforms at turn off waveform and losses for a load of 14.8% of the rated power, f=20 kHz and no snubber. 190

Figure 7.4 Low voltage switch current and voltage waveforms for the full rated power, f=20 kHz, and no snubber..... 191

Figure 7.5 Low voltage switch current, voltage waveforms and losses at turn off for the full rated power, f=20 kHz, and no snubber. 191

Figure 7.6 High voltage switch current and voltage waveforms for a load of 14.8% of the rated power, f=20 kHz, and no snubber. 192

Figure 7.7 High voltage switch current, voltage waveforms and losses at turn off for 14.8% of the rated power, f=20 kHz and no snubber 193

Figure 7.8 High voltage switch current, voltage, and losses waveforms at turn on for full rated power, f=20 kHz, and no snubber. 193

Figure 7.9 High voltage switch current and voltage waveforms for full rated power f=20 kHz and no snubber 194

Figure 7.10 High voltage switch current, voltage waveforms and losses at the turn off from for full rated power, f=20 kHz and no snubber. 194

Figure 7.11 The low voltage bridge total losses by using the current and voltage waveforms with no snubber..... 197

Figure 7.12 Comparison between the low voltage bridge IGBT conduction losses by applying the practical and analytical approaches..... 198

Figure 7.13 A comparison between the low voltage bridge diode conduction losses by applying the practical and analytical approaches..... 198

Figure 7.14 The un-snubbered high voltage bridge total losses measured using the current and voltage wave forms. 199

Figure 7.15 Low voltage switch current and voltage waveform for 85.5% of the rated power and f=20 kHz..... 201

Figure 7.16 High voltage switch current and voltage waveform for 85.5% of the rated power and f=20 kHz..... 202

Figure 7.17 The low voltage switch current and voltage waveform for rated power, f=20 kHz, and 22 nF. 204

Figure 7.18 The low voltage switch current and voltage waveform for rated power, f=20 kHz, and 47 nF. 205

Figure 7.19 The low voltage switch current and voltage waveform for rated power, f=20 kHz, and 68 nF 205

Figure 7.20 The low voltage switch current and voltage waveform for rated power, f=20 kHz, and 22 nF. 206

Figure 7.21 The low voltage switch current and voltage waveform for rated power, f=20 kHz, and 47 nF the losses was 206

Figure 7.22 The low voltage switch current and voltage waveform for rated power, f=20 kHz, and 68 nF. 207

Figure 7.23 The low voltage switch current and voltage waveform for a 29.5 % of the rated power, f=20 kHz and 22 nF. 208

Figure 7.24 The low voltage switch current and voltage waveform for a 43.8 % of the rated power, f=20 kHz and 47 nF. 208

Figure 7.25 The low voltage switch current and voltage waveform for a 58.3 % of the rated power, f=20 kHz and 68 nF. 209

Figure 7.26 The low voltage bridge losses by using the current and voltage waveforms with snubber capacitor value of 22 nF. 212

Figure 7.27 The low voltage bridge losses by using the current and voltage waveforms with snubber capacitor value of 47 nF. 212

Figure 7.28 The low voltage bridge losses by using the current and voltage waveforms with snubber capacitor value of 68 nF. 212

Figure 7.29 Comparison between the low voltage bridge IGBT turn off losses under different snubbering scenarios. 214

Figure 7.30 Comparison between the low voltage bridge IGBT turn-on losses under different snubbering scenarios. 216

Figure 7.31 Comparison between the low voltage bridge total losses under different snubbering scenarios 218

Figure 7.32 Comparison between the low voltage bridge efficiency under different snubbering scenarios: 221

Figure 7.33 Comparison between a three multi-cell 3ϕ DAB converters low voltage bridge losses made out of 4 modeller cells with different snubbering. 225

Figure 7.34 Comparison between a three multi-cell 3ϕ DAB converters low voltage bridge efficiency for a converter made out of 4 modeller cells with different snubbering. 225

Figure 7.35 Proposed power management for a converter made of three heavily snubbered and one un-snubbered cell 226

Figure 7.36 Proposed power management for the converter made of four un-snubbered cells 226

Figure 7.37 Proposed power management for a converter made of three differently snubbered cells and one un-snubbered cell 227

List of tables

Table 2.1 The generation capacity in Libya per generation technology [8]. 10

Table 2.2 The total installed distance at each voltage level [8]: 12

Table 2.3 Number of stations and the installed power at each voltage level [8]. 13

Table 2.4 A sample of consumer distribution in three major cities in Libya [16]. 18

Table 2.5 The average annual consumption of each consumer group [16]: 18

Table 2.6 The electricity needs for Almarhan Well Village [10] 20

Table 2.7 The details of the installed systems rating for the Almarhan Well Village [10]. 21

Table 4.1 The diversity factor for the Libyan grid [53]. 58

Table 4.2 The losses equation constant values for SUNNY BOY 3000HF 65

Table 4.3 The losses equation constant values for the SUNNY TRIPOWER 17000TL..... 67

Table 4.4 The losses equation constant values for the SUNNY CENTRAL 800CP. 68

Table 5.1 The converter comparison parameters: 118

Table 5.2 An analytical comparison between the snubbered and unsnubbered total turn-off switching losses for one converter cell switching at 20 kHz: 138

Table 6.1 The 3ϕ DAB converter cell design specifications:. 145

Table 6.2: Litz wire gauge from The New England Wire Technology Company [77]. 151

Table 6.3 The chosen wire of the transformer: 154

Table 6.4: The specifications of the inductor 158

Table 6.5 The fabricated inductor specifications: 164

Table 6.6 Minimum rating of the 20 kW converter IGBTs: .. 165

Table 6.7 The characteristics of the chosen devices: 165

Table 6.8 The parameters used to calculate the design points: 167

Table 6.9 The value of snubbers which are going to be used for the high and the low voltage bridges. 168

Table 6.10 The two ordered water-cooled heat sink: 169

Table 6.11 The UL30BC0360 capacitor rating: 169

Table 6.12 The chosen gate drive DC/DC converter. 172

Table 7.1 The measurable steps for the voltage and current. 182

Table 7.2 The achievable measurements step and accuracy of each voltage or current probe. 183

Table 7.3 Achievable measurements step and accuracy for the power measurements: 184

Table 7.4 IGBT used in the test. 188

Table 7.5 The practical 3 DAB circuit parameters: 188

Table 7.6 The losses values for one device for the low voltage bridge with 200V DC load, 20 kHz and no snubber..... 196

Table 7.7 The loss values for one device for the high voltage bridge with 200V DC load on the low voltage side, 20 kHz and no snubber 199

Table 7.8 The losses values for one device for the low voltage bridge with 200 VDC load and 20 kHz and with snubber capacitor value of 22 nF. 210

Table 7.9 The losses values for one device for the low voltage bridge with 200 VDC load and 20 kHz with snubber capacitor value of 47 n F. 211

Table 7.10 The losses values for one device for the low voltage bridge with 200 VDC load and 20 kHz and 68 nF. 211

Table 7.11 Comparison between the low voltage bridge IGBTs turn off losses under different snubbering scenarios. 214

Table 7.12 Comparison between the low voltage bridge IGBT turn-on under different snubbering scenarios. 215

Table 7.13 The analytical critical soft switch turn on current limits. 217

Table 7.14 The observed practical soft switched turn on limits. 217

Table 7.15 Comparison between the low voltage bridge total losses under different snubbering scenarios. 219

Table 7.16 Comparison between the low voltage bridge efficiency under different snubbering scenarios (efficiency is in %): 220

List of Acronyms

AC	Alternative current.
DC	Direct current.
PV	Photovoltaics.
DAB	Dual active bridge.
LVDC	Low voltage direct current.
LED	Light-emitting diode.
GECOL	General electric company of Libya.
ISS	The international space station.
SSPCM	Solid state sower controller module.
DG	Distributed generation.
P_G	Active power at generation bus.
Q_G	Reactive power at generation bus.
P_L	Active power at load bus.
Q_L	Reactive power at load bus.
$\%VUF$	The voltage unbalance factor.
V_-	Negative voltage sequence.
V_+	Positive voltage sequence.
IHD	Individual limits on harmonics distortion.
THD	Total harmonic distortion factor.
CS1	Converter stage one.

CS2	Converter stage two.
CS3	Converter stage three.
CREST	Centre for renewable energy systems technology.
$P_{T\ load}$	The total connected load.
DEF	Demand factor.
LF	Load factor.
DF	Diversity factor.
$DEFA$	Demand factor for air-conditioning and motors.
$DEFL$	Demand factor for the house load excluding motors and air conditioning.
n	Appliance number in a dwelling.
$P_{app\ n}$	The power rating of appliance number n.
$P_{T\ load}$	The connected load of one dwelling.
$P_{L\ \max}$	The maximum load of one dwelling.
$P_{L\ av}$	The average power of the load.
$P_{T\ load\ A}$	The connected air conditioner and motors load of dwellings.
$P_{T\ loadL}$	The house load excluding motors and air conditioners.
M	Number of houses in the dwellings group.
$P_{T\ load\ A\ M}$	The connected air conditioner and motors load of dwelling number M .

$P_{T\,loadL\ M}$	The house load excluding motors and air conditioners of dwelling number M .
$P_{L\,av\,M}$	The average load for a group of M dwellings.
$P_{L\,\max}$	The maximum load for a group of M dwellings.
$DF_{\ M}$	The diversity factor for a cluster of M dwellings.
A_{PV}	The required PV area.
$P_{solar\ av}$	The average solar power.
$P_{solarIn}$	The instantaneous power output from the PV.
η_{pv}	The solar cell efficiency.
E_{batt}	The battery rating.
T_{av}	The monthly average of the time when the sun is not available.
T_{day}	The duration of the day the sun energy is available.
$P_{out\ solarIn}$	The instantaneous output power from the PV.
P_{loadIn}	The instantaneous power transfer to the Load.
X_n	The normalized power of the converter.
(RMSE)	The root mean squared error.
$P_{solarIn}$	The instantaneous power transfer from the PV.
P_{loadIn}	The instantaneous power transfer to the Load.
P_{battIn}	The instantaneous power transfer to the battery.

$P_{grid\ In}$	The instantaneous power transfer to the grid.
ϕ	Phase shift angle.
N	The transformer number of turn.
P_{out}	The converter output power.
L	The Linking inductance.
V_i	The sending bridge DC voltage of the converter.
V_o	The receiving bridge DC voltage.
d	The DC voltage gain referred to the sending bridge.
V_L	The Linking inductor voltage.
P_{out}	The converter output power.
IGBT	Insulated-gate bipolar transistor.
I_{com}	The IGBT current at turn off.
V_{CE}	Collector-emitter voltage.
V_{CE0}	The zero current forward voltage drop.
r_C	The collector-emitter forward resistance.
$p_{ct}(t)$	The instantaneous IGBT conduction losses.
P_{CT}	The averaged value of the IGBT conduction losses.
t_f	The IGBT current fall time.
C_{cr}	The critical snubber value.

ZVC	Zero voltage switching.
t_{crit}	The critical commutation time.
$t_{diode\ com}$	The diode commutation time.
$\phi^{o}_{\max}$	The maximum phase shift angle.
$I_{HV\ rms}$	The converter high voltage side current.
$I_{LV\,rms}$	The low-voltage side current.
kVA_T	The apparent power transformer rating.
Rac	The AC resisteor of wire.
Rdc	The DC resistor of wire.
AWG	American wire gauge.
J	The current density.
A_e	Effective core cross section area.
$B_{\max}$	The maximum flux density.
K_u	Winding factor.
P_m	Specific core losses.
W_a	Core window area.
A_c	Core cross-section area.
G	The winding length.
l_g	The air gap length.
F	The fringing factor.

$C_{\min}$ The minimum snubber value.

$C_{\max}$ The maximum snubber value.

$E_{turn\ off\ \ IGBT}$ The turn off energy of the IGBT.

$t_{off\ Start}$ The average power dissipated in the IGBT due to the turn off losses.

$t_{off\ Start}$ The turn off start time.

P_{out} The turn off end time.

$E_{turn\ on\ IGBT}$ The IGBT turn off energy.

$P_{turn\ on\ IGBT}$ The average power dissipated in the IGBT due to the turn off losses.

$t_{on\ Start}$ The turn on start time.

$t_{on\ End}$ The turn on end time.

$E_{con\ \ D}$ The diode conducting energy.

$P_{con\ \ D}$ The power dissipated in the diode due to conducting.

$P_{out}t_{con\ D\ Start}$ The time when the diode start conducting.

$t_{con\ D\ End}$ The time when the diode finishes conducting.

Chapter 1

Introduction

1.1 Introduction

AC or DC, this has been at the centre of debate since the birth of the electrical system a war of currents raged between the founders of the electric systems the DC by Thomas Edison and Nicola Tesla's AC system. AC gained major successes due to the lack of an effective DC transmission system due to the non-existence of DC /DC converters in the early days of the power system. Despite this DC has been always present in many applications and areas such as telecommunication. And DC has already overcome AC in areas such as transmission

where HVDC is proven to be more economical over a long distance with elevated power and voltages. While DC has some disadvantages such as the difficulty to be isolated due to the non-existing of zero current crossing which make it more difficult to isolate DC currents.

The situation is now changing, as DC has found its own transformers, the DC-DC converters which are at the forefront of technological advancement. Additionally, there is an emergence of distributed generation, many of which generate DC, as for example solar panels, which are the fastest growing renewable energy by 50% a year [1] or have DC embedded inside them such as wind turbines. Furthermore, the nature of most appliances, such as TV, washing machines, LED lighting, heaters and DC inverter driven air conditioning (which is estimated to save about 25.3% to 38% on air conditioning energy requirements [2]), allows for connecting homes to a DC distribution grid. This will have a major impact on electrical grids, especially within the Libyan context, where the grid is currently under an excessive burden from air conditioning loads as will be further elaborated on later within this thesis.

Current electrical grids are facing great challenges, especially high-power demand with grids such as in the Germany's countryside [3] working near the edge of its capabilities (hosting capacities). Furthermore, electrical grids are under increasing demands due to the introduction of electric cars and ground-source heat pumps, while some areas of the world are yet to be electrified such as in the Sub-Saharan Africa, where more than 620 million people do not receive electricity [4]

despite the abundance of free solar energy in that region of the world.

Using DC voltages seems a viable option to meet the earlier mentioned challenges as DC brings many advantages to the electrical system, such as voltage quality enhancement in the DC grid as the voltage will suffer from fewer flickers due to the presence of converter [5] [6]. Secondly, LVDC (low voltage direct current) networks can have its own localised protection areas thus the fault can be isolated in the LVDC resulting in fewer disturbances in a grid made from one more than one zone [5] and the services can be resumed faster due to the non-existent of frequency draft in DC networks. Furthermore, DC has higher transmission abilities, hence thinner cables can be used and expenses can be cut [5]. Moreover, in DC systems, there is no need for an individual rectifier for each DC consuming appliance, reducing the required converters to link the DC loads and resulting in reduced losses and costs. Additionally, there are no reactive currents in DC systems and as consequence, the current and losses are lower and the utilisation of cables is increased. The use of LED lighting combined with a centralized converter will result in less heat in houses. Furthermore, the author of [7] stated that by changing to DC supplied computers in an office, a reduction of 16% of the total carbon emissions is achieved. Thus, if a DC grid is to be used to supply the houses and offices, the air conditioning requirements could be reduced and the internal building environment could be enhanced.

Despite the multiple benefits that DC voltages can bring to the electrical system, the concept of a complete DC grid is still to

be achieved due to challenges such as the grid layouts, the converter selection, the control and protection present when proposing the use of DC at the distribution level. Thus, the work of this thesis was proposed to look for possible DC grid arrangements layouts, to serve the last mile of the grid just before homes in city centres and rural areas, and to serve the other part of the world yet to be electrified and to investigate possible DC voltage levels and DC/DC converters to serve the proposed DC grid layouts.

To achieve the thesis' goals several studies will be carried out. At first, the Libyan grid will be studied. Next, the DC distribution grid layout will be investigated based on the converter losses in the DC distribution grid. A suitable DC/DC converter to serve the proposed DC grid will be chosen, modelled and studied. Finally, the chosen multi-cell-multi-snubber three phase dual active converter will be practically designed, tested and validated.

This thesis is a push forward on deciding the futuristic DC grid layout to serve the current and yet-to-be-constructed grids and to identify and test the required DC/DC converters to link its different voltage levels.

1.2 Project aims and objectives

This thesis focuses on the evaluation of using DC voltages in distribution grids which can be used to serve the areas not yet electrified in the world such as in Sub-Saharan Africa and to serve the last mile of the existing electrical distribution system

such as in crowded city centres. The Libyan grid is the case study of this thesis, thus an investigation on its current situation will be performed first. Next, a suitable DC voltage level and DC grid arrangement layout to serve the proposed DC distribution grid are going to be identified. Finally, a DC/DC power converter to drive the chosen DC grid arrangement is going to be proposed, analysed, designed, built and tested. Figure 0.1 shows the concept of complete DC distribution grid

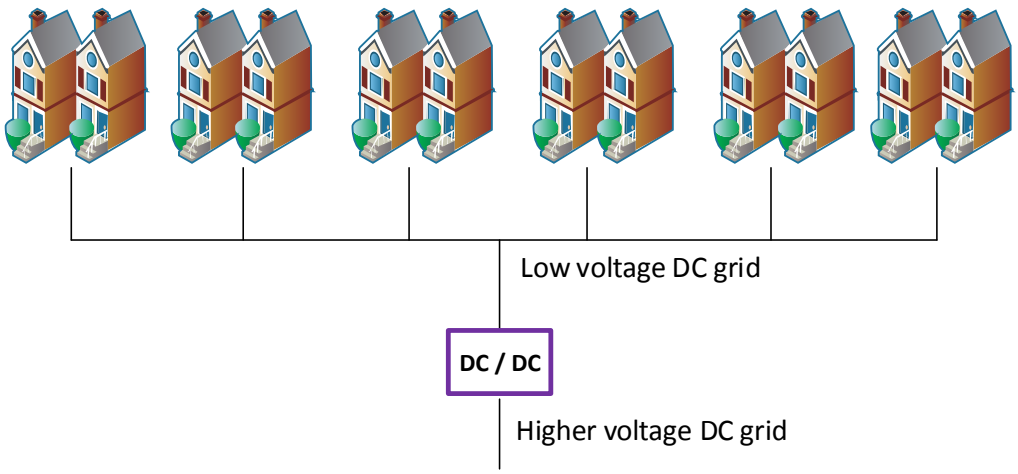


Figure 0.1 The concept of complete DC distribution grid

The objectives of this thesis are:

- To investigate the Libyan grid structure, loads, and generation, in order to recommend a suitable method to improve its performance.
- To explore existing electrical systems utilising DC voltage in order to identify the possible advantages and effects of replacing AC with DC in the distribution systems.

- To propose suitable DC voltage levels to serve the last mile of the distribution system.
- To investigate the possible DC distribution arrangements and to design, simulate and compare their performance based on the converter losses. And identify the DC grid and converter requirements.
- To choose, analyse, design, build and test a DC/DC converter to serve the proposed DC distribution grid layout and to further improve the chosen converter performance by using a multi-cell variant of it.

1.3 Thesis outlines

This thesis is consists of 8 chapters:

Chapter two, the generation, distribution, and consumption of electrical power in Libya: this chapter investigate the generation, transmission, and distribution of power within the Libyan grid- connected and standalone grids and the impact that the potential change to DC voltages might have on them.

Chapter three, current DC usages in electrical system: this chapter presents the applications using DC voltage and the DC voltage levels used within them. This chapter also includes an overview of the technical aspects impacting the distribution grid hosting capacity.

Chapter four, DC Grid layout and converter configuration assessment based on the losses and installed power of the

grid converters: a study and comparison among four potential DC distribution grid layouts are presented within this chapter. The study includes load and PV energy estimations, the converter rating, the power managements used to perform the comparison.

Chapter five, three-Phase Dual-Active Bridge (3ϕ DAB) converter, theory, and analysis: this chapter presents the advantages of using 3ϕ DAB converter within the proposed DC distribution grid, an analytical losses estimation for the 3ϕ DAB converter, an analytical study of snubbers and their effect on the soft switching areas of the 3ϕ DAB converter. Furthermore, the concept of a novel Multi-cell 3-ϕ DAB converter is presented in this chapter.

Chapter six, hardware implementation: This chapter includes the design and implementation steps of a 3ϕ DAB converter cell in the laboratory.

Chapter seven, experimental results: This chapter includes the practical investigation results of the 3ϕ DAB converter cell. It also includes an assessment of the novel multi-cell multi-snubbered 3ϕ DAB converter efficiency.

Chapter eight, conclusion: a summary of this thesis's achievements and proposed future work are presented in this chapter.

Chapter 2

The generation, distribution, and consumption of electrical power in Libya

2.1 Introduction

The Libyan electrical grid is state run under the General Electric Company of Libya (GECOL) [8]. The main generation is based on steam turbine located in the north on the seacoast using gas and diesel and heavy fuels as their energy source [8]. The transmission network comprises mostly of a long

radial transmission lines rated at 220kV AC with extra 400kV AC lines added recently [8]. The Libyan transmission network stretches over long distances with a high number of load centres located deep in the desert far from the central seacoast generation, such as Sabha with 700km transmission lines, and Gat at a distance of 1400km [8]. This results in high power losses and voltage deviations in the transmission grid [9]. There are also some isolated grids in the desert, powered by diesel generators and solar energy [10] [11]. This might change in the future due to the availability of solar energy, where each house in Libya could have its own generation.

This thesis chapter will highlight the present situation of the Libyan grid and why a DC distribution grid might be a better call of action to solve the Libyan grid challenges.

2.2 Libyan electrical generation

Libyan electricity is mainly generated using steam and gas powered plants concentrated on the sea coast. The main fuels used in these plants are diesel, gas or heavy fuels. The total generation capacity of the Libyan power plants is 8,375 GW [8] which is distributed among the generation technologies as in Table 2.1 [8]:

In Libya, 40% of customers do not pay for their electricity and the electricity price is 60% subsidised by the government [12]. It was estimated that if the subsidies were removed, it could lead to a reduction in the total consumption by 20 %,

which might waiver the need to install new power generation plants [12].

Table 2.1 The generation capacity in Libya per generation technology [8].

Plant type	Number of turbines	Installed power MW
Steam turbine	20	1,747
Gas turbine	36	4,245
Combined cycle	15	2,355
Total	71	8,375

Another effect of such subsidies is the impact on the exploitation of renewable energy sources which are one of the highest in the world, with a daily solar radiation average of 7.1 $kWh/m^2/day$ in the northern sea coast areas and 8.1 $kWh/m^2/day$ [12] in the southern desert. This solar potential now accounts for almost zero of the total generation in Libya due to the electrical subsidies from the government [12]. As a result, solar generation is used only in remote islanded locations away from the central grid, which will be discussed later in this chapter.

The situation for wind is not better than solar even though the wind is the cheapest form of renewable energy, costing around 4-7 $-cent per kW [12] in the international market. Libya is far behind the rest of the world in the use of wind generation. The first Libyan wind farm rated at 60MW is under construction in

Dernah and more feasibility studies for other wind farm sites are under investigation [13].

At the present, renewable energy accounts for less than 0.06% of the total generation in Libya [14]. This provides an extra motivation to identify potential DC distribution network technology and converter topologies, suited for the Libyan grid to smooth the transition to more renewable-based generation, which might encourage the Libyan government to cut down energy subsidies for the costumers and use the funds available to increase the installation of renewable energies.

2.3 Libyan transmission and distribution lines

The Libyan transmission and distribution system relies traditionally on voltage levels from 0.4 kV AC to 220 kV AC. In the recent years, a new voltage level of 400 kV AC was introduced [8]. The new voltage level was introduced due to power quality problems in the grid, such as voltage sags and blackouts. These power quality problems are present in the distribution grid even after the introduction of the higher 400kV AC transmission lines thus different solutions should be investigated [9]. Figure 2.1 illustrates the Libyan electrical transmission grid [13].

The transmission and distribution lines are constructed from voltage levels of 0.4 kV to 400 kV [8]. Table 2.2 indicates the total distance installed at each voltage level [8], while Table 2.3 indicates the number of stations and the installed power for each voltage level in 2010 [8].

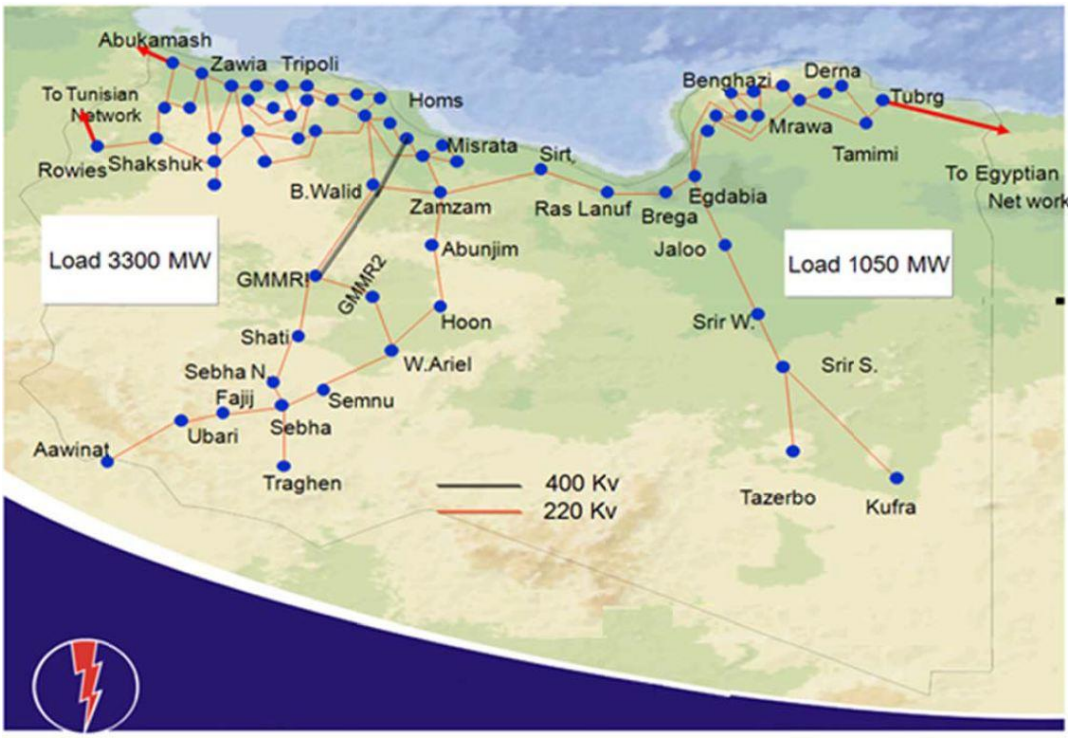


Figure 2.1 Libyan electrical transmission grid (reprinted from [13]).

Table 2.2 The total installed distance at each voltage level [8]:

Voltage (kV)	Length (km)
400	2,290
220	13,706
66	14,312
33	11,142
11	51,482

Table 2.3 Number of stations and the installed power at each voltage level [8].

Voltage (kV)	Number of Stations	Total installed power (MVA)
400	13	9,600
220	81	15,785
66	195	4,359
33	460	13,884
11	12,800	not reported

From Table 2.2 and Table 2.3 it can be noticed that the installed length of the 11kV lines was around 51,482 km. While the number of 11kV stations was 12,800 in all Libya. Moreover, most of the 11kV stations are using transformers without any voltage regulation capability such as tap-changing thus they cannot be used to regulate the voltage at the medium and low voltage level. Thus grid reinforcements are currently performed at this voltage level in order to increase the grid capacity. Furthermore, loads and distributed generation are normally connected at the 11 kV voltage level or the 230V 1-phase, 400V 3-phase levels. This highlights the importance to focus the study on the lower voltage levels in order to reform the Libyan grid and solve the Libyan energy challenges.

2.4 Libyan loads

The nature of loads in the electrical grid is one of the key factors which determine its optimal transmission, distribution, generation, and storage strategies.

The peak load in the Libyan grid has increased from 2.6 GW in 2000, to around 6 GW in 2012. Figure 2.2, Figure 2.3 and Figure 2.4 [15] illustrate the total Libyan grid load for the days of the highest, medium and the lowest Libyan power consumption in 2012. This un-published information was provided by (GECOL) [15].

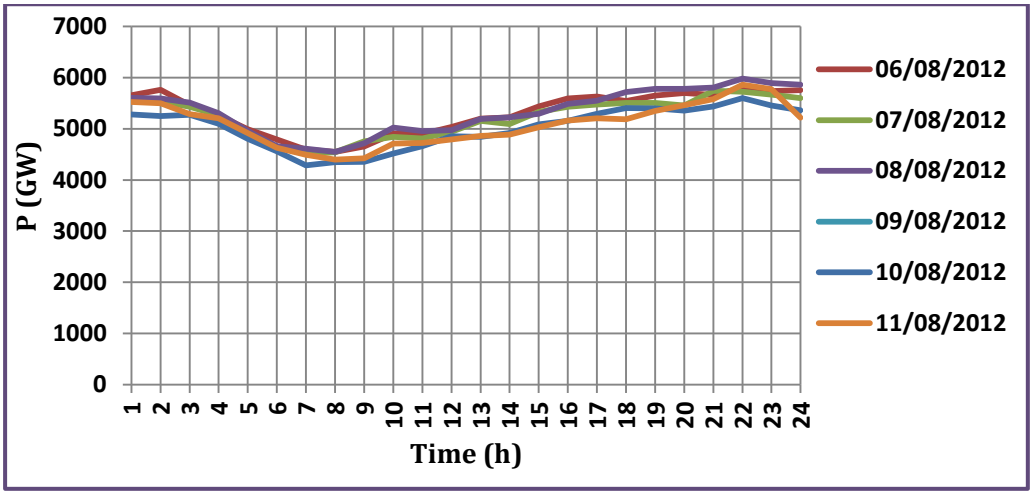


Figure 2.2 The daily load curves in Libya for the week with highest loading in 2012 [15].

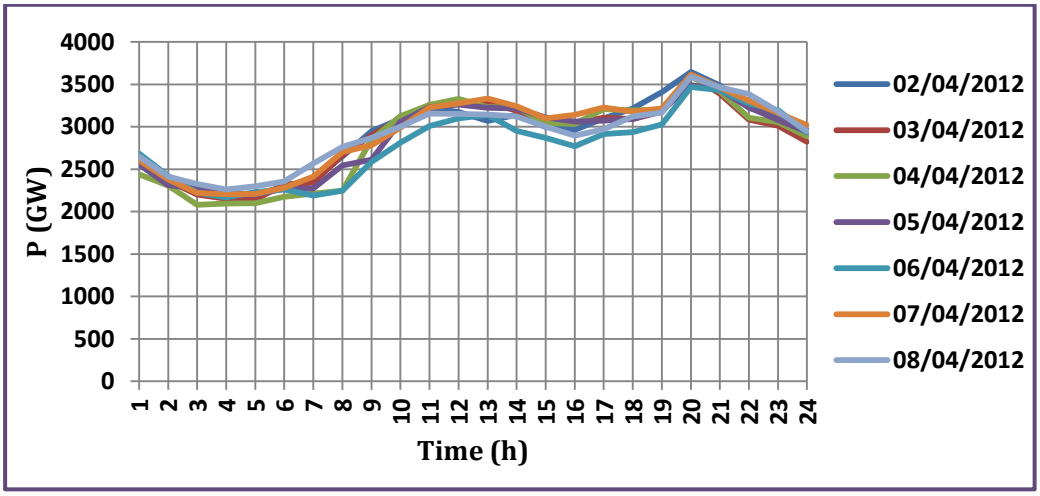


Figure 2.3 The daily load curves in Libya for the week with the lowest loading [15].

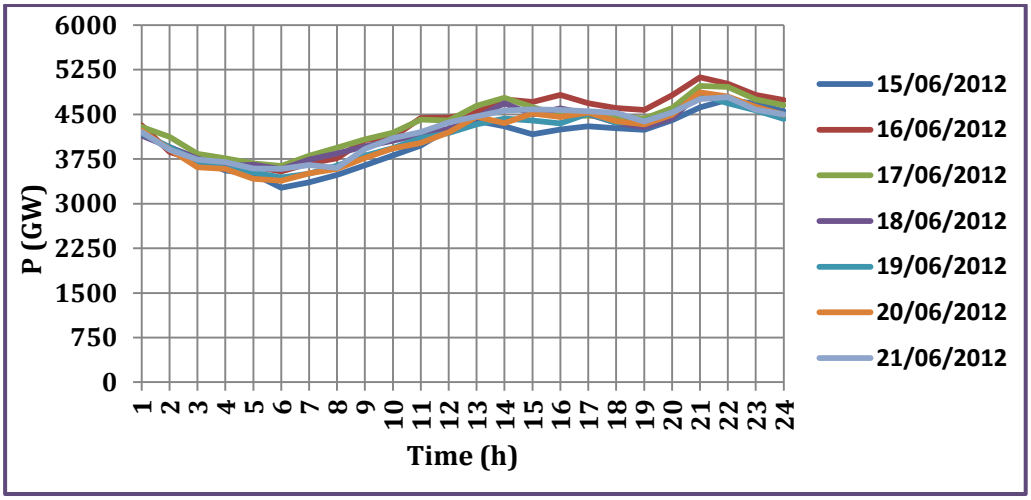


Figure 2.4 The daily load curves in Libya for the week with medium loading [15].

From Figure 2.2, it can be noticed that the load does not change much during the day, which is mainly because August is the most humid month in Libya and thus the usage of air-conditioning has dominated the load and almost a flat curve can be noticed.

While for Figure 2.3 and Figure 2.4 it can be noticed that the Libyan grid follows the normal patterns expected to be seen in any electrical grid, where the two peaks linked to the human activity during the day are present and the lowest usage of electricity happens during the night.

April is the most pleasant month in Libya, thus there is no need for air-conditioning or space heating, which caused the electricity consumption to be the lowest in that month as seen in Figure 2.3.

To further understand the effect of loads on the Libyan grid, a closer look should be given to the consumer types within the Libyan grid which is indicated in Figure 2.5 [14].

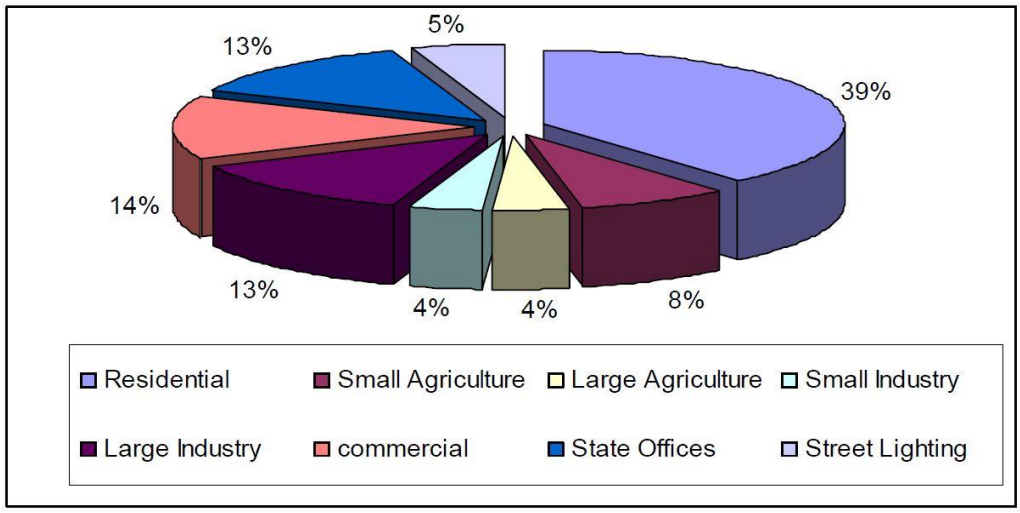


Figure 2.5 The consumer types within the Libyan grid (reprinted from [14]).

From Figure 2.5 it can be noticed that the domestic loads account for around 39% of the total load in Libya, followed by commercial (refers to shops and similar activities) load of around 14% and state offices' of around 13%; these three

loads account for 66% of the total Libyan load thus a change in these loads will lead to a reform of the Libyan electricity usage.

In order to fully understand the trend of consumption within the Libyan grid, the domestic loads, which are the highest load, should be examined more closely. A study was previously conducted in three major Libyan cities Tripoli, Benghazi, and Sabha. The aim of the study was to identify the nature of the Libyan residential loads and the devices present in a Libyan household [16]. In that study, consumers were classified based on the total installed power of electrical appliances in the house into three categories, small consumers: 0-5,000kWh/year, medium consumers: 5,001-10,000 kWh/year and large consumers: over 10,001 kWh/year [16]. Table 2.4 presents a sample of the distribution of consumers for each city and

Table 2.5 provides the average consumption of each consumer group.

Knowledge of the equipment present in the Libyan household is required to assess the appropriate dc voltage levels as well as possible grid arrangement and converter design. A detailed description of the typical Libyan household electrical equipment is presented in appendix (A) [16].

To conclude, the domestic load is the highest load in the Libyan grid, where air-conditioning is the leading consumer of electricity within the Libyan household. This situation is encouraged by the energy subsidies provided by the Libyan

government which leads to overconsumption of electricity, mainly for air-conditioning. Thus a change to a high-efficiency

Table 2.4 A sample of consumer distribution in three major cities in Libya [16].

Area		Small consumer	Medium consumer	Large consumer	Total
Tripoli	Number	112	69	39	220
	Percentage	51%	31%	18%	55%
Benghazi	Number	43	42	15	100
	Percentage	43%	42%	15%	25%
Sabha	Number	13	27	42	82
	Percentage	16%	33%	51%	20%
Libya	Number	168	138	96	402
	Percentage	42%	34%	24%	100%

Table 2.5 The average annual consumption of each consumer group [16]:

	Tripoli (kWh)	Sabha (kWh)	Benghazi (kWh)	Libya Average (kWh)
Small consumer	3,356	3,762	3,954	3,640
Medium consumer	7,006	6,729	7,378	6,994
Large consumer	16,064	14,469	14,928	15,318

DC drive air- conditioning seems a good option to improve the Libyan grid voltage quality and might reduce the need for grid reinforcements

2.5 Libyan standalone grids

The standalone solar energy systems in Libya include communications systems, water pumping systems, and isolated villages electrical systems [17].

Libyan standalone grid systems are mainly small villages away from the central grid and due to the large size of Libya and the scattered distribution of inhabitants; some areas in Libya are not connected to the main Libyan grid for economic reasons.

The GECOL defines the areas which are not economically viable to be connected to the main grid as those areas with about 200 inhabitants per location and at a distance of 5km or more from the 11kV lines or those with 500 inhabitants per location and about 15km distance from the 11kV line [17] .

It was estimated that the number of people in Libya fall into the last two categories to be around 25,000 and the GECOL decided to build renewable electrical systems in 370 locations in order to serve them [17].

These local systems can be divided into two different formats, either the houses are connected to the islanded grids or is

consist of standalone houses systems. The following are examples of these two systems:

2.5.1 Standalone PV system for Almarhan Well Village [10]

This is an example of a system where the houses are not connected to a local grid. 30 families live in a village in the middle of a large area of pastures which is about 80km from the nearest city [10]. Furthermore, it has a school and all other services and therefore it is considered as a centre of services in the local area [10]. This village is far from the main grid and needs electricity for houses and water pumping. The electricity needs of the village are given in Table 2.6 [10].

Table 2.6 The electricity needs for Almarhan Well Village [10]

Unit	Number	Power per unit (W)	Total energy consumption (Wh/day)
Residential	47	170	1,220
School	1	1,020	9,660
Services	1(11)	5,180	35,430
Total	47	14,390	93,030

Table 2.6 does not include about 60 m^3 of water pumping and street lighting. Figure 2.6 illustrates one of the systems in this village [10].



Figure 2.6 One of the solar systems in the Almarhan Well Village (reprinted from [10]).

The overall electrical village system is made of 47 independent systems which are not connected to a local grid with ratings as presented in Table 2.7 [10].

Table 2.7 The details of the installed systems rating for the Almarhan Well Village [10].

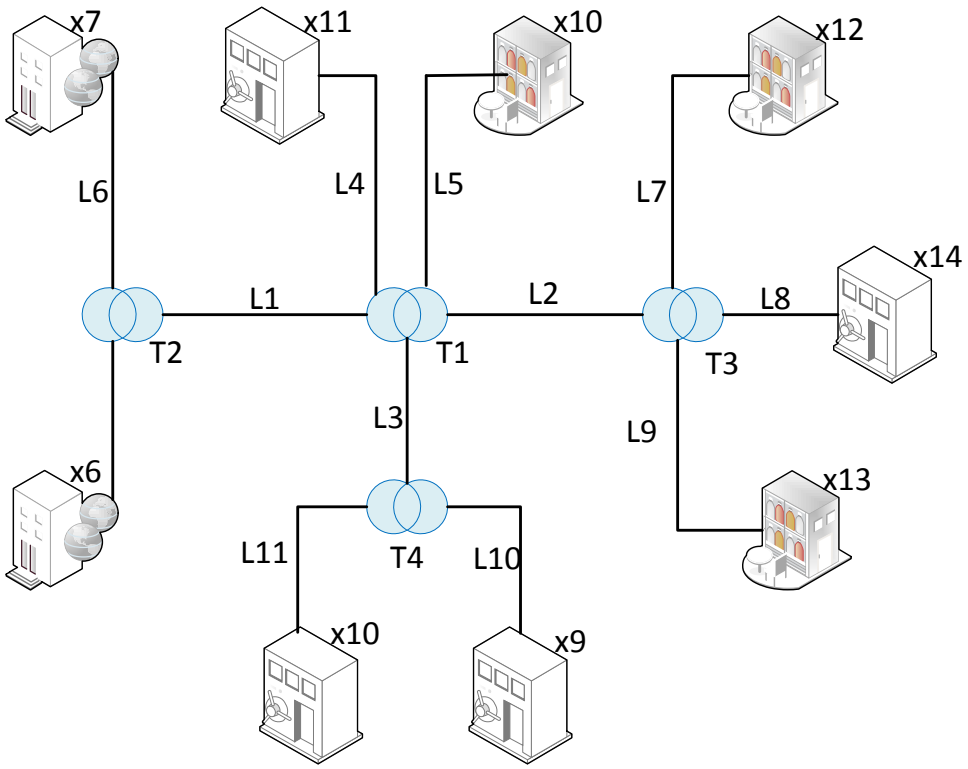
Unit	Number	Solar panel (W)	Battery charging regulator (A)	Battery capacity (kWh)	Inverter (W)
Residential	21	375	30	5.040	-
School	1	3,600	180	60.48	3,500
Services	1(11)	14,400	540	230.88	8,000
Lighting	9	75	-	-	-

2.5.2 Hybrid diesel/solar system for Misread Valley village:

This village is far from the grid as the nearest city is about 95km away [11]. The village has 45 houses and some extra service buildings such as a health centre and a school. All the buildings are connected to a local grid [11]. Figure 2.7 presents the lay out of the system.

The local grid used to be supplied by a central diesel generator, which provided power for a limited time due to the high costs and the repeated breakdowns of the diesel generator thereby limiting the electricity supply to the village. In order to upgrade the grid, a hybrid diesel/solar generation system was proposed, while keeping the old local grid. The resulting system specification is as follows [11]:

- Electrical over-head line 11kV 5km.
- One 200kVA 400V/11kV step up transformers.
- Three 75 kVA 11kV/400V step-down transformers.
- 67.2 kW solar panels.
- 873.6 kWh Battery.
- 14 Battery charging regulators.
- Two inverters of 15 kW each.
- 75 kVA Diesel generator [50].



Transformer 400V/11kV		11kV line		230V phase	
N	Rating (kVA)	N	L (km)	N	L (km)
Step-up		L1	1.5	L4,L8,L11	0.7
T1	200	L2	1	L5,L9	0.4
Step-down		L3	0.5	L6	1.5
T2	75			L7	0.6
T3-T4	50			L10	0.3

Figure 2.7 The layout of the islanded electrical network in the Misread Valley village [11]



Figure 2.8 The solar panels in the Misread Valley Village reprinted from [11]

This project was proposed mainly for the purpose of testing the performance of solar panels, batteries, and converters in the Libyan desert and to check the acceptance of the technology by the local population.

2.6 Conclusion of the Libyan Grid

The Libyan electrical system is mainly connected into a main grid with some isolated grids located in the desert. The residential loads are the highest loads were energy is heavily used to heat water and for air-conditioning. There is a great potential of using PV as the main source of generation for the Libyan grid due to the availability of high solar radiation, which is one of the highest in the world, within all areas of Libya.

The air-conditioning loads which use induction motors can significantly affect the distribution system performance and cost due to the presence of high reactive currents, which lead to poor power quality, such as high losses, voltage sags and drops, and blackouts. This caused the GECOL engineers to perform expensive grid reinforcements on regular basis at the distribution system level.

In order to improve the Libyan grid, there is a need for a system, which can accommodate PV generation, support air-conditioning loads, and distribute power over the short range at suitable voltage levels. Thus a DC system seems a viable option to resolve the Libyan grid challenges.

The next chapter will include a review of the current use of DC voltage systems, and the impact a change to DC voltages might have on the distribution grids generally and the Libyan grid specifically.

Chapter 3

Current DC usages in electrical systems

3.1 Introduction.

This chapter presents a review about the current usages of DC voltages, and the impact a change to DC voltages might have on the distribution grids. Different DC applications will be reviewed in order to explore what DC voltage levels are used and what knowledge can be transferred to the DC distribution grid.

Next, the grid hosting capacity will be defined; the factors impacting it will be investigated, in order to examine the benefits a switch to DC voltages might bring to the grid hosting capacity.

The main focus of this chapter is to assess the present use of DC voltages in grids and to examine the possible impacts and improvements DC voltages might bring to the distribution grid.

3.2 DC applications in electrical systems.

DC is already present and gained grounds in many applications; these vary in installed power from the high voltage GW DC transmission systems to the micro application of Led lighting. DC voltage is also used in well-established systems such as train and tram grids which rely on DC voltages for their operation [18]. Next, a range of DC application and systems will be explored.

3.3.1 The International Space Station (ISS).

The ISS has the largest DC system ever sent to space [19]. The ISS electrical distribution system is organised in a hierarchical arrangement. The ISS electrical system is made from hundreds of DC-DC converters arranged into several system structures [19]. The DC distribution systems onboard the ISS can be classified based on the DC voltage levels into two main classes: an American 120 VDC, and a Russian 28 VDC [19]. A set of the DC/DC converters are used to link

between the American and Russian voltage levels and arranged as a Solid State Power Controller Module (SSPCM). The SSPCM has two 120V DC inputs (main and secondary) and contains three 1100W DC/DC converters delivering 28V to loads [20]. The ISS energy comes from two solar cell arrays rated at 25KW each [21]. The ISS utilises six batteries; the batteries are made of two Orbital Replacement Units, each unit capable of storing 81 Ah. The international space station electrical systems were built over a long period of time from components supplied by different companies. This clearly indicates that DC systems can be easily expanded over time, which is intersting for the DC distribution system.

3.3.2 Shipboard power systems.

Modern ships are fully electrically driven, the main shafts linking engines and propellers are replaced with electrical cables. Furthermore, most of the traditional shaft propelled ships have large electrical loads and depend on electrical systems such as radars and other navigation equipment. The modern electrical distribution system in ships relies on DC zonal distribution; in this systems, AC voltage is first converted to high voltage DC, which is then distributed throughout the ship [22]. DC zonal distribution system advantages in comparison to the conventional system include:

- Enhanced reliability of the shipboard distribution system [23].

- DC zonal systems require simpler algorithms to detect faults and restore services [22].
- The system enhances power density, thus leading to a material and weight saving.
- The power electronic in the DC system has a dual functionality of power conversion and protection, allowing the use of fewer circuit breaker and protection equipment.
- The use of DC voltages allow a higher power to be distributed at the same voltage levels, thus wiring and insulation materials can be reduced [23].

Figure 3.1 indicates a shipboard DC zonal distribution system [23].

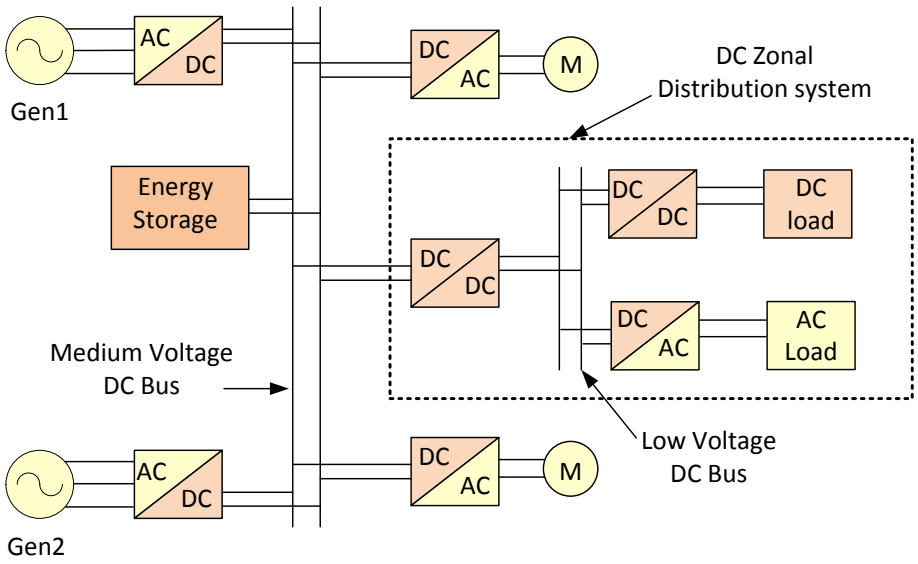


Figure 3.1 Shipboard DC zonal electrical distribution system [23]

The shipboard DC zonal system is a good example where DC voltage can bring multiple benefits to the distribution system.

3.3.3 Data centres.

Data centres play an important role in our modern society, due to the immense amount of information processed and stored in them. This effect services such as telecommunication, the internet, and banking. Subsequently, a reliable and uninterrupted power supply is a must for data centres.

The data centres are significant energy consumers, their energy needs were approximated in 2005 to be around 40 TWh in The United States and 120 TWh worldwide [24]. The author of [25] valued their market at around $9.84 billion.

In a classic data centre which typically uses 400/480 VAC distribution system [26]; cooling of electronics consumes more than half of the energy delivered while computing loads uses the other half. Due to the high losses in this sector, some papers proposed a change to a new distribution strategy. The author of [24] stated that using the 400 VDC will give a better performance with an efficiency of around 73%, while the efficiency of the existing AC system is about 55%. Figure 3.2 indicates a possible DC grid arrangement for data centres. [27]

Finally, using DC distribution system will allow the reduction of one conversion stage the computers input rectifier stage, resulting in fewer converters, thus making of more reliable

power source which is the main requirement of data centres and modern power supplies.

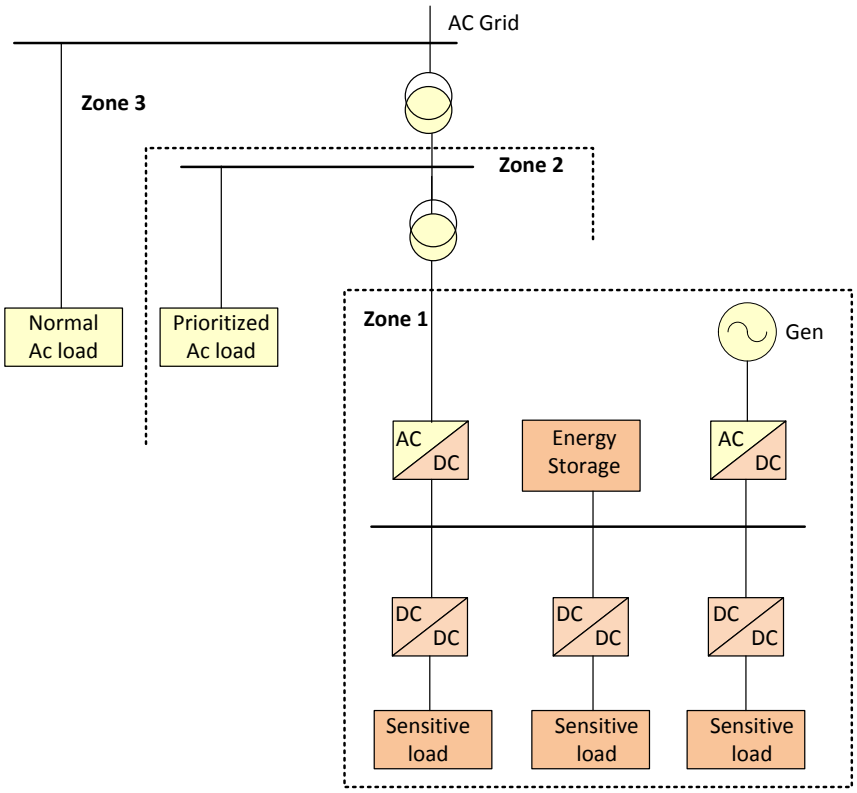


Figure 3.2 Structure of DC grid for data centres [27].

The most important points to gain from the data centre trials is the potential increase of high efficiency and energy saving due to the decrease of converter stages in the system, the high reliability, last but not least, the reduction of cooling loads which is of a great important in a hot climate such as in Libya.

3.3.4 Railway systems

The railway system is increasingly relying on electricity due to the high price of diesel. For example, a contract was

signed 2009 in Spain to upgrade 16 train lines to electrical, worth of a total of 413,7 M€ [28].

Furthermore, when an electrical rail system is used, regenerative braking can be applied, increasing the efficiency of the overall system. This efficiency improvement gained the UK electric rail the title of best carbon dioxide emissions reduction among all sectors of the UK economy when the emissions were reduced by 26% over the period from 1995-2005 [18].

The electrical railway uses DC voltage systems such as 600-1000 VDC systems for Metros and light Railways, the 1500 VDC systems are used for heavier Metros, and the 3000 VDC systems are utilised for the main and out-of-town lines while higher AC voltage are used for the longer distances [29].

3.3.5 LED lighting.

Lighting energy consumption is estimated to be 22% of total energy consumed in buildings [30]. LED lighting is the most advanced Lightning with a great potential to be the dominant light source in the future, due to high efficiency, extended lifespan, and low maintenance required [31]. LED lighting is capable of achieving the same illumination with less than 45% energy consumption, in comparison with fluorescent lamps systems [31] as the florescent lamps uses extra parts such as the power factor correction stage [32]. Furthermore, higher efficiency LED lighting systems can be designed by deploying LVDC, resulting in smaller LED lighting units [33].

Figure 3.3 indicates a proposed LVDC arrangement, which can be used with LED lighting [31]. The LED lighting units are rated at 1.5 V [34], and the LVDC works with 24 VDC [31].

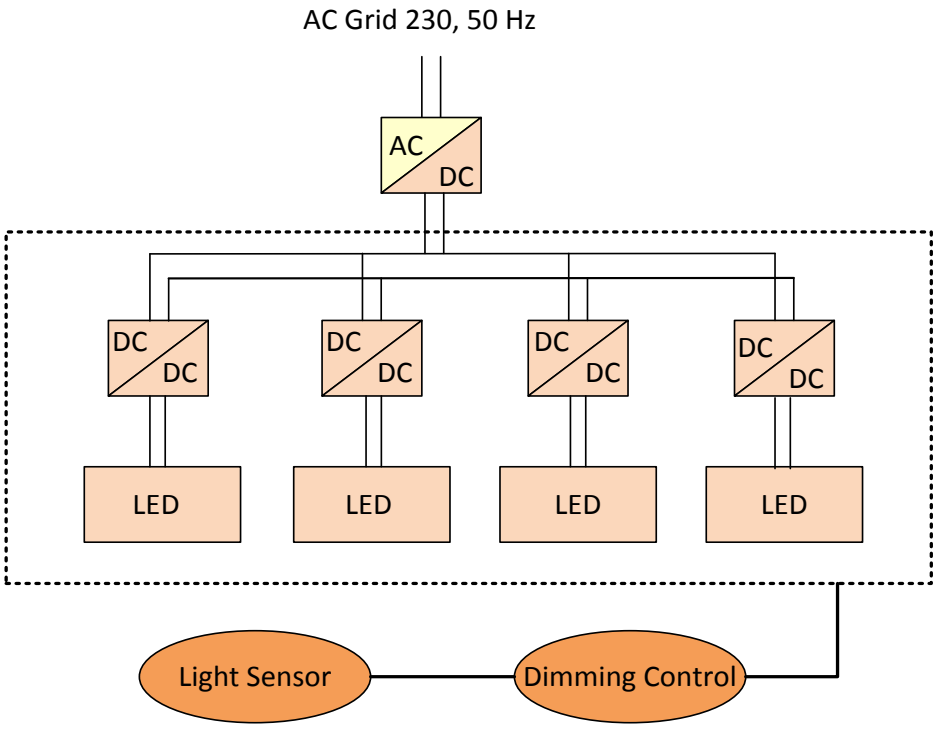


Figure 3.3 Proposed arrangement for low LVDC for LED lighting [31].

LED produces light without infrared [33], thus residents comfort in hot countries (such as Libya) can be increased which reduces air-conditioning requirements. Furthermore, using a converter to drive LED lighting results in simpler light dimming control [33].

Furthermore, the LVDC network can be expanded to accommodate more dwellings loads as in [7] where the author stated that changing the normal 50 computer office

from 230 VAC into 28.5 VDC will lead to an increase in the efficiency of the system by around 15%.

To sum up, DC is not an alien technology and is already in use in the grid. Thus a complete low voltage DC distribution grid seems feasible as most component and required expertise are available due to the present of DC in many applications. Next, the voltage levels used in the present DC applications will be presented.

3.3 The current used DC voltage levels

In this part of the thesis, the academic work and the present used DC voltage levels will be investigated and explored. This will allow for a better understanding of the most suitable DC voltage levels to be used in DC grids. The DC voltages levels which have been reported by in publications, can be classified into three main categories according to the International Electrotechnical Commission (IEC) standard 60038 voltages [35]:

3.3.1 Extra-low voltage:

The voltage level is this category are voltages lower than 120 VDC and are classified as low-risk voltages according to the IEC standard [35]. The reported extra-low voltage levels include:

- 20 VDC is the most suitable for small electrical devices, which usually supplied from an external DC supply [36].

- 48 VDC is heavily used in telecommunication, resulting in the accessibility of components required to build a grid with this level [35]. Furthermore, this voltage level is also considered safe. Therefore, no protection against direct contact is required [38], resulting in a simpler system. On the other hand, the authors of [39] claimed that 48 VDC is not a useful option in the distribution grid to supply houses with energy as it has lower power transfer capability which limit it is use in the distribution grid. The authors of [39] state that this 48 VDC voltage level can be used in applications where small distance and low power is required such as inside houses.

- 120 VDC can be used as an intermediate voltage level between the present AC voltage, and lower voltage levels [35].

3.3.2 Low voltage:

This category includes voltages from 120 VDC up to 1500 VDC which have a potential hazard of electric shock according to the IEC standard [35]. The reported low voltage levels include:

- 230 VDC has the same value as the RMS of the AC single phase value. Thus single phase AC resistive loads can be linked to this voltage without modification [36].

- 325 VDC is identical to the magnitude of the peak of the 230 VAC. If a large enough capacitor is present in the DC link after a device rectifier stage connected to

230 VAC a 325 VDC can be obtained [37], thus a numerous electronic equipment use this voltage level in their internal DC [38] [36].

- 400 VDC is commonly used in data centres [38]. The NTT facilities in Japan has been developing power distribution systems for data centres and telecommunication based on this voltage level [39].

- 600-1000 VDC: Metros and small railways use 600-1000 VDC systems [29].

- 1500 VDC: The 1500 VDC systems can be used for heavier Metros [40].The author of [6] stated that the ± 750 VDC bipolar will allow for a higher power transmission than the 1500 unipolar solution.

3.3.3 High voltage:

This covers voltages higher than 1500 VDC and has the risk of electrical arcing according to the IEC standard [35]. High DC voltage levels are present in many applications such as:

- 3000 VDC: The 3000 VDC systems are in use for main and out-of-town train and metro lines [40].

- 7500 VDC: this voltage level is in use in electrical ships and is usually made up from +3.75 kVDC and -3.75 kVDC resulting in 7.5 kVDC [41].

It can be concluded that the most suitable voltage level to be easily transferred to from the present 230 VAC will be the 325 VDC. Due to the electronic devices at houses which have

it as interim voltage, such as DC driven air-conditioning, and due to it is identical to the magnitude of the peak of the 230 VAC.

Another voltage level for use inside the house will be the 48 VDC, based on the availability of the components in the market, the experience with this voltage in telecommunication, and the fact that it's a good interim voltage between 325 VDC and the low voltage devices.

The European Union specification DIRECTIVE 2014/35/EU [40] allows for up to 1000 VAC in the low voltages grid, while it allows the use of DC voltage up to 900 VDC between earth and conductor and 1500 VDC between two conductors. Thus, the possibility of using DC voltages to replace AC voltages in the distribution system increases.

The European Union specification of 1500 VDC between two conductors will be considered as the boundaries for the highest voltage in this thesis work.

3.4 The technical aspects impacting the distribution grid hosting capacity:

The hosting capacity is described as the maximum rating of distributed generation (DG) at which the grid behavior becomes intolerable [41] which varies based on the performance index used.

Figure 3.4 illustrate the hosting capacity concept [41] This performance indicator can be based on many factors such as

losses, under frequency, under volatge, volatge sags, etc. From

Figure 3.4 it can be noticed that the grid has a range where the deterioration with the increase of the (DG) is acceptable but as the DG increases, the deterioration in the hosting capacity will become intolerable and the operation will move in the unacceptable deterioration region.

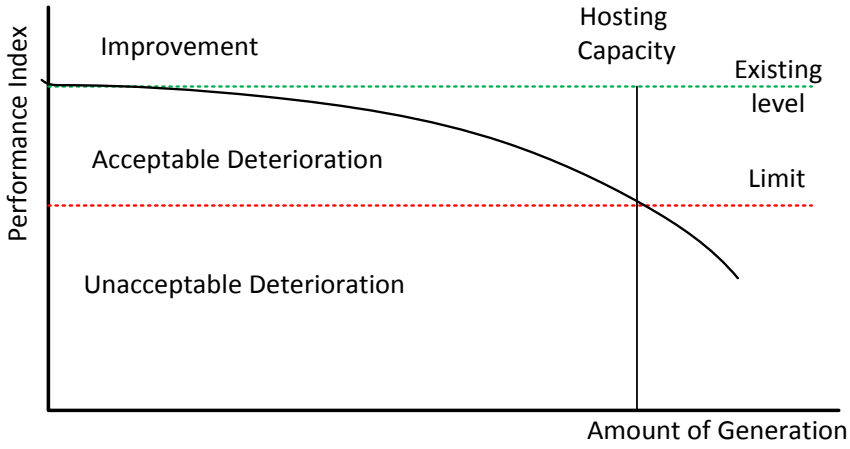


Figure 3.4 The hosting capacity concept [41].

Due to high pressure from governments and public to increase the amount of distributed generation (DG) and renewables in grids, as a future path towards higher renewable generation discussed in [42], there is a high demand for increasing the hosting capacity of electrical distribution networks. However, areas inside cities centres are not likely to be the key regions utilised for achieving these goals of increasing renewables energy utilisation. Hence, suburban and rural areas are likely to accommodate the increase in renewables sources.

The grids in suburban and rural areas are mainly built using radial systems. This might give rise to problems such as voltage unbalance, and voltage drop as they are fed only from one end and due to the long distance usually involved in this kind of systems, thereby, restricting the amount of DG that can be fed into the grid, This is noticeable in Germany's countryside where the grids are near their hosting limit [3]. Furthermore, areas inside cities are currently under high electrical loads which are likely to worsen with the introduction of more electrical cars thus a change to a more suitable distribution system such as DC distribution systems seems a good alternative. The main performance indicators impacting the hosting capacity are discussed next.

3.4.1 Voltage deviations.

Voltage deviations might lead to a complete collapse of the system. It was observed to increase in radial distribution systems if an electrical car charger is in operation due to the high current required by the car charger which mainly impacts areas inside city centres [43]. Equation (2.1) indicates the origin of this problem. Here, P_G and Q_G are the active and reactive power from the generation, P_L and Q_L are the active and reactive power demands from the loads [44] Figure 3.5 indicates the a diagram of the generation and load and the connecting line.

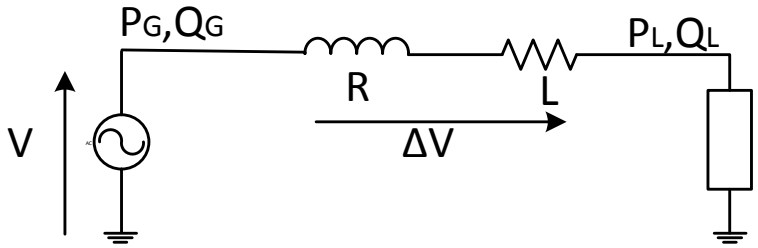


Figure 3.5 Diagram of the generation and load

$$\Delta V \approx \frac{(P_G - P_L)R + (Q_G - Q_L)X}{V} \tag{2.1}$$

Voltages levels are regarded as acceptable being between 96%-110% of the nominal value [45]. The author of [46] stated that the use of DC interconnection links, in a rural grid with high PV penetration, will improve the voltage deviation due to lower current and reduced voltage drop in the absence of reactive currents in DC systems.

By reducing the voltage deviation of the system, as presented in equation (2.1) were the voltage deviation will be resulted for the drop over R. Such as through the change to a more suitable DC distribution system, more DG and electrical loads such as electrical cars can be connected to the distribution grid, increasing its hosting capacity

3.4.2 Distribution grid current, power losses, and thermal limits.

For the same voltage level of DC and AC, root mean square voltages the use DC will lead to lower currents in the distribution grid, thus to lower power losses due to the non-existing of reactive current and reactive power. Equation (2.2) can be used to calculate the losses in the AC system where V is the line voltage at the point of common coupling [44].

$$P_{losses} = I^2 R = \frac{(P_G - P_L)^2 + (Q_G - Q_L)^2}{V^2} \times R \qquad (2.2)$$

When using equation (2.2) to describe DC system the reactive power term will be equal to zero, thus the current and losses will be lower at the same voltage level. The author of [46] stated that the use of DC interconnection links will lead to lower losses in the grid as the current will be lower and thus the power losses will be lower. If a cable voltage is changed from AC to DC for the same peak voltage level the cable will be able to carry more current and power, hence the hosting capacity of the system will increase.

Power losses will give rise to thermal stress on the grid component as all grid elements have a thermal rating representing the highest current a component can tolerate for an indefinite amount of time. The introduction of high installed power of DG and loads, such as electrical cars and PV, will lead to higher currents in the existing AC distribution system and thus higher thermal stress that in some cases, may exceed the hosting capacity limits of the grid, which is

limited to the thermal ratings of the grid's component. Reducing the reactive power in the distribution lines will enhance voltage and thermal limits [47]. If the system voltages are changed from AC to DC the losses will be lower, thus the same cables can be used to carry more power for the same voltage levels [44].

To sum up, future grids will rely more on DG and electrical cars resulting in higher current and losses in the feeders. The total current, power losses, and thermal stress will be lower if the same DC voltage levels are used to replace AC voltages in the distribution grid. Therefore, more electrical loads and DG can be connected increasing the hosting capacity of the system.

3.4.3 Voltage unbalance and frequency deviation

The introduction of high single phase distributed generation and loads, such as solar arrays and electrical cars, may cause voltage unbalance. The voltage unbalance factor ($\%VUF$) in a three phase system is defined as "as the ratio of the negative (V_-) to the positive (V_+) sequence voltage component " [44]. Equation defines the voltage unbalance factor.

$$\%VUF = \frac{V_-}{V_+} \times 100 \tag{2.3}$$

The voltage unbalance boundary in the UK is 1.3% [48]. This will limit the amount of generation or load per phase while in the DC system this problem is not present, Hence, giving a great preference for DC over AC, especially in grids with

electrical cars and high DG such as inner cities system or rural areas. This would allow for a higher percentage of DG or electrical loads to be integrated into the system and would increase its hosting capacity.

The grid's frequency is a factor of the load and generation levels in the grid. The UK frequency limit is 1% [44]. A DC system does not suffer from under frequency thus this limit does not apply to the DC system. Furthermore, if a local system was working in isolation from the grid after fault, reconnecting the systems zones is easier in DC than AC due to the not existence of frequency drift between the system zones. The last points give preference for DC over AC in the distribution network.

3.4.4 Harmonics and distortion level.

Harmonics impact on grids are likely to become more apparent with the introduction of electrical cars and DG as they are using power electronics to connect to the grid which might increase the harmonics present in general in the grid. The effects on the grid include:

- An initial small connection may stop the connection of a further customer, due to the fact that the grid has reached, it's tolerable harmonic limits.
- More filters may be required, resulting in extra cost [49]

Grid voltage harmonics can be assessed using the following factors:

- Individual limits on Harmonics Distortion (IHD)

$$V_{b,m}^{h} \leq IHD^{h,+} \tag{2.5}$$

- Total Harmonic Distortion Factor (THD):

$$\frac{\sqrt{\sum_{h=2}^{H}(V_{b,m}^{h})^{2}}}{V_{b,m}^{1}} \leq THD^{+} \tag{2.6}$$

Where:

$V_{b,m}^{h}$ is the voltage distortion at location (b) for harmonic number (h)[49]

The author of [50] states that by using DC-DC converters, lower distortion level will be present thus increasing the DC hosting capacity in comparison to the AC system. On the other hand it should be noticed that even with the use of DC systems, problems such as distortion and power oscillations still exist [51] thus a study should be carried out in order to compare the AC and the DC systems from this point of view which should be the scope of further studies.

3.5 AC systems hosting capacity improvement techniques.

The hosting capacity of AC systems can be increased through:

- Grid resizing which involve replacing cables and transformers. This is affecting city centres as more electrical loads such as cars and ground heat pumps are introduced. This will lead to a higher cost of refitting new cables in city centres which are not an option in historical cities. Also, it is expensive to implement and will have to be redone if the cable size was not correctly designed.

- Capping DG at times of high generation, the PV is capped at high solar radiation to prevent high current from penetrating to the grid [41]

The change to DC voltage may delay the need to any of the last expensive complex measures as the same cables can be used [52] and will allow for an ease in the introduction of more energy storage as they will have a higher capacity if DC voltages are used as explained earlier in this chapter. However, the only extra cost will be the cost of the power electronics, which, will be present in all future DC or AC grids to connect most DG and loads such as electrical cars and PV. Moreover, DC is more difficult to be isolated due to the non-existent of the zero current crossing in the DC this might lead to sparks in the DC switch gear which is usually bigger in size than the AC switchgear.

3.6 Conclusions:

This chapter presented a literature review on the DC voltage usages in the electrical systems. DC is present in many applications such as train and tram networks, DC shipboard system and data centres.

DC has the potential to overcome the challenges present in the low voltage AC distribution grid such as the Libyan grid as discussed in chapter two. In DC no reactive power is present, thus the grid losses and efficiency can be improved if DC is used to replace AC in the low voltage distribution network. This will lead to a better utilisation of cables and other components of the low voltage grid, increasing its hosting capacity, which might delay the need for grid reinforcements as the existing cables can be used to supply city centre's rapid increasing electrical loads.

The proposed solution to resolve the low voltages grid challenges would be a DC system with more than one voltage level, where the low voltage level of 325 VDC is used to connect local houses and the higher voltage level of 1500 VDC is used to distribute power over longer distances.

The next chapter of this thesis includes a detailed study of the performance of different proposed DC grids arrangements.

Chapter 4

DC Grid layout and DC/DC converter configuration assessment

4.1 Introduction

This chapter includes a simulation study to evaluate four DC distribution grid system layouts based on the total converter's losses and rating. Chapters two and three of this thesis included an assessment of the current situation of the Libyan grid and the benefits DC voltages might specifically bring to it and to distribution grids in general. These benefits included a possible reduction of converter losses due to the lower number

of conversion stages required in DC grids between the PV and the DC loads. Thus this chapter's study was proposed to investigate the effect of the possible different DC network structures on converter losses and installed power.

This chapter contains a study about DC grids and aims to achieve the following:

- Evaluate the DC distribution grid layout based on the converter losses.
- Investigate the converter configuration (two /three port) to serve the proposed DC distribution grid layout.

In order to achieve this study objectives, a group of four different DC grid arrangements will be simulated for varying house numbers. The case study will be the Libyan electrical grid while the methods and results are applicable to any general situation. Five different minute-by-minute daily load profiles for each home will be used to calculate the power transfers and the total losses for each grid arrangement, the average losses will then be calculated. Finally, a comparison will be made to evaluate the best grid arrangement and converter number of ports based on the total converter losses.

The method used will be explained in details in this chapter but it can be summarized as follows:

1- System design:

- Estimate the total load of the houses, based on the house appliances, and generate loading profiles for each house.

- Design the grid's PV, battery, and estimate converter rating.

2- Estimate the power transfer profiles between the converters.

3- Use the power transfer profiles and the converter losses contestant to calculate the converter losses.

4- Compare the grid and converter arrangements under consideration.

First, the grid layouts under consideration will be presented:

4.2 Grid arrangements under test.

For future DC grids, many possible grid arrangements are proposed. The proposed grid arrangements consist of two sections of different DC voltage levels linked using a DC/DC converter. The high voltage level will be used to link clusters of loads which are far from each other, while the low voltage level will be used to connect the nearby houses into a cluster. A high-voltage level of 1500 VDC was selected due to that this is the highest voltage the European Union specification allows to be used in a low voltage grid as a possible application is in European city centres.

325V DC was chosen for the low voltage side due to that the 325V DC is identical to the magnitude of the peak of the 230V AC voltage, and a great number of electrical appliances within the houses such as TVs, washing machines, and computers

have it as an internal bus. By using DC voltage in distribution grids the rectification stage in these appliances could be eliminated leading to fewer conversion stages and to higher efficiencies.

A group of possible DC grid arrangements was chosen to perform the study on. Figure 4.1, Figure 4.2, Figure 4.3 and Figure 4.4 present the chosen grid arrangements.

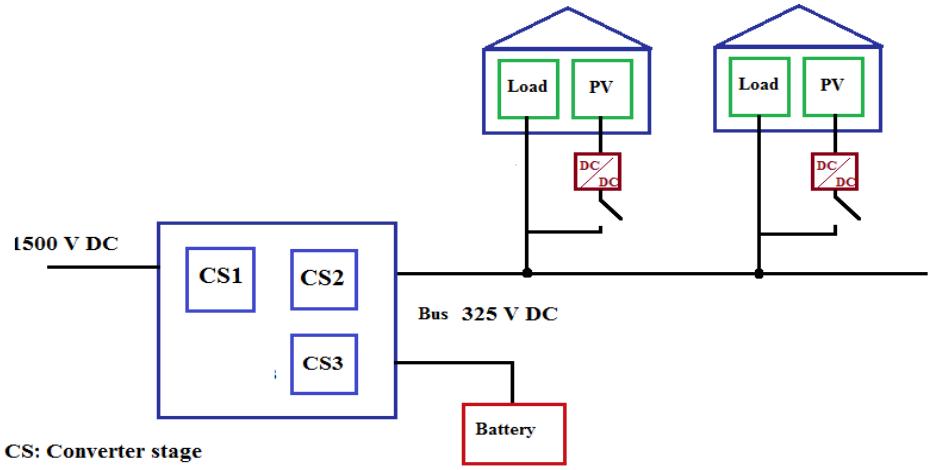


Figure 4.1 Arrangement ONE, three port converter with the battery connected to three port converter.

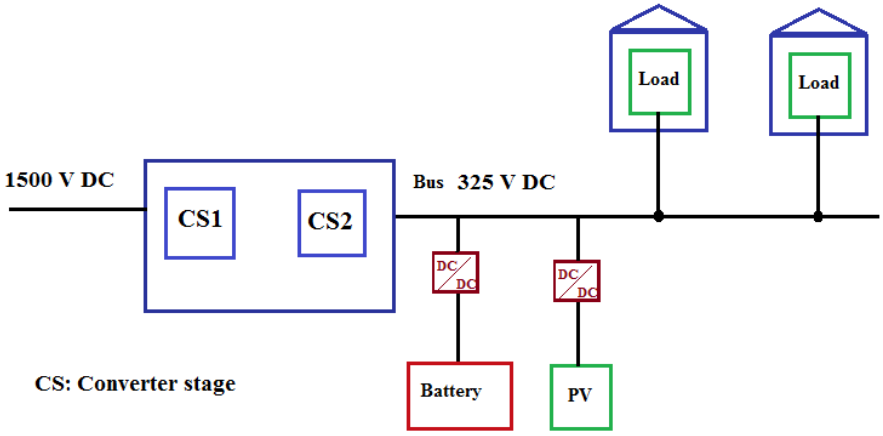


Figure 4.2 Arrangement TWO, two port converters with the battery connected through separate converter and centralized PV.

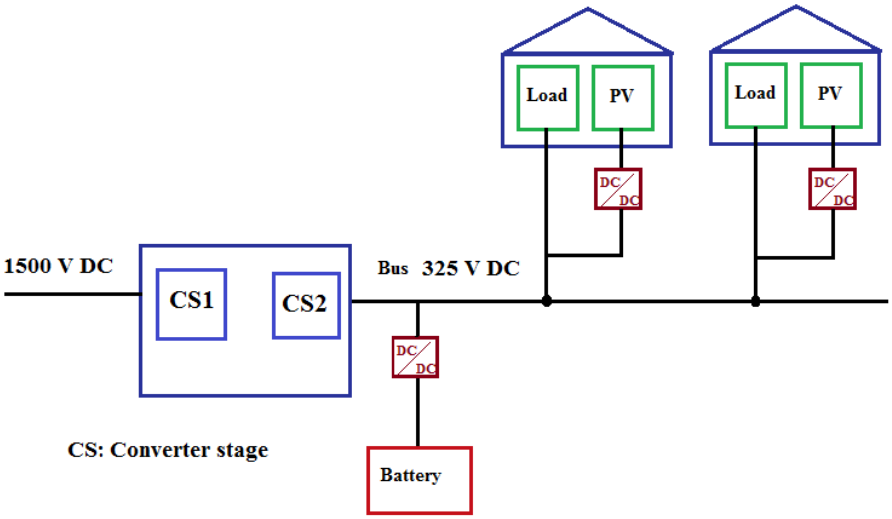


Figure 4.3 Arrangement THREE, two port converter with the battery connected through separate converter and distributed PV.

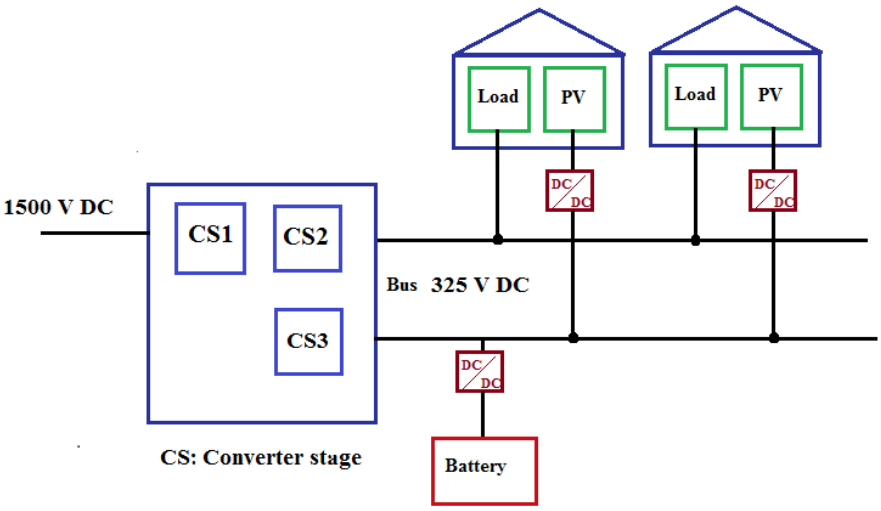


Figure 4.4 Arrangement FOUR, three port converter with two buses: a generation bus and a load bus.

CS1, CS2, and CS3 stand for converter stage which is a bridge used to transfer between the internal high-frequency transformer and the external DC bus as it will be discussed later in chapter 5.

Furthermore, the grids under consideration are a good combination of different grid scenarios: in Figure 4.1 arrangement ONE is presented which has a three port converter with the battery connected to three port converter and PV located inside the houses. Arrangement TWO is presented in Figure 4.2 with a two port converter, a central battery and a central PV connected directly to the low voltage DC bus. Figure 4.3 presents arrangement THREE, where the two port converter with separate batteries connected to the low voltage bus and distributed PV. Finally, Figure 4.4 presents arrangement FOUR, which has a three port converter and two buses, a generation bus and a load bus.

The study will consider the following scenarios based on the four grid arrangements:

- Isolated group of dwellings with variable house number
- Grid connected group of dwellings with variable house number.

4.3 The system design.

In this thesis, four different grid arrangements are under consideration. For each grid arrangement an estimation of the system component rating is going to be carried out. The system components sizes should be adequate for handling the grid's extreme power transfers. Due to the fact that the systems under consideration are systems using solar energy as the main source of generation, the maximum solar radiation available, in June in Libya, will lead to the most

extreme power transfers within the system. Thus the maximum solar radiation of June will be used as the guideline when sizing the converters which will allow them to handle these extreme power transfers. In order to size the system, the available PV resources and the expected system loads have to be estimated first.

4.3.1 Load estimation.

Estimating the connected loads is one of the key factors in designing a grid. The consumers' loading profiles should be estimated in order to evaluate power transfers and losses within the grid. The load estimation will be based on the design procedures and specifications issued by the Libyan general electricity company as Libya is the case study considered in this thesis [53]. The appliances for each house are allocated based on a previous study which was performed to estimate the probability of the Libyan household appliances [16]. The results of this study were presented in Table 2.4,

Table 2.5 in the chapter (2) and appendix (A). Table 2.4 and

Table 2.5 included the distribution and the load of houses within the Libyan grid. This information can be used when allocating the houses' sizes in this study. The distribution of electrical appliances within Libyan houses is presented in appendix (A). This information can be used when allocating appliances to the houses in this study.

After the house electrical load size and appliances are identified, the daily loading profiles for houses can be generated using the Domestic Electricity Demand Model

version one, developed at CREST (the Centre for Renewable Energy Systems Technology) at Loughborough University [54].

The CREST Demand Model version one produces minute by minute electricity house demand which results in 1440 points daily for the electrical load profile. The model uses data related to the activity of people in a house obtained from the surveyed time-use data [55], combined with information about the possible appliances in a Libyan house [16]. It results in a minute-by-minute loading profile from the CREST model, which can be used to estimate the power transfers and losses in the grid. Figure 4.5 shows the daily load profile for a Libyan house as generated using CREST model.

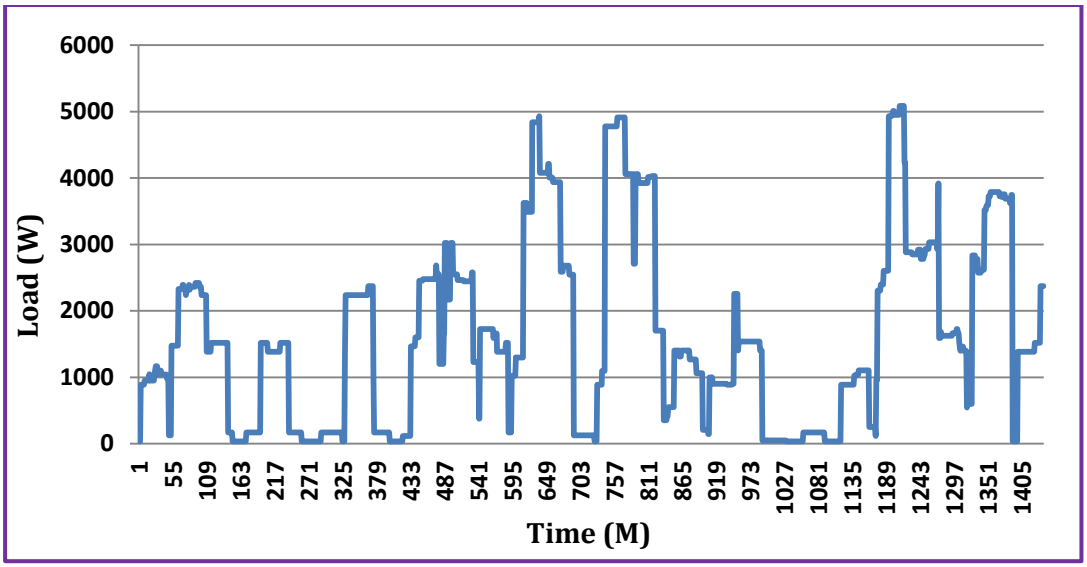


Figure 4.5 The daily load profile for a Libyan house as generated using CREST model.

In order to estimate a load of a grid some terms have to be defined first:

- The total connected load $P_{T\ load}$: "is the summation of the power rating of the total appliances connected to the grid" [53].

- Demand factor DEF: "is the ratio of the maximum demand of a system to the total connected load of the system" [56].

- Load factor LF: "Load factor is the ratio of the average load over a designated period of time to the maximum load occurring in that period" [56].

- Diversity factor DF: "is the ratio of the sum of the maximum power demands of the consumers or the sub-division of any system to the maximum demand of the whole of the system under consideration" [56] the inverse of this factor gives the simultaneity factor:

$$P_{T\ load} = Sum_{1}^{n}(P_{app\ \ n}) \tag{4.1}$$

$$P_{L\ \max} = P_{T\ load\ A} \times DEFA + P_{T\ loadL} \times DEFL \tag{4.2}$$

$$P_{L\ av} = P_{L\ \max} \times LF \tag{4.3}$$

Where:

$DEFA$ Demand factor for air-conditioning and motors.

$DEFL$ Demand factor for the house load excluding motors and air conditioning.

n Appliance number in a dwelling.

$P_{app\ n}$ The power rating of appliance number n.

$P_{T\ load}$ The connected load of one dwelling.

$P_{L\ \max}$ The maximum load of one dwelling.

$P_{L\ av}$ The average power of the load.

$P_{T\ load\ A}$ The connected air conditioner and motors load of dwellings.

$P_{T\ loadL}$ The house load excluding motors and air conditioners.

The maximum load and the average loads for a cluster of M dwellings can be calculated using (4.4) and (4.5) [53]:

$$P_{av\ cluster} = \frac{\sum_{1}^{M} P_{L\ av\ m}}{M} \qquad where\ \ m\ 1\ \ to\ \ M \tag{4.4}$$

$$P_{L\ \max\ M} = P_{T\ load\ M} \times DEF \tag{4.5}$$

Equation (4.5) can be rewritten for a house with both motors and normal loads as in equation (4.6)

$$P_{L\ \max\ M} = P_{T\ load\ A\ M} \times DEFA + P_{T\ loadL\ M} \times DEFL \tag{4.6}$$

$$P_{Max\ cluster} = \frac{\sum_{1}^{M} P_{L\ \max\ m}}{DF_M} \qquad where\ \ m\ \ from\ 1\ \ to\ \ M \tag{4.7}$$

Where:

$P_{av\ cluster}$ The average load for a group of dwellings.

$P_{T\ load\ A\ M}$ The connected air conditioner and motors load of dwelling number m.

$P_{T\ loadL\ M}$ The house load excluding motors and air conditioners of dwelling number m.

M Number of houses in the dwellings group.

$P_{L\ av\ M}$ The average load for a group of M dwellings

$P_{L\ \max}$ The maximum load for a group of M dwellings.

DF_{M} The diversity factor for a cluster of M dwellings.

The Libyan specification has two demand factors, 0.5 for the general appliances in a dwelling and 0.63 for air-conditioning and motors. While the load factor for the standard house in Libya is around 0.41 [53] the Libyan specification gives the simultaneity factor which is the inverse of the diversity factor as in Table 4.1 [53]:

The presented methodology is used to calculate the maximum load value and the average load value of a cluster of houses, which can be used to design the rating of the rest of the grid component. The same methodology can be applied to any general design, still, the specifications might change based on the location the system. Next, the methodology used to

calculate the rating of the different parts of the grid is going to be presented.

Table 4.1 The diversity factor for the Libyan grid [53].

No. of consumers	Simultaneity factor	No. of consumers	Simultaneity factor
2-5	0.753	31-35	0.493
6-10	0.630	36-40	0.471
11-15	0.630	41-45	0.450
16-20	0.547	46-50	0.429
21-25	0.541	51 and more	0.410
26-30	0.516	-	-

4.3.2 PV estimation.

The size of a PV string depends mainly on the available solar radiation. The location for the Misread Valley Village which is situated in the Libyan desert was chosen as the location for the solar radiation estimation.

The Misread Valley Village is located at, (Lat. 30.0°N, long. 13.0°E, alt. 400 m) [11]. The location of the village was fed to the PVSYST4 program in order to obtain the solar radiation [57]. It was found from the PVSYST4 analyses that a panel with a tilt of 45° and azimuth 180 (facing south) will receive in June a solar radiation profile as presented in **Error! Reference source not found.**.

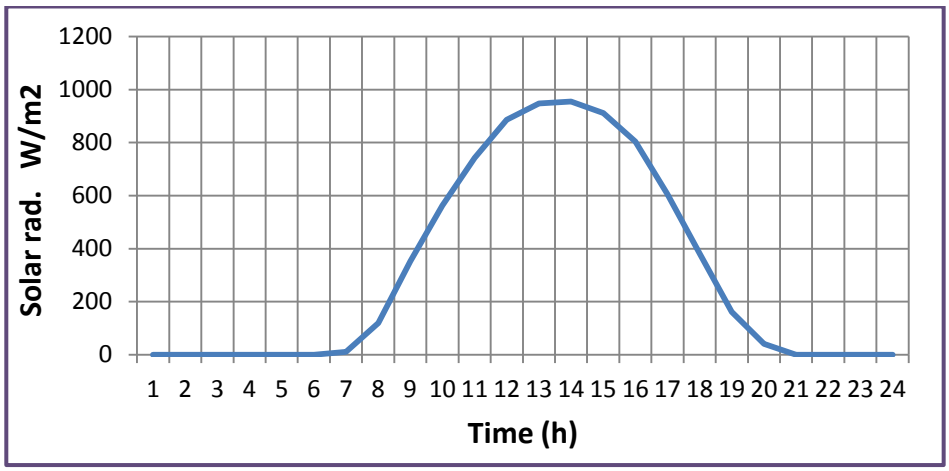


Figure 4.6 The solar radiation design data for a day in June.

The data from **Error! Reference source not found.** can be used to estimate the average PV power using (4.8) [58]:

$$P_{solar\ av} = \frac{\int_0^t P_{solarIn}}{T} dt \tag{4.8}$$

Then the required PV size to supply a load can be calculated using (4.9) [58]:

$$A_{PV} = \frac{P_{av\ cluster} \times \eta_{pv}}{P_{solar\ av} \times K_{loss}} \tag{4.9}$$

Where:

A_{PV} The required PV area.

$P_{solar\ av}$ The average solar power.

T The time over which the averaging was done over.

$P_{solarIn}$ The instantaneous power output from the PV.

K_{loss} A factor to compensate for the system losses K_{loss} =1.05.

η_{pv} The assumed efficiency of the solar cell η_{pv} =0.14.

The data from Figure 4.6 combined with the load profiles obtained from the CREST demand model will be used to calculate the power transfer within the system.

4.3.3 The battery rating.

In an electrical system, voltage blackouts and quality are the main considerations. A system with a battery connected will suffer from less blackouts and energy disturbance. Additionally, the battery can be used in the grid connected systems to store energy if a variable tariff is available, which enhances the grid economy.

In isolated systems, the battery will be used to store the PV energy during the day and provide it at night to the loads. The battery should be rated to supply the load at times when the sun is not available (T_{av}) within the day. The PVSYST4 used to calculate the sunshine for June.

$$T_{av} = \frac{sum_1^K T_{day}}{K} \tag{4.10}$$

$$E_{batt} = P_{L\ av} \times (24 - T_{av}) \times 1.2 \tag{4.11}$$

Where:

E_{batt} The energy rating of the battery in (Wh).

T_{av} The monthly average of the time when the sun is not available.

T_{day} The duration of the day the sun energy is available.

1.2 A security factor to ensure power availability.

K Number of days the averaging was conducted over.

Furthermore, the battery is going to be assumed to be an ideal voltage source for the scope of this study.

4.3.4 Converter rating

The grid arrangements under study have many converters; the converter rating has to be large enough to handle the extreme power transfers. For instance, if a converter is used to supply the power to a load it should be able to support the maximum possible load and if it in the solar power path the converter should have enough rating to handle the extreme power transfer which might flow at the peak of solar generation. The same applies for the grid side converters as they should be able to transfer the power to the grid when the solar is at maximum generation and the load is low, or when there is no PV generation combined with maximum load.

In the previous part of the thesis, the load profiles, battery and PV sizes were estimated. In order to link a system of loads, battery, PV, and grid, a suitably sized converter should be used based on the maximum power transfers within the system.

Thus, the rating of the system converters should be as follows:

Rating of PV converter $= MAX_0^t P_{out\ solarIn}$ (4.12)

Rating of load converter $= MAX_0^t (P_{out\ solarIn} OR\ P_{loadIn})$ (4.13)

Rating of battery converter $= MAX_0^t (P_{out\ solarIn} OR\ P_{loadIn})$ (4.14)

Grid side converter $= MAX_0^t (P_{out\ solarIn} OR\ P_{loadIn})$ (4.15)

Where:

$P_{out\ solarIn}$ The instantaneous output power from the PV.

P_{loadIn} The Instantaneous power transfer to the Load.

T The time the PV was measured over.

PV converter is the converter linking PV panels' grid.

Battery converter is the converter linking the battery to the grid.

Grid side converter is the grid side converter linking the cluster of houses to the higher voltage grid.

Load converter is the converter linking the load side of the cluster.

The rating of the converter estimated by (4.12)-(4.15) represents the maximum rating of the converter required to run the grid and the losses within the converter will be estimated based on the power transfer through them and the losses of the converter. Next, the method used to estimate the converter's losses will be described.

4.4 Modelling of converter losses.

In this thesis, the comparison is done between different DC grid arrangements based on the total grid converters losses. The converter losses vary with the converter loading and as a consequence, the overall losses performance of a grid is linked to the variation of the converters efficiency curves. Therefore, the converter losses variation with load should be presented as accurately, which are representative of the real converter loading.

This will be done by using equations which represent the converter loss change with the converter loading. The converter efficiency can be represented by (4.16) [59]:

$$\eta = 1 - \frac{1}{X_n}(A + B \times X_n + C \times X_n^2) \tag{4.16}$$

$$X_n = \frac{P_{in}}{P_{conv_rated}} \tag{4.17}$$

Where:

X_n is the normalized power of the converter

A, B and C constants representing the converter efficiency.

$$\eta = \frac{P_{in} - P_{losses}}{P_{in}} = \frac{P_{in}}{P_{in}} - \frac{P_{losses}}{P_{in}} = 1 - \frac{P_{losses}}{P_{in}} \quad (4.18)$$

From (4.15) and (4.17):

$$1 - \frac{P_{losses}}{P_{in}} = 1 - \frac{1}{X_n}(A + B \times X_n + C \times X_n^2) \quad (4.19)$$

Thus the converter losses can be represented by (4.19):

$$P_{losses} = P_{conv_rated} \times (A + B \times X_n + C \times X_n^2) \quad (4.20)$$

Equation 4.20 represents the losses of the converter as the converter loss change with the loading of the converter. Also, the efficiency curves follow different trends of change for small and big converters. Thus the same loss equation constants cannot be used to represent big and small converters. As in this thesis, the number of houses within the grid will be swept from 1-50 and hence the converter loss equation constants should be different for small and big converters.

To represent the converter losses for grids size varying from 1-50 homes, three SUNNY BOY converters were chosen to represent the losses [60].

Based on the converter installed power calculated to serve a grid with a certain number of homes, the converter loss

equation constants will be allocated. These constants combined with the converter installed power and the converters daily loading profiles will be used to calculate the daily total converter loss. Finally, the converters losses will be accumulated to calculate the total grid converters losses.

4.4.1 Low power converters (less 10kW).

For converters with a rating of less than 10kW, the SUNNY BOY 3000HF efficiency curve was chosen as the model to calculate the constants in the losses equation. The constants were obtained by using curve fitting of the provided data in a spreadsheet [60].

Table 4.2 The losses equation constant values for SUNNY BOY 3000HF

A	B	C
0.006	0.015	0.0488

In order to validate the model, a comparison between the original efficiency curve and the points obtained from equation 4.19 using the constants of Table 4.2 is presented in Figure 4.7

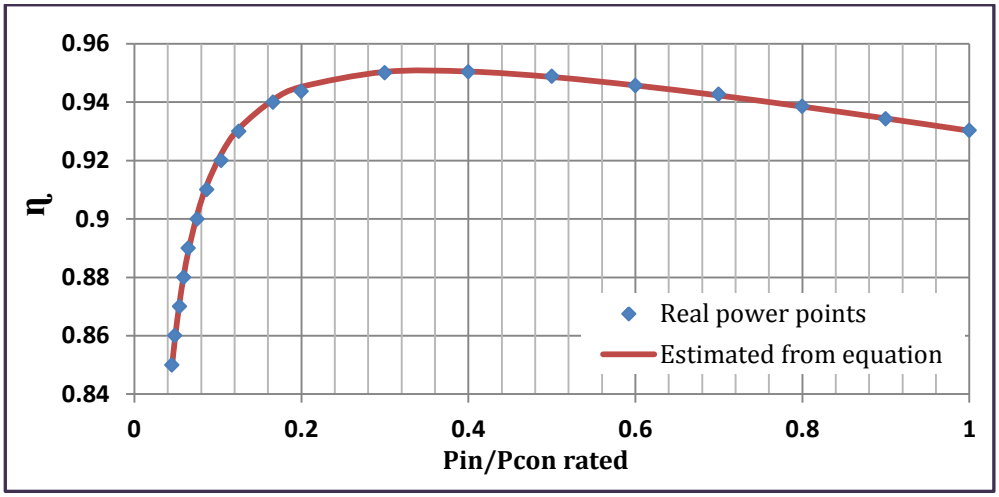


Figure 4.7 Comparison between the original efficiency curve and the efficiency curve obtained from the losses equation for the SUNNY BOY 3000HF.

The Root Mean Squared Error (RMSE) can be predicted using the following equation [61]:

$$RMSE = \sqrt{\frac{1}{n}\sum_{1}^{i}(y_i - \hat{y}_i)^2} \tag{4.21}$$

And was found to be RMSE=0.00103 with the the SUNNY BOY 3000HF fitting constants.

4.4.2 Medium power converters (between 10 kW to 100kW).

For converters with a rating between 10 kW and 100 kW, the TRIPOWER 17000TL efficiency curve was chosen as the model to calculate the losses equation constants [60].

Table 4.3 The losses equation constant values for the SUNNY TRIPOWER 17000TL.

A	B	C
0.00165	0.018	0.017

In order to validate the model, a comparison was run between the original efficiency points and the curve obtained from the constant in Table 4.3 is presented in Figure 4.8

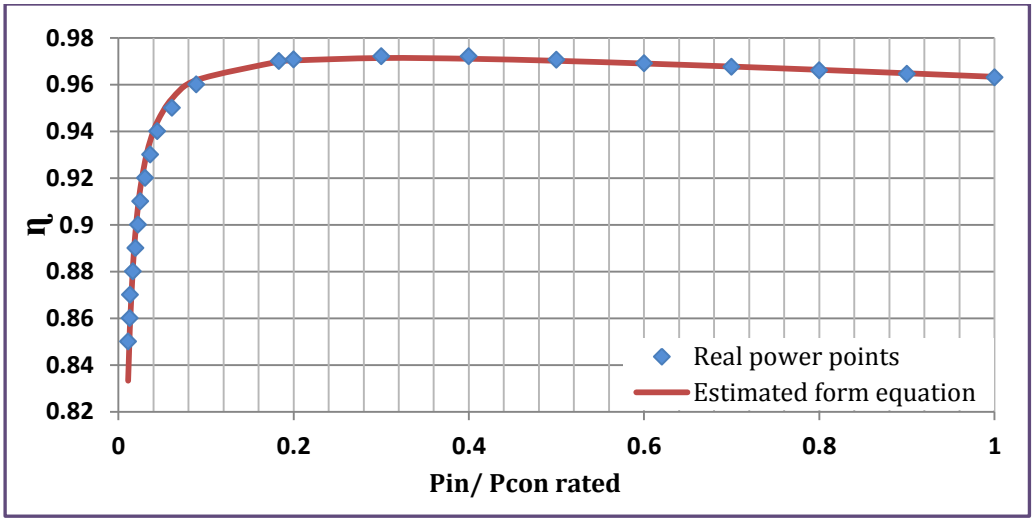


Figure 4.8 Comparison between the original efficiency curve and the efficiency curve obtained from the loss equation for the SUNNY TRIPOWER 17000TL

The RMSE for the TRIPOWER 17000TL fitting was calculated using equation (4.21) and was found to be equal to RMSE= 0.00581

4.4.3 High power converter (more than 100kW).

For converters with a rating of more than 100 kW, the SUNNY CENTRAL 800CP efficiency curve was chosen as the model to

calculate the loss equation constants which were obtained as explained in 4.3.1[60].

Table 4.4 The losses equation constant values for the SUNNY CENTRAL 800CP.

A	B	C
0.0021	0.007	0.0105

In order to validate the model a comparison was run between the original efficiency points and the curve obtained from the equation (4.19) is presented in Figure 4.9.

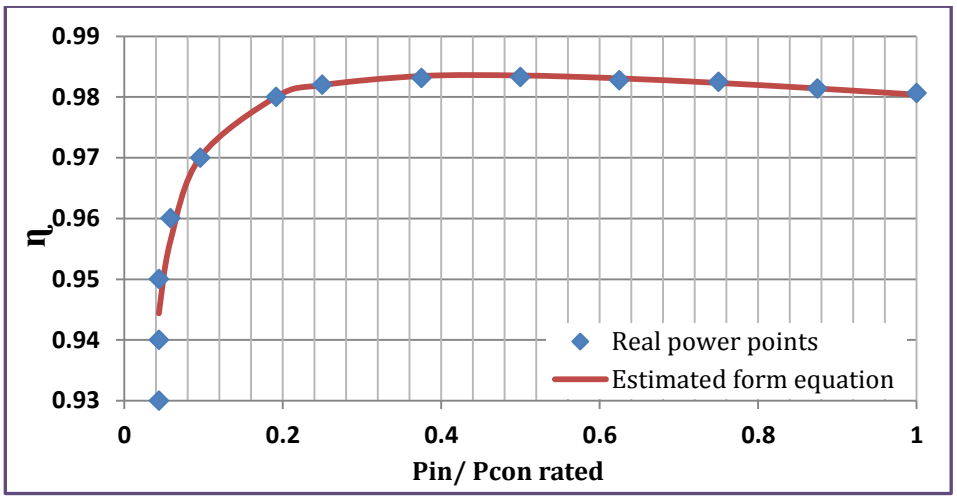


Figure 4.9 Comparison between the original efficiency curve and the efficiency curve obtained from the loss equation for the SUNNY CENTRAL 800CP.

The RMSE for the SUNNY CENTRAL 800CP fitting was calculated using equation (4.21) and was found to be equal to RMSE= 0.02.

4.5 Power managements.

In order to calculate the losses, the power management's strategy between the entire grid parts has to be established first. A simplified power management plan will be used for all the grid arrangements. The battery will act as the main energy source/sink in the cluster, storing energy when the generation is higher than the load and releasing it when the load is higher than the generation. When the battery is empty, the extra energy will be sent to the grid and if the battery is flat the grid will supply the load with energy. If the grid is working in an isolated mode and the battery is full the PV converter will be disconnected.

The power management between the grid parts can be described as follows:

In a standalone cluster of houses:

Power of the PV converter= $P_{solarIn}$ (22)

Power of the PV converter= $P_{solarIn}$ (23)

Power of the battery converter = $P_{solarIn} - P_{loadIn}$ (24)

In a Grid connected cluster:

Power of the PV converter= $P_{solarIn}$ (25)

Power of the PV converter= $P_{solarIn}$ (26)

Power of the battery converter = $P_{solarIn} - P_{loadIn} \pm P_{grid}$ (27)

Power of the grid converter = $P_{solarIn}$ - $P_{loadIn} \pm P_{battiIn}$ (28)

Where:

$P_{solarIn}$ The Instantaneous power transfer from the PV.

P_{loadIn} The Instantaneous power transfer to the Load.

P_{battIn} The Instantaneous power transfer to the battery.

$P_{grid\ In}$ The Instantaneous power transfer to the grid.

The transfer of power from and into the grid will be limited to times when the battery cannot supply the load or to times when the PV generation is higher than the loads and the battery is full.

Based on the power management strategy three modes of operation can be defined:

4.5.1 Modes of operation

4.5.1.1 Mode (1) The PV is equal to zero:

In this mode, the PV output will be equal to zero and the PV converter will be disconnected and its losses will be assumed to be equal to zero. Figure 4.10 indicates this mode of operation.

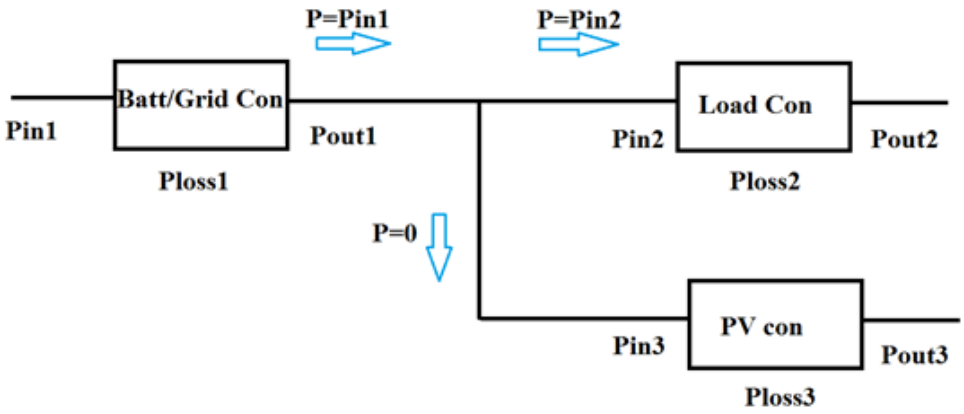


Figure 4.10 Power transfers in mode (1) where the PV output is equal to zero.

4.5.1.2 Mode (2) the PV output is higher than the load:

If the PV generation is higher than the one consumed by loads the extra power will be sent to the battery first and when the battery is fully charged the extra power will be sent to the grid. It should be noted that the grid converter will be always connected and producing losses as it is required to stay online to support the grid voltages at no load conditions. Figure 4.11 illustrates mode (2).

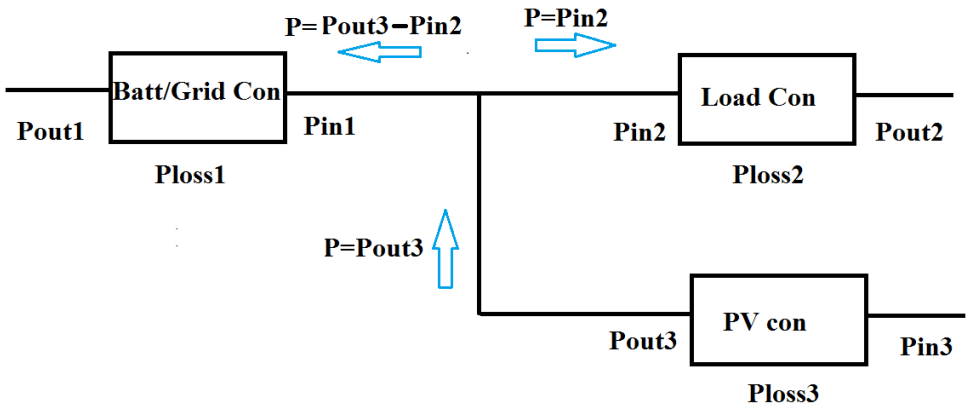


Figure 4.11 Power transfers in mode (2) the PV output is higher than the load.

4.5.1.3 Mode (3) the PV output is less than the load:

If the PV generation is lower than the connected loads, the required extra power will come from the battery first and once the battery is discharged, the load will be supplied from the grid. Figure 4.12 illustrates this mode (3).

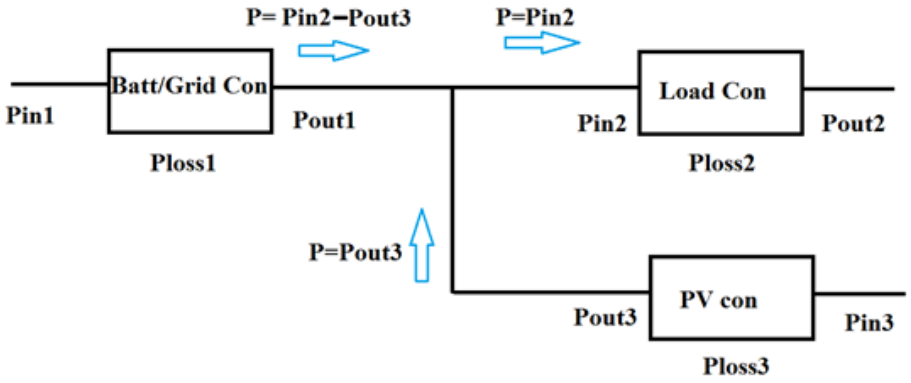


Figure 4.12 Power transfers in mode (3) the PV output is less than the load

In order to explain the power management for the grid arrangement under consideration, detailed power transfer maps will be presented for grid arrangements TWO and FOUR.

To avoid repetition, grid one and three power transfer maps will not be presented as they are easily followed from the power transfers maps for grid TWO and FOUR.

4.5.2 Arrangement TWO and FOUR power management:

4.5.2.1 Without grid:

When arrangements TWO and FOUR are working in isolation from the grid, three distinctive power transfers modes are possible.

In mode one, the PV is not generating any power while all the losses and loads are supported by the battery. Figure 4.13 and Figure 4.14 illustrate arrangement TWO and FOUR working in mode one.

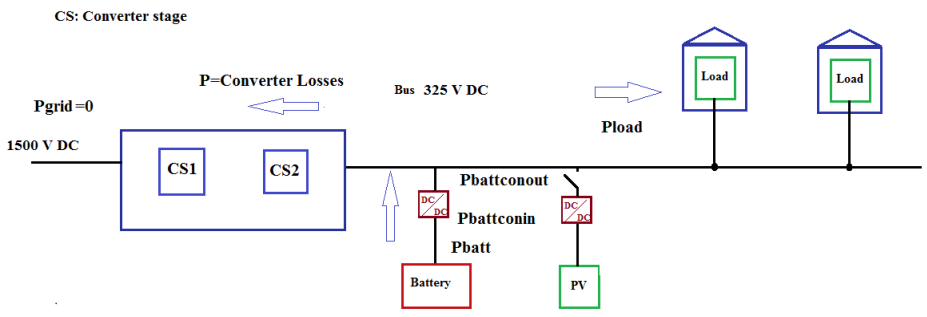


Figure 4.13 Arrangement TWO working isolated from the grid in mode 1.

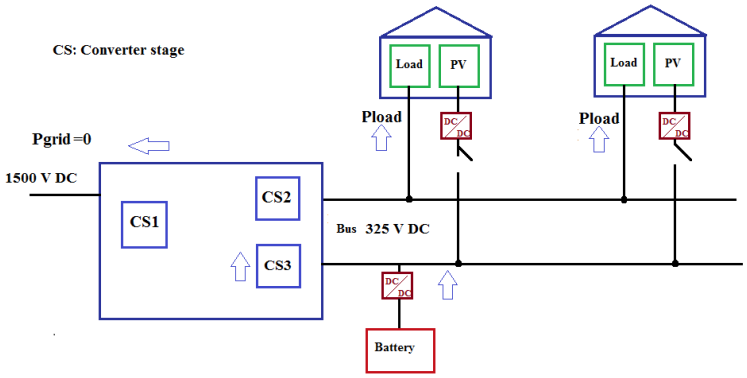


Figure 4.14 Arrangement FOUR working isolated from the grid in mode 1.

In mode two, the PV generation is higher than the load and any extra energy is stored in the battery. Figure 4.15 and Figure 4.16 illustrate arrangement ONE and FOUR working in mode two.

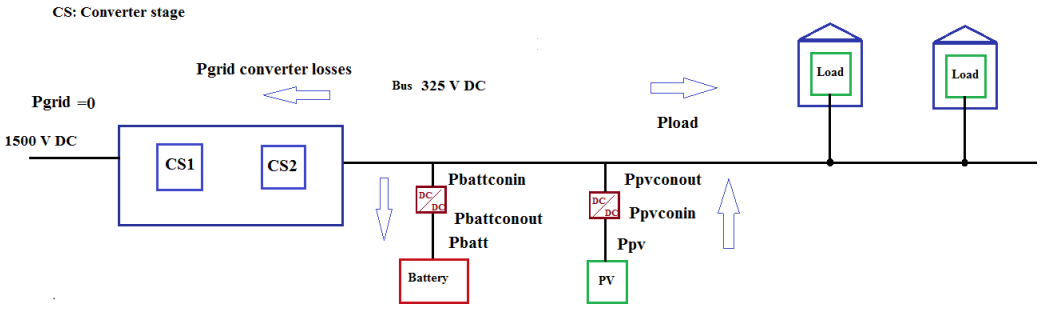


Figure 4.15 Arrangement TWO working isolated from the grid in mode 2.

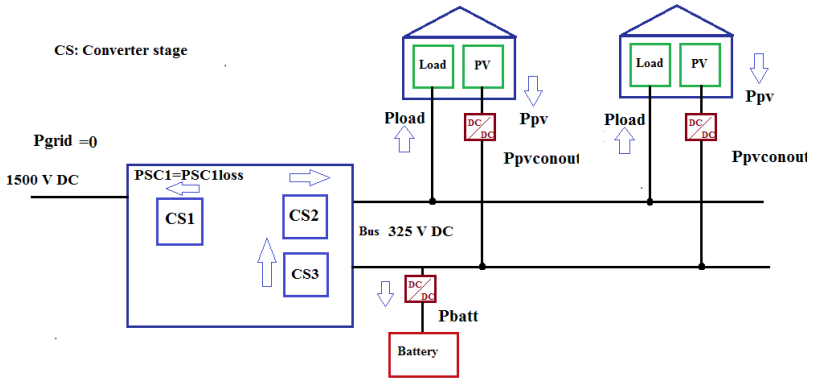


Figure 4.16 Arrangement FOUR working isolated from the grid in mode 2.

In mode three, the PV generation is lower than the load, the extra energy required from the load will come from the battery. Figure 4.17 and Figure 4.18 illustrate arrangement TWO and FOUR working in mode three.

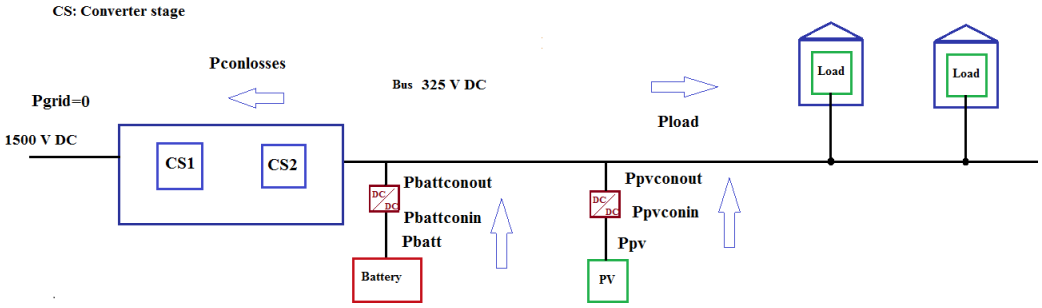


Figure 4.17 Arrangement TWO working isolated from the grid in mode 3.

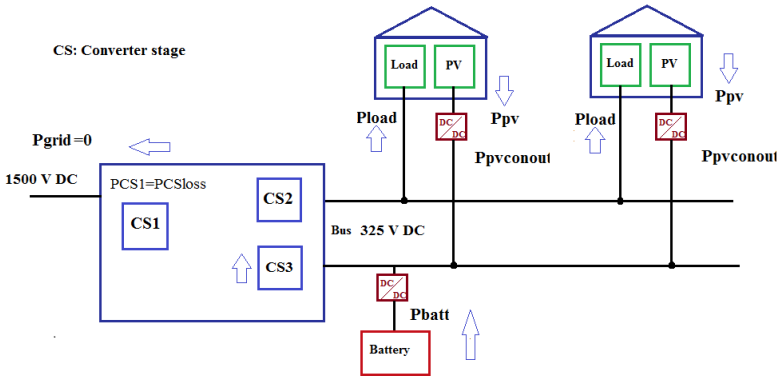


Figure 4.18 Arrangement FOUR working isolated from the grid in mode 3.

4.5.2.2 With grid:

Connecting arrangements TWO and FOUR to the grid results in three distinctive power transfer modes:

In mode one, the PV is not generating any power, all the losses and loads will be fed from the battery or the grid if the battery is fully discharged. Figure 4.19 and Figure 4.20 illustrate arrangement TWO and FOUR working in mode one.

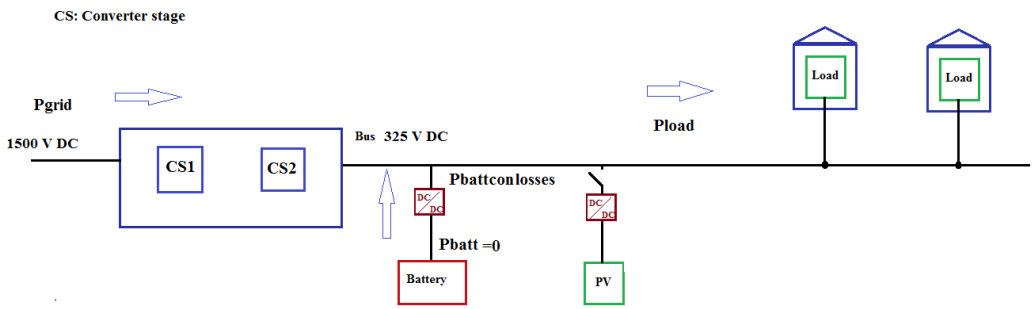


Figure 4.19 Arrangement TWO connected with the grid in mode 1.

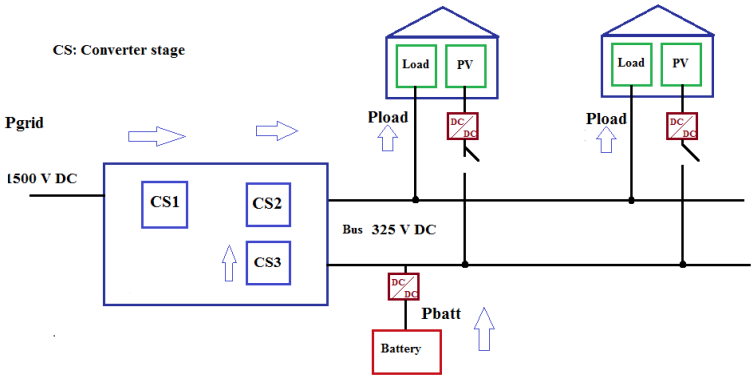


Figure 4.20 Arrangement FOUR connected with the grid in mode 1.

In mode two the PV generation is higher than the load needs and any extra power is stored in the battery or sent to the grid if the battery is full. This mode for arrangement TWO and FOUR is presented in Figure 4.21 and Figure 4.22.

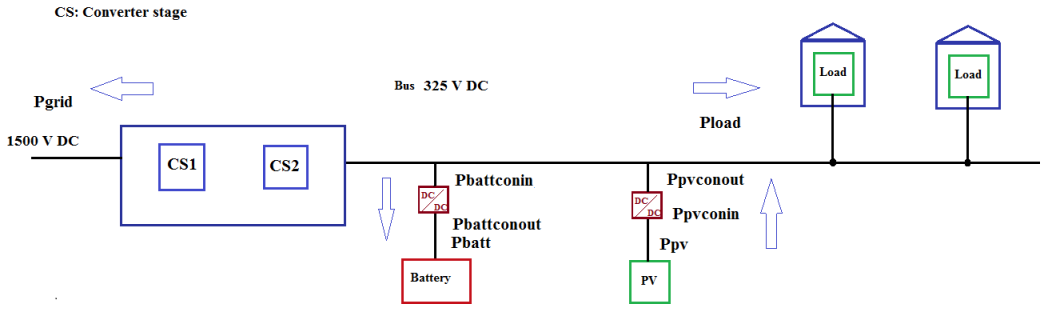


Figure 4.21 Arrangement TWO connected with the grid in mode 2.

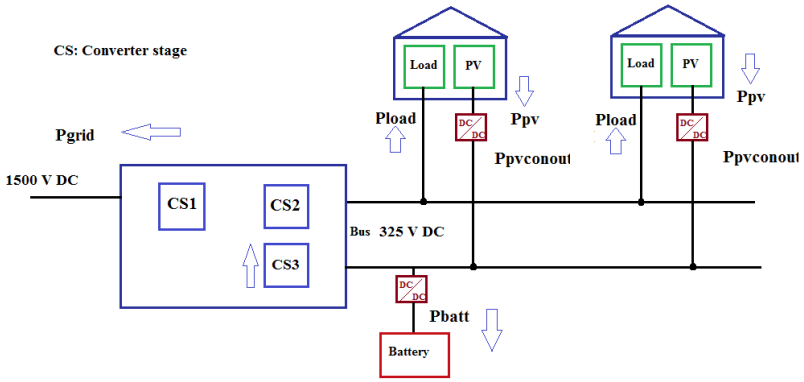


Figure 4.22 Arrangement FOUR connected to the grid in mode 2.

In mode three, the PV is not generating enough power to supply the load. The load energy will hence come from the battery or the grid if the battery is fully discharged. This mode for arrangement TWO and FOUR is presented in Figure 4.23 and Figure 4.24.

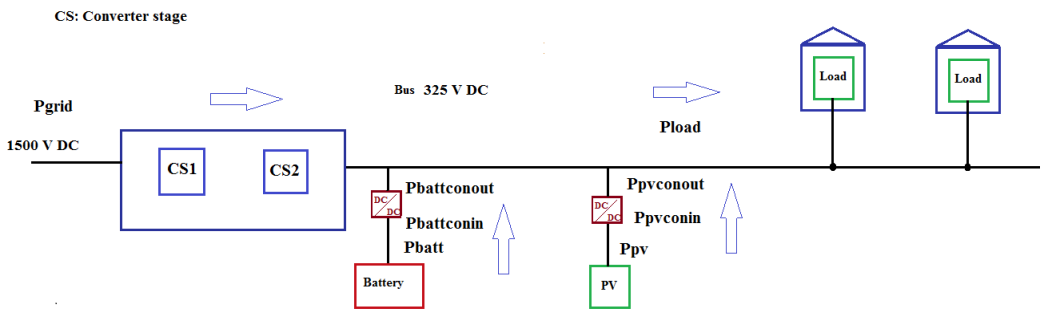


Figure 4.23 Arrangement TWO connected to the grid in mode 3.

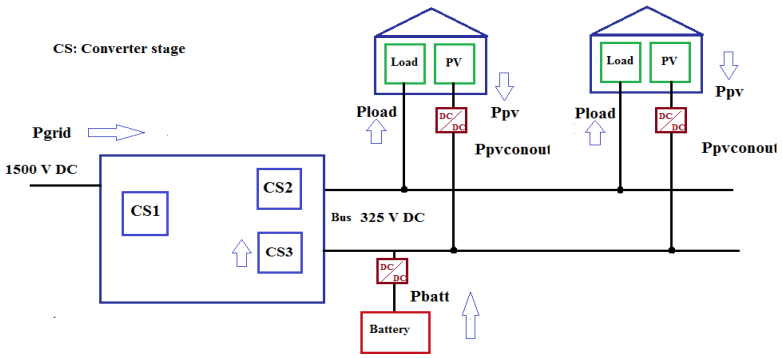


Figure 4.24 Arrangement FOUR connected to the grid in mode 3.

In this part of the thesis, the four different DC grid arrangements under test, the methodology used to estimate the load and PV resources as well as the design procedures for the different parts of the system such as the PV, batteries, and converters were presented. Furthermore, the method used to present the converter losses was also discussed and the power transfer method was explained.

In order to compare the different grid arrangements, a MATLAB C-code will be developed to simulate all grids. The next parts of the thesis explain the developed MATLAB C-code.

4.6 MATLAB coding and equations executions

MATLAB codes were used to automate the processes of system design, power management calculation, converter losses calculation and all other required calculations. Figure 4.25 indicates the flow chart of the codes designed to achieve the arrangements comparison:

At first, the available PV power on the site was estimated using the PVSYST 4 and the daily load curves were estimated using the CREST demand model, which generated minute-by-minute daily loading profiles for each house.

Five daily loading profiles will be used for each house in order to get the average losses from five different sets of loading profiles. The community size will be limited to 51 houses, as the diversity factor will be have a minimal effect on the load variation during the day for house number bigger than this and hence a minimal effect on power transfer and losses.

Then MATLAB codes were written to run the different design and losses equations. Therefore the final code is large and has been distributed among several files in order to ease the interpretation, debugging, and acceleration the code execution:

- An introduction file: this file was used to interface the input data gained from the PVSYST program and CREST Demand Model which was saved as excel data sheet.
- A system design file: this file was used to design the system converters and PV panel sizes based on the house number and the appliances connected to each house.
- Solar panel output file: this file was used to estimate the output of the PV panel and the losses of each PV converter.

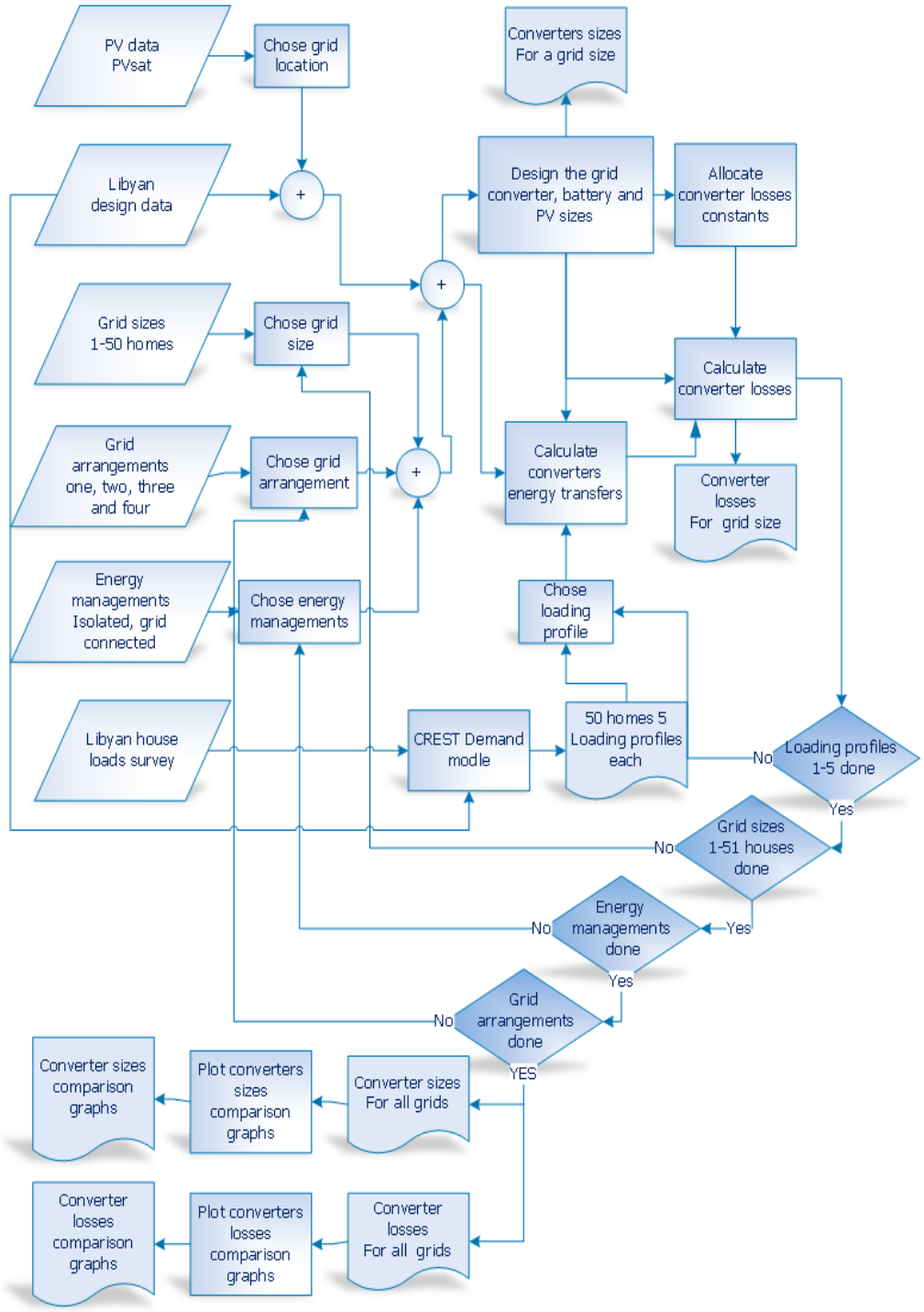


Figure 4.25 Flow-chart of the MATLAB code used in the grid arrangements comparison study.

- Converter efficiency allocation file: this file was used to allocate each converter with a unique losses equation

parameters based on its size which can be used to calculate the losses of each converter.

- The main file: this file is used to calculate the power transfers between the system converters and to calculate the converters power losses. This file used the minute by minute daily loading profiles to calculate the power transfers between all the grid converters and the losses of each converter.

- An execution file: this file was used to call all the five earlier files. the file will run five times with different loading profiles and the average losses will be calculated from the five times and will be repeated 51 times for cluster sizes from 1 to 51 dwellings. The last two steps will be also repeated for each grid arrangement (ONE-FOUR) and power managements (isolated- grid connected).

- A merger file: this file was used to merge all the results from the previous files before in order to produce output figures, which then is used to compare the grid arrangements.

Finally, it needs to be noticed that each grid comes with a unique set of converters with its own power transfer function and thus for each grid arrangement, all the earlier six files had to be modified in order to represent the arrangements unique converters and layouts. Figure 4.26, Figure 4.27 and Figure 4.28 indicate the results obtained from a simulation with a grid size of 20 homes and for the grid connected and the isolated power managements strategies:

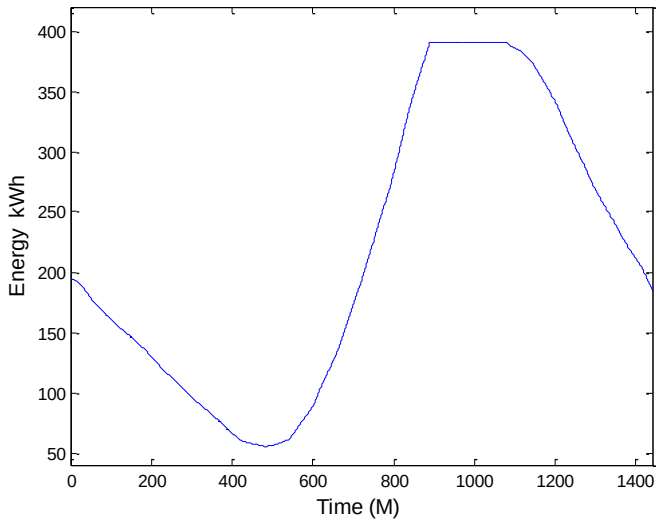


Figure 4.26 The battery energy for arrangement TWO with 20 houses.

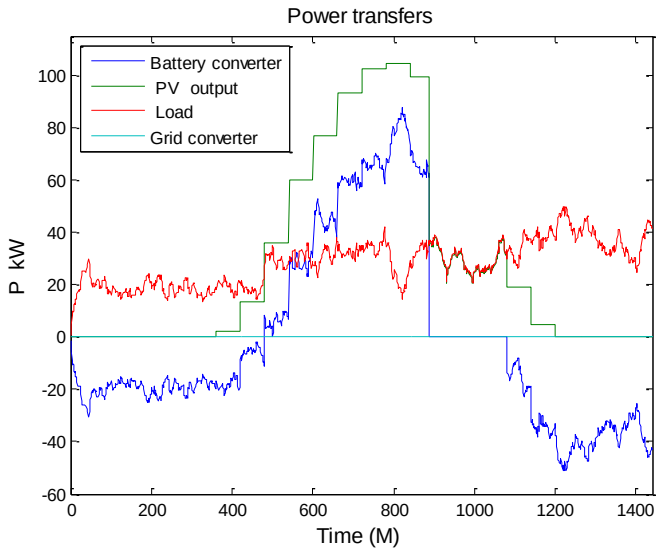


Figure 4.27 Power of the PV converter, the grid converter, the battery converter over a day. The load consists of 20 houses and the cluster is grid connected.

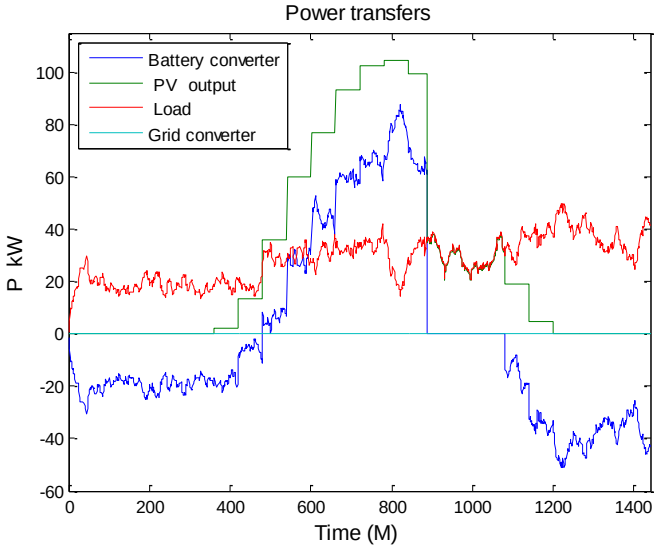


Figure 4.28 Power of the PV converter, the grid converter, the battery converter over a day. The load consists of 20 houses and the cluster is not grid connected.

Figure 4.26, Figure 4.27 and Figure 4.28 indicate the power transfers between the different grid arrangements as the load power has to be supplied either from the grid or from the battery and the PV power has to be consumed by the loads and any extra power has to be sent either to the battery or to the grid if the battery is full.

Figure 4.27 it can be noticed that the grid converter will start working the moment the battery reaches its capacity limit and power will be sent to the grid. While in Figure 4.28, it can be noticed that when the battery's state of charge hits its upper limit, the battery converter will simply stop charging the battery and due to the fact that the grid is in an islanded mode the grid converter will not send any power to the grid.

The previous power management curves are used with the converter rating and losses equations to estimate the losses of

the system for each loading point, the results from the losses comparison are presented in the next part of this chapter.

4.7 Results and findings.

The MATLAB programs were run for the different grid arrangements and for cluster sizes from 1-51 houses. The programs were successfully able to calculate the rating for the different parts of the grid based on the equations of this chapter and to estimate the power transfers and converter losses for all the grid arrangement under study for the target cluster sizes.

The main aims of this study were to evaluate the DC distribution grid layout based on the converter losses and to investigate the best converter configuration (two /three port) for serving the proposed DC distribution grids.

In order to achieve the aims of this study, two main factors will be the focus of the analysis: the first one is how the total converter installed powers and losses for the different grid arrangements for a variable cluster houses number.

4.7.1 Converter and battery installed power.

The converters installed power and number has a direct impact on the initial and running cost of grids. The grid arrangements with lower overall installed power and lower count of power electronics units will be preferred over others. From Figure 4.1, Figure 4.2, Figure 4.3 and Figure 4.4 it can be noticed that arrangement TWO; three and one have fewer

converters in comparison to arrangement FOUR. Figure 4.29 shows a comparison between the total converter ratings for different grid arrangements sizes:

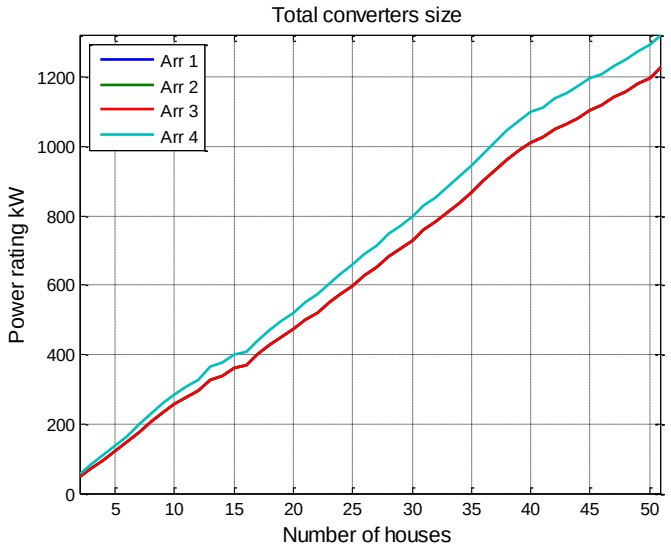


Figure 4.29: Relation between the total connected converter installed power and the number of houses for different grid arrangements (red curve superposed arrangements, ONE, TWO, and THREE)

It can be noticed from Figure 4.29 that arrangement FOUR has a higher total converter installed power as it needs more converters to transfer the power. Besides, Figure 4.29 indicates that the difference in converter installed power is not so high between the various grid arrangements. This is due to the fact that the converters were designed to handle the extreme cases where the total PV will be either sent to the grid or to the battery, if the load is small. The converter installed power might be lowered if an optimization is carried out which is outside the scope of this work.

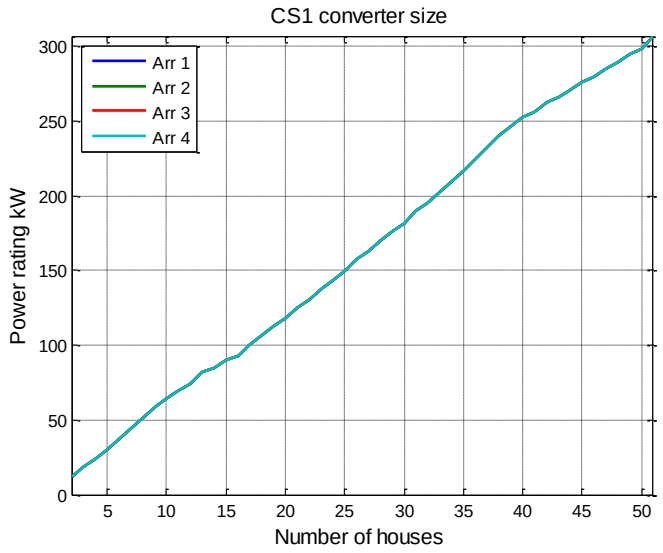


Figure 4.30 Relation between grid side converter CS1 installed power and the number of houses.

It can be noticed from Figure 4.30 that the grid side converter has the same installed power for all the grid arrangements under consideration. Also, this converter has a rating of 300 kW for 51 homes. The required battery size is indicted in Figure 4.31.

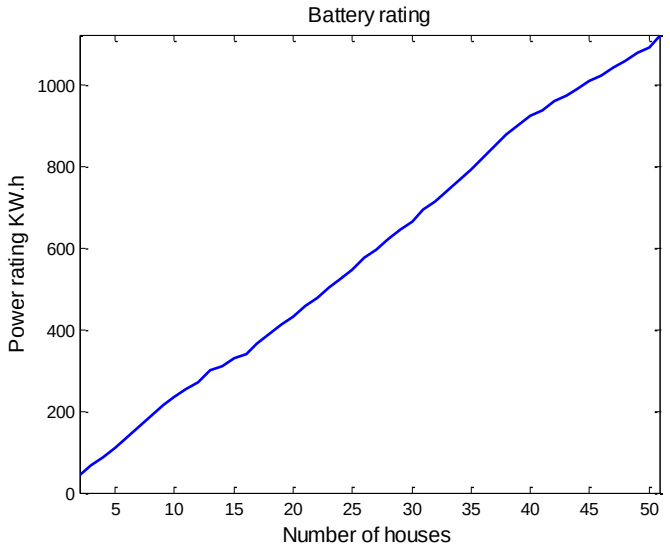


Figure 4.31 The required battery size for all grid arrangements.

It should be noticed that when rating of the battery the battery was rated for the average load which is common between all grids. Still, if the losses in the converter and grid are be taken in consideration the required battery will be smaller for the grid with the lowest losses.

While the total energy transferred for arrangement TWO for a day is presented in Figure 4.32.

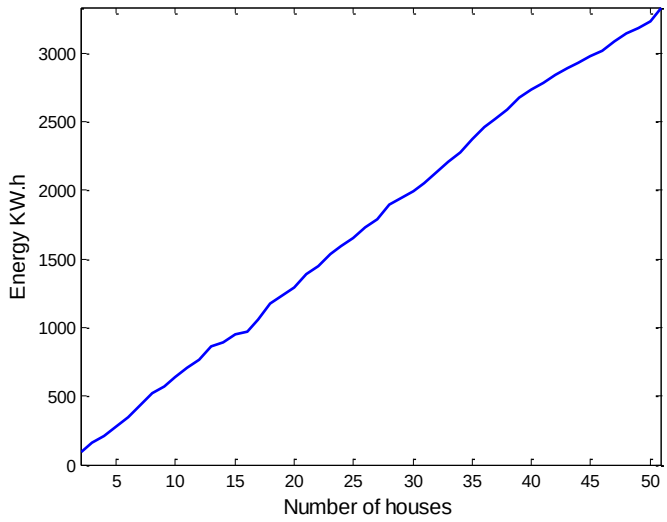


Figure 4.32 Total energy transferred through arrangement Two for a day

To conclude, arrangement FOUR has a higher converter count and installed power when compared to the other arrangements, which gives preference to the other arrangements over arrangements FOUR.

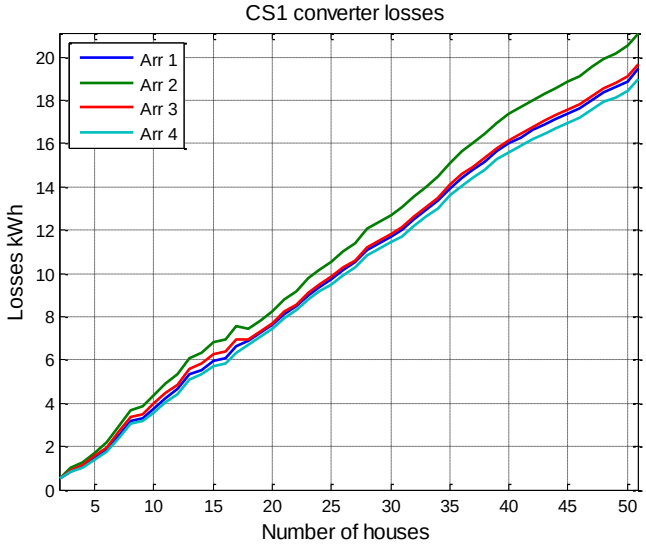
4.7.2 Converter losses:

The converter losses are mainly influenced by the installed power, location and the power transfer strategy used. The losses presented here are the results from a simulation, which

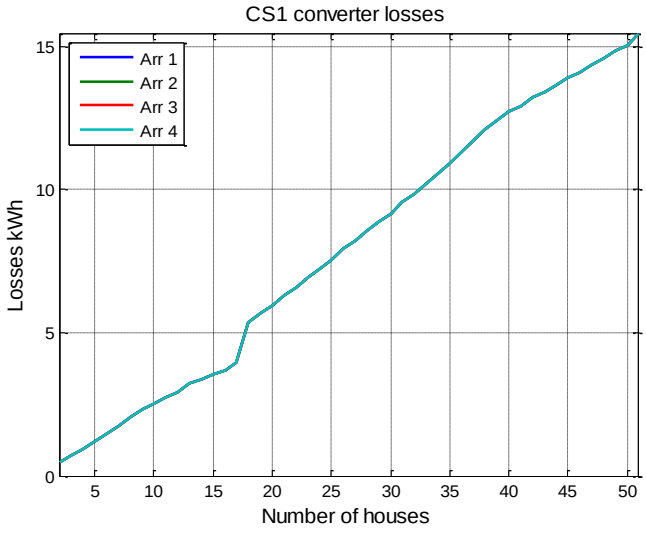
included the previously mentioned factors for the different grids arrangements.

4.7.2.1 Investigating converter CS1 energy losses:

The losses are calculated using the losses constant in conjunction with the converter power transfer and an average of the losses obtained using different 5 daily loading profile of each house are used to calculate the losses of the converter. From Figure 4.33 b it can be noticed that without a grid connection, the grid converter stage CS1 has the same converter losses for all grids as there is no power transfer with the grid and the losses are the standalone losses of this converter stage in this case. The losses in the cause with no connection with the grid will be the no-load losses as no power is been exported or imported to the grid. In Figure 4.33 a it can be noticed that converter CS1 in arrangement TWO has the highest losses this is due to it having the lowest overall losses and thus more power is available to be transferred to the grid through CS1 and hence more losses are resulted.



a.



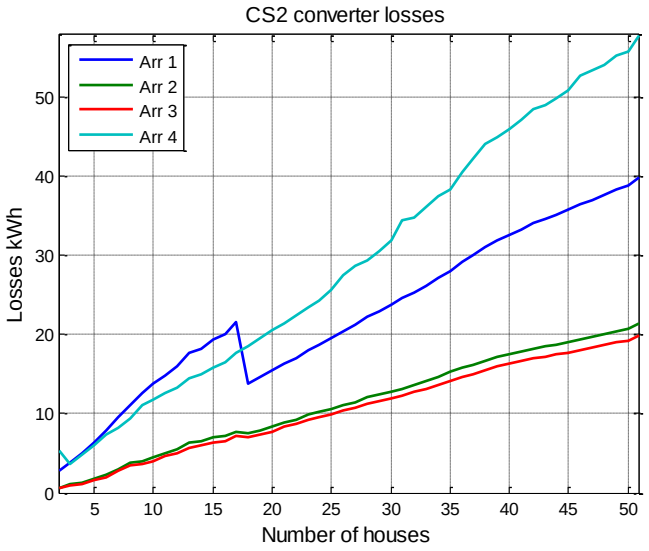
b.

Figure 4.33 Comparison between the converter CS1 energy losses over one day with the number of houses. a with grid .b. without grid.

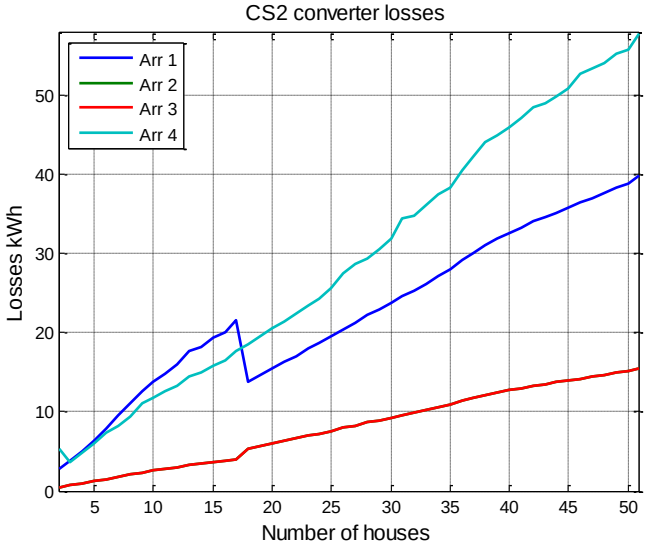
4.7.2.2 Investigating Converter CS2 energy losses.

From Figure 4.34 it can be noticed that there is a difference in the losses behavior in arrangement ONE, primarily because in this grid arrangement the battery is not linked to a bus with generation as in grid two, three and four thus the solar energy would have to go through CS2 to reach the battery to be stored .

While for arrangement FOUR, the power will go from the battery or the PV through CS2 to supply the load depending on the PV power generation and the load and CS2 is not required to handle PV power.



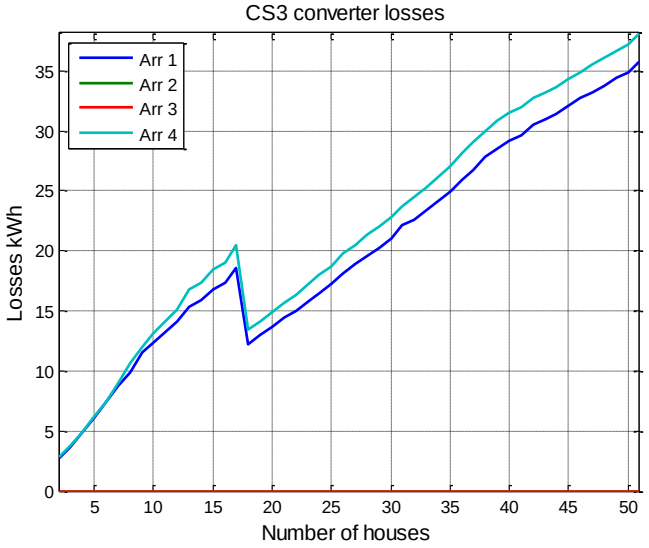
a.



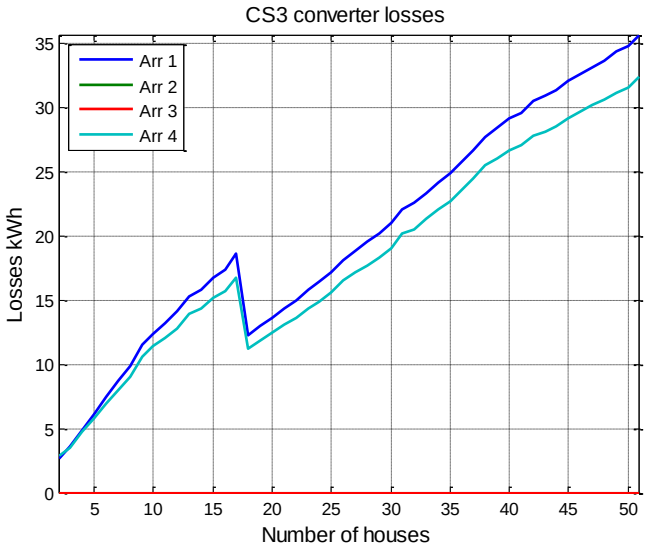
b.

Figure 4.34, Comparison between the converter CS2 losses, the number of houses for different grid arrangements. a. with grid b. without grid (arrangements THREE, TWO in red).

In Figure 4.34 b it can be noticed that the converter losses are identical for arrangements TWO and THREE and this is due to the fact that there is no power going through converter CS2 in the isolated mode of operation and the losses are the standby losses as this converter is required to maintain the high voltage through converter CS1. Also from Figure 4.34, it can be observed that at around 18 homes there is a change in the total losses for arrangement ONE. This is due to the fact that the converter losses equation constants change from their values in Table 4.3 to their values in Table 4.4, resulting in lower losses. The same change in converter losses can be observed for the other converter as will be shown next.



a.



b.

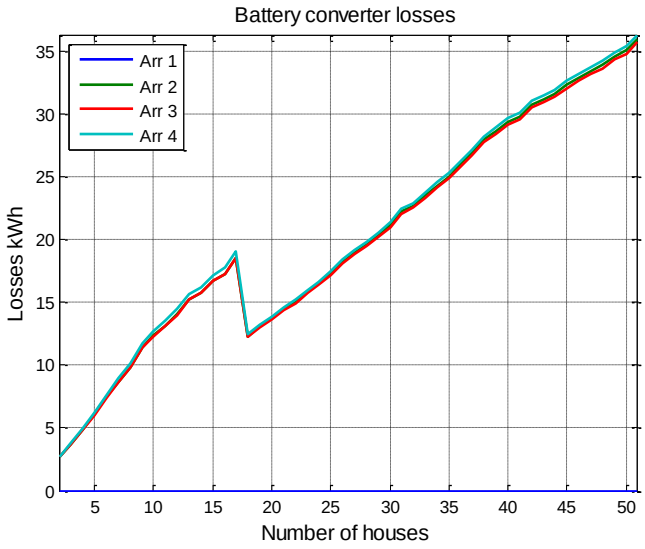
Figure 4.35 Comparison between the converter CS3 losses, with the number of houses for different grid arrangements. a. with grid b. without grid.

4.7.2.2 Investigating converter CS3 energy losses.

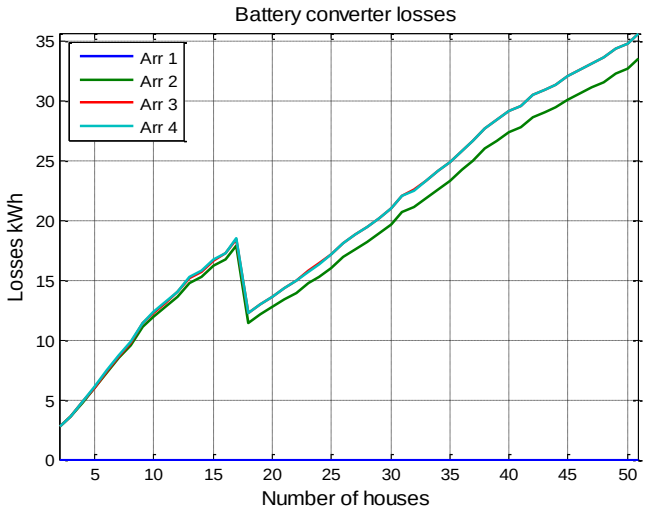
The converter CS3 does not exist in arrangement TWO and THREE and hence they are presented as zero in Figure 4.35. It can be noticed that CS3 in arrangement FOUR has lower losses in the case without grid as less power will flow through, due to not having any export of energy to the grid.

4.7.2.3 Battery converter energy losses.

The battery converter does not exist in arrangement ONE and the battery is connected through the CS3**.**



a.



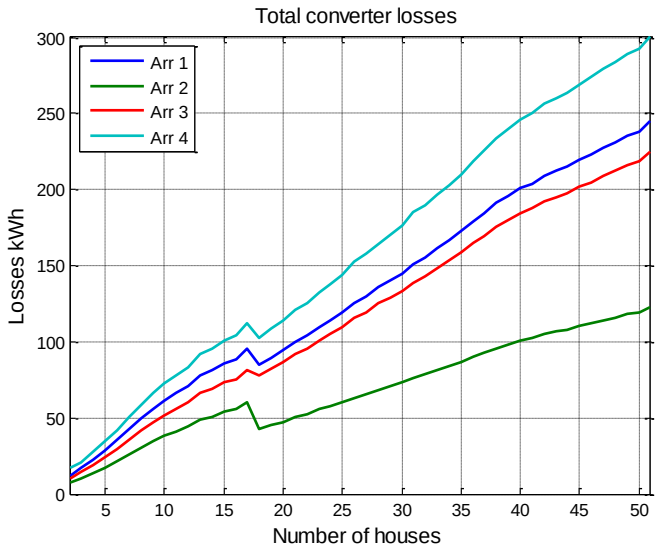
b.

Figure 4.36 Comparison between the battery converter energy losses, the number of houses for different grid arrangements. a. with grid, b. without grid.

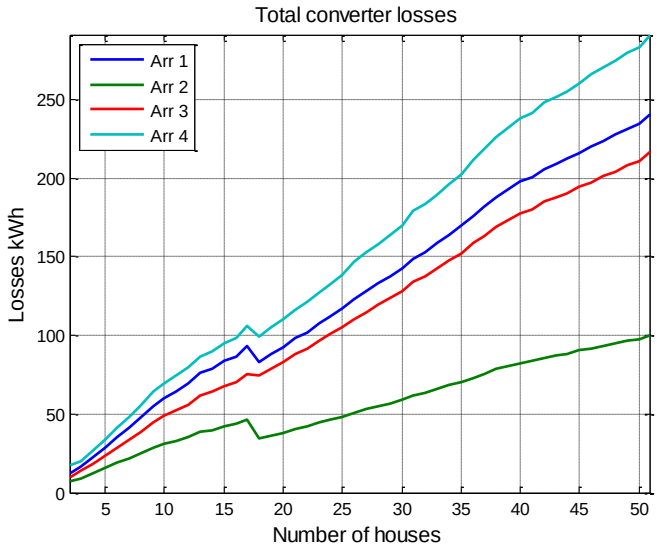
It can be noticed from Figure 4.36 b that arrangement TWO has the lowest losses among all arrangement, thus the battery reach its full state faster than the other arrangements as more energy is available to charge the battery.

4.7.2.4 Total converter losses.

From Figure 4.37 it can be observed that arrangement TWO has the smallest losses of all the arrangements. Additionally, arrangements TWO and THREE have lower losses than arrangement ONE and FOUR, and this is mainly because the power flows through fewer converters between the PV, battery and the loads, as in the cause of arrangement TWO where the energy flows through less converters when compared with arrangement FOUR.



a.



b.

Figure 4.37 Comparison between the converters energy losses, the number of houses for different grid arrangements. a. with grid, b. without grid.

To conclude, the arrangements using two ports converters, arrangements TWO and THREE, have lower losses when compared to arrangements using three ports converters, while

arrangement TWO offers lower total losses than arrangement three due to the centralization of PV arrays in one location which is served by one converter.

Thus, the preferred converter configuration is the two ports converter and the grid layout should be based on arrangement two with centralized PV arrays.

4.8 Summary.

This chapter presented a study on evaluating four different possible DC distribution grid arrangements to serve the last mile of the grid and the isolated grid. This chapter also included:

- An assessment of the daily electrical load profiles of the Libyan household.
- The steps followed to estimate the DC distribution grid components such as converters, battery and PV arrays.
- A description of the power management methods used within these DC distribution systems.
- A description of the codes used to design, simulate, and compare the different DC grids arrangements.
- Finally, the converter losses and installed power analysis were carried out for the different grid arrangements under study.

In conclusion, arrangements which use two port converters have lower converter losses when compared with arrangements which use three ports converter. And the converter installed power to link the grid cluster of 51 houses to DC grid should be rated at around 300 kW. As explained earlier in section 4.7.1.

The following chapter will include a detailed analysis of a two port DC/DC converter which can be used to serve the proposed two ports DC grid arrangement. Besides, it will also include a method to improve the performance of the chosen DC/DC converter.

Chapter 5

Three-Phase Dual-Active Bridge DAB's, theory and analysis.

5.1 Introduction.

In chapter 4 of this thesis, different configurations of DC grids were investigated. The outcome of the study preferred grid layouts which use two port converters to link high and low DC voltage levels. Moreover, the two port DC/DC grid-connected converter is required to provide the following functionalities:

- High efficiency over a wide range of loading operation.

- Galvanic isolation between the high and the low voltage sides due to the grid application requirements [62].
- Bidirectional power flow.
- Large voltage ratio between the converter terminals.
- Small range of the voltages on the high and the low voltage sides.

Dual active bridge (DAB) converters are an obvious choice as they can offer the desired performance and requirements of the proposed DC grid. DAB converters offer galvanic isolation between the high and the low voltage levels [62]. Also, DAB converters provide bidirectional power flow which will enable the integration of distributed generation to the grid. Furthermore, DAB converters can offer high voltage transfer ratios between the high and the low voltage sides through the use of high frequency transformers.

A number of different DAB converter structures have been proposed including resonant ones [62-67]. This work only considers the non-resonant DAB versions due to the fact that they offer the application requirements of high efficiency over a wider range of loading profiles.

Non-resonant DAB converters can be either single phase (1ϕ DAB) or three phase (3ϕ DAB) and both offer soft turn on capabilities [68]. The main advantages that 3ϕ DAB converters can offer when compared to 1ϕ DAB are that the 3ϕ DAB converter offers high efficiencies in the soft-switched area [66]

and the 3ϕ DAB converter offers lower DC side current ripple when compared to 1ϕ DAB [65], thus a smaller capacitor is required to filter the current ripple leading to a reduction in the installed power and cost of the converter [62]. Additionally, the 3ϕ DAB adds a factor of redundancy when compared to the 1ϕ DAB, due to the fact that if one of the converter legs fails, the remaining two legs can be used to supply the loads or the grid with power, thereby reducing the possibility of a complete grid blackout [62]. Thus, in this thesis, a 3ϕ DAB converter is proposed to be used in conjunction with the proposed DC grid.

This chapter includes a description of the proposed 3ϕ DAB converter and its operation principles. Also, analysis of the losses will be presented. Finally, a multi-cell 3ϕ DAB will be proposed to further enhance the efficiency of the 3ϕ DAB converter under a wide range of loading profiles.

5.2 Three-Phase Dual-Active Bridge.

The three phase Dual-Active Bridge converter (3ϕ DAB) has four main parts, two three-phase bridge inverter stages, a Y-Y high-frequency transformer used to isolate the high-frequency AC ports of the three phase bridges [66] and a linking inductor placed between the two bridges to allow the control of power flow. The linking inductance may be fully incorporated in the leakage inductance of the isolation transformer or can be provided as a separate inductor in addition to the transformer

leakage inductance. Figure 5.1 shows a diagram of 3ϕ DAB [69].

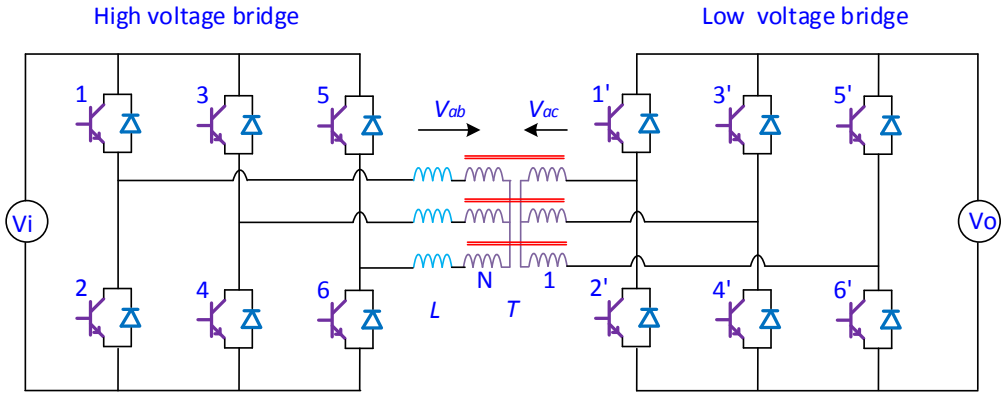


Figure 5.1 3ϕ DAB converter.

Power transfer between the ports of the converter is controlled using the phase shift angle (ϕ) across the linking inductor [68].

Each leg of the 3ϕ DAB converter produces a high-frequency square wave with a fixed duty cycle of 50 %, each leg is phase shifted with respect to the other phases in the same bridge by $120°$, This results in six-step voltage waveforms being produced across the linking inductor. [68]

The next section of the thesis provides an analysis of the 3ϕ DAB converter.

5.2.1 Analysis of the 3ϕ DAB converter.

In order to analyse the 3ϕ DAB converter, an idealised circuit is considered. The power flow direction will be assumed to be from the high voltage (sending bridge) to the low voltage bridge (receiving bridge). The total linking inductance is equal to the sum of the external inductor value and the transformer leakage inductance. The low DC voltage (receiving bridge) is referred to the high voltage bridge (sending side). And hence the transformer turn ratio (N) assumed to be 1:1 for the later analyses. The transformer resistance is neglected. Furthermore, the effect of snubber capacitors will be neglected for this analysis and will be considered later in section 5.4. Figure 5.2 presents the simplified 3ϕ DAB converter circuit.

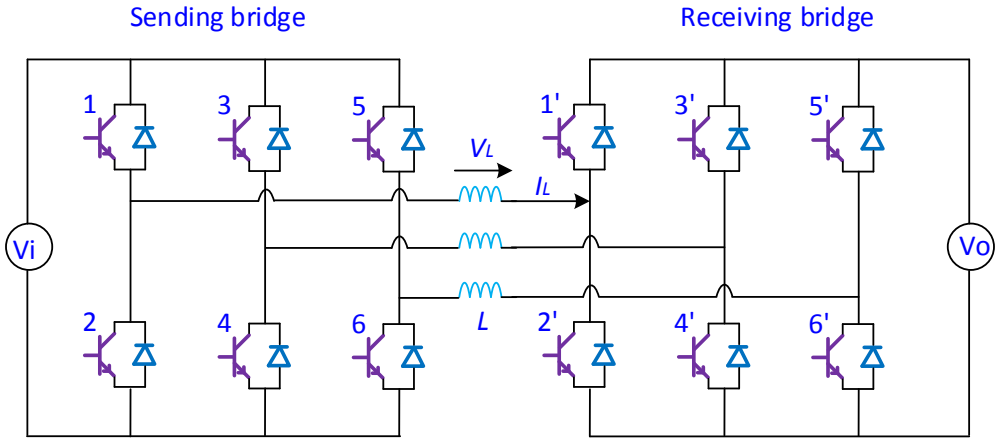


Figure 5.2 Simplified 3ϕ DAB converter circuit referred to the sending bridge [68].

Based on the phase shift angle (ϕ) of the 3ϕ DAB between output voltage of the two bridges, two operation regions can be identified. Region (1) $0 \le \phi < \frac{\pi}{3}$ and region (2) $\frac{\pi}{3} \le \phi < 2\frac{\pi}{3}$. In

this thesis, the focus will be on the region (1) as the power control range will be limited to less than $\phi < \frac{\pi}{3}$ which gives the desired output power.

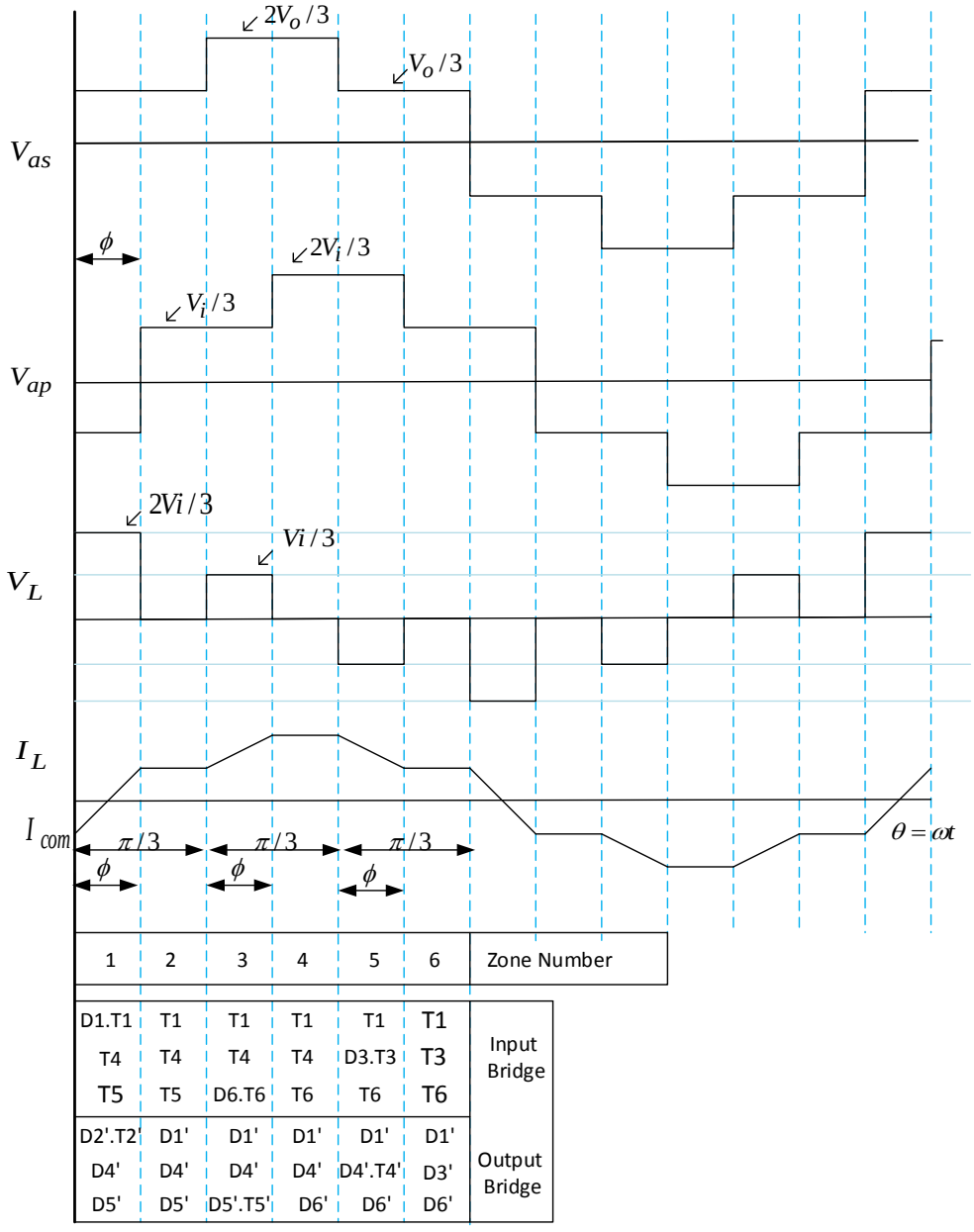


Figure 5.3, 3ϕ DAB voltage and current waveforms.

The DC voltage gain referred to the sending bridge d is defined as in equation (5.1) [68].

$$d = \frac{V_o^{'}}{V_i} \tag{5.1}$$

V_i The sending bridge DC voltage of the converter.

$V_0^{'}$ The receiving bridge DC voltage referred to the sending bridge of the converter [68].

Typical waveforms for the condition d=1 and $\phi < \frac{\pi}{3}$ are shown in Figure 5.3. The linking inductor current has six distinct zones in the region from $0 < \theta \leq \pi$ and $V_L = V_{as} - V_{ap}$, while the other half-cycle of the waveform $\pi < \theta \leq 2\pi$ can be constructed easily from the first half-cycle due to symmetry. Thus, the current in the inductor is defined by different equation in each of the six zones [68]. For example, the current in zone 1 is given by equation (5.2):

$$i(\theta) = i(0) + \frac{V_i(1+d)}{3wL}\theta \qquad for\ \ 0 \leq \theta \leq \phi \tag{5.2}$$

Appendix (B) gives the expression for the other zones. [64]

Considering that $i(0) = -i(\pi)$ and using the equations for the 6 current zones it is possible to determine the current at zero as given in equation (5.3): [67]

$$I_0 = -I_{com} = \frac{V_i}{3\omega L}\left[\frac{2\pi d}{3} - d\phi - \frac{2\pi}{3}\right] \tag{5.3}$$

The current at an angle ϕ (end of zone one) is given by:

$$i(\phi) = \frac{V_i}{3\omega L}\left[\frac{2\pi d}{3} + \phi - \frac{2\pi}{3}\right] \tag{5.4}$$

The power output of the converter can be determined by considering the contribution of each leg current to the DC side current and is given by (5.5) [68].

$$P_{out} = \frac{V_i^2}{\omega L}.d.\phi.\left[\frac{2}{3} - \frac{\phi}{2\pi}\right] \text{ For } 0 \le \phi \le \frac{\pi}{3} \tag{5.5}$$

Where:

P_{out} The converter output power.

L The Linking inductance (sum of the transformer leakage inductance and the external inductance).

The next section discusses the soft switching range of the converter.

5.2.2 Three phase DAB converter soft-switching region boundaries.

The 3ϕ DAB converter has a soft turn on characteristics; each IGBT will be gated on when the anti-parallel diode is conducting the inductor current. Subsequently, as the inductor current reverses polarity the paired IGBT will start conducting and, as a result, the IGBT will be turned on at zero voltage and zero current and soft switching at turn on can be achieved.

However, the 3ϕ DAB soft switching capability operation range is limited. The soft-switching boundaries change with two factors, the voltage ratio (d), and the converter loading. In theory, soft switching can be always maintained as long as the converter is running at ($d=1$). The soft switching boundaries for the range $0\le\phi\le\pi/2$ were presented in [68]. Generally, soft switching is achieved if the conditions $i(0)\le 0$ and $i(\phi)\ge 0$ are met [67].

The receiving bridge soft switching locus can be derived by finding the value of d which corresponds to $i(\phi)=0$ and as a result the receiving bridge soft switching boundaries can be obtained from (5.4) [68].

$$d_{\,output\ bridge}=1-\frac{3\phi}{2\pi} \tag{5.6}$$

The soft switching boundaries of the sending bridge can be obtained by solving the equation $i(0)=0$ from (5.3) [68].

$$d_{\,input\ bridge}=\frac{1}{1-\frac{3\phi}{2\pi}} \tag{5.7}$$

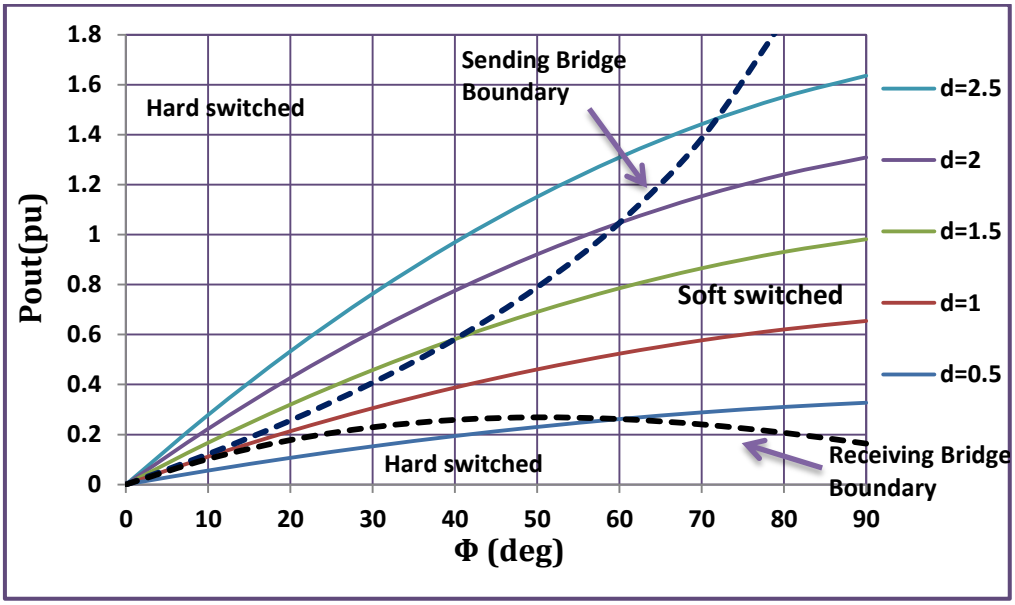


Figure 5.4 Soft switching region of the 3ϕ DAB converter [68].

Equations 5.6 and 5.7 represent the soft switching boundaries of the 3ϕ DAB and are graphically presented in Figure 5.4 [68]

A 3ϕ DAB converter used in the proposed DC/DC grid is likely to be operating in the soft switching region most of the time due to the fact that the converter will be working very close to $d=1$ at light loading.

A highly loaded converter might be required to regulate the grid voltage and thus will be working in a slightly wider range of d than the low loading situation. Still, the converter will be in the soft switching region due to the wider soft operation range at high loading as indicated in Figure 5.4.

Further detailed converter operation and losses will be investigated for the case when $d=1$ for simplicity. This is

justified by the fact that the converter will always be working close to $d=1$ in the application under consideration.

5.3 3ϕ DAB power loss estimation

The previous part of the thesis included the motivation behind choosing the 3ϕ DAB and a general characterisation of the 3vDAB. In order to design the 3ϕ DAB converter, the converter operation and losses should be studied and evaluated.

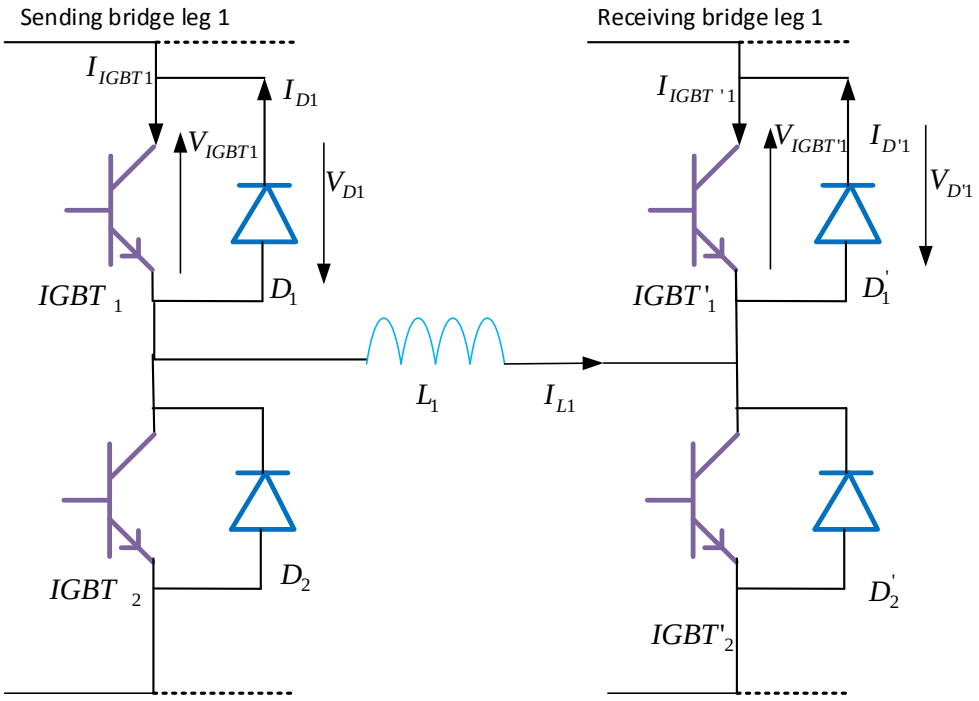


Figure 5.5 3ϕ DAB converter one leg circuit

In order to study the semiconductor conduction and switching losses, the current and voltage waveforms of each device in the 3vDAB converter should be determined and steady state analyses should be performed. Figure 5.5 shows leg one in the sending and receiving bridges of the 3ϕ DAB in more detail.

The IGBT and diode current and voltage waveforms in leg one corresponding to Figure 5.5 are presented in Figure 5.6 which presents the current and voltages of one leg of the 3ϕ DAB.

The devices can be either soft or hard switched based on the current and the voltage at the point of commutation. It can be noticed from Figure 5.6 that all the IGBTs are soft switched turn on and hard switched turn off. The soft switching operation and the proposed solution for mitigating the hard switched turn off will be discussed later in this chapter.

The other outcome of studying the waveforms of the 3ϕ DAB IGBTs and diodes, besides understating the converter operation is the ability to determine the conduction losses analytically

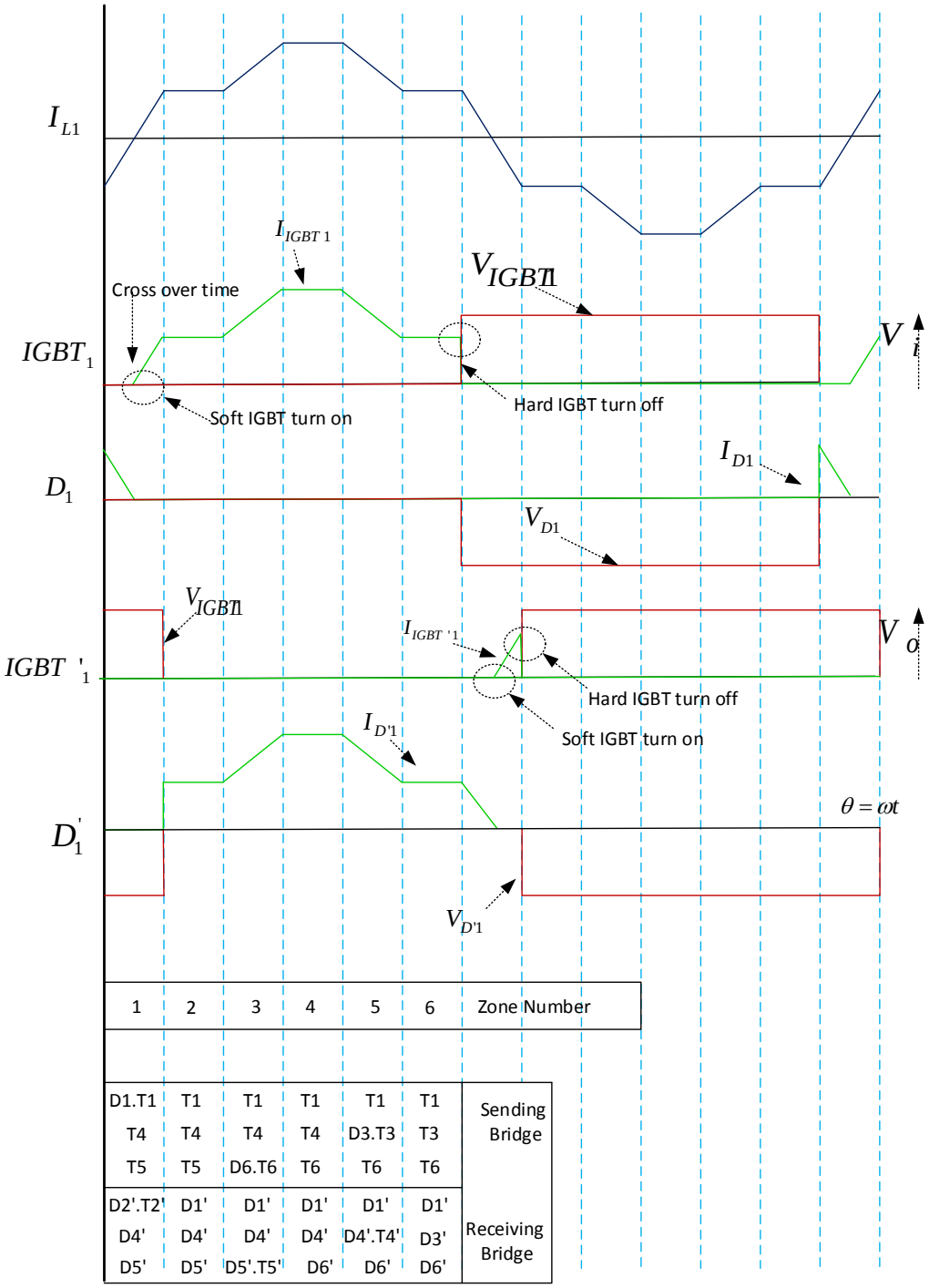


Figure 5.6 IGBT and diode voltage and current waveforms for the upper devices of leg one of the 3 ϕ DAB.

From Figure 5.6 it can be noticed that the inductor current is built-up from a combination of diode and IGBT currents, this

allows for the individual device current to be determined based on the expressions presented in appendix (B). The analytical expressions for the diode and IGBT currents can be used to calculate the conduction losses of the converter as presented in the next section.

5.3.1 IGBT and Diode conduction losses estimation.

The IGBT conduction loss estimation is based on an approximation, where the on state IGBT collector-emitter voltage (V_{CE})is represented by a series DC voltage source (V_{CE0}), which is the zero current forward voltage drop, combined with the voltage drop from the collector-emitter forward resistance (r_C)[70].

$$V_{CE}(i_C) = V_{CE\,0} + r_C.i_C(t) \tag{5.8}$$

The same applies for the anti-parallel diode resulting in [70]:

$$V_D(i_D) = V_{D0} + r_D.i_D(t)$$

(5.9)

The instantaneous IGBT conduction losses $p_{ct}(t)$ can be calculated using equation (5.10)[70]:

$$p_{CT}(t) = v_{CE}(t).i_C(t) = V_{CE0}.i_C(t) + r_C.i_C^2(t) \tag{5.10}$$

The averaged value of the IGBT conduction losses $p_{ct}(t)$ can be found by integrating the instantaneous losses [70]:

$$P_{CT} = \frac{1}{T_{SW}} \int_0^{T_{SW}} P_{CT}(t)dt = \frac{1}{T_{SW}} \int_0^{T_{SW}} (V_{CE0}.i_C(t) + r_C.i_C^2(t))dt \\ = V_{CE0}.I_{Cav} + r_C.I_{Crms}^2 \quad (5.11)$$

The same can be applied to determine the conduction losses of the Diode [70]:

$$P_{CD} = \frac{1}{T_{SW}} \int_0^{T_{SW}} P_{CD}(t)dt = \frac{1}{T_{SW}} \int_0^{T_{SW}} (V_{D0}.i_D(t) + r_D.i_D^2(t))dt \\ = V_{D0}.I_{Dav} + r_D.I_{Drms}^2 \quad (5.12)$$

The values, r_C, V_{CE0}, V_{D0} and r_D can be calculated from the data sheet for Infineon-FS100R17KE3-B17 using the approach illustrated in Figure 5.7 and

Figure 5.8 [70]. It should be noticed that this approximation might lead to some errors such as the approximation errors and the temperature difference errors.

Thus in order to calculate the device losses, the average and RMS values of the diode and IGBT currents have to be calculated first.

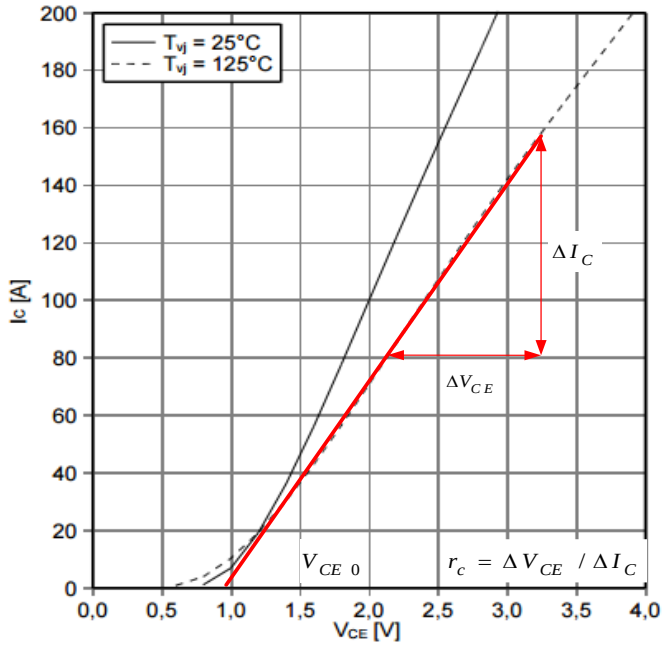


Figure 5.7 Extracting V_{CE0} and r_C from an Infineon-FS100R17KE3-B17 IGBT data sheet.

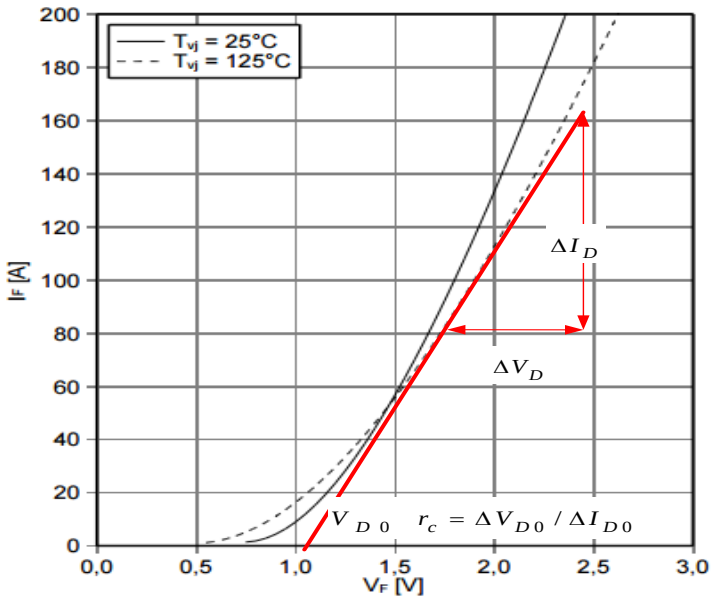


Figure 5.8 Extracting V_{D0} and r_D from an Infineon-FS100R17KE3-B17 diode data sheet

5.3.2 IGBT and diode RMS and average current derivation

The inductor current is built-up from a combination of diode and IGBT currents. Each half cycle of the inductor current is made-up from the current of one switch of the converter leg. Thus, in order to calculate the IGBT and diode current for one switch the time when the current changes between the IGBT and diode, which is named the cross over time should be evaluated.

5.3.2.1 The crossover time

As shown in Figure (5.6) the crossover time is the time when the current commutates from an IGBT to a diode or vice-versa.

The crossover time for the sending bridge occurs in the angle range ($0 \le \theta \le \phi$) at the instant when the current is equal to zero ($i(\theta) = 0$), thus from equations (5.2) and (5.3):

$$\begin{aligned} i(\theta) &= i(0) + \frac{V_i (1+d)}{3wL}\theta \\ &= \frac{V_i}{3\omega L}\left[\frac{2\pi d}{3} - d\phi - \frac{2\pi}{3}\right] + \frac{V_i (1+d)}{3wL}\theta \end{aligned} \qquad \text{For } 0 \le \theta \le \phi \qquad (5.13)$$

The angle ($\theta_{cross\ over}$) at which the current will be equal to zero can be calculated by placing ($i(\theta) = 0$) in equation (5.13) and solving the equation for the angle (θ).

$$0 = \frac{V_i}{3\omega L}\left[\frac{2\pi d}{3} - d\phi - \frac{2\pi}{3}\right] + \frac{V_i (1+d)}{3wL}\theta_{cross\ over} \qquad (5.14)$$

Assuming ($d = 1$)

$$0 = \frac{V_i}{3\omega L}\left[\frac{2\pi}{3} - \phi - \frac{2\pi}{3}\right] + \frac{V_i \times 2}{3wL}\theta_{cross\ over} \tag{5.15}$$

From which

$$\theta_{cross-over} = \frac{\phi}{2} \tag{5.16}$$

5.3.2.2 Calculating (I_{rms}) and (I_{av}) for the sending bridge IGBTs and the diodes.

The average and the RMS current values can be calculated using the current waveforms Figure 5.6 it can be noticed that the diode (D_1) will be conducting the current over the angle range from ($0 \le \theta \le \frac{\phi}{2}$) while $IGBT_1$ conducts over the range ($\frac{\phi}{2} \le \theta \le \pi$). Expressions for the diode and IGBT currents are given in appendix (B) [65] along with the determination of the expressions for the mean and RMS current this yields what follows:

$$I_{RMS\ D} = \frac{V_i \times \phi\sqrt{\phi}}{6 \times \omega L \times \sqrt{3 \times \pi}} \tag{5.17}$$

$$I_{AV\ D} = \frac{V_i \times \phi^2}{8 \times 3\omega L \times \pi} \tag{5.18}$$

$$I_{RMS\ IGBT} = \frac{V_i \times \phi}{3\omega L}\sqrt{1 - \frac{7 \times \phi}{12\pi}} \tag{5.19}$$

$$I_{AV\ IGBT} = \frac{V_i}{6\omega L \times \pi}\left(-0.75 \times \phi^2 + \frac{4}{3} \times \phi \times \pi\right) \tag{5.20}$$

5.3.2.3 Calculating (I_{rms}) and (I_{av}) for the receiving bridge IGBTs and diodes

From Figure 5.6 symmetry between the sending and the receiving bridges currents can be noticed. The IGBT currents in the receiving bridge correspond to the diode current in the sending bridge. The RMS and average values should be multiplied by the transformer turns ratio (N) if it is not equal to one and in that case, the bridge will be referred to as the low voltage bridge:

$$I_{AV\ IGBT} = N \times \frac{V_i \times \phi^2}{8 \times 3\omega L \times \pi} \tag{5.21}$$

$$I_{RMS\ IGBT} = N \times \frac{V_i \times \phi\sqrt{\phi}}{6 \times \omega L \times \sqrt{3 \times \pi}} \tag{5.22}$$

The diode currents in the receiving bridge correspond to the IGBT current in the sending bridge while taking the number of turns (N) into account:

$$I_{RMS\ D} = N \times \frac{V_i \times \phi}{3\omega L}\sqrt{1 - \frac{7 \times \phi}{12\pi}} \tag{5.23}$$

$$I_{AV\ D} = N \times \frac{V_i}{6\omega L \times \pi}\left(-0.75 \times \phi^2 + \frac{4}{3} \times \phi \times \pi\right) \tag{5.24}$$

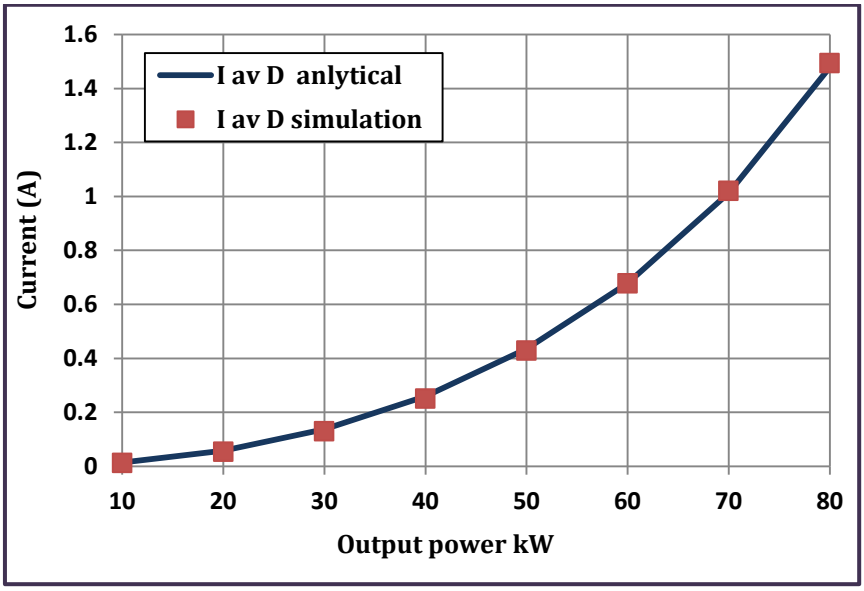
In order to validate the analysis, a comparison between the current values obtained from the analytical approach and a switch based simulation of the 3ϕ DAB was conducted. Figure 5.9 shows a comparison between the analytical and the simulation results.

The comparison was executed for a converter with the parameters presented in Table 5.1. The converter power rating was chosen to be 80kW to allow the assessment of building the required grid converter of 320 kW, which is a representation of the converter value calculated in section 4.7.1, from four 80 kW cells as discussed later in section 5.5. The design of the converter inductor was performed using the approach outlined later in section 6.4. The power flow direction is considered from the high voltage (sending bridge) to the low voltage (receiving bridge).

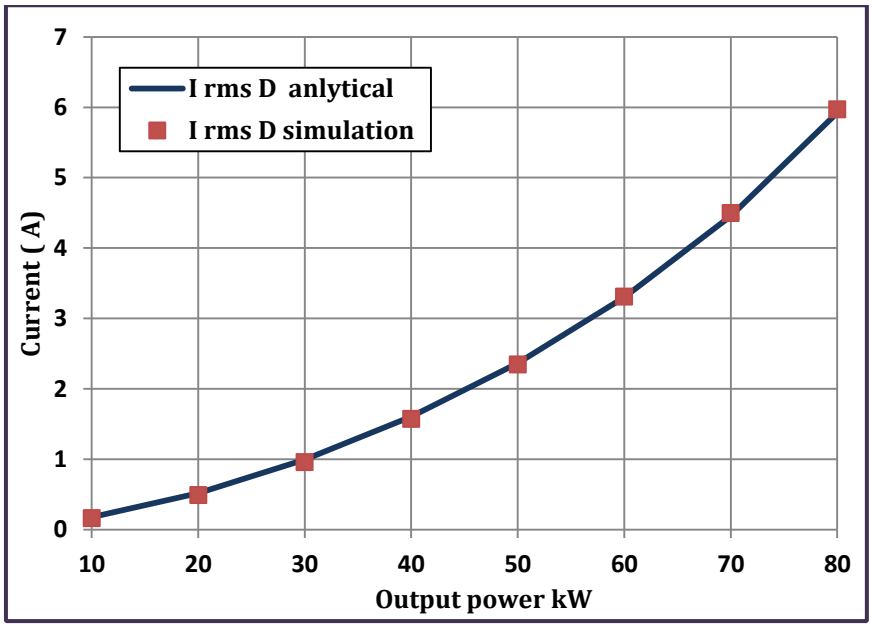
Table 5.1 The converter comparison parameters:

$f\ (kHz)$	$P(kW)$	$V_{in}\,(VDC)$	$V_{out}\,(VDC)$	$L_{HV}\ (mH)$	ϕ^o
20	80	1500	325	1.03	50

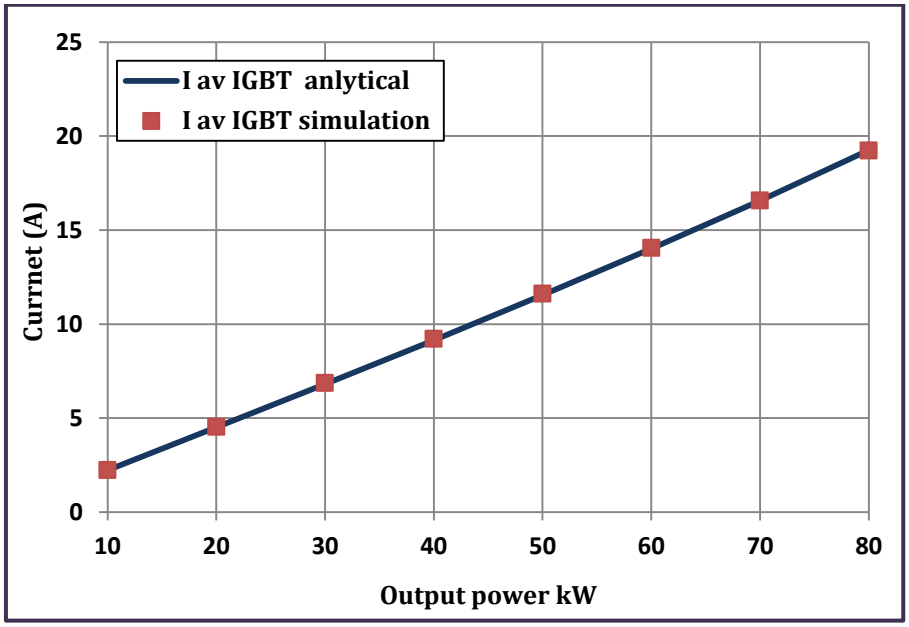
Figure 5.9 shows a good match between the simulation and the analytical values, which validates the analysis. This match represent an ideal cause were the dead time is not present if a dead time is used in the simulation it might lead to more deviation between the simulation and analyses.


I av D anlytical
I av D simulation
Current (A)
Output power kW
1.6
1.4
1.2
1
0.8
0.6
0.4
0.2
0
10
20
30
40
50
60
70
80

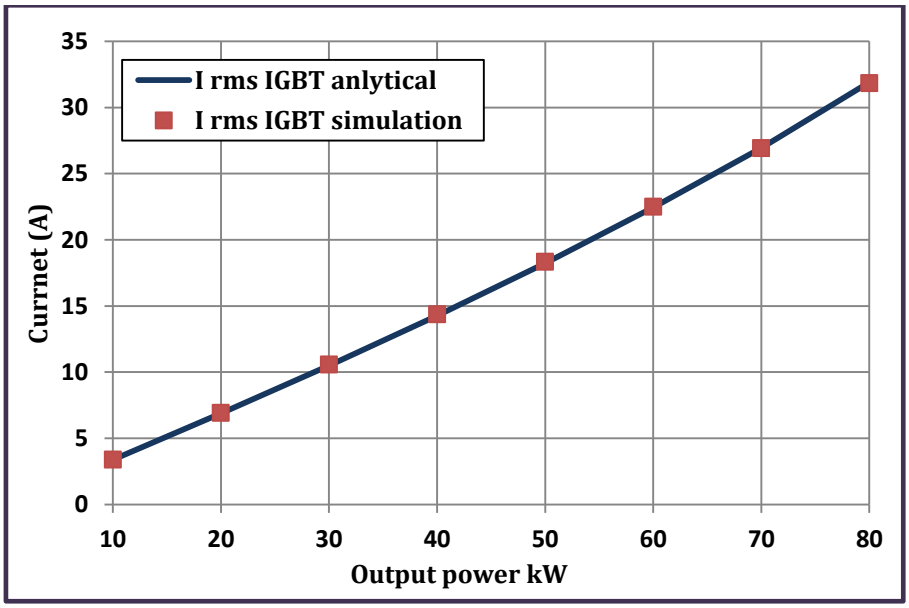
a.


I rms D anlytical
I rms D simulation
Current (A)
Output power kW
7
6
5
4
3
2
1
0
10
20
30
40
50
60
70
80

b.



c.



d.

Figure 5.9 A comparison between switched based simulation and the analytical device currents for the sending (high voltage) bridge a. The D1 average current, b. The D1 RMS current, c. The IGBT1 average current, d. The IGBT1 RMS current.

5.3.3 The conduction losses at the sending bridge

After the average and the RMS currents for the IGBTs and diodes are calculated the values of the conduction losses for one device can be estimated using equations (5.25-5.26).

$$\begin{aligned} P_{C\,IGBT} &= V_{CE0}.I_{Cav} + r_C.I_{Crms}^2 \\ &= V_{CE0} \times \frac{V_i \times \phi^2}{8 \times 3\omega L \times \pi} + r_c \left(\frac{V_i \times \phi}{3\omega L} \sqrt{1 - \frac{7 \times \phi}{12\pi}} \right)^2 \end{aligned} \tag{5.25}$$

$$\begin{aligned} P_{C\ D} &= V_{D0}.I_{Dav} + r_D I_{Drms}^2 \\ &= V_{D0} \times \frac{V_i \times \phi^2}{8 \times 3\omega L \times \pi} + r_D \times \left(\frac{V_i \times \phi\sqrt{\phi}}{6 \times \omega L \times \sqrt{3 \times \pi}} \right)^2 \end{aligned} \tag{5.26}$$

5.3.4 The conduction losses at the receiving bridge

Again from waveform symmetry, the losses in the receiving bridge can be determined as (5.27-5.28):

$$\begin{aligned} P_{C\,IGBT} &= V_{CE0}.I_{Cav} + r_C.I_{Crms}^2 \\ &= V_{CE0} \times \frac{N \times V_i \times \phi^2}{8 \times 3\omega L \times \pi} \times + r_c \times \left(\frac{N \times V_i \times \phi\sqrt{\phi}}{6 \times \omega L \times \sqrt{3 \times \pi}} \right)^2 \end{aligned} \tag{5.27}$$

$$\begin{aligned} P_{C\ D} &= V_{D0}.I_{Dav} + r_D.I_{Drms}^2 \\ &= V_{D0} \times \frac{N \times V_i \times \phi^2}{8 \times 3\omega L \times \pi} + r_D \times \left(\frac{N \times V_i \times \phi}{3\omega L} \sqrt{1 - \frac{7 \times \phi}{12\pi}} \right)^2 \end{aligned} \tag{5.28}$$

The total conduction losses of each bridge can be calculated by multiplying the total device conduction losses by the number of devices (6). It should be noticed that the power flow will be assumed from the high voltage (sending bridge) to the low

voltage (receiving bridge) for the following analysis and assessment of the converter.

To confirm the loss analysis, a simulation was conducted and a comparison between the simulation results and the results from the analysis is presented next.

5.3.5 Conduction losses simulation and analytical model comparison

For comparison, commercially available devices were used and the devices selected are the Infineon-FS100R17KE3-B17 for the high voltage side while for the low voltage side the SEMIKRON SEMiX402GAR066HDs was considered as they have enough current rating for the low voltage and high voltage side. It should be noted that for the high voltage side it is recommended to use devices with higher voltage rating as the 1700 V device might not be able, in practice, to withstand the high voltage spikes present but it has enough voltage rating for analytical comparison. The comparison was conducted for the converter cell rating presented in Table 5.1, Figure 5.10 to Figure 5.13 show a comparison between the losses determined using a simulation model in PLECS and the analytical expression. The results presented are for one device thus the total bridge losses should be the results in the figures multiplied by 6.

The high voltage bridge device the Infineon-FS100R17KE3-B17 parameters were estimated by applying the outlined methods in section 5.3 and are as follows: $V_{CE0} = 0.941V$, $r_C = 0.0147\ \Omega$, $V_{D0} = 1.11V$, and $r_D = 0.0079\ \Omega$. While The low voltage bridge

device the SEMIKRON SEMiX402GAR066HDs parameters are $V_{CE0} = 0.68V$, $r_C = 0.0038\ \Omega$, $V_{D0} = 0.9V$, and $r_D = 0.0022\Omega$.

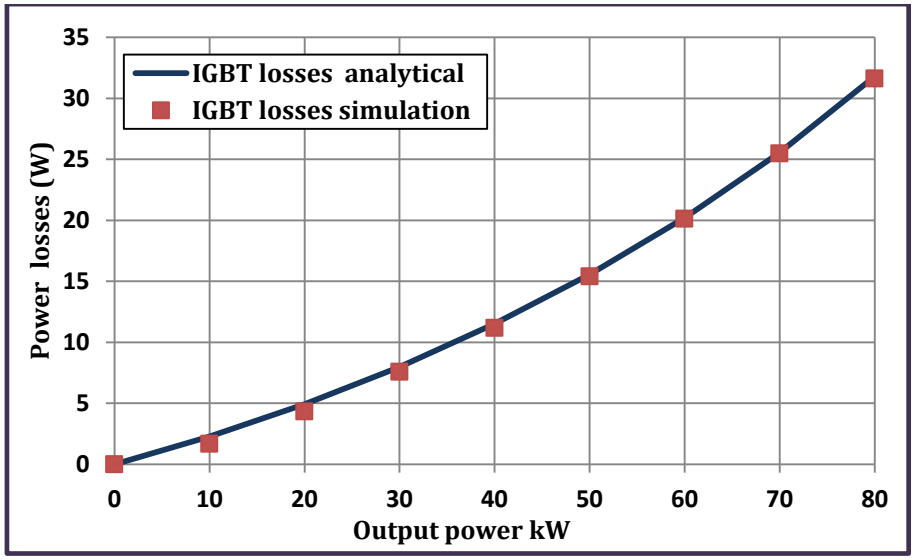


Figure 5.10 High voltage bridge IGBT conduction losses comparison between analytical and simulation.

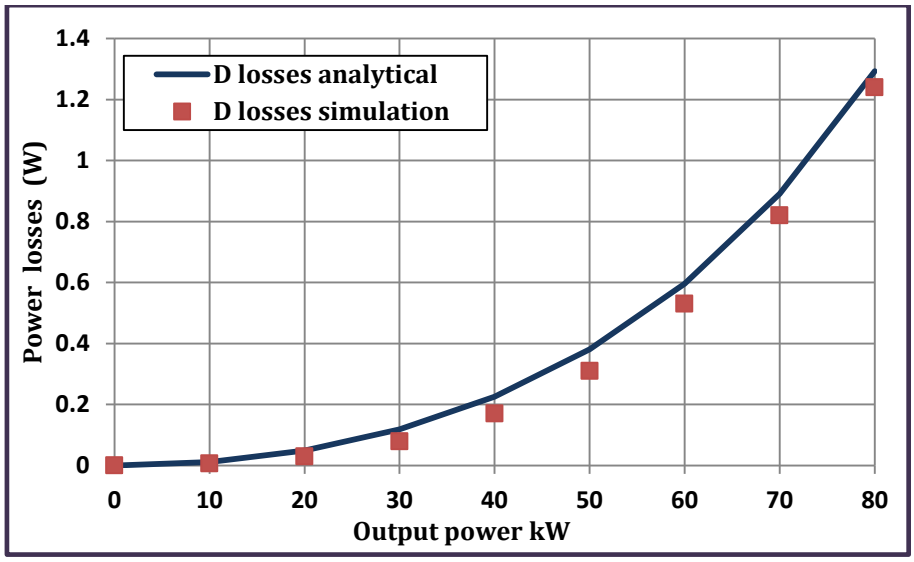


Figure 5.11 High voltage bridge diode conduction losses comparison between analytical and simulation.

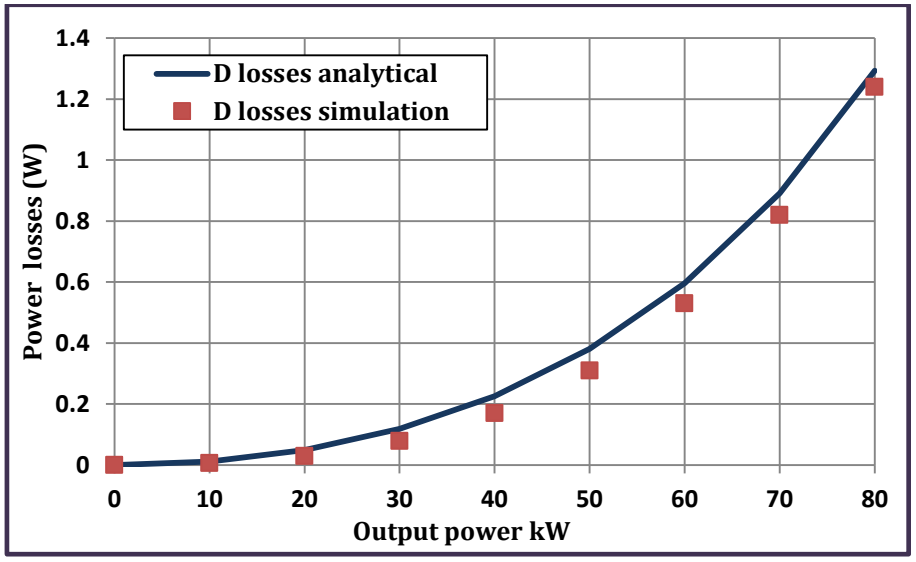


Figure 5.12 Low voltage bridge IGBT conduction losses comparison between analytical and simulation.

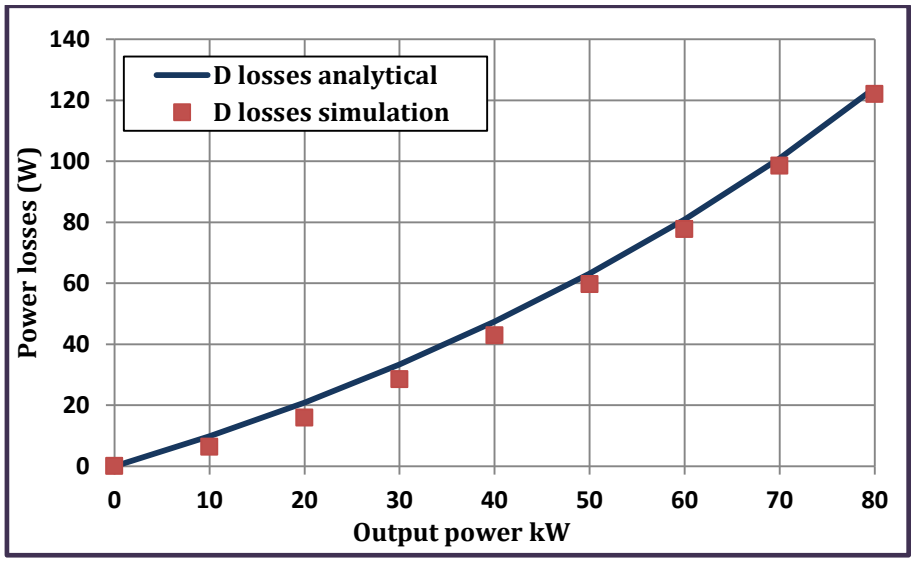


Figure 5.13 Low voltage bridge diode conduction losses comparison between analytical and simulation.

It can be noticed from Figure 5.11 and Figure 5.13 that there is a small difference between the analytical and the simulation results. This small different is expected due to the fact that the analytical model loss equations use linear approximations of the on state voltage and current curve of the IGBT and diodes to

describe the conduction losses while the PLECS simulation utilises look-up tables for the loss [71]. Overall a good match between the simulation and the analytical model validates the analytical model which was derived in this thesis.

5.4 The switching losses of the converter and the effect of snubber capacitors on the switching losses

This part of the thesis considers the switching losses of the converter and the use of snubbers to mitigate the turn-off loss is also considered.

As discussed in section 5.2.2 all the IGBTs are soft switched at turn on and hard switched at turn off in the soft-switched area.

The switching losses of 3ϕ DAB converter can be divided into three main losses:

- IGBT turn-on losses.
- IGBT turn-off losses.
- Losses due to diode reverse recovery.

The IGBT turn-on losses are theoretically zero and will be negligible due to the fact that the IGBT is soft switched at turn on. The IGBT turn-off losses are the main cause of switching losses and will be examined in more details.

The diode reverse recovery has no effect on the switching losses of the 3ϕ DAB converter in the range under consideration due to the fact that diode reverse recovery causes losses in the IGBTs and diodes only if the diode is forced to turn off while conducting current. In the operation range under consideration, the diodes are switched off at zero current and thus diode reverse recovery will not introduce any losses in the IGBT or in the diode.

5.4.1 IGBT turn-off losses estimation

The 3ϕ DAB loss model presented in this thesis is based on the analysis of the converters presented in [72-74]:

5.4.1.1 Estimating the IGBT turn-off losses without a snubber capacitor

The turn-off losses of the IGBT will be analysed and estimated initially with the assumption that the IGBT voltage will rise rapidly to V_i with negligible rise time. Figure 5.14 shows the simplified waveforms of the IGBT voltage and current at turn-off without a snubber[75].

The losses in the IGBT can be calculated using equation (5.29)[75]:

$$E_{IGBT\ loss} = \int_0^{t_f} V_{in} \times I_{\ IGBT}\, dt \qquad (5.29)$$

The IGBT current can be represented using equation (5.30)

$$I_{IGBT} = I_{com} - \frac{t \times I_{com}}{t_f} \tag{5.30}$$

Where:

I_{com} : is the IGBT current before the turn-off.

t_f : is the IGBT current fall time.

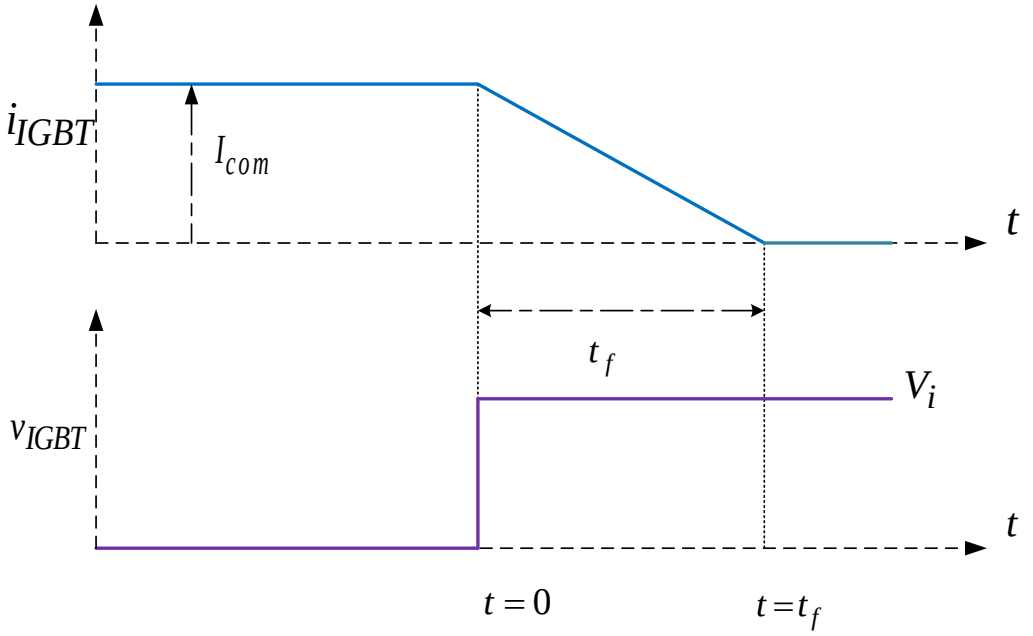


Figure 5.14 Simplified voltage and current the waveform of IGBT at the turn off without a snubber [75].

Substituting 5.30 into 5.29 and integration yields:

$$E_{IGBT\ loss} = \frac{V_{in} I_{com} t_f}{2} \tag{5.31}$$

5.4.1.2 Estimating the IGBT turn-off losses with a snubber capacitor

When a snubber capacitor is present, it will conduct the device turn off current, thereby reducing dv/dt. At the instant of device turn off, the inductor current will start charging the snubber capacitor connected with the outgoing IGBT. Conversely, the snubber connected with the incoming IGBT will start to discharge. This will continue until the outgoing IGBT snubber capacitor is charged to (V_i) and the incoming IGBT snubber capacitor is discharged to zero.

The simplified waveforms of the current and the voltage are presented in Figure 5.15 [75].

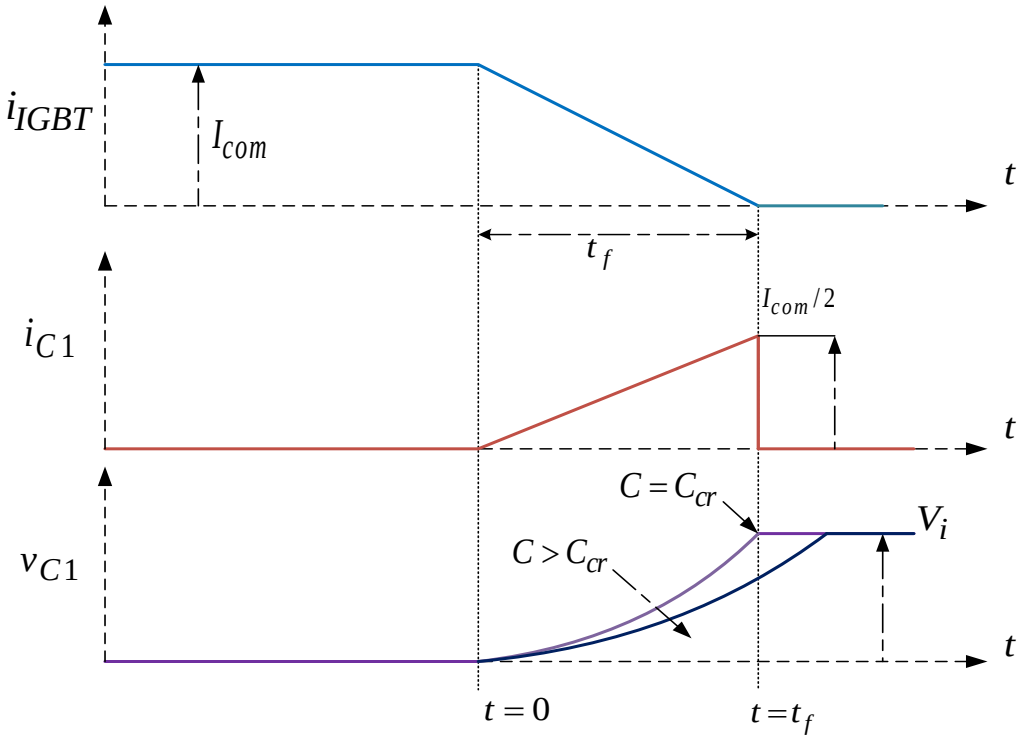


Figure 5.15 The simplified voltage and current waveform of IGBT at the turn off with a snubber [75].

It should be noticed that the snubber capacitor will charge in time t_f to the voltage V_i if a specific value of snubber capacitor is used which is called the critical snubber C_{cr} . It will take a longer time if snubber value higher than the critical snubber is used as presented in Figure 5.15. Additionally, it should be noticed that the effect of the IGBT tail current is not considered for this analyses and will be considered later in chapter 6 for the practical snubber capacitor calculation.

The current on the IGBT and the snubber can be determined using equations (5.32) and (5.33):

$$i_{IGBT} = I_{com} - \frac{t \times I_{com}}{t_f} \tag{5.32}$$

$$i_{C1} = \frac{t \times I_{com}/2}{t_f} \tag{5.33}$$

The capacitor voltage can be represented using equation (5. 34):

$$v_{C1} = \frac{1}{C}\int i_{C1} dt = \frac{I_{com}}{2C} \times \left[\frac{t^2}{2t_f} \right] \tag{5.34}$$

While the energy losses in the IGBT are calculated using equation (5.35):

$$E_{IGBT\ \ loss\ with\ \ Snubber} = \int_0^{t_f} p dt = \int_0^{t_f} v_{C1} \times i_{IGBT}\, dt \tag{5.35}$$

Thus by replacing (I_{C1},V_{C1}) from equations (5.33) and (5.34) into equation (5.35), the IGBT losses can be estimated as follows [75]:

$$E_{IGBT\ loss\ with\ Snubber} = \int_0^{t_f} \frac{I_{com}}{2C} \times \left[\frac{t^2}{2t_f} \right] \times \left[I_{com} - \frac{t \times I_{com}}{t_f} \right] dt$$

$$E_{IGBT\ loss\ with\ Snubber} = \frac{I_{com}^2 t_f^2}{4C} \left[\frac{1}{3} - \frac{1}{4} \right] = \frac{I_{com}^2 t_f^2}{48C} \qquad (5.36)$$

It should be noticed that equation 5.36 is only valid a for capacitor value higher than or equal to the critical snubber.

The voltage across the capacitor will reach $V_C = V_i$ when $t = t_f$ if a critical snubber is used and by substituting this condition into equation (5.34), the value of the required critical snubber can be estimated[75]:

$$V_{C1} = V_i = \frac{I_{com}}{2C_{cr}} \times \left[\frac{t^2}{2t_f} \right] = \frac{I_{com} t_f}{4C_{cr}} \qquad (5.37)$$

Thus

$$C_{cr} = \frac{I_{com} t_f}{4V_i} \qquad (5.38)$$

The energy losses of the IGBT with a critical snubber capacitor can be estimated by replacing the snubber capacitor value from (5.38) into the IGBT energy losses equation [75](5.46)

$$E_{IGBT\ \ loss\ \ with\ \ critical\ \ Snubber} = \frac{I_{com}^2 t_f^2 \times 4V_i}{48 \times I_{com} t_f} = \frac{I_{com} t_f V_i}{12} \tag{5.39}$$

5.4.2 Minimum current requirement for ZVS with snubber capacitor

A 3ϕ DAB converter working within the soft switching region has ZVS/ZCS IGBT turn-on. Adding a snubber capacitor to the 3 ϕ DAB converter will lead to a violation of the ZVS turn-on of the IGBT. In order to have a soft turned on of the IGBT, the voltage across the IGBT at the turn on should be zero and the incoming IGBT snubber capacitor should be fully discharged. A snubber capacitor will require a certain level of the commutation current to discharge it to zero before the dead time finishes and the incoming IGBT is turned on. If the turn-off current is lower than this limit, the incoming IGBT snubber capacitor will not fully discharge within the dead time. The remaining energy in the incoming IGBT snubber capacitor will be discharged in the incoming IGBT at turn on causing turn-on losses.

The analysis of the soft switch turn on boundaries of the 3ϕ DAB was presented in [74] and will be reinvestigated in this thesis using different approach The 3ϕ DAB converter circuit has to be analysed at the moment of turn off to estimate the turn off current required to fully discharge the incoming IGBT snubber capacitor before the dead time is finished and the incoming IGBT turns on. For this analysis, the IGBT fall time will be assumed to be zero and the analysis will be accurate for

the case where the snubber capacitor is significantly larger than the critical value.

During the turn off instance of the IGBT, the circuit and the conducting elements (in red) in the 3 ϕ DAB are presented in Figure 5.16. The turning on IGBTs are as presented in Figure 5.3 as the converter is working in zone 1.

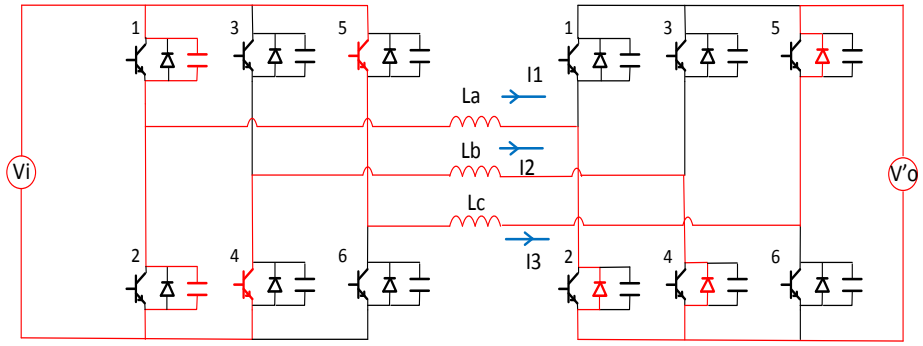


Figure 5.16 Current path and conducting devices at snubber commutation

The circuit in Figure 5.16 can be rearranged and analysed to estimate the minimum current requirement for ZVS turn-off as presented in appendix (D). The relation between the current and voltage at the moment of commutation is presented in equation (5.40)

$$\frac{dv_c(0)}{dt} = \frac{I_{com}}{2} \tag{5.40}$$

Equation (5.40) can be solved and equations 5.40 and Figure 5.17 shows the snubber current and voltage at commutation if the diode is ignored.

$$v_c = V_{c\max}\sin(\omega t) \tag{5.41}$$

$$i_c = I_{com}\cos(\omega t) \tag{5.42}$$

$$V_{c\max} = I_{com} Z_0 \tag{5.43}$$

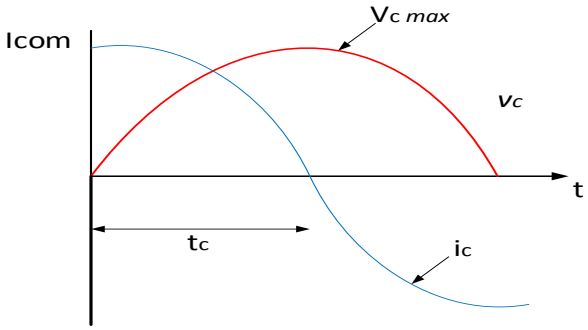


Figure 5.17 The snubber capacitor voltage and current at commutation

The converter will be in ZVS when the $V_{c\max} = V_i$ thus after solving the equation as presented in appendix (D) the minimum current requirement for ZVS can be calculated as follows as L represents the total inductance of the transformer and the external inductor:

$$I_{com} = \frac{V_i}{Z_0} \tag{5.44}$$

Where:

$$Z_0 = \sqrt{\frac{3L}{4C}} \tag{5.45}$$

$$\omega = \frac{1}{\sqrt{3LC}} \tag{5.46}$$

$$t_c = \frac{\pi}{2\omega} \tag{5.47}$$

A converter can be working at ZVC limit if the turn-off current is equal or higher than the required current for ZVC. Figure 5.18 indicates the three possible situations for the current at the turn-off. Due to the fact that a snubber capacitor is significantly greater than the critical value, if it is assumed that t_c is significantly larger than the t_f for the IGBT in this analysis [74].

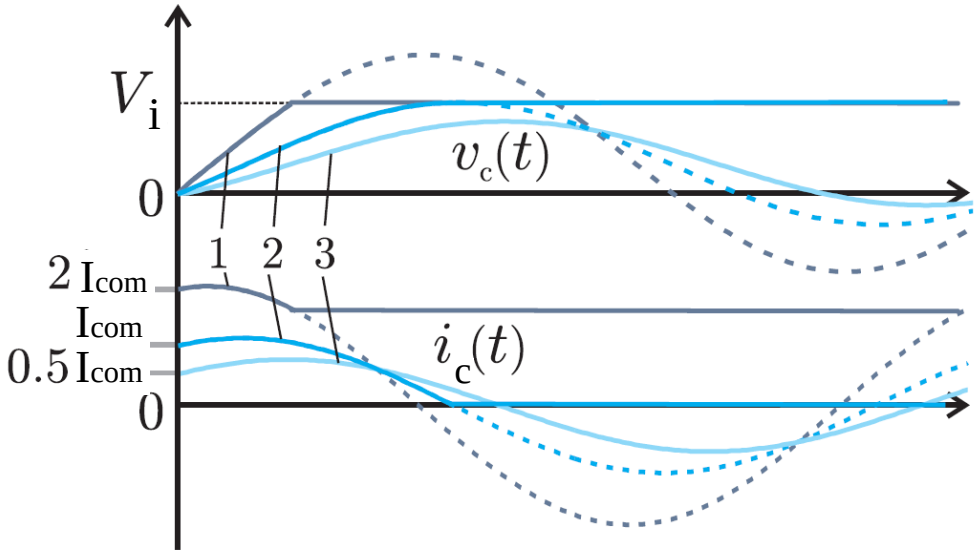


Figure 5.18 Snubber voltage and current at three different turn off current levels [74].

In order to maintain the soft switching, it is important to fully charge the outgoing IGBT snubber capacitor within the dead time before the incoming device is turned on. .

- If $I_{com} < V_i / Z_0$ (5.48)

  The outgoing IGBT snubber will not charge to V_i and the ZVS cannot be achieved.

- If $t_d < \frac{1}{\omega}\sin^{-1}(\frac{V_i}{I_{com}Z_0})$ (5.49)

The incoming device will be fired before the outgoing IGBT snubber capacitor is charged to V_i and the ZVC is lost.

- The dead time should be in the right range to allow for ZVC and should not be so large to cause the outgoing IGBT capacitor discharge and loss of ZVC.

The dead time should be higher than the value in equation (5.49) to allow for the outgoing IGBT capacitor to be fully charged before gating the incoming IGBT. However, if the dead time is too large, the inductor current will reach zero and as consequence, the outgoing IGBT capacitor will start discharging and when the incoming IGBT is turned on therefore the ZVS will be lost.

If $I_{com} = V_i / Z$, the outgoing IGBT capacitor will be charged to V_i and the current will reach zero this commutation time is the critical commutation time (t_{crit}).

$$t_{crit} = \frac{\pi}{2\omega} \quad (5.50)$$

The required time for the current to reach zero can be calculated as the summation of the time of the equivalent snubber/inductor commutation $t_{com\,end}$ and the time $t_{diode\ com}$ required for the diode current to decrease from its initial value $I_{com\,end}$ at the end of the equivalent snubber/ inductor commutation to when it reaches zero

$$t_{com\,end} = \frac{1}{\omega}\sin^{-1}\left(\frac{V_i}{I_{com}\ Z_0}\right) \tag{5.51}$$

$$I_{com\,end} = I_{com}\ \cos\left(\omega t_{com\,end}\right) \tag{5.52}$$

The time required for the current going through the diode and the inductor depends on the initial voltage across the inductor which is equal to $2V_i/3$. And by using the relation between the inductor voltage and current $V = L(di/dt)$ the $t_{diode\ com}$ can be calculated as in (5.53)

$$t_{diode\ com} = \frac{3\ L\ I_{com\,end}}{2V_i} \tag{5.53}$$

$$t_{diode\ com} = \frac{3\ L\ I_{com}\ \cos\ (\omega t_{com\,end})}{2V_i} \tag{5.54}$$

So the maximum dead time $t_{d\ \max}$ should be smaller than $t_{com\,end} + t_{diode\ com}$ in order to keep the ZVC of the bridges at specific I_{com}

$$t_{d\ \max} = t_{com\,end} + t_{diode\ com} \tag{5.55}$$

To sum up for each turn off current and specific snubber capacitor the required dead time should be bigger than the time required for the outgoing IGBT snubber to be fully charged as calculated in equation 5.49 still it should not be so large, as calculated in equation 5.55, or it will cause the diode current to reach zero that will cause the outgoing IGBT snubber to start to discharge and the ZVS will be lost.

5.4.3 Switching losses comparison between snubbered and un-snubbered situations.

In this part of the thesis, an analytical comparison between the snubbered and the un-snubbered converter cell is performed in order to investigate the advantages and disadvantages of adding a snubber to the converter.

The comparison was conducted using a converter cell as rated in Table 5.1. The IGBTs used are the same as stated in section 5.3.5.

The study was conducted using the critical snubber values of 1.7nF for the high voltage side and 7.8nF for the low voltage side and they were calculated using equation (5.38). While the range of ZVS turn-on was calculated using equation (5.40), the shaded area in Table 5.2 represent the no ZVS area. The losses of the unsnubbered IGBT were calculated using the turn-off losses available from the device data sheet.

From Table 5.2 a high reduction of the turn-off losses can be observed between the snubbered and the unsnubbered cells in the soft switching range.

For the high voltage bridge, the switching losses were reduced from 2750 W to 150.2 W at full power, while the reduction in losses was from 1620W to 28.5 W at half rated power. For the low voltage bridge, the losses at full power where 1440W and was reduced to 32.7W and at half rated power the losses were decreased from 773W to 6.2W. Thus a high turn-off losses saving was noticed when using snubber capacitors in the soft switching range.

On the other hand, it was noticed that the in the low power range the snubbered cell lost its advantage. It was noticed that the snubbered high voltage bridge will lose its turn on soft switching at around 20% of the rated power while the snubbered low voltage bridge lost its turn on ZVS at around 12.5% of its rated power.

Table 5.2 An analytical comparison between the snubbered and unsnubbered total turn-off switching losses for one converter cell switching at 20 kHz:

P(kW)	High voltage bridge switching losses (W)		Low voltage bridge switching losses(W)	
	Un-Snubbered	Snubbered	Un-Snubbered	Snubbered
0	750		156	
10	952		379	
20	1,163		504	1.4
30	1,385	15.2	635	3.3
40	1,620	28.5	773	6.2
50	1,870	47.1	920	10.3
60	2,138	72.4	1,079	15.8
70	2,429	105.8	1,250	23.1
80	2,750	150.2	1,440	32.7

The snubbered bridges will suffer from high turn-on losses at this range highlighted in blue in Table 5.2, as the remaining charge in the snubber capacitor will lead to snubber energy dump in the IGBT as explained in section 5.4.

In order to best utilise the advantages of the snubbered and unsnubbered converter cells and to avoid their drawbacks, a multi-cell multi-snubbered arrangement is proposed next.

5.5 Multi-cell multi-snubbered 3ϕ DAB converter

The 3ϕ DAB converter is well suited for the application under consideration, DC distribution grids. As discussed earlier in this thesis, the DC grid requires a DC-DC converter with high efficiency over a wide operation range; the 3ϕ DAB converter is capable of achieving this condition but cannot fully cover the whole range of operation. In this part of the thesis, the idea of further advancing the 3ϕ DAB converter performance by building a 3ϕ DAB converter from multi-cell multi-snubbered converter is going to be investigated.

The idea of multi-cell multi-snubbered 3ϕ DAB converter was realized from the converter losses analysed under different snubbering situations. It was noticed that the switching losses of the 3ϕ DAB converter vary with the converter's loading and snubbering. A converter cell working at currents higher than the soft switching turn on current limit will have lower turn-off losses if the converter cell is snubbered, while a snubbered converter working at currents lower than the soft switching turn on limit will be hard switched turn on with high losses due to snubber capacitor energy discharge in the device.

The conditions which affect the total losses of a multi-cell multi-snubbered 3ϕ DAB converter are:

- The number of cells supplying the load.
- The number of snubbered and un-snubbered cells used.
- The power management strategy in place between the cells.

Based on the last three factors, an efficient wide power range operation converter can be achieved if a mix of snubbered and un-snubbered converter cells is used. The snubbered cells will be used at higher loading profiles and the unsnubbered cells will be used to supply the load at low loading range. Thus a converter made of a group of snubbered and unsnubbered cells can supply the load with high efficiency over the entire operation range. Figure 5.19 indicates a multi-cell multi-snubbered 3ϕ DAB converter.

In order to identify the achievable efficiency from the converter, a 3ϕ DAB converter cell was built in the laboratory to test the achievable practical efficiencies of the 3ϕ DAB converter cell under different loading and different snubbering situations. After that, the effects of building a multi-cell multi-snubbered converter will be highlighted.

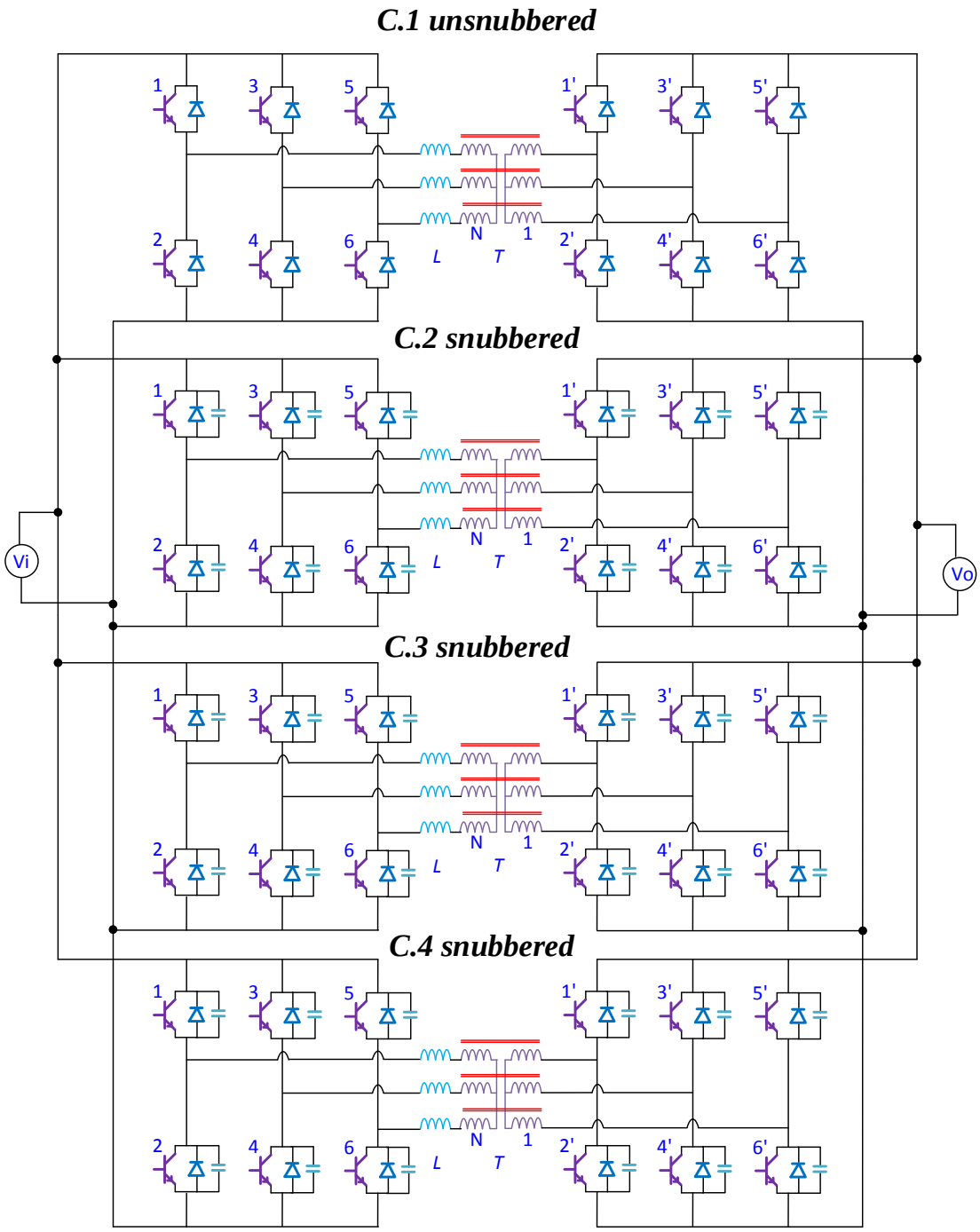


Figure 5.19 The multi-cell multi-snubbered 3ϕ DAB converter concept

5.6 Summary:

This chapter presented the motivation behind selecting the 3ϕ DAB converter to serve the proposed DC/DC grid in chapter 4. Furthermore, analytical models to describe the conduction losses of the 3ϕ DAB converter were developed. The effect of snubbers on the 3ϕ DAB converter was also studied and evaluated. Finally, the idea of a multi-cell multi-snubbered 3ϕ DAB converter was proposed in this chapter.

The following chapters will include the design and testing of a scaled 3ϕ DAB converter cell prototype, followed by an evaluation of the proposed multi-cell multi-snubbered 3ϕ DAB converter.

Chapter 6

Hardware Implementation.

6.1 Introduction

This chapter presents the design and implementation of a 3ϕ DAB converter cell in the laboratory.

A detailed design of each part of the converter is presented, in this chapter, including the high-frequency transformers inductors, snubber capacitors, IGBTs, high and low voltage capacitor filters, gate drivers, DSP, FPGA, and the measurements board.

6.2 The experimental rig

The main boundaries when choosing the implemented practical converter were the voltage and power levels which should be as close as possible to the required converter rating of 320 kW as discussed in chapter 5, whilst still within the laboratory and project funding limits.

In order to achieve this vision, one cell of the multi-cell 3ϕ DAB converter was proposed to be built. The proposed cell has the rating as presented in Table 6.1. The application converter has a rating of 320 kW thus four cells of 80kW can be used to build this converter as discussed in chapter 5. In the laboratory, a scaled version of the 80 kW cell rated at 20 kW was built, after considering the funds and laboratory limitation. This leads to a four cells converter with a total rating of 80 kW.

The practical converter design voltages were kept identical to the required application voltages of 1500 VDC and 325 VDC as specified in chapter three due to the availability of a power supply capable of supplying the high voltage of 1500VDC at the required power rating of 20kW. A 20 kHz switching frequency was chosen in order to operate above the audible frequency range.

Table 6.1 The 3ϕ DAB converter cell design specifications:

P_{out} *(kW)*	V_i (DCV)	V_o (DCV)	$f_{AC\ link}$ *(kHz)*	d	$\phi^o_{\max}$
20	1500	325	20	1	50

The proposed converter-cell will be used to test the performance of the individual cells in the proposed multi-cell converter under different loading and snubbering situations, which can then be used to examine the performance of the complete multi-cell multi-snubber converter.

Next, the experimental component design will be considered.

6.3 The high frequency high power transformer.

6.3.1 Transformer rating and specifications:

The transformer isolates the high from the low voltage levels. It is connected between the two bridges, thus a high-frequency transformer can be used leading to a weight and losses saving when compared to a standard 50Hz AC grid transformers at the power level under consideration [74]. The required transformer rating will be calculated. The transformer is star/ star connected as in figures Figure 6.1.

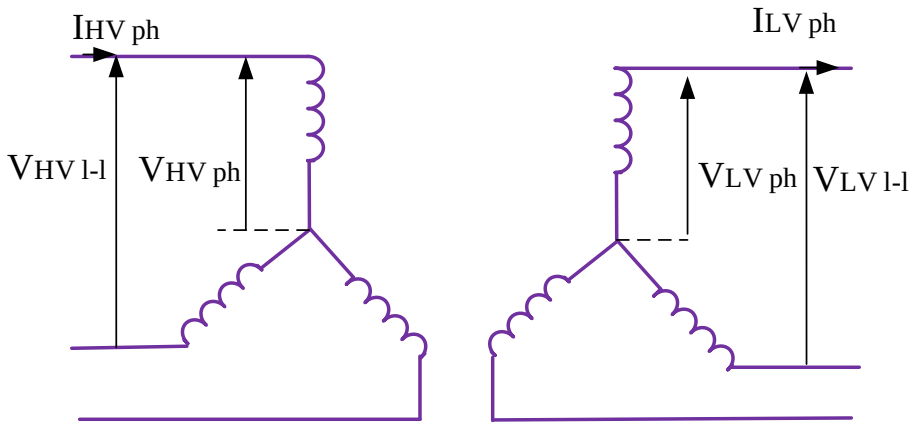
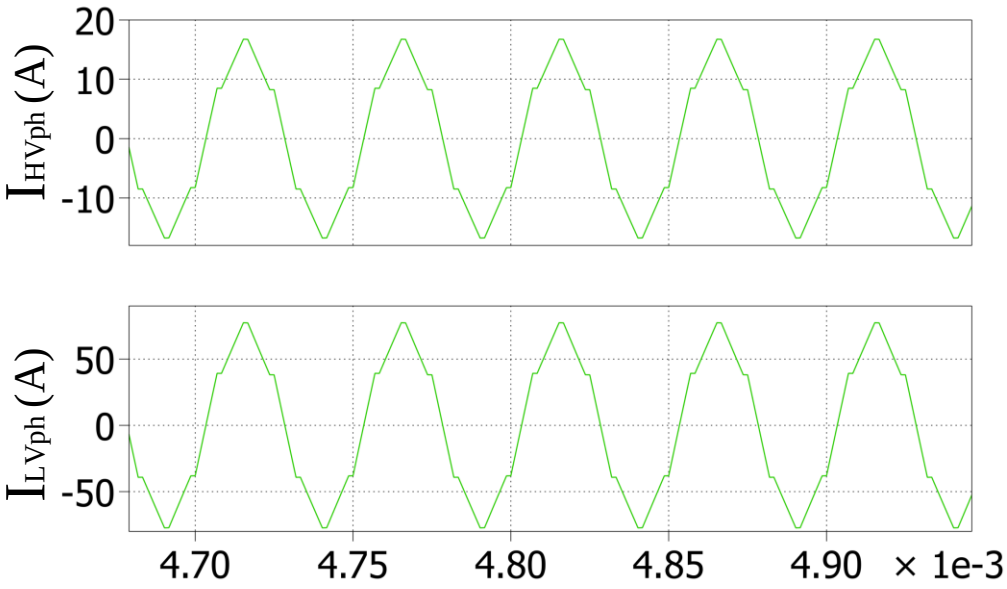
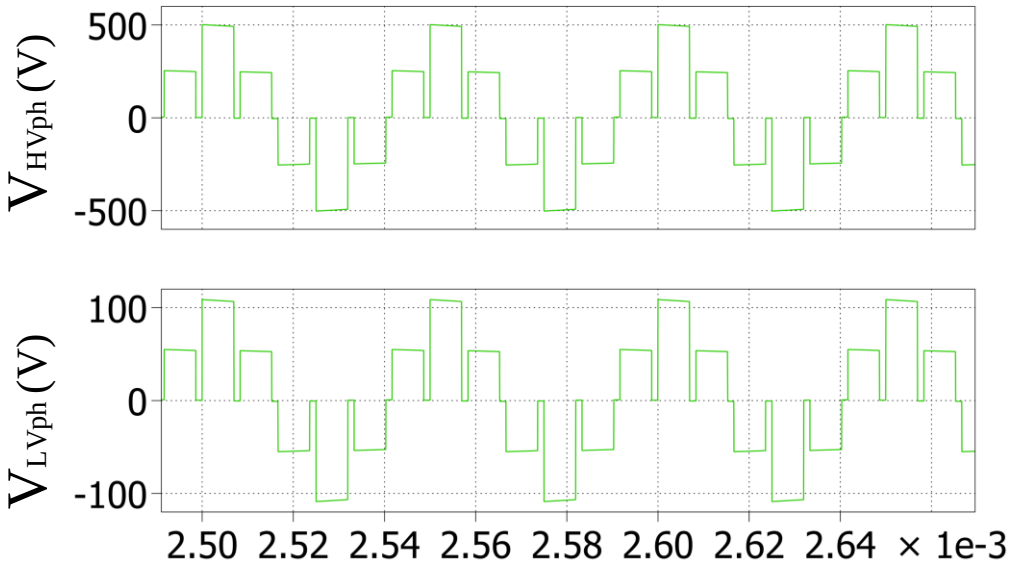


Figure 6.1 The star/star connection of the transformer.

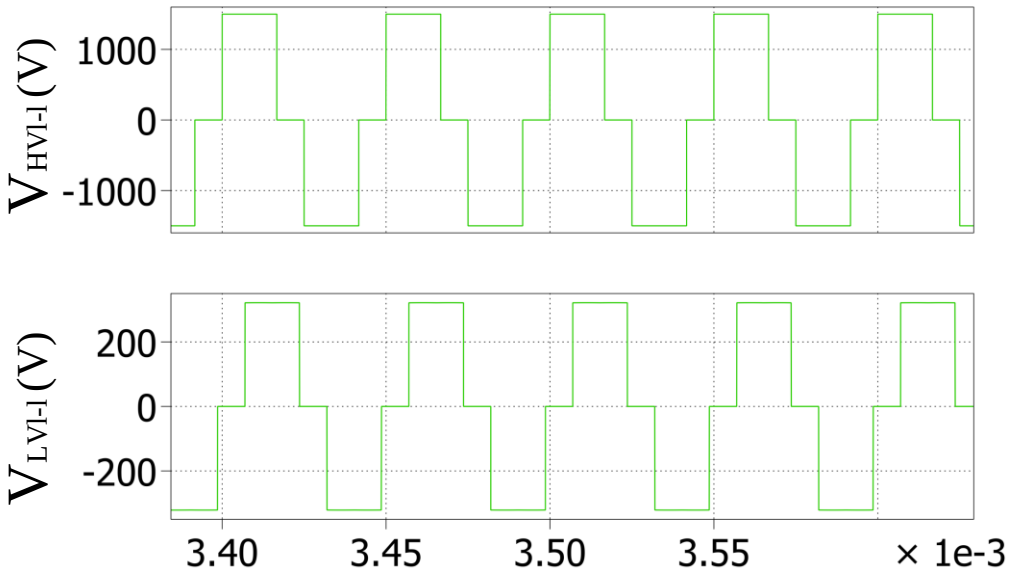
Figure 6.2 indicates the current and the voltage waveforms at different locations of the transformer.



a.



b.



c.

Figure 6.2 The three phase dab transformer current and voltages, a. The high and low voltage side current, b. The high and low voltage phase voltages, c. The high and low voltage lone to line voltages.

The converter high voltage side current $I_{HV\ rms}$ can be calculated using equation (6.1)

$$I_{HV\ rms}=\frac{V_i \times \phi}{3\omega\ l}\sqrt{2-\frac{\phi}{\pi}}=11.05A \quad (6.1)$$

The low-voltage side current can be calculated using equation (6.2)

$$I_{LV\,rms}=I_{HV\ rms}\times\frac{V_{HV\,l-l}}{V_{LV\,l_l}}=51A \quad (6.2)$$

The apparent power rating of the transformer (kVA_T) is calculated using equation (6.3) [68].

$$kVA_T=\frac{V_{HV}(1+d)I_{HV\,rms}}{\sqrt{2}}=23.4\ kVA \quad (6.3)$$

The transformer will be connected in a star/star as in Figure 6.1 and will be built from three single phase transformers due to the simplicity of design and fabrication. The required inductor can be incorporated in the transformer leakage inductor [76] still, it will be designed as separate extra inductor within this thesis due to the simplicity of design. The rating of the single phase transformer is:

$$KVA_{T(Single\ \ phase)}=\frac{KVA_{T(Threephase)}}{3}=7.8kVA \quad (6.4)$$

$$V_{HV-ph}=\frac{V_{HV-l-l}}{\sqrt{3}}=866\ V \quad (6.5)$$

$$V_{LV\ ph} = \frac{V_{LV-l-l}}{\sqrt{3}} = 187.63\,V \tag{6.6}$$

$$I_{HV\ ph\ rms} = I_{HV\ l-l\ rms} = 11A \tag{6.7}$$

$$I_{LV\ ph\ rms} = I_{LV\ l-l\ rms} = 51A \tag{6.8}$$

6.3.2 Transformer design.

In order to design a transformer with the required specification, the core material type and size has to be selected. Also the conductor type, size and number of turns for the high and low voltage have to be chosen.

The design is done by following the simplified flowchart presented in Figure 6.3.

The Litz wire was the conductor of choice due to the following:

- The Litz wire is flexible and easy to be wound.
- The availability of the Litz wire for use in this project.

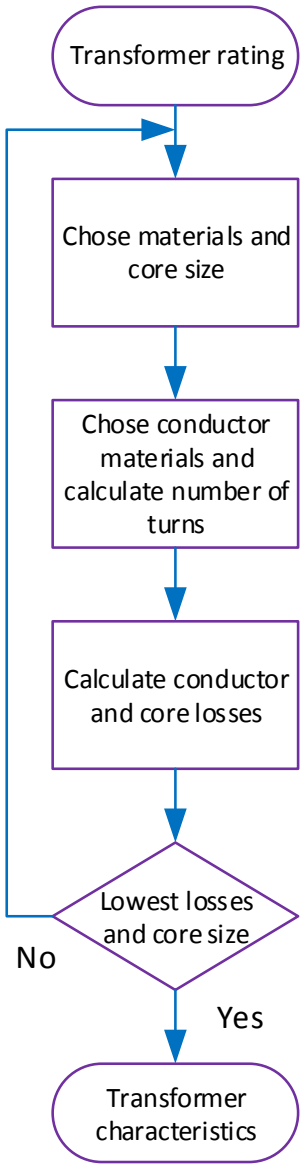


Figure 6.3 Flow chart showing the transformer design steps.

The required Litz wire gauge depends on the converter operational frequency. The available wires to be used are round 32 and 38 AWG Litz wires from the Pack Feindrahte Company. According to the New England Wire Technology company gauge wire table presented in Table 6.2 The available wires can be used at a switching frequency of 20 kHz and provide a Rac/Rdc ratio of 1 [77].

Table 6.2: Litz wire gauge from The New England Wire Technology Company [77].

Frequency	Recommended wire gauge	Nominal diameter over Copper	Single strand Rac/Rdc
60Hz/1 kHz	28AWG	0.0126	1
1kHz-10 KHz	30AWG	0.0100	1
10KHz-20kHz	33AWG	0.0071	1
20kHz-50kHz	36AWG	0.0500	1
50kHz-100kHz	38AWG	0.0040	1

Next, the core material will be considered. There are many candidate materials for the high-frequency transformer core such as Nanocrystalline, ferrite and amorphous materials. The main consideration when selecting a high-frequency core is the core losses.

The Nanocrystalline NANOPERM cores from MAGNETEC GmbH Company provide the lowest losses among the candidate materials thus will be used to design the transformer. Figures 6.4 shows the specifications of the NANOPERM core [78].

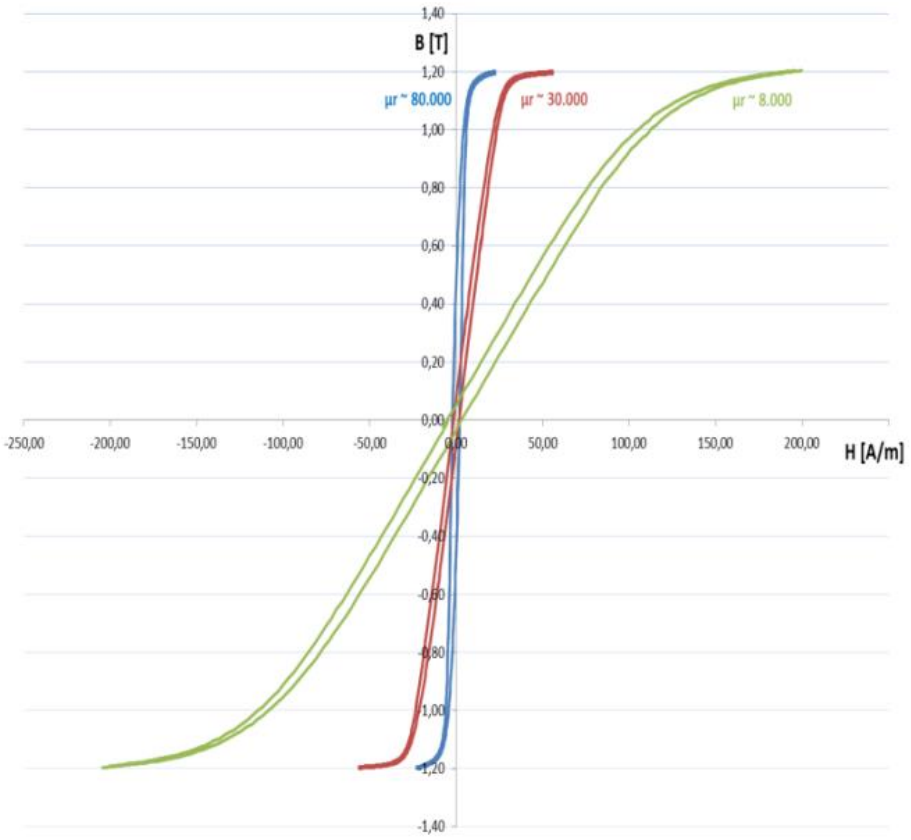
To start the transformer design the total cross-sectional area of the Litz wire has to be calculated, $J=4.5A/mm^2$ is suitable current density as the litz wire will have a Rac/Rdc=1 thus the

losses will be low and high current density can be utilised. The required Copper area for the high and the low voltage sides is as follows:

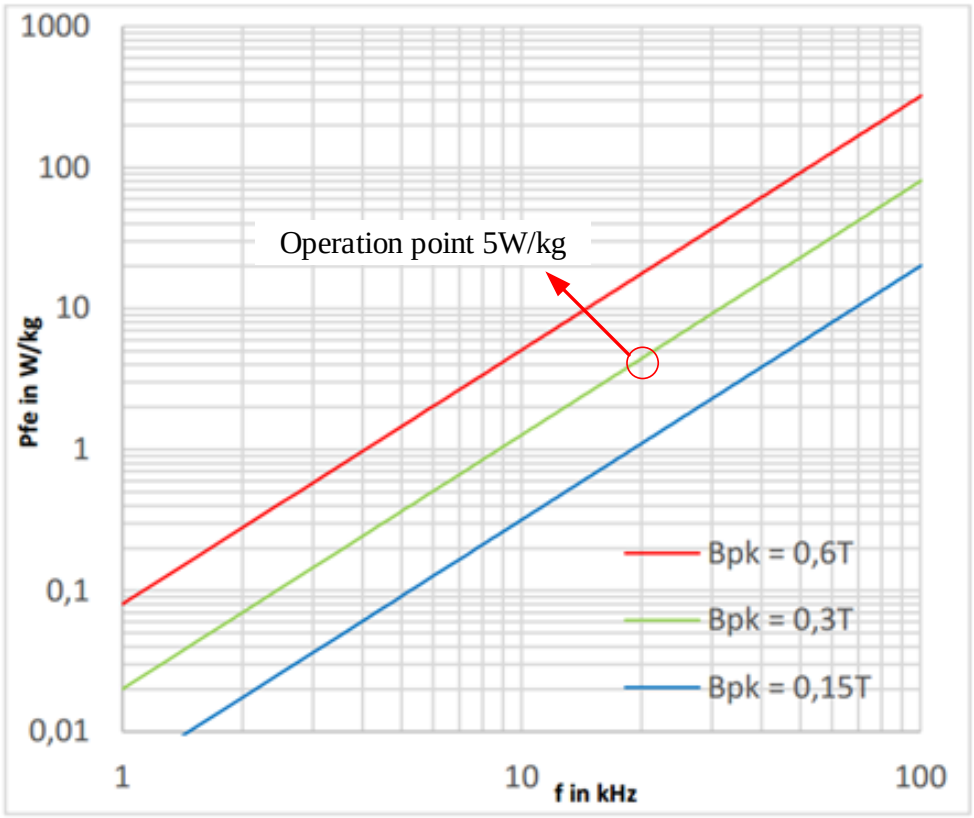
$$J = \frac{I_{rms}}{W_{A1}} \tag{6.9}$$

$$W_{A\ HV} = \frac{I_{HV\ ph\,rms}}{J} = \frac{11}{4.5} = 2.44mm^2 \tag{6.10}$$

$$W_{A\,LV} = \frac{I_{LV\ ph\ rms}}{J} = \frac{50}{4.5} = 11.1mm^2 \tag{6.11}$$



a.



b.

Figures 6.4 The Nanocrystalline NANOPERM core M-142 specifications a. Hysteresis loop of core M-142 (reprinted from [78]) b. Specific Losses of core M-142 [78].

Thus for the high voltage side, one wire of the Round AWG 32 is suitable to carry the current while for the low voltage side two Litz wires of the round AWG 38 wire have to be connected in parallel.

Next, the available Nanocrystalline NANOPERM cores were investigated in order to check for a core with suitable cores section and window areas to house the required number of turns.

Table 6.3 The chosen wire of the transformer:

	Wire type	N of strands	D of single strands mm	Copper cross section mm^2	Rdc $m\Omega/m$
High voltage side	Round AWG 32	100	0.2	3.14	5.5
Low voltage side	Round AWG 38	630	0.1	4.95	3.5

The relation between the flux and the core cross section area is presented in equation (6.12)

$$B = \frac{1}{NA_e}\int Vdt == \frac{1}{N_1 A_e} \times (\frac{V}{K_f \times f}) \quad (6.12)$$

Where:

B The peak flux density

N The number of turns

A_e Effective core cross section area

V The applied voltage

The transformer will be working in a symmetrical operation thus the peak change in flux will be equal to two times the Bmax:

$$\Delta B = 2 \times B_{\max} \quad (6.13)$$

From equation (6.12) and (6.13), the number of turns can be calculated. The number of turns at the low voltage is determined by the required voltage ratio between the high and low voltage side:

$$N_{LV} = \frac{V_{LV-l-l}}{V_{HV-ph}} \times N_{HV} \tag{6.14}$$

Thus for each core size and operating flux density, there is a required number of turns, the total number of turns should fit within the winding area of the core which can be calculated using equation (6.15)[79].

$$Aw = \frac{(W_{A\ HV} \times N_{HV} + W_{A\ LV} \times N_{LV})}{K_u} \tag{6.15}$$

It should be noticed that the total wire size is not equal to the total copper size as the Litz wire will have a considerable amount of insulation to insulate each Copper strand. Thus, the winding factor K_u is used to accommodate the Litz wire. Although winding factor greater than 0.6 can be achieved for some transformers [79] an acceptable winding factor in this design could be lower than 0.6 due to the required isolation between the Litz wire strands.

The final step is to check the core and Copper losses this can be done using the following equations:

The core losses can be estimated using Figures 6.4 or using the Steinmetz equation (6.16) [74]:

$$P_m = K.f^{\alpha}B^{\beta} \tag{6.16}$$

Where:

P_m Specific core losses (W/Kg)

K, β, α Steinmetz equation constants.

The Copper losses can be calculated using equation (6.17).

$$\begin{aligned}\text{Copper losses} &= \text{N}_{\text{HV}} \times I^2{}_{HV\ \ ph\ rms} \times \text{Length}_{one\ turn} R_{AC}(\Omega/m) \\ &+ \text{N}_{\text{LV}} \times I^2{}_{LV\ \ ph\ rms} \times \text{Length}_{one\ turn} R_{AC}(\Omega/m)\end{aligned} \quad (6.17)$$

After investigating the available cores, the final design was made using NANOPERM M-142 oval core 130x100x20mm, Nanocrystalline cores from MAGNETEC GmbH Company [78]. It should be noticed that the core is slightly oversized as it was the only core with oval shape which could be bought from the supplier. The oval shape gives the advantage of using foil if the transformer is to be redesigned. While the number of turns was 108 at the high voltage side and 23.4 (double wire) at the low voltage side

$$\begin{aligned}\text{Copper losses} &= 108 \times 11^2 \times 0.132 \times 5.5 \times 1e-3 \\ &+ 23.4 \times 51^2 \times 0.132 \times 3.5/2 \times 1e^{-3} \\ &= 9.48 + 1.4 = 10.88\text{W}\end{aligned}$$

The working flux can be calculated using equation (6.12)

$$B_{\max} = \frac{V}{A_e \times 2 \times N_1 \times K_f \times f} = \frac{866}{(2.1/10000) \times 2 \times 108 \times 4 \times 20000} = 0.23\ T$$

The total Copper losses were calculated to be 10.88 W. core weight is less than 1kg and the working flux is 0.23 and the working frequency is 20 kHz. Thus from Figures 6.4 the losses

and the weight of the transformer the core losses will be 5W/Kg which sums up to be 5W/Kg×1kg=5W. This low losses level will not cause a transformer temperature rise which was confirmed by monitoring the transformer temperature using the thermal camera and thermocouples when the transformer was in operation. The transformer windings were built as a single layer, with secondary layer sets on top of the primary. Figure 6.5 indicates the completed fabricated transformer.



Figure 6.5 The completed fabricated single phase transformer

6.4 High- frequency high-power inductor.

6.4.1 Inductor rating and specifications.

In this part of the thesis, the design of an inductor for the 3ϕ DAB converter will be considered. Due to the availability of a Litz wire suitable for the high current side, the inductors were positioned at the low voltage (high current side) of the

transformer. The inductor value can be estimated using equation (6.18) where $\phi = 50° = \frac{50}{180}\pi = 0.872\ rad$:

$$\begin{aligned} L_{HV} &= \frac{V_i^2 \times d \times \phi}{P_{Nom} \times \omega}\left(\frac{2}{3} - \frac{\phi}{2\pi}\right) \\ &= \frac{1500^2 \times 1 \times 0.8720}{20000 \times 2 \times \pi \times 20000}\left(\frac{2}{3} - \frac{0.872}{2\pi}\right) \\ &= 0.4123mh \end{aligned} \qquad (6.18)$$

Thus the total required inductance referred the transformer low voltage side is equal to $L_{LV} = 19.38\mu H$.

A test was performed to identify the leakage inductance as seen from the low voltage side of the fabricated transformer which was found to be equal $L_{LV\,T} = 1.54\mu H$

Thus, the required inductor value is equal to:

$$L = L_{LV} - L_{LV\,T} = 19.38 - 1.54 = 17.84\mu H \qquad (6.19)$$

The specifications of the inductor to be designed can be found in Table 6.4.

Table 6.4: The specifications of the inductor

Frequency (kHz)	Current (A) RMS	Voltage (V) RMS	Inductor value (μH)
20	50	153	17.84

6.4.2 Inductor design:

In order to design an inductor the core size and material, the conductor number of turns and the air gap length has to be calculated [80]. This can be done by following the simplified flowchart presented in Figure 6.6. Still, the final design might not be fully optimized due to the available Litz wire constraint.

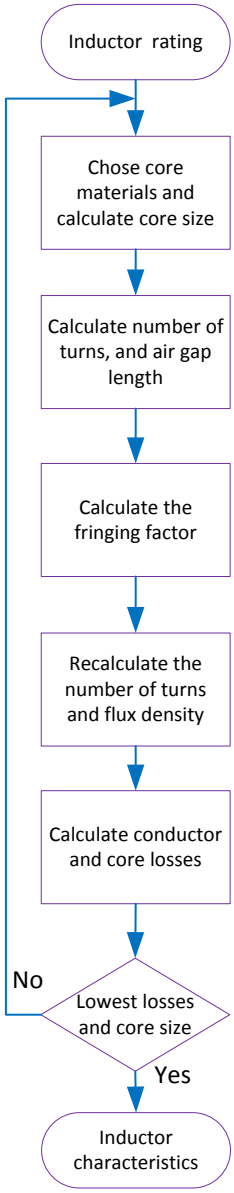


Figure 6.6 Design flow chart of the inductor design.

The core material which provides the lowest losses at the converter operational frequency and power rating is the Nanocrystallized, still due to the lack of suitable Nanocrystallized cut cores; a C cut core made of the Metglas® amorphous alloy 2605SA1 was used [81]. Figure 6.7 shows the relation between the losses and the flux density for the chosen Metglas® amorphous alloy 2605SA1 [82]

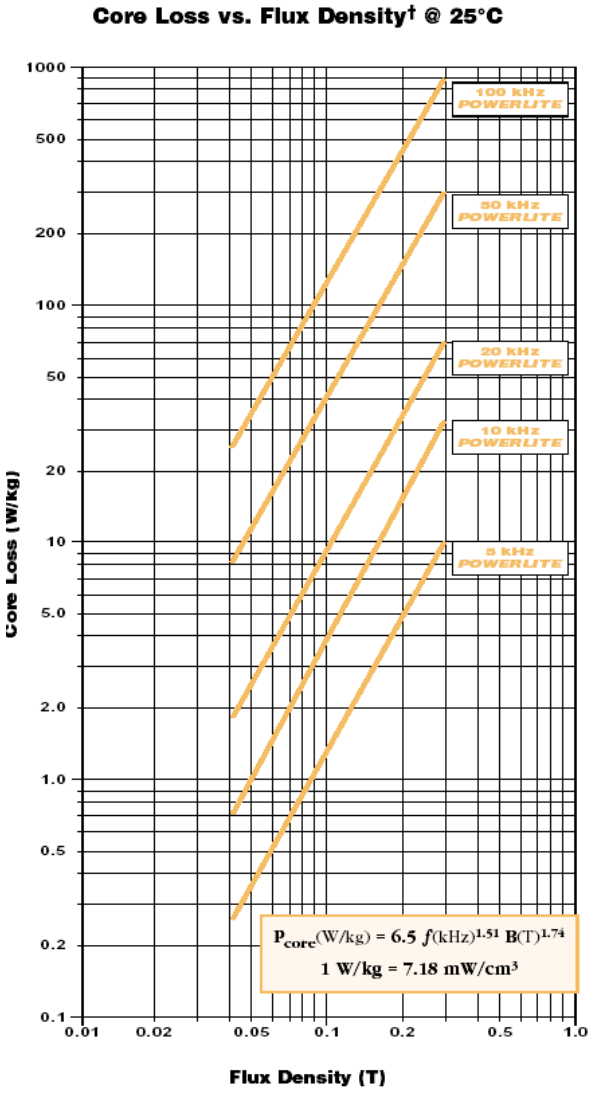


Figure 6.7 Relation between core losses and flux density for the Metglas® amorphous alloy 2605SA1 (reprinted from [79]).

To start the design, the required area product has to be calculated This can be done using equation (6.20) [79]:

$$A_p = \frac{LI^2}{K_u B_{ac} J} = \frac{17.84\times10^{-6}\times50^2\times10^4}{0.6\times0.4\times450} = 4.1\ cm^4 \qquad (6.20)$$

Where:

B_{ac} The peak flux.

I The RMS values of the current.

J The current density $J = 4.50\,A/mm^2$.

K_u Window filling factor.

The next step is to look for a core which has an area product higher than the minimum area product calculated from (6.20).

The area product for a given core can be calculated using equation (6.21): [79]

$$A_p = W_a \times A_c \quad (mm^4) \qquad (6.21)$$

Where:

A_p Area products.

W_a Window area.

A_c Cross-section area.

The next step is to vary the flux density and to calculate the number of turns and the air gap length for the different cores

under considerations. The combination of the air gap length, flux density, number of turns, and the smallest core size offering the least losses should be the combination of choice. This calculation was done using equations (6.22,6.23) [79] the following calculation are for the AMCC80 core.

$$N = \frac{V_{ac}}{K_f \times B_{ac} \times f \times A_c} = \frac{153}{4 \times 0.3 \times 20000 \times (5.2/10000)} = 12.25 \qquad (6.22)$$

$$L = \frac{\mu_0 N^2 A_c}{l_g} \qquad (6.23)$$

$$l_g = \frac{\mu_0 N^2 A_c}{L} = \frac{4 \times \pi \times 10^{-7} \times 12.25^2 \times (5.2/10000)}{17.8 \times 1e^{-6}} = 5.5 \ mm$$

Equations (6.22, 6.23) do not account for the fringing flux thus equation (6.24) can be used to calculate the fringing factor (F) [79]:

$$F = 1 + \frac{l_g}{\sqrt{A_c}} \ln\left(\frac{2G}{l_g}\right) = 1 + \frac{5.5}{\sqrt{5.2}} \ln\left(\frac{2 \times 7}{5.5}\right) = 1.78 \qquad (6.24)$$

Where:

G The winding length.

l_g The air gap length.

The fringing factor will result is a change of the number of turns and the operational flux density. Thus, they have to be recalculated this can be done using equations (6.25, 6.26) [79]

$$N_{new} = \sqrt{\frac{Ll_g}{\mu_0 A_c F}} = \sqrt{\frac{17.8\times 1e-6\times(5.5/1000)}{4\times\pi\times 10^{-7}\times(5.2/10000)\times 1.78}} = 9.18 \qquad (6.25)$$

$$B_{ac\ new} = \frac{V_{ac}}{K_f \times N_{new} \times f \times A_c} = \frac{153}{4\times 9.18\times 20000\times(5.2/10000)} \qquad (6.26)$$
$$= 0.4\ T$$

The window area was checked to make sure that it has enough area to accommodate the wire for the chosen combination.

Finally, the losses from the inductor should be evaluated for each combination of core size, air gap length, flux density, and number of turns. The chosen core was the AMCC80 from the Hitachi Metglass.

The inductor core losses can be estimated using the equation (6.27), while the Copper losses can be estimated using equation (6.28)

$$\begin{aligned} Core\ losses &= (6.5 f(kHz)^{1.51} B(T)^{1.74}) core\ weight \\ &= 6.5\times(20)^{1.51}(0.4)^{1.74}\times 0.938 \\ &= 114\ \ W \end{aligned} \qquad (6.27)$$

$$\begin{aligned} \text{Copper losses} &= \text{N}_{\text{new}} \times I^2_{LV\ ph\ rms} \times \text{Length}_{one\ turn} R_{AC}(\Omega/m) \\ &= 9.2\times 50^2\times 0.123\times 3.5/2\times 1e^{-3} = 5W \end{aligned} \qquad (6.28)$$

The losses was chosen which has core losses of 114 W and Copper losses of 4.9 W it should be noticed that the inductor was not fully optimized due to the available Litz wire constant and the lack of a suitable Nanocrystalline cut core. The temperature rise of the inductor was monitored using the thermal camera and thermo-cable when the inductor was in

operation the inductor temperature was stable at around 36 degrees during the test. Table 6.5 indicates the specifications of the fabricated inductor while Figure 6.8 indicates the fabricated high-frequency inductor.

Table 6.5 The fabricated inductor specifications:

Chosen Core	N	l_g mm	B_{ac} (T)
AMCC 80	9.2	0.55= 0.275mm/leg	0.48



Figure 6.8 The fabricated high-frequency inductor .

6.5 IGBT selection

The IGBT choice is mainly dominated by its operational voltage and current. It is standard practices to rate the IGBTs to

withstand at least 1.5 of the DC bus voltage, and 1.5 of the DC side current. Thus, the minimum rating of the IGBT is calculated according to Table 6.6.

Table 6.6 Minimum rating of the 20 kW converter IGBTs:

	High voltage side	Low voltage side
Voltage (V)	$V = 1500 \times 1.5 = 2{,}250$	$V = 325 \times 1.5 = 487.5$
Current (A)	$I = \frac{20000}{1500} \times 1.5 = 20$	$I = \frac{20000}{325} \times 1.5 = 92.24$

Next, a survey of the available semiconductors devices in the market was conducted in order for suitable devices to be identified. The investigated manufacturers included:

Semikron, IXYS, Infineon, Mitsubishi, Fuji, Sanken, Hitachi, Toshiba, ABB, DYNEX, and IR.

The devices in Table 6.7 were chosen:

Table 6.7 The characteristics of the chosen devices:

	Device name	Voltage (V_{CES})	Current (I_C)
High voltage side	DYNEX DIM100PHM33	3300	100
Low voltage side	Semikron SKM 145GB066D	600	150

It should be noticed that there was no available device with a compatible current rating and with a voltage rating of less

than 3.3 kV, which could support the required voltage 2.25 kV. Furthermore, the chosen device for the high voltage side was the device with the lowest current rating among the available range of devices rated at 3.3 kV. For the low voltage bridge, a 600V/150A device was chosen.

6.6 Snubber capacitors design

This part of the thesis includes a calculation of the required snubber values for testing the practical 20 kW converter cell. Snubber capacitor values should be chosen to provide ZVS turn-off. Additionally, the snubber value should be reasonable to prevent high loss of the ZVS turn-on range. The snubber capacitor value should be higher than the required critical snubber for ZVS turn-off and lower than this value will cause a loss of the ZVS turn on at a specific dead time and turn off current as explained in 5.4.3.

The critical snubber value can be calculated using equation (5.38). Equation (5.38) does not account for the tail current as explained in 5.4.1.2. In order to account for the tail current, the fall time should be multiplied by a factor of 5 [83] as it will give more time for the IGBT to fully switch off. Equation (6.29) shows the minimum snubber calculation after accounting for the tail current.

$$C_{\min} = \frac{5 \times I_{com} t_f}{4V_i} \tag{6.29}$$

The current at commutation can be calculated using equation (5.3). The dead time should be high enough to allow for the inductor/snubber commutation to be finished before turning on the IGBT as calculated in equation (5.47). The dead time should not be so high, as this will limit the control range and prevented achieving the required output voltage and power. A dead time value of 2 μs is a reasonable value to achieve this balance, which was chosen after running converter simulation with different values of snubbers and dead time.

The value of the maximum snubber allowed can be calculated using equations (5.44) and (5.45) which yields the following equation:

$$C_{\max} = \frac{3LI_{com}{}^2}{4V_i{}^2} \qquad (6.30)$$

The maximum, minimum snubber values and converter parameters are presented in table 6.8.

Table 6.8 The parameters used to calculate the design points:

	V	L(mH)	$t_{dead}(\mu s)$	F kHz	ϕ	$t_f(ns)$	I_{com}	$C_{\min} nF$	$C_{\max} nF$
HV	1500	0.4123	2	20	50	170	8.42	2	9.7
LV	325	0.019	2	20	50	46	38.86	6.8	203

After the snubber range has been established, a group of practical snubbers are used to conduct the test as presented in Table 6.9. Some of the chosen snubber capacitor values were higher than the upper limit in order to test the effect of the

snubber outside the operation range. The test will be carried with the chosen capacitors and dead time to examine the losses of the converter under this operating range.

Table 6.9 The value of snubbers which are going to be used for the high and the low voltage bridges.

	Snubber values µF		
High voltage bridge	***0.0022 µF*** VISHAY MKP1845222204	***0.01 µF*** LCR PC/HV/S/WF	***0.022 µF*** LCR PC/HV/S/WF
Low voltage bridge	***0.022 µF*** CORNELL 940C20S22K-F	***0.047 µF*** LCR PC/HV/S/WF	***0.068 µF*** VISHAY MKP1845222204

6.7 DC link capacitors, power planes, and heat sinks

The selection and choice of the DC link capacitors, the power plane, and the heat sinks dominates the final converter size and weight. Thus, special attention should be given when choosing these parts.

For the heat sink, a water-cooled heat sink was chosen, which was based on the fact the water heat sink provides more cooling than the air-cooled heat sink if they were of a comparable sizes. The only drawback from using water cooled heat sink is the need for extra equipment such as a cooler and pipes when installing the water-cooled heat sink. Thus, in a commercial converter, an air-cooled heat sink might lead to a

lower price, less complex system, which would be lighter and smaller in size.

Table 6.10 The two ordered water-cooled heat sink:

High voltage	AAVID THERMALLOY Hi-Contact Liquid 6 Pass; 305mm
Low voltage	Wakefield-Vette COLD PLATE 4PASS 6X5.5X0.690"

For the power plane and capacitors, the DC link capacitors should be capable of reducing any ripple which might be present in the DC link voltages:

During this project, UL30BC0360 dielectric capacitors were available for use. Table 6.11 includes the rating of this capacitor:

Table 6.11 The UL30BC0360 capacitor rating:

CAP (μF)	VDC	I Peak (Amps)	ESR
360	600	3845	0.0076

For the high voltage side the voltage rating is 1500 V, thus four capacitors with a rating of 600 each were serially connected to bank of 4*600 =2400 V, which is enough to handle the output voltage from the converter.

Thus the total capacitor of the DC link will be equal to (360 μF) /4 = 90 μF. Finally, a suitable power plane was designed and ordered.

For the low voltage side, a suitable ready fabricated high current power plane was available. This power plane can host two series connected capacitors. These capacitors, when connected in series, will give 360/2=180 μF with a voltage rating of 1200 V, which is more than enough for the low voltage DC link.

The completed high and low voltage bridges are presented in Figure 6.9 and Figure 6.10.

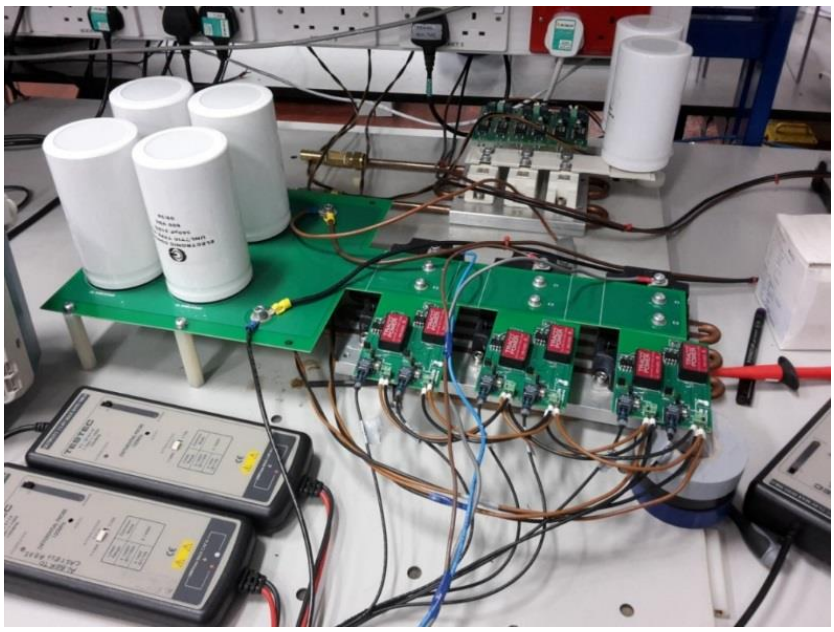


Figure 6.9 The completed high voltage bridge being tested (at the front).

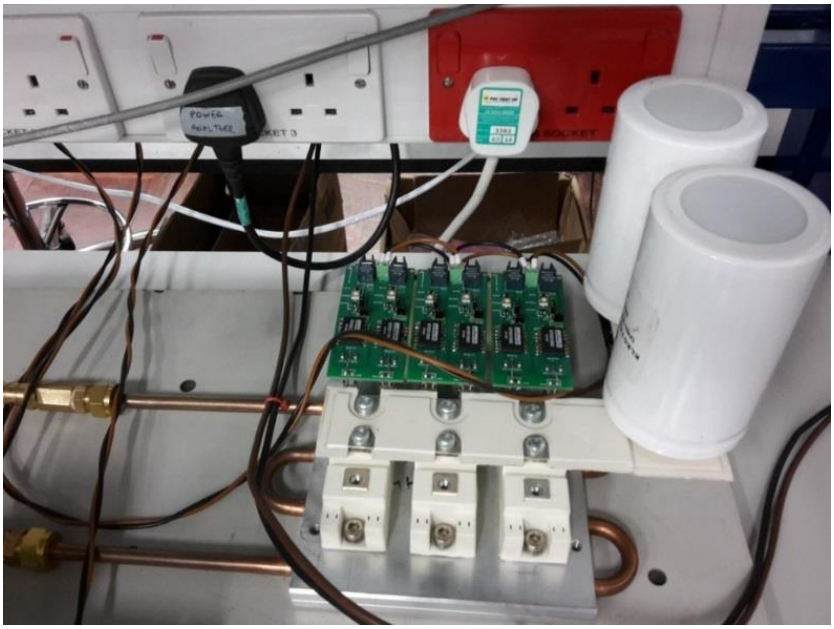


Figure 6.10 The completed low voltage bridge being tested.

6.8 The gate driver design

The gate drive provides the following functions [84]:

- It isolates the DSP and the FPGA from the bridge high voltage.
- It provides the voltages and the control pulses required to drive IGBTs.

The gate driver has many components: the DC/ DC converter, which is used to provide the ± 15 VDC required to drive the IGBT; The optocoupler, this is needed to provide extra protection to the digital component due to its isolation, the chosen optocoupler is the 2.5A HCPL-3120-000E AVAGO TECHNOLOGIES and in order to protect the IGBT from over-voltages, two Zenner diode were used. The connections

between the DSP/ FPGA stack and the gate drives were made using fibre optic links, which is used to isolate the DSP/FPGA stack from the high voltage, and to prevent the noise generated in the high voltage area from propagating to the controller. [84].

Finally, the DC/DC converter power rating can be designed based on equation (6.31)

$$P_d = fc \times \left(|+Q| + |-Q|\right) \times \left(|+V_{GE} + |-V_{GE}|\right) \quad (6.31)$$

After the DC/DC converter rating was calculated which needed 0.9 watts for the low voltage side and 1.5 watts for the high voltage side, suitable DC/DC converters were chosen as presented in Table 6.12:

Table 6.12 The chosen gate drive DC/DC converter.

Bridge	DC/DC name	Power rating	Isolation	Vin	Vout
Low voltage bridge	Murata NTH0515MC	2W	1kVDC	5V	± 15 V
high voltage bridge	TRACOPOWER THB 3-0523	3 W	4800 VAC rms	5V	± 15 V

Finally, the gate drives were fabricated. Figure 6.11 and Figure 6.12 illustrate the gate drivers for the high and the low voltage side.



Figure 6.11 Gate driver for the high voltage bridge

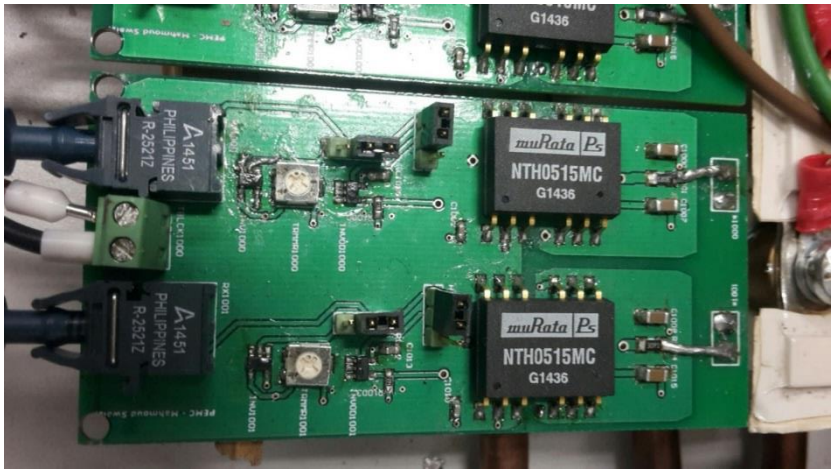


Figure 6.12 Gate driver for the low voltage bridge

6.9 Measurement board design

The measurements board provides the controller with the values of currents and voltages in the circuit. These values are then used for control and protection. The measurements were performed for the output voltage and the three-phase AC current. Figure 6.13 indicates the measurements circuit.

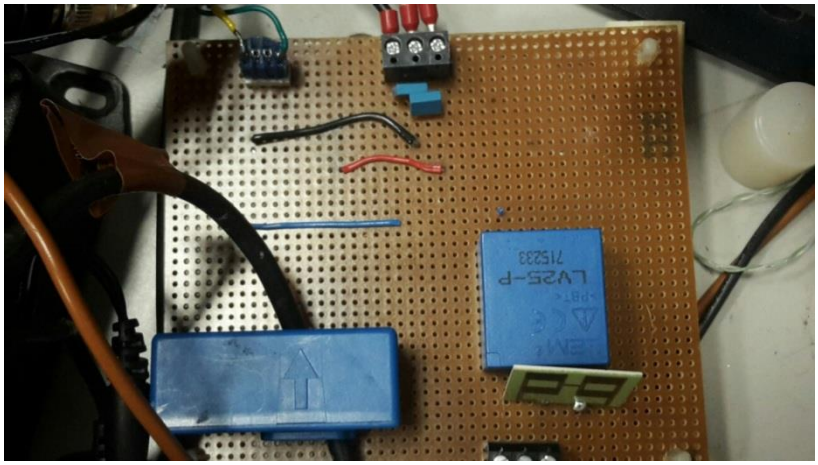


Figure 6.13 The measurements board.

The chosen voltage transducer was the LV 25-P and the chosen current transducer is the LA 125-P.

6.10 Control unit DSP and FPGA

The control platform developed at the PEMC group of the University of Nottingham.

The control platform comprises of a TMS320C6713 225 MHz floating-point digital signal processor (DSP) developed by Texas instrument. This is combined with a Field programmable gate array (FPGA) Actel ProAsic 3.FPGA which is used to produce PWM, provide protection and to read the measured voltages and currents. [84]

The FPGA board has 10 analogue to digital input ports which used to connect the external feedback signals to the control platform.

An extension board was available to be used in this project which is used to extend the FPGA card output to 12 fibre optic outputs which are required for the converter. The completed control unit stack is shown in Figure 6.14.

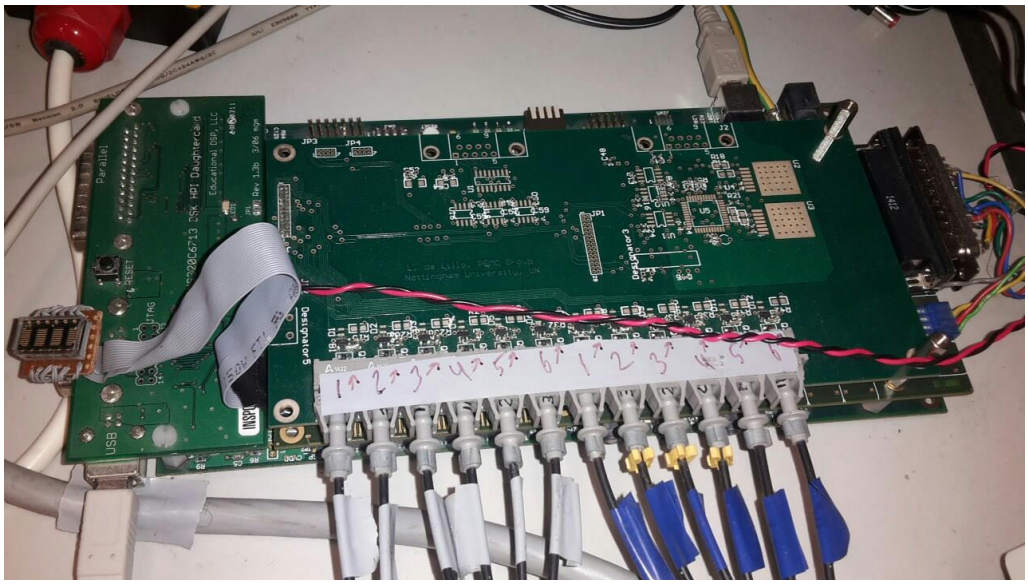


Figure 6.14 The complete control unit stack.

6.10.1 The DSP processing unit TMS320C6713

The TMS320C6713 DSP is a 32-bit floating point signal processor. The DSP is used to execute the control program. The DSP is programmed in C, using the Code Composer Studio developed by Texas instruments [85].

6.10.2 The FPGA Field programmable gate array

The FPGA board was developed by the PEMC group utilising the Actel ProAsic 3 FPGA chip. The other components on the board include:

- Analogue input ports: this is used to interface the measurements from the current transducers into the A/D through burden resistors[84].

- Burden resistors: these are used to interface the measured analogue values from the transducers into the A/D input.[85]

- 10 A/D converters.[84]

- Fibre optics output links: these are used to transfer the gate signals generated by the FPGA to the IGBT's gate drivers.

- Buffers: these are bidirectional buffers and based on their setting, the specific FPGA pins can be configured as input or output.

- Programming port: this is used to interface the FPGA to the programmer.

The FPGA is working at speed of 50 MHz and when the switching commences, first all the measurements values such as the converter voltages and currents are read and stored, which is used to control the converter. Due to time constrain at the end of the project the converter was run in an open loop manner, by inputting the phase shift angle directly.

The required modulation data then gets stored in a register based on the First In First Out FIFO principle. The register is then accessed from the FPGA. Finally, the FPGA will translate the FIFO data into the switching modulation required to drive the IGBT to achieve the required functionality.

6.11 Summary

This chapter presented the steps followed to design and build a 20 kW, 20 kHz, 1500 V DC to 325 VDC 3ϕ DAB converter cell. The main parts rated or designed or built and tested included: the IGBTs, the snubber capacitors, the inductor, the transformer, the DC link capacitors, the power planes, the heat sinks, the gate drivers, and the control platform (DSP/FPGA).

The following chapter will include the practical results obtained from the 20 kW 3ϕ DAB converter cell built as described in this chapter.

Chapter 7

Experimental Results.

7.1 Introduction

This chapter of the thesis includes the practical results of the 3 ϕ DAB converter described in chapters 5 and 6.

The main purpose of this chapter is to compare the efficiency of the 3ϕ DAB converter with and without snubbers. Thus, the benefits and limitations of using the proposed multi-cell converter built from a combination of snubberred and un-snubbered cells can be investigated.

To achieve this goal, the converter will be tested first without snubbers and following that testing with different snubber capacitor values will be undertaken.

Finally, a multi-cell multi-snubber converter will be proposed based on the converter cell performance with and without snubbers.

7.2 Equipment used and test procedures

In this part of the thesis, the equipment used and the procedures followed in order to measure the converter efficiencies will be described.

In order to calculate the power, losses, and efficiencies of the converter bridges the power analyser and oscilloscope were used. The test setup is presented in Figure 7.1.

"kinetiQ PPA2530" power analysers were used as presented in Figure 7.1.The power analysers were connected at the input and output DC sides to measure and monitor the DC voltage and power. An HF100 high current external resistor shunt with a rating of (100A and $1\ m\Omega$) was used to probe the low-voltage side current due to the internal shunt limitation of 30 A.

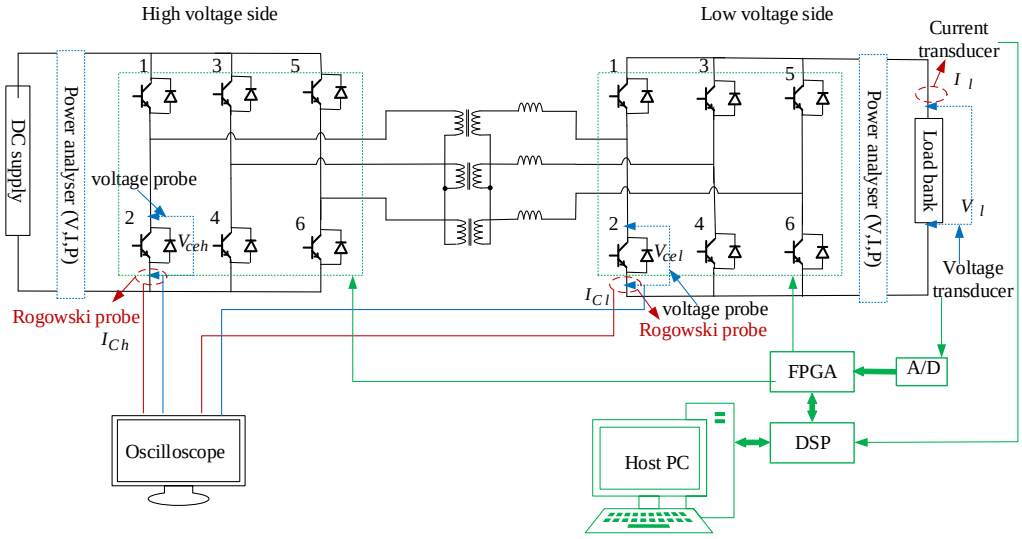


Figure 7.1 3 three ϕ DAB converter test set-up:

For waveform measurements, a group of voltage and current probes, as presented in Figure 7.1 were used to measure the voltage (V_{ce}) across the device and the total current ($I = I_c + I_F$) through the device. These currents and voltages were then used to calculate the turn-off, the turn on (if present), and the conduction losses of IGBTs and diodes.

The equipment used to perform this task included:

1- 12-bit wave runner HR064Zi oscilloscope. This was chosen due to the high resolution available from the 12 bit, up to 15 bits with enhanced resolution (ERES), which will give better results resolution than the other 8 bit oscilloscopes available in the laboratory [86].

2- PEM Ch3 CWT 3B ultra-mini Rogowski current probe. It was chosen due to the fit of the measurements terminals of this current probe in the confined space available near the power module. This probe has a high accuracy of ±

2% of reading and a sensitivity of 10 mV/A [87]. And has a peak current of 600A and peak voltage of 1.2kV.

3- Test Tec TT-SI 9110, and TT-SI51 voltage probes. These probes were chosen due to the high accuracy of the TT-SI51 which is around ±1 % of reading and due to the TT-SI 9110 can be used for the high voltage level, even though it has a slightly lower accuracy at ±2 % of reading [88, 89]. The Test Tec TT-SI 9110 voltage probe has a peak voltage of ±1.4kV (DC + Peak AC) or 1000Vrms while the Test Tec TT-SI51 voltage probe has a peak voltage of ±700V (DC + peak AC) or 600Vrms.

It should be noted that due to the power analyser rating limitations, which was not foreseen at the design phase of the project, the test was conducted at a voltage level of 930 V at the high voltage side instead of the originally planned 1500 V. While, the low voltage side bridge voltage was 200 V instead of the initially proposed 325 V.

Using the data available from the probes and the oscilloscope data sheets the minimum measurable step and the accuracy of each of the four measured values can be estimated.

The resolution can be defined as "the smallest change in the value of an input signal that changes the value of the digital output by one count" [90].

The Wave Runner HR064Zi is a high-resolution 12-bit oscilloscope and the steps in the measured values can be calculated as follows:

Step value = $Value/2^N$ (7.1)

Where:

Step value The minimum step in the measurements made by the oscilloscope

Value The value of measurements using the oscilloscope

N The oscilloscope number of bits.

In this study, four different values of voltage and current will be measured for the low and high voltage bridges. This will yield step values as presented in Table 2.1. It should be noted that when taking the probe sensitivity and the probe attention setting in the oscilloscope into consideration, the result is a representation of the voltage and current in V and A.

Table 7.1 The measurable steps for the voltage and current.

	High voltage bridge		Low voltage bridge	
	V	I	V	I
Value	930	13	200	60
Step value	0.227	0.003	0.0488	0.014

The minimum achievable measurable values combined with the total accuracy of the measurements device is presented in Table 7.2:

Table 7.2 The achievable measurements step and accuracy of each voltage or current probe.

	High voltage bridge		low voltage bridge	
	V	I	V	I
Achievable step	0.5	0.05	0.05	0.05
Accuracy	2%	$\pm$ 2%	$\pm$ 1%	$\pm$ 2%

The voltage and current are going to be used to calculate the power this will yield the following equation for the measured power accuracy:

$$P = V \times I \tag{7.2}$$

$$\frac{\delta P}{P} \approx \frac{\delta V}{|V|} + \frac{\delta I}{|I|} \tag{7.3}$$

Thus the accuracy of the measured power is almost equal to the sum of the accuracy of the voltage and current probes which yield an achievable measurements step and accuracy for the power as presented in Table 7.3.

After the tests were conducted, the current and the voltage waveforms were saved and further processing was performed using MATLAB.

Table 7.3 Achievable measurements step and accuracy for the power measurements:

	High voltage bridge	Low voltage bridge
Achievable measurements step (W)	0.5	0.05
Accuracy	± 4%	± 3%

The waveforms were first imported to MATLAB, then the losses at the turn-off, turn-on and the conduction losses were calculated (the turn-on losses are usually only present in a limited number of cases, further explanations will be given for each case). The procedures used to calculate the turn on and turn off and the conduction losses are presented next:

7.2.1 Turn off losses:

The total turn off losses, including the tail current losses, are considered for this work. The turn-off losses are defined as the losses between the times where the turn off voltage reaches 5 % of its final value until when the turn off current reaches 2% of its turn off peak value. This definition was used as it gives the best separation between the turn-off losses and the conduction losses.

$$E_{turn\ Off\ \ IGBT} = \int_{t_{off\ Start}}^{t_{off\ End}} V_{ce} I_c \, dt \tag{7.4}$$

$$P_{turn\ off\ \ IGBT} = f_{sw} \times E_{turn\ off\ \ IGBT} \tag{7.5}$$

Where:

$E_{turn\ off\ \ IGBT}$ The turn off energy of the IGBT.

$P_{turn\ off\ \ IGBT}$ The average power dissipated in the IGBT due to the turn off losses.

$t_{off\ Start}$ The time when turn off voltage reaches 5 % of its final value.

$t_{off\ End}$ The time when the turn off current reaches 2% of its turn off peak value [91].

7.2.2 Turn on losses.

Due to the turn-on losses being mainly a consequence of a capacitor discharging (stray capacitor or snubber capacitor) while the IGBT is soft turn on the other situations, the turn-on losses will be defined as the losses between the time the turn on current starts increasing at the start of snubber discharge to the moment when the current goes back to zero at the end of the snubber discharge turn on event.

$$E_{turn\ on\ IGBT} = \int_{t_{on\ Start}}^{t_{on\ End}} V_{ce} I_c \, dt \tag{7.6}$$

$$P_{turn\ on\ IGBT} = f_{sw} \times E_{turn\ on\ IGBT} \tag{7.7}$$

Where:

$E_{turn\ on\ IGBT}$ The turn off energy of the IGBT.

$P_{turn\ on\ IGBT}$ The average power dissipated in the IGBT due to the turn off losses.

$t_{on\ Start}$ The time when the turn-on current start increasing at the start of snubber discharge.

$t_{on\ End}$ The time when the turn-on current goes back to zero at the end of snubber discharge.

7.2.3 The conduction losses:

The conduction losses are straightforward to be estimated. The IGBT and diode data sheets were used in combination with the IGBT and diode measured currents to estimate the conduction losses. First, the IGBT and diode voltages are estimated using the VI curves from the data sheet. The conduction losses were then estimated by multiplying the measured currents with the voltages estimated using the data sheet. The last step was to integrate the losses over the conducting time of the IGBT and the diode, which gives the losses in J.

$$I_C \text{ or } I_F \Rightarrow (use\ the\ IGBT\ or\ diode\ data\ sheet) \Rightarrow V_{CE} \text{ or } V_F$$

$$E_{con\ \ IGBT} = \int_{t_{con\ IGBT\ Start}}^{t_{con\ IGBT\ End}} V_{CE}\ I\ dt \tag{7.8}$$

$$P_{con\ \ IGBT} = f_{sw} \times E_{con\ \ IGBT} \tag{7.9}$$

Where:

$E_{con\ \ IGBT}$ The conduction energy of the IGBT.

$P_{con\ \ IGBT}$ The power averaged dissipated in the IGBT.

$t_{con\,IGBTStart}$ The time when the IGBT start conducting.

$t_{con\,IGBT\,End}$ The time when the IGBT finish conducting.

$$E_{con\ \ D} = \int_{t_{con\,D\,Start}}^{t_{con\,D\,End}} V_{CE}\ I\,dt \tag{7.10}$$

$$P_{con\ \ D} = F_{sw} \times E_{con\ \ D} \tag{7.11}$$

Where:

$E_{con\ \ D}$ The conducting energy of the diode.

$P_{con\ \ D}$ The power dissipated in the diode due to conducting.

$t_{con\,D\,Start}$ The time when the diode start conducting.

$t_{con\,D\,End}$ The time when the diode finishes conducting.

7.3 Test set up.

The experiments were set up using the probes mentioned earlier in this chapter, while the circuit components were chosen and designed based on chapters (5) and (6) of this thesis. The tests were conducted with IGBTs parameters as presented in Table 7.4 while the rest of the parameters are presented in Table 7.5.

Table 7.4 IGBT used in the test.

IGBT at high voltage side	DNX_DIM100PHM33
IGBT at the low voltage side	SKM145GB066D

The SKM 145GB066D parameters were estimated by applying the outlined methods in section 5.3 and are as follows: $V_{CE0} = 0.7V$, $r_C = 0.0067\ \Omega$, $V_{D0} = 0.8V$, and $r_D = 0.005\ \Omega$. While the DNX_DIM100PHM33 parameters are $V_{CE0} = 0.94V$, $r_C = 0.147\ \Omega$, $V_{D0} = 1.11V$, and $r_D = 0.008\Omega$.

The load was made of a group of resistors connected in parallel and series, which gives a final load varying from 45.2 Ω to 5.2Ω.

Table 7.5 The practical 3 DAB circuit parameters:

F kHz	L_{LV} μH	$N1:N2$	$C_{DC-Link-HV}$ μF	$C_{DC-Link-LV}$ μF	t_{dead_time} μs
20	17.84	108:23.4	90	360	2

The tests were then conducted for different loading scenarios and different snubber values, and the results are presented in the next part of this chapter. It should be noted that for the sake of the clarity of the figures and to avoid repetition, the green lines refers to the current Ic and the lines in blue refer

to the voltage Vce in all the figures which include these two waveforms together.

7.4 Practical Results

7.4.1 Test without snubber

To establish the converter base efficiency a test without any snubber was first conducted. The test was conducted using the probes and components described earlier. As the converter is bidirectional the test can be performed for the cause where the high voltage bridge is working as an inverter and the low voltage bridge is working as rectifier which is not covered in this chapter due to time and laboratory limitations. However, the idea of the multi-cell multi-snubbered converter is fully covered and validated using the cause where the low voltage bridge is working as inverter and the high voltage bridge is working as a rectifier.

It should be noticed that the waveforms deskewing is of a great important to make sure that all the delays between the measured values and the oscilloscope it accounted for. A test was carried out to measure the Rogowski coils delays using a shunt resistor as a reference. The delays value was then compared with the Rogowski current probe data sheet. A close match was observed between the two delay times, which validate the waveform deskewing approach. It should be noticed that the losses values are calculated using the approach described in section 7.2 where the turn off losses is the value when the current reaches 2% of it is final value and

the turn on losses is the value when the current goes back to zero:

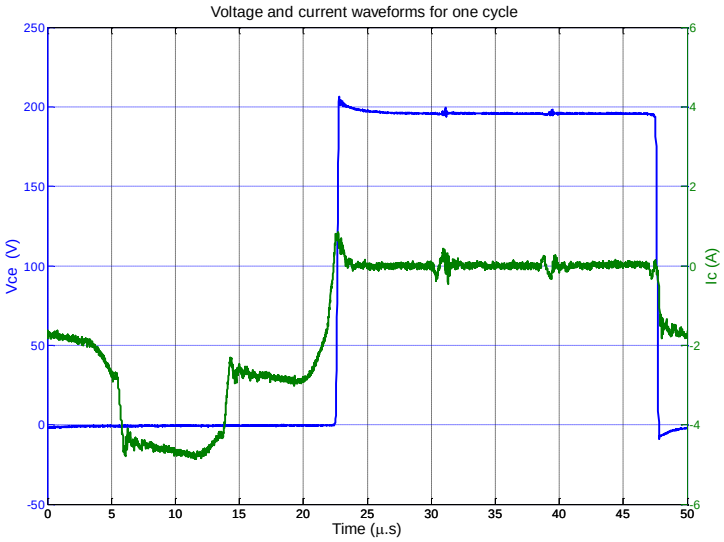


Figure 7.2 Low voltage switch current and voltage waveforms for a load of 14.8% of the rated power, f=20 kHz, and no snubber.

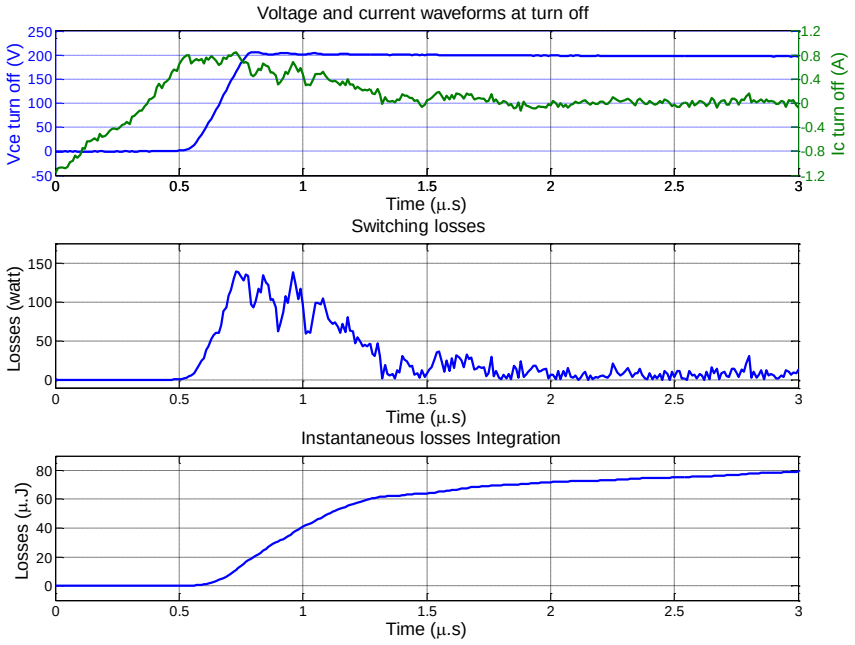


Figure 7.3 Low voltage switch current, voltage waveforms at turn off waveform and losses for a load of 14.8% of the rated power, f=20 kHz and no snubber.

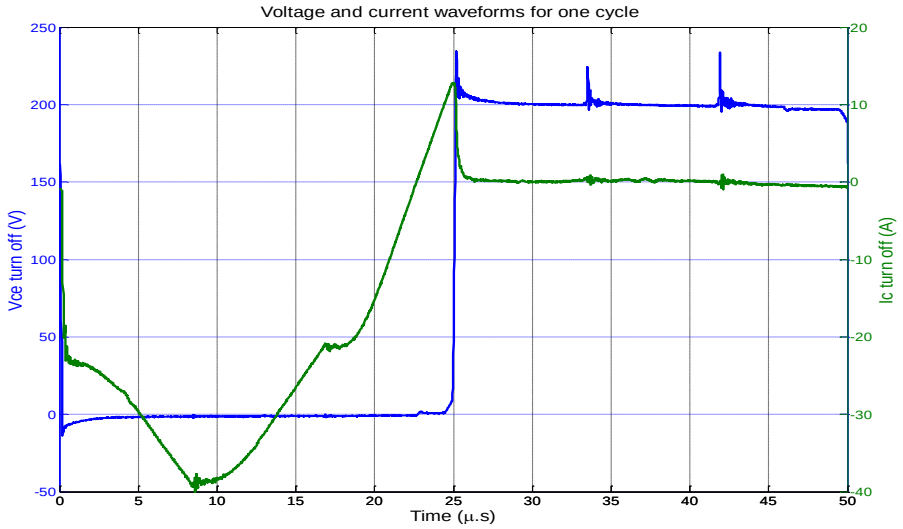


Figure 7.4 Low voltage switch current and voltage waveforms for the full rated power, f=20 kHz, and no snubber.

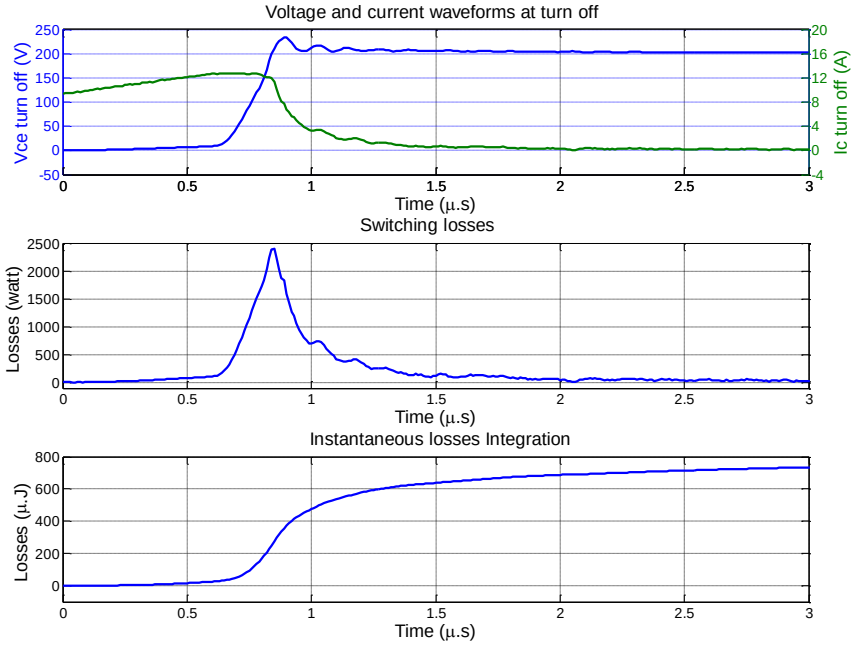


Figure 7.5 Low voltage switch current, voltage waveforms and losses at turn off for the full rated power, f=20 kHz, and no snubber.

From the figures Figure 7.2 to Figure 7.5 it could be noticed that the turn-off losses increased when the turn off current increased, it was only around 80 μJ with turn off current of 0.8 A, and then increased to around 700 μJ at 13 A turn off current.

The next figures indicate the situation at the high voltage bridge side.

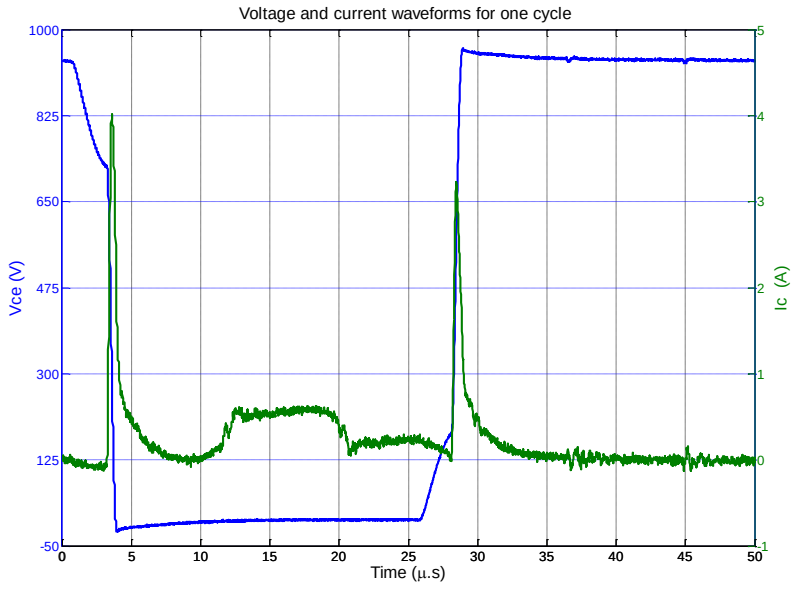


Figure 7.6 High voltage switch current and voltage waveforms for a load of 14.8% of the rated power, f=20 kHz, and no snubber.

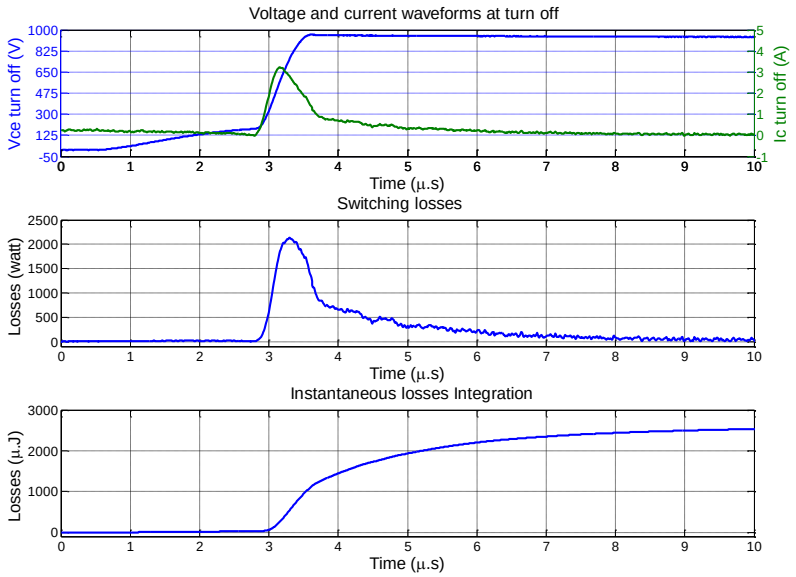


Figure 7.7 High voltage switch current, voltage waveforms and losses at turn off for 14.8% of the rated power, f=20 kHz and no snubber

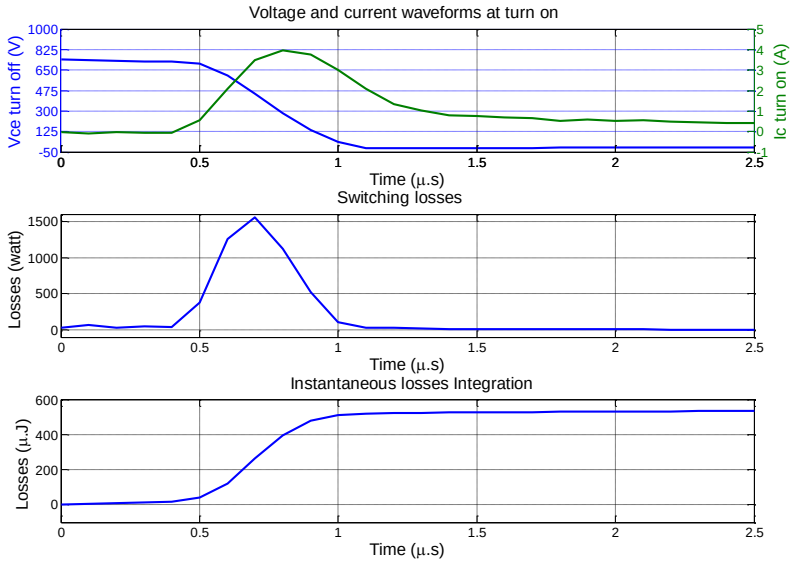


Figure 7.8 High voltage switch current, voltage, and losses waveforms at turn on for full rated power, f=20 kHz, and no snubber.

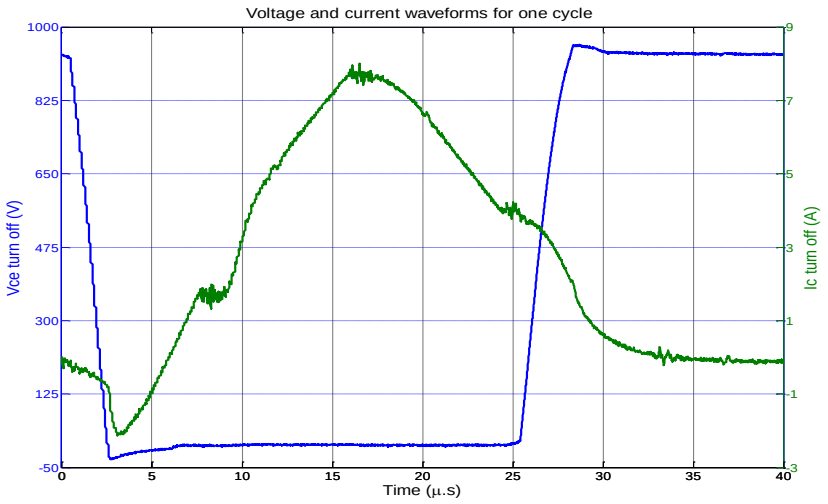


Figure 7.9 High voltage switch current and voltage waveforms for full rated power f=20 kHz and no snubber

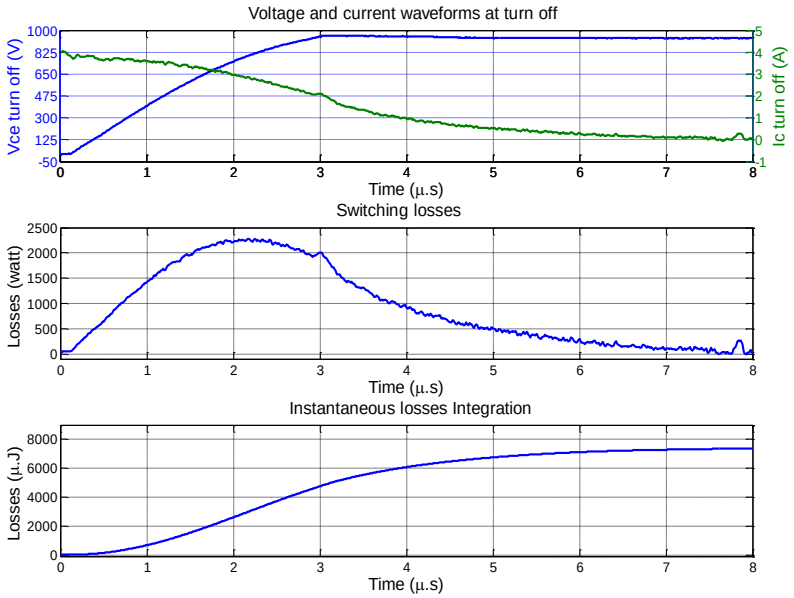


Figure 7.10 High voltage switch current, voltage waveforms and losses at the turn off from for full rated power, f=20 kHz and no snubber.

After analysing the high voltage bridge results some undesired behaviours were noticed. First, in Figure 7.6 it can be noticed that there are turn on losses at the high voltage bridge at a

low current. These losses should not be present normally in the bridge as the 3ϕ DAB high voltage side IGBT's are softly turned on. These turn on losses are present in the converter due to the fact that the turn-off current is less than 1 A, which is not sufficient to discharge the IGBT capacitance under testing within the dead time. The remaining charge in the internal capacitance will discharge in the IGBT after it is turned on which will result in turn on losses in the IGBT. These turn on losses are around 550 μJ. Turns on losses in the IGBT are indicated in Figure 7.8.

The second issue is present in Figure 7.9 and Figure 7.10 It can be noticed that the high voltage IGBT has high turn-off losses of around $7500\ \mu J$. These turn-off losses are present in the IGBT due to the long tail current this high voltage IGBT has. This combined with the high switching frequency used, caused high losses in the high voltage bridge which are not tolerable as the turn-off losses will cause almost 1,100 Won average to be dissipated in the bridge which will degrade the bridge efficiency to lower than 85%. Furthermore, these high losses if left undissipated might cause a thermal run away and break down of the devices.

The last two factors are limiting factors from the high voltage IGBT, which will lead to lower converter efficiency. However, this cannot be improved on due to the chosen IGBT for the high voltage bridge DIM100OHM33, which was the best-rated IGBT available in the market to choose. It has the smallest current rating, with an appropriate voltage level of 3.3 kV, which can be safely used with the originally planned input

voltage of 1.5 kV. However, if a more suitable rated IGBT was available, better results could be obtained. Development of a suitable Silicon Carbide SiC device with a rating of 2.5 kV and 30A into the market, for example, would maximize the desired converter performance at the design frequency of 20 kHz.

The tests were conducted over all the range of loads and the losses are presented in the following tables:

Table 7.6 The losses values for one device for the low voltage bridge with 200V DC load, 20 kHz and no snubber

P (%)	$IGBT_{turnoff}$ (μJ)	$IGBT_{con}$ (μJ)	D_{con} (μJ)	Bridge Efficiency%
0	10.3	0	0	-
14.8	57.8	0	24.6	98.8
29.5	57.8	0	170.6	98.4
43.8	71.7	1	297	98.3
58.3	478.5	1	271	97.5
72	569.6	4	359	97.4
85.8	652.0	6	470	97.4
100	732.6	15.3	565.1	97.4

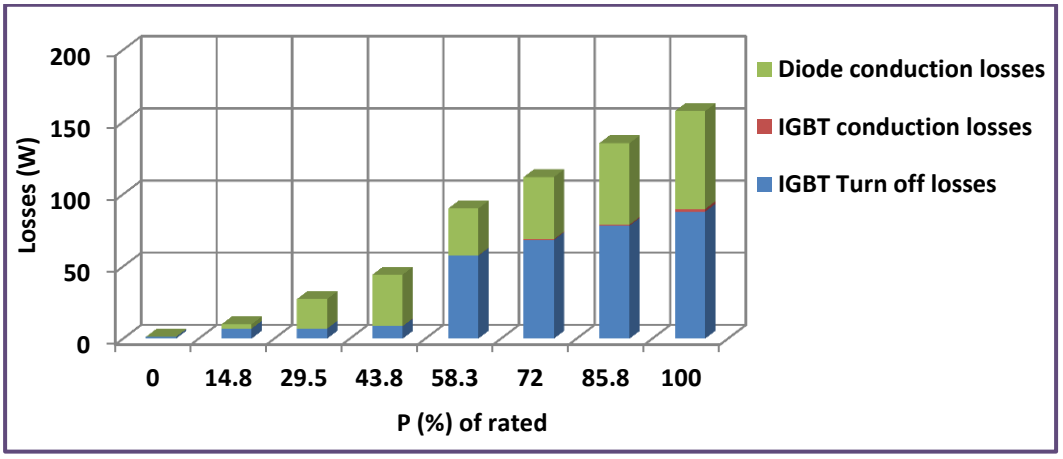


Figure 7.11 The low voltage bridge total losses by using the current and voltage waveforms with no snubber

From Table 7.6 and Figure 7.11 it can be noticed that the low voltage bridge has a high efficiency over most of the operation range as the converter is working with soft switching turn on.

Furthermore, the conduction losses of the converter switches can be analytically calculated as explained in section 5.3. The SKM 145GB066D [92] was used in the low voltage bridge, and by applying the outlined methods in section 5.3 its parameters were estimated as follows: $V_{CE0} = 0.7V$, $r_C = 0.0067\ \Omega$, $V_{D0} = 0.8V$, and $r_D = 0.005\,\Omega$. Figure 7.12 and Figure 7.13 indicate a comparison between the low voltage bridge IGBT and diode conduction losses by applying the practical and analytical approaches. The high voltage bridge will not be considered for the comparison due to the earlier highlighted issues with the available high voltage IGBTs.

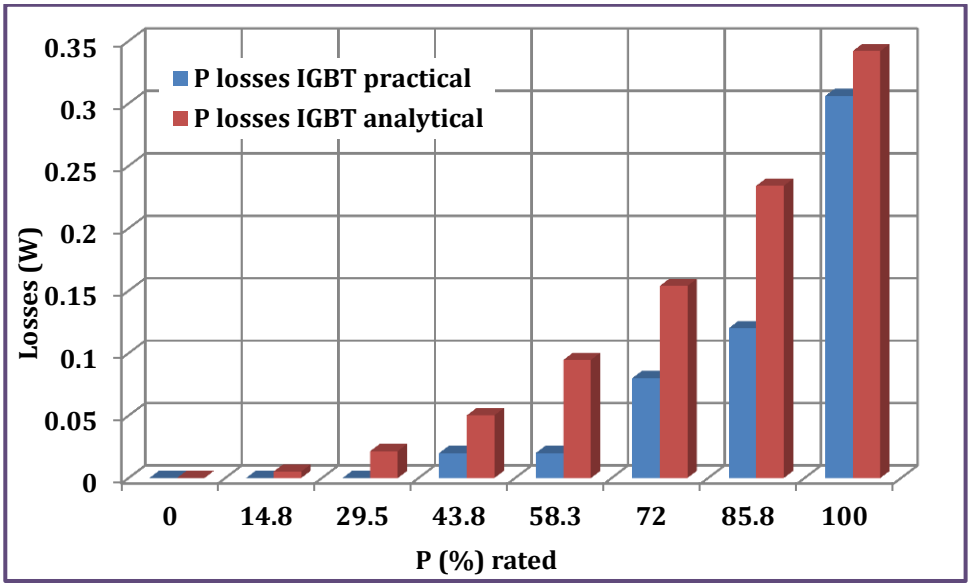


Figure 7.12 Comparison between the low voltage bridge IGBT conduction losses by applying the practical and analytical approaches

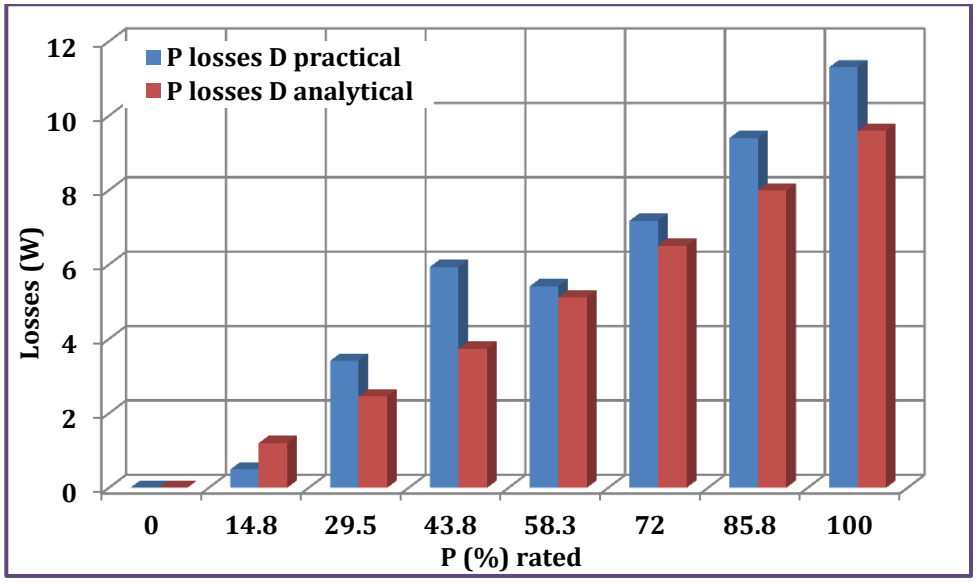


Figure 7.13 A comparison between the low voltage bridge diode conduction losses by applying the practical and analytical approaches

From Figure 7.12 and Figure 7.13 a good match between the analytical and practical results was obtained which validates

the followed process for calculating the analytical and practical conduction losses.

Table 7.7 The loss values for one device for the high voltage bridge with 200V DC load on the low voltage side, 20 kHz and no snubber

P (%)	$IGBT_{turnon}$ μJ	$IGBT_{turnoff}$ μJ	$IGBT_{con}$ μJ	D_{con} μJ	Bridge Efficiency%
0	591	550	0	0	-
14.8	525	2,548	2	0	73
29.5	637	5,687	12	0	68
43.8	0	6,263	24	0	77
58.3	0	6,550	27	0	82
72	0	6,664	36	0	85
85.8	0	7,313	46	1	86
100	0	9,295	58	5	84

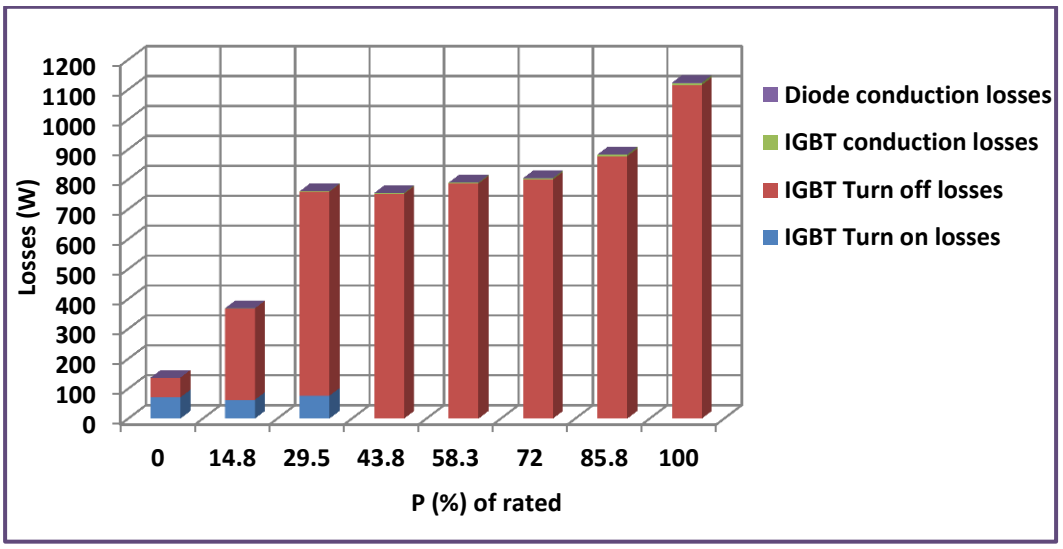


Figure 7.14 The un-snubbered high voltage bridge total losses measured using the current and voltage wave forms.

From Table 7.7 it can be noticed that the high voltage bridge best efficiency was around 86% at 85.8% of the rated power. While the efficiency falls from 73% at 14.8% of the rated power to 68% at 29.5% this happens as the current start going more in the diode in this control angle range. It can be further noticed from Figure 7.14 that the greatest contributor to the converter losses was the IGBT turn-off losses. This is due to the IGBT long tail current which when multiplied with the 930 V off state voltage results in high losses at the converter. Also, the IGBT turn-on losses are present at lighter loading as the turn-off current is not high enough to discharge the stray IGBT capacitance at turn off, which then discharge at the IGBT at the turn on event. As the available device of the high voltage bridge is overrated this lead to higher switching losses as the large chip area leads to high capacitance [93]. The switching losses of the high voltage IGBT for the low current level were not available in the data sheet and were not anticipated to be at this high level at the design phase of the project.

The next part of the thesis will look at the practical results obtained when snubbers are connected to the converter IGBTs.

7.4.2 Test with snubbers at both bridges

The main idea of adding snubbers is to try to limit the tail current of the IGBT, thus reducing the IGBT turn-off losses in both the IGBT in the high and the low voltage bridge. In order to perform this test, a group of snubbers was ordered. The first test was conducted using snubbers with the following

values which were designed in chapter six 2.2 nF for the high voltage side and 68 nF for the low voltage side. The test was performed for the whole load range and the result of this case with of 85.5% the rated power is presented in Figure 7.15 and Figure 7.16:

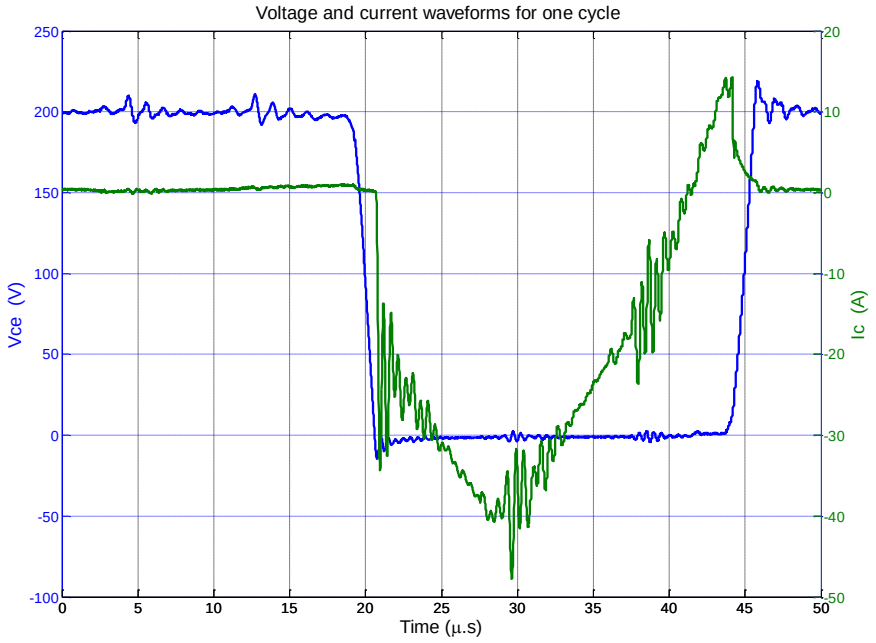


Figure 7.15 Low voltage switch current and voltage waveform for 85.5% of the rated power and f=20 kHz

From Figure 7.15, for the low bridge, it can be noticed that the snubber is working as expected with the current limited at the moment of turn off. This will lead to a decrease in the turn-off losses in comparison to the case where no snubber is used. Moreover, it should be noted that the bridge is working almost as rectifier as most of the current goes through the IGBT. While, From Figure 7.16 an undesired behaviour from the circuit can be noticed. Turn on losses is present in the high voltage bridge and these losses will increase the total losses of

the bridge. Additionally, the introduction of snubber capacitor to the circuit did not provide any improvement to the tail current reduction at the moment of a turn-off, and the turn-off losses still exist in the high voltage bridge.

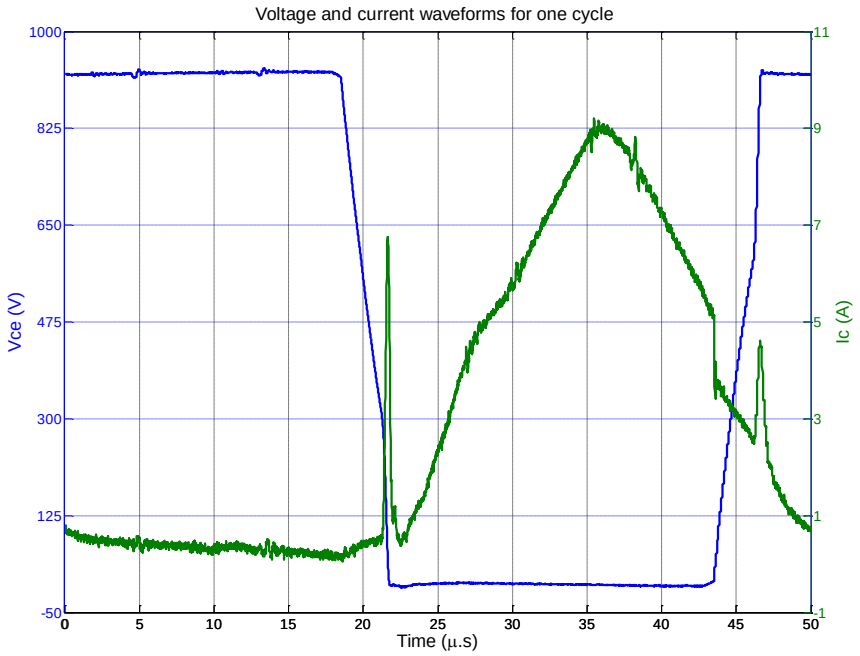


Figure 7.16 High voltage switch current and voltage waveform for 85.5% of the rated power and f=20 kHz

This is mainly due to the fact that the IGBT in the high voltage bridge has a long tail current and thus in order to snubber it, a snubber with a higher value is required. Still, if high-value snubber capacitors were to be used, more turn on losses, due to snubber capacitor discharge, will be present, unless the inductor current at the moment of commutation is high enough to discharge the snubber capacitors before firing the IGBT as explained in chapter 5 which would further increase the losses of the circuit. Furthermore, higher value snubber capacitor cannot be used with high frequency due to their

higher dead times requirements, which would further limit the control range of the converter and thus it would not be possible to achieve the desired output voltage if a higher value snubber was to be used.

In conclusion, when a snubber is used in the high voltage bridge the turn-off losses are not improved, while the turn-on losses, due to capacitor discharge, increased as a result, even at the highest current the set up allows. Furthermore, higher value snubbers cannot be used as this will further worsen the losses and a higher dead time would make the required output voltage and power not achievable at this frequency level. A frequency reduction was proposed in order to reduce the switching losses and investigate the performance at lower frequencies which will allow for higher snubber capacitor and higher dead times to be used to limit the high tail current at IGBT turn-off of the high voltage bridge. Therefore, when inductor redesigns using the available cores was attempted the lower frequencies resulted in a lower inductor operational current. The lower redesigned inductor current will not be high to enough to discharge the planned bigger snubber required snubber the high voltage IGBT tail current. This combined with the limitation of currents available from the test setup led to a decision to focus the snubber testing on the low voltages side where a reasonable comparison can be made between the different snubber values within the available control range. Also, the effect of snubber capacitor on the turn off losses can be generalized to high voltage side as well if a more suitable IGBT will be available in the market.

7.4.3 Test with the snubber capacitor connected only at the low voltage side

To conduct this test, three sets of six snubbers with the values of 22 nF, 47 nF, and 68 nF were used with the low voltage inverter bridge IGBT while the high voltage bridge IGBT were left un-snubbered due to the reasons indicated in 7.4.2. The circuit was set up using the circuit values and the same probes presented in 7.2 and 7.3 were used. The test was conducted for the same range of power loading. It should be noted that the turn off current are small as the bridge is working almost as rectifier and most of the current goes through the diodes. Higher benefits of the snubber could be yielded if the bridge is working at higher turn off currents of the IGBT. The following figures indicate the results obtained from these three tests with different snubbers:

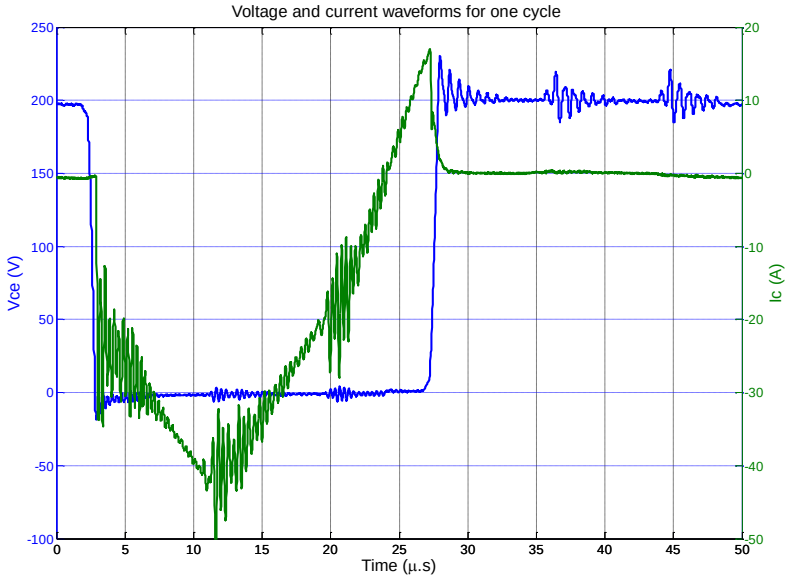


Figure 7.17 The low voltage switch current and voltage waveform for rated power, f=20 kHz, and 22 nF.

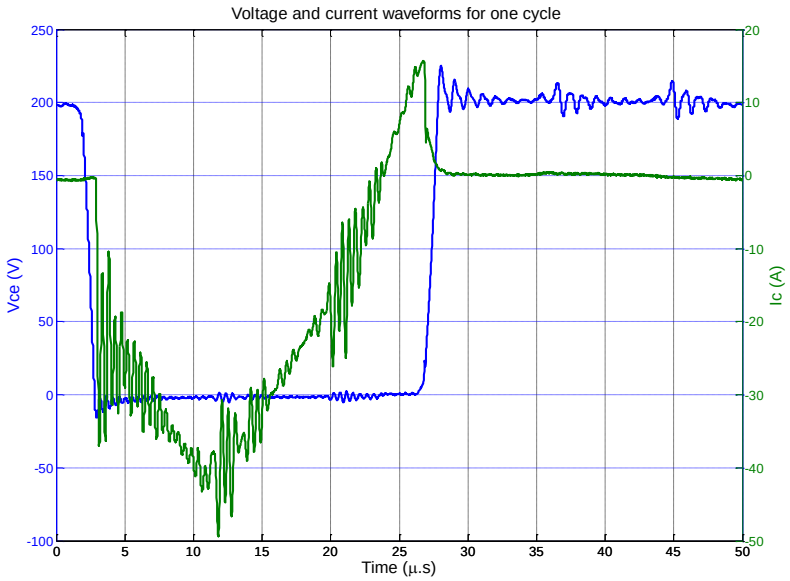


Figure 7.18 The low voltage switch current and voltage waveform for rated power, f=20 kHz, and 47 nF.

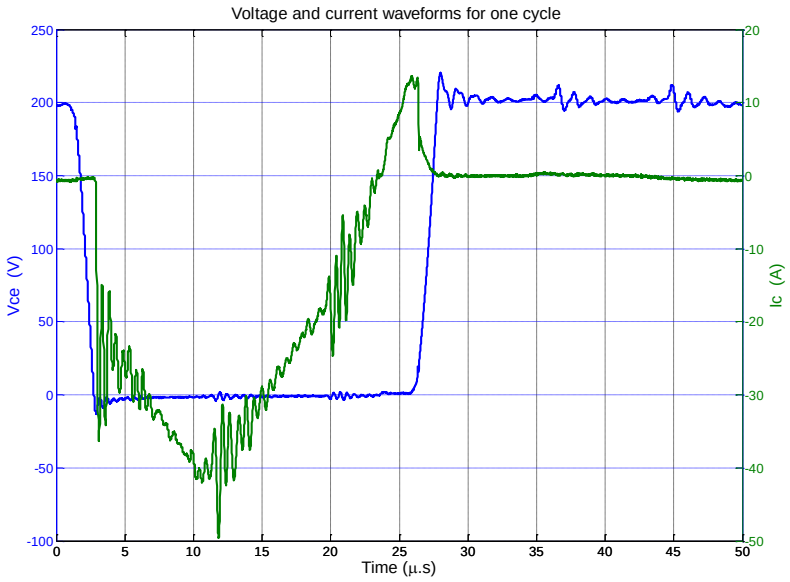


Figure 7.19 The low voltage switch current and voltage waveform for rated power, f=20 kHz, and 68 nF

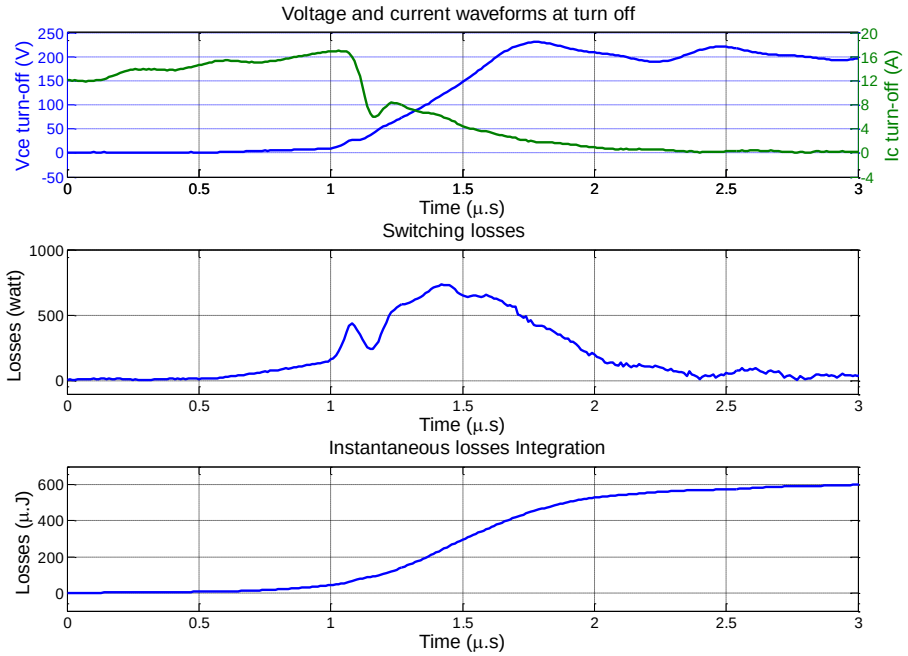


Figure 7.20 The low voltage switch current and voltage waveform for rated power, f=20 kHz, and 22 nF.

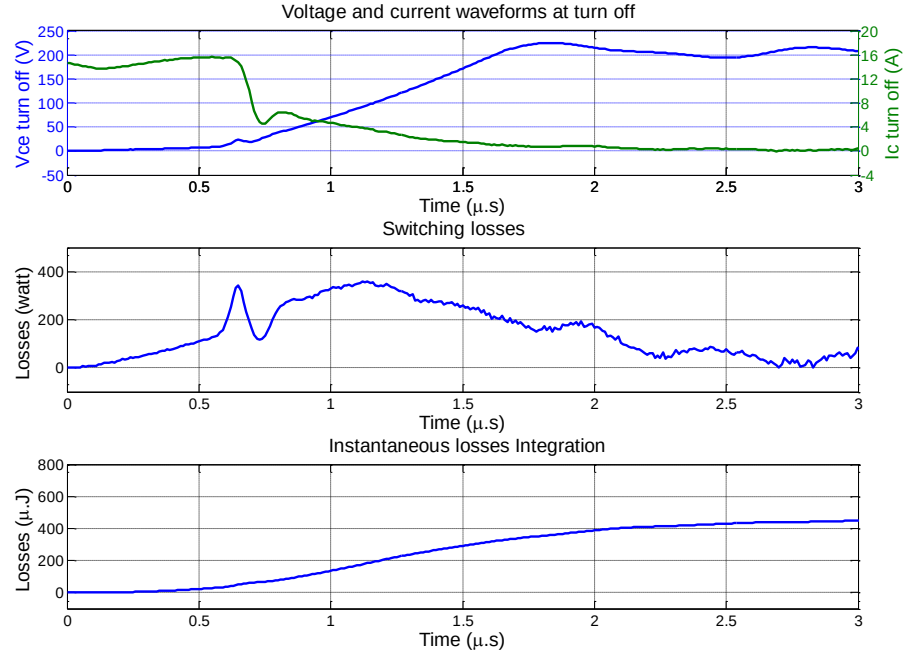


Figure 7.21 The low voltage switch current and voltage waveform for rated power, f=20 kHz, and 47 nF the losses was .

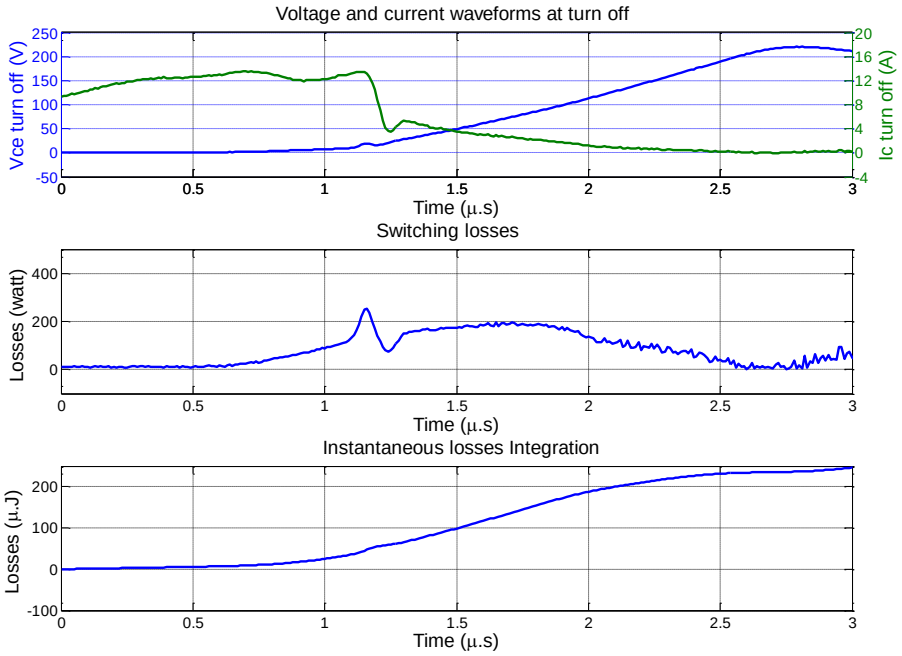


Figure 7.22 The low voltage switch current and voltage waveform for rated power, f=20 kHz, and 68 nF.

From Figure 7.17 to Figure 7.22, it can be noticed that the snubber is working as expected as the current is snubbered during the turn-off. This is true for the case where the current is high enough to discharge the snubber at the turn-off. Still, for the lower values of turn-off current, the snubbers might not be fully discharged, as shown in

Figure 3.1 to Figure 7.26: indicates this cause:

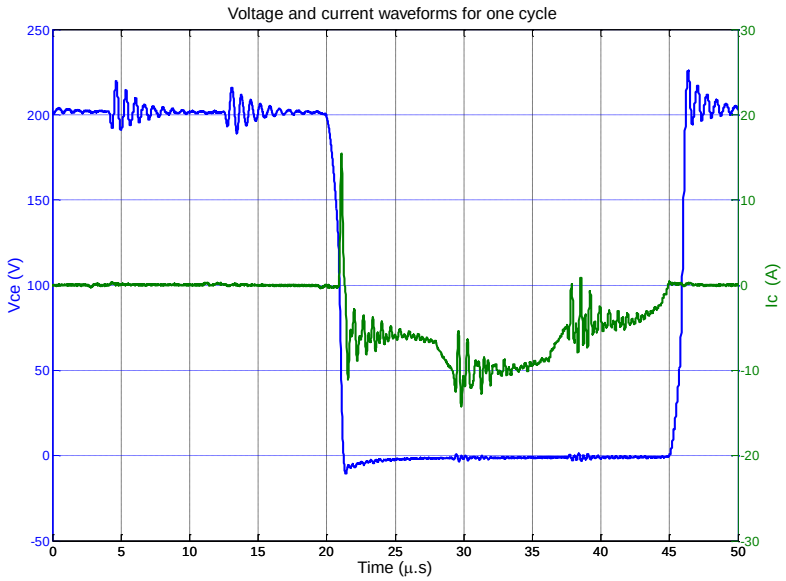


Figure 7.23 The low voltage switch current and voltage waveform for a 29.5 % of the rated power, f=20 kHz and 22 nF.

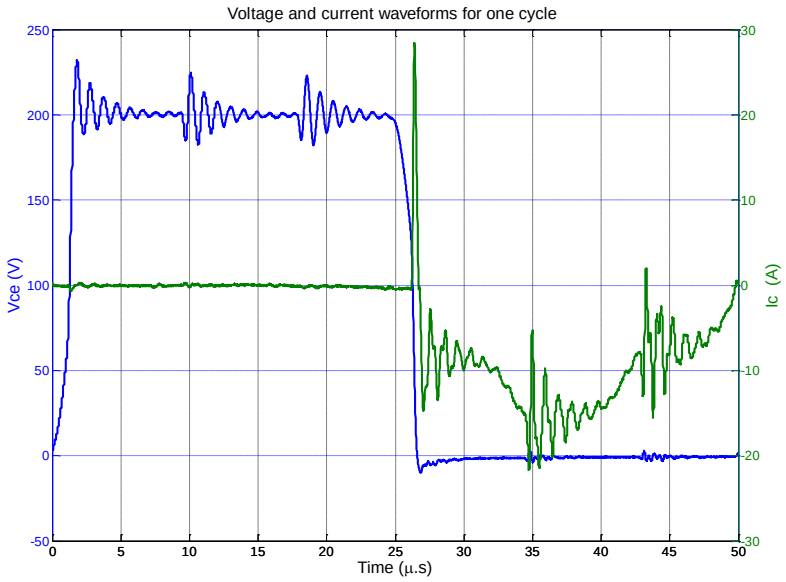


Figure 7.24 The low voltage switch current and voltage waveform for a 43.8 % of the rated power, f=20 kHz and 47 nF.

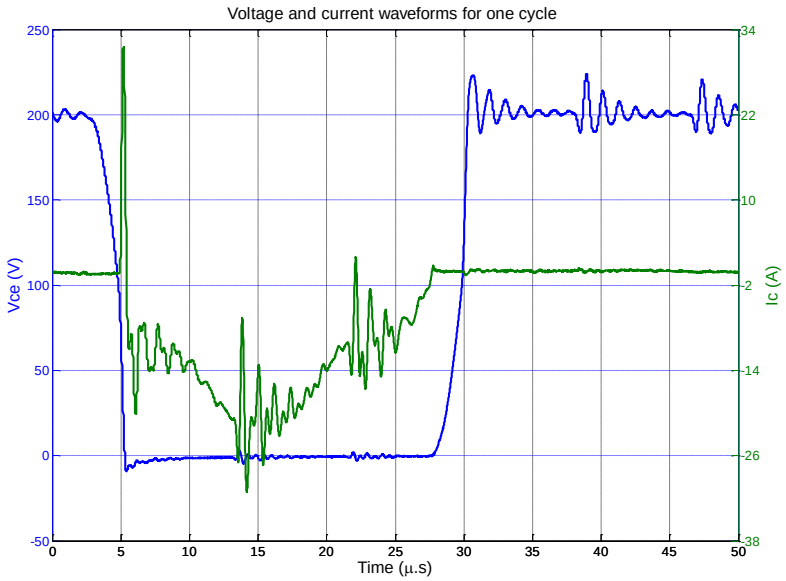


Figure 7.25 The low voltage switch current and voltage waveform for a 58.3 % of the rated power, f=20 kHz and 68 nF.

It can be noticed from Figure 7.23 to Figure 7.25 that a current spike is present at the turn on and increases with snubber capacitor value. This current spike resulted from the remaining capacitor energy, due to the fact, that the current is not high enough to discharge the capacitor fully before the IGBT is turned on. The load value, at which the current spike happens, changes depending on the value of the snubbers. Therefore, the soft switch turn on area of the converter becomes narrower as the snubber value increases. It can be noticed from Figure 7.23 that with a snubber capacitor value of 22 nF, the converter is soft switched at load values higher than 29.5 % of the rated power, while from Figure 7.24 it can be noticed that the converter is working at soft switching in the area of higher loads with 43.8 % of the rated power with snubber value of 47 nF. The soft switching area becomes narrower with 68 nF snubber as indicated in Figure 7.25 the

converter is soft switched at loads higher than 58.3 % of the rated power.

The losses were evaluated for all the load regions for the three snubber values and the results are presented in the following tables and figures:

Table 7.8 The losses values for one device for the low voltage bridge with 200 VDC load and 20 kHz and with snubber capacitor value of 22 nF.

P (%)	IGBT Turn off losses μJ	IGBT conduction losses μJ	Diode conduction losses μJ	IGBT Turn on losses μJ	Eff (%)
0	22.4	≈ 0	≈ 0	540	-
14.8	40.6	≈ 0	40.9	353.5	94.4
29.5	6.8	≈ 0	73	146.5	98.5
43.8	47.2	0.1	154	≈ 0	99.0
58.3	242.6	2	200	≈ 0	98.5
72	347.5	7	278	≈ 0	98.3
85.8	435.0	12	378.9	≈ 0	98.1
100	564.7	17	473	≈ 0	97.9

Table 7.9 The losses values for one device for the low voltage bridge with 200 VDC load and 20 kHz with snubber capacitor value of 47 n F.

P (%) rated	IGBT Turn off losses μJ	IGBT conduction losses μJ	Diode conduction losses μJ	IGBT Turn on losses μJ	Eff (%)
0	62.9	≈ 0	≈ 0	1213	-
14.8	60.1	≈ 0	64	926.8	87.4
29.5	50.7	≈ 0	91.5	701.5	94.5
43.8	23.8	≈ 0	139.9	370.5	97.6
58.3	45.7	0.2	198	≈ 0	99.1
72	157.4	2	267	≈ 0	98.8
85.8	241.9	6	363	≈ 0	98.6
100	400.3	13	458	≈ 0	98.3

Table 7.10 The losses values for one device for the low voltage bridge with 200 VDC load and 20 kHz and 68 nF.

P (%) rated	IGBT Turn off losses μJ	IGBT conduction losses μJ	Diode conduction losses μJ	IGBT Turn on losses μJ	Eff (%)
0	64.1	≈ 0	≈ 0	1718.8	-
14.8	56.3	≈ 0	60.8	1422.8	82.6
29.5	66.8	≈ 0	119	1174.2	91.5
43.8	70.2	≈ 0	157.9	895	95.1
58.3	39.2	≈ 0	190.2	390	97.9
72	88.3	0.3	259	≈ 0	99.0
85.8	187.6	4	346	≈ 0	98.8
100	198.2	12	443	≈ 0	98.7

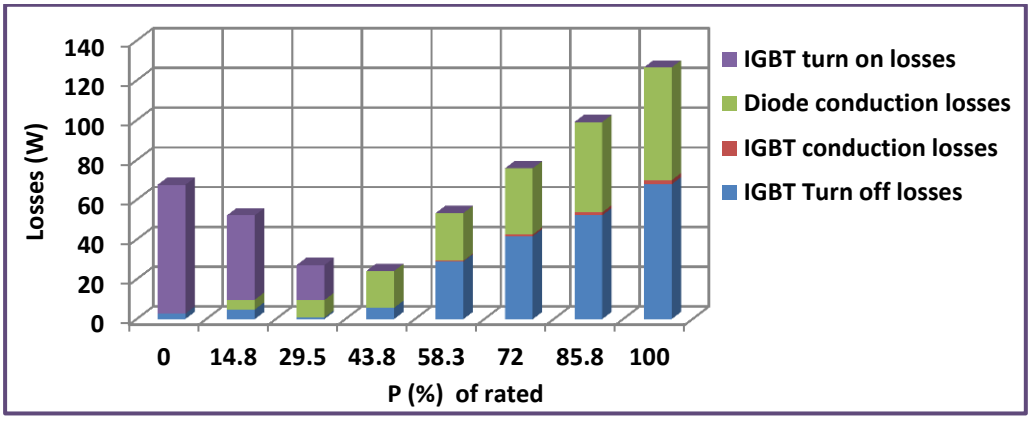


Figure 7.26 The low voltage bridge losses by using the current and voltage waveforms with snubber capacitor value of 22 nF.

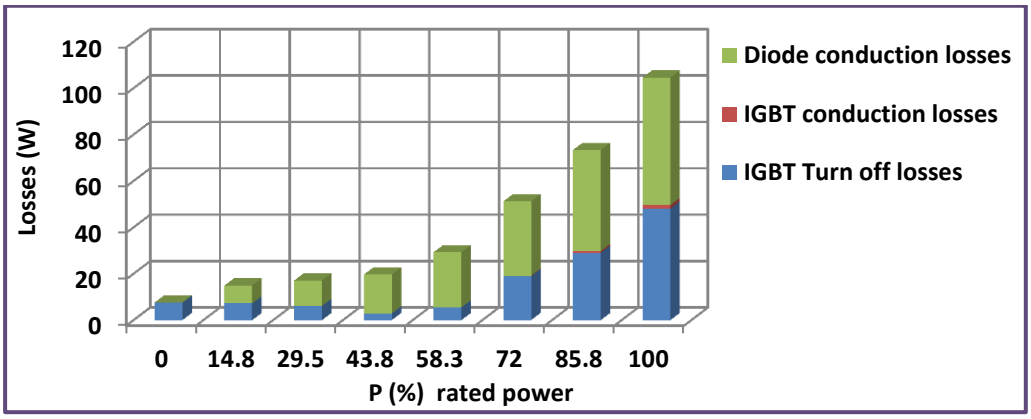


Figure 7.27 The low voltage bridge losses by using the current and voltage waveforms with snubber capacitor value of 47 nF.

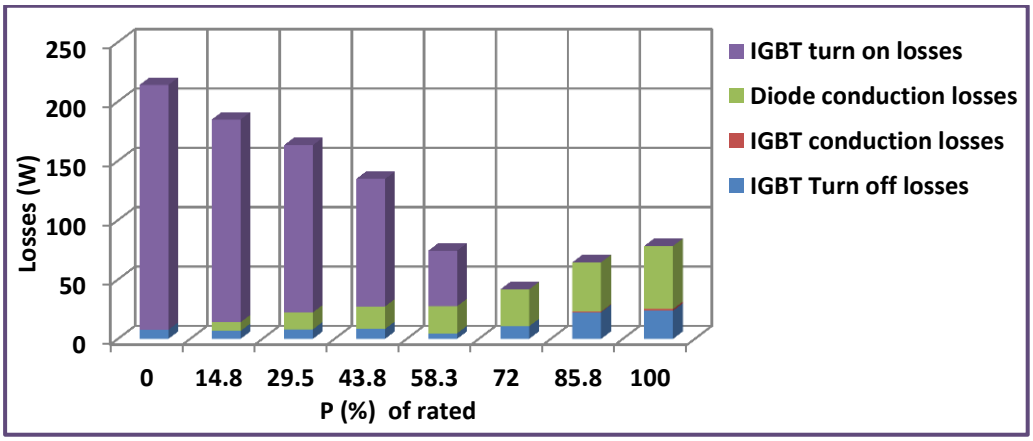


Figure 7.28 The low voltage bridge losses by using the current and voltage waveforms with snubber capacitor value of 68 nF.

It can be noticed from Figure 7.26 to Figure 7.28 and Table 7.8 to Table 7.10 that the turn-on losses start to be present at current values lower than the critical turn off current required to discharge the capacitor fully. These losses further increase the total losses at a low load in comparison to the un-snubbered case, while the snubber reduces the losses at the higher loading of the converter.

7.5 Comparison between the snubbered and the un-snubbered situations

7.5.1 IGBT turn-off losses

The use of snubbers is intended to reduce the switch turn-off losses. The relation between different snubber sizes and the associated turn off losses is presented in Table 7.11 and Figure 7.29.

It can be noticed from Table 7.11 and Figure 7.29 that the turn-off losses decrease when a snubber is connected to the IGBT as the higher the snubber value, is the lower the turn-off losses will be. The turn-off losses were 87.9 W in the case with no snubber and these losses have reduced to 23.8 W when the snubber of 68 nF is used at the full load current.

Table 7.11 Comparison between the low voltage bridge IGBTs turn off losses under different snubbering scenarios.

	Turn off losses (W)			
P (%) rated	No Snubber	22 nF	47 nF	68 nF
0	1.2	2.7	7.6	7.7
14.8	6.9	4.9	7.2	6.7
29.5	6.9	0.8	6.1	8.0
43.8	8.6	5.7	2.8	8.4
58.3	57.4	29.1	5.5	4.7
72	68.3	41.7	18.9	10.6
85.8	78.2	52.2	29.0	22.5
100	87.9	67.8	48.0	23.8

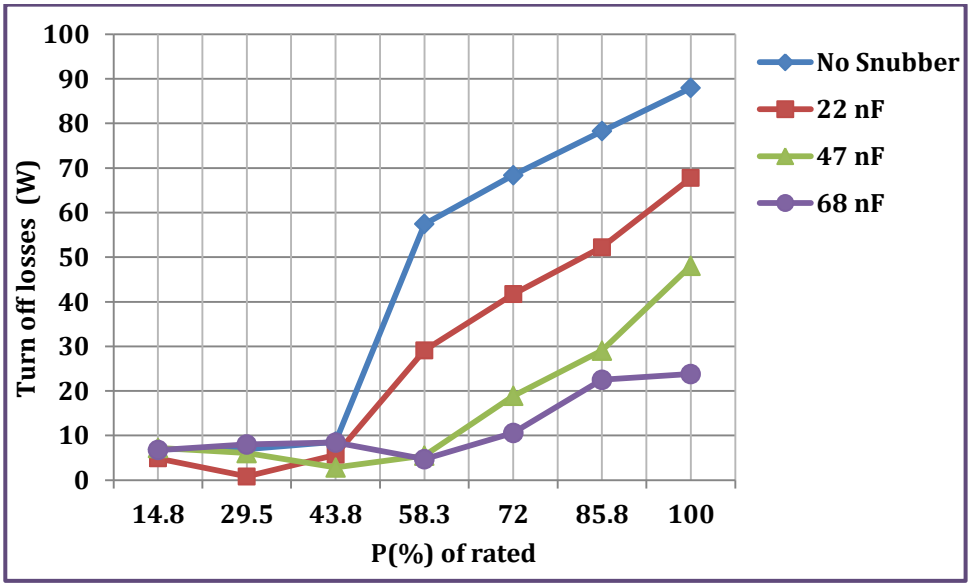


Figure 7.29 Comparison between the low voltage bridge IGBT turn off losses under different snubbering scenarios.

7.5.2 IGBT turn-on losses

Even though no turn on losses should be present in a converter operating at soft switching, the introduction of snubber resulted in IGBT turn-on losses. These turn on losses are mainly due to the fact that the current at the turn off is not high enough to discharge the capacitors at the moment of turn off and this extra energy left in the snubber capacitor will be discharged in the IGBT at the moment of turn on, which will lead to turn on losses. Table 7.12 and Figure 7.30 present a comparison between the turn-on losses under different snubbering situations:

Table 7.12 Comparison between the low voltage bridge IGBT turn-on under different snubbering scenarios.

	Turn on losses (W)			
P (%) rated	No Snubber	22 nF	47 nF	68 nF
0	≈0	64.8	145.5	206.2
14.8	≈0	42.4	111.2	170.7
29.5	≈0	17.6	84.9	140.9
43.8	≈0	≈0	44.5	107.4
58.3	≈0	≈0	≈0	46.8
72	≈0	≈0	≈0	≈0
85.8	≈0	≈0	≈0	≈0
100	≈0	≈0	≈0	≈0

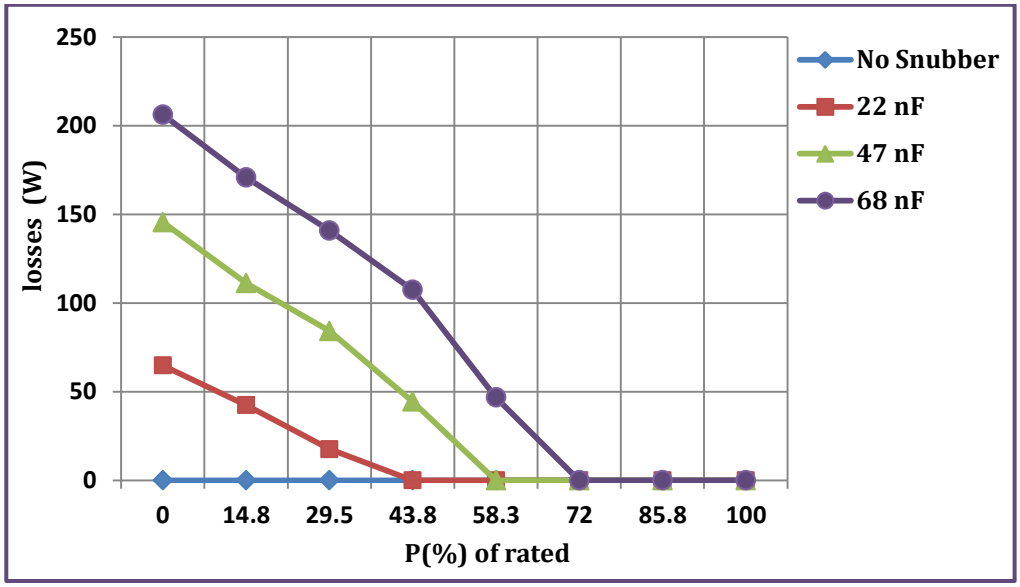


Figure 7.30 Comparison between the low voltage bridge IGBT turn-on losses under different snubbering scenarios.

It can be noticed from and Table 7.12 that the converter will have high turn-on losses at the moment of turn on and theses losses will increase as the snubber value increases. It can be noticed also that the turn-on losses start to be present at higher load values when a higher snubber value is used. It can be noticed clearly from this that the soft turn on range become narrower as the snubber value increases.

These two effects are due to the fact that the bigger the value of the snubber capacitor used, the higher the energy stored in the snubber capacitor and the longer the commutation times, which leads to higher turn-on losses.

The IGBT soft switch turn on limit can be calculated analytically by using equations 5.44 and 5.45 which are restated next. These equations yield the low voltage bridge critical turn off current limits for different snubber capacitor values as presented in Table 7.12.

$$I_{com} = \frac{V_i}{Z_0} \tag{7.12}$$

Where:

$$Z_0 = \sqrt{\frac{3L}{4C}} \tag{7.13}$$

Table 7.13 The analytical critical soft switch turn on current limits.

Snubber value nF	22	47	68
I_{com}(A)	7.78	11.37	13.68

The converter is in soft switching operation in the highlighted region of Table 7.12. the exact IGBT soft switching turn on boundary cannot be pinpointed due to the discrete nature of the available resistive load. Table 7.14 includes the power levels and the associated calculated turn-off current limits at the observed soft switched turn on edge.

Table 7.14 The observed practical soft switched turn on limits.

Snubber value μF	22	47	68
P(%) rated	43.55	58.62	72.02
I_{com} (A)	6.86	9.46	11.90

After comparing Table 7.13 and Table 7.14, it can be noticed that the soft switching turn on occurs at a current level slightly lower than the calculated current levels. This was predicted

due to the presence of a small resistor in the current path which is not incorporated in the model. Nevertheless, overall good matching between the analytical and practical results validate the soft switch turn on analysis of the converter.

7.5.3 Total losses and efficiency.

The last part included studying the effect of snubbers on the turn on and turn off losses; this part of the thesis includes the effect of snubbers on the total losses of the converter. Figure 7.31 and Table 7.15 indicates the total losses of the converter under different loading and snubbering situations:

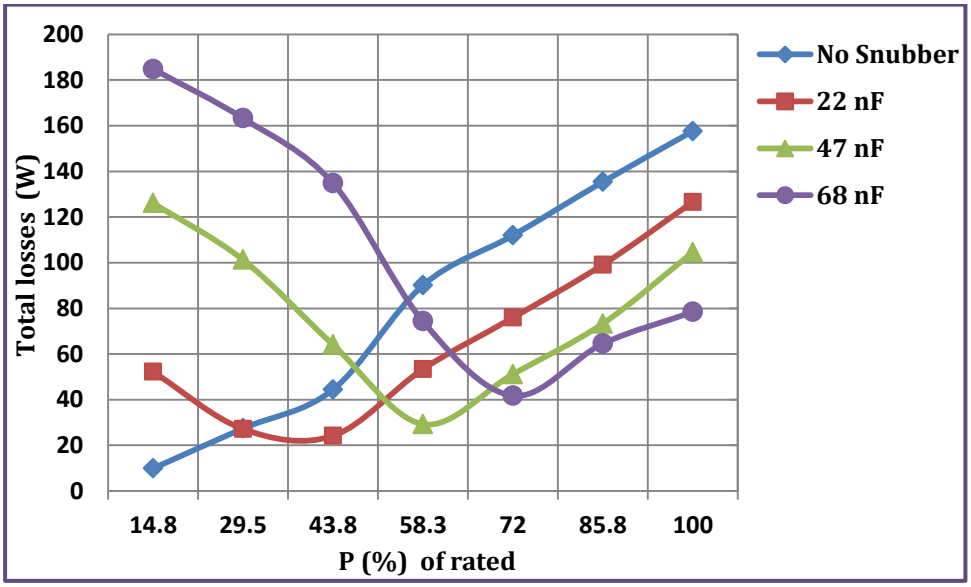


Figure 7.31 Comparison between the low voltage bridge total losses under different snubbering scenarios

From Figure 7.31 and Table 7.15 it can be noticed that when the low voltage converter is working with high load, the total converter losses decrease as the snubber capacitor value increases. The total losses were 157.6 W at full load with no snubber, which then decreased to 78.4 W with a snubber

value of 68 nF. When the converter is working at low power level, the total converter losses have the opposite behavior with the losses increasing as the snubber value increases.

Table 7.15 Comparison between the low voltage bridge total losses under different snubbering scenarios.

	Total losses (W)			
P (%) rated	No Snubber	22 nF	47 nF	68 nF
0	1.2	67.5	153.1	213.9
14.8	9.9	52.2	126.1	184.8
29.5	27.5	27.2	101.2	163.2
43.8	44.4	24.1	64.1	134.8
58.3	90.1	53.3	29.3	74.3
72	111.9	75.9	51.7	41.7
85.9	135.4	99.1	73.3	64.5
100	157.6	126.6	104.6	78.4

This behavior is expected when a converter is working with different snubbering levels and is mainly due to the effect the snubber has on the turn on and turn off losses, as discussed earlier in section 5.4 and section 7.4.2.

The last changes in the losses with the different snubbers have an impact on the converter efficiency. Figure 7.32 and Table 7.16 demonstrate the converter efficiency under different loadings and snubbering situations:

From Figure 7.32 and Table 7.16 an efficiency trend can be noticed, the efficiency of the converter will be the highest at a full load and an efficiency increase from 97.4% to 98.7% can be noticed when the converter is equipped with 68 nF snubber.

Table 7.16 Comparison between the low voltage bridge efficiency under different snubbering scenarios (efficiency is in %):

	Efficiency (%)			
P(%) rated	No Snubber	22 nF	47 nF	68 nF
14.8	98.9	94.4	87.4	82.6
29.5	98.4	98.5	94.5	91.5
43.8	98.3	99.0	97.6	95.1
58.3	97.5	98.5	99.1	97.9
72	97.5	98.3	98.8	99.0
85.89	97.4	98.1	98.6	98.8
100	97.4	97.9	98.3	98.7

In contrast, at 14.8% of the full load, the converter efficiency suffers from decline if a snubber is to be used with the converter. The efficiency at the low load declined from 98.9 % to around 82.6 % if heavy snubbering of 68 nF is used.

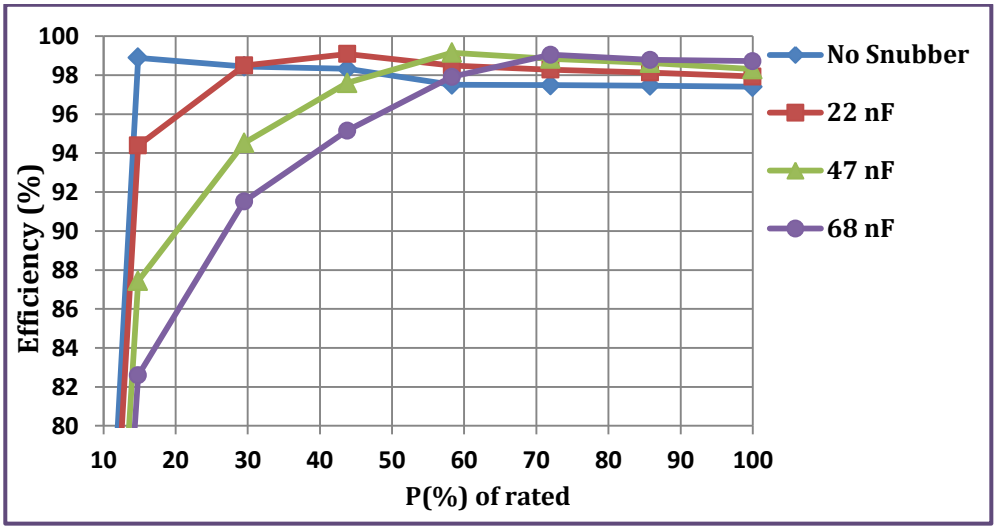


Figure 7.32 Comparison between the low voltage bridge efficiency under different snubbering scenarios:

In the medium loading range of the converter, the converter achieved the highest possible efficiency over the whole range if a medium snubbering is used. If a snubber of 22 nf is used, the converter achieves 99.08 % at 43.8% of the total load while the highest efficiency was achieved with snubber 47 nF at 99.1% and a 58.3% of the total load.

In conclusion, each snubber values have a different loading point where it has its peak efficiency. Thus by using a converter made from cells with different snubber values, a multi-cell modular converter with high efficiency over a wide loading range can be achieved, which is required from the grid application under consideration to achieve a high efficiency over a wide range of operation. The idea of a modular multi-cell multi-snubber converter will be the focus of the next part of this thesis.

7.6 Evaluation of multi-cell multi-snubbered 3ϕ DAB converter.

As was presented earlier in section 5.2.2 of this thesis, the 3ϕ DAB converter has a high efficiency over a wide power loading range and it was proposed to further improve its efficiency by using a multi-cell multi-snubberd variant of it as this required in the application under consideration which is grid connected application.

As noted earlier in this chapter the losses of the 3ϕ DAB low voltage bridge vary depending on the snubbering and the loading of the 3ϕ DAB converter cells. A highly snubbered cell will perform the best at high loads, while losses will be lowest for a un-snubbered cell working at a low loading. For medium loading, a cell with medium snubbering will perform the best, as presented in Table 7.15 of the converter total losses. In Table 7.12, the 3ϕ DAB cell which offers the lowest losses is highlighted in green and the snubbered 3ϕ DAB cells operation should be avoided in the blue highlighted range. A wide range high efficiency multi-cell multi-snubbered 3ϕ DAB converter can be achieved based on the relation between losses, snubbering and loading of the converter cells.

The converter should be built out of modular multi-snubbered cells and each cell will be utilised at it is maximum efficiency points. The cases under consideration include:

- A multi-cell multi-snubbered 3ϕ DAB converter made of four un-snubbered cells.

- A multi-cell multi-snubbered 3ϕ DAB converter made of one un-snubbered cell and three heavily snubbered cells.

- A multi-cell multi-snubbered 3ϕ DAB converter made of one un-snubbered cell and three cells with different snubbers.

The power sharing between the converter cells is based on the available cell/cells, which can/could provide the required power with the lowest converter losses. The cells will be working at unequal power sharing as some of the cells will be loaded differently from others. For example, if the required output power is at a low level, the best cell to be used is the un-snubbered cell. If the required power from the converter increases to around 25% of the rated, a cell with the highest snubber value should be used as it will be working at around 100% of its rating and with the lowest losses amongst all the available cells.

If the required power is more than 25 % and less than 50 % of the rated power, two cells will have to be activated where the cell with the highest snubbering will be working at its maximum power rating combined with other cells, which can be either snubbered or un-snubbered based on the required power level. Furthermore, if the required power is more than 50% of the rated power and less than 75% the rated power, two cells with the highest snubbering should be used at their full rating, while the extra power could be supplied using a

third cell which should be either snubbered or un-snubbered based on the extra power required.

Lastly, for the range of 75% to 100% of the rated power, three cells will be working at their maximum power, which are going to be the cells with snubbering, while the fourth unsnubbered cell will supply the required extra power. This concept of cell management based on the loading profile for the proposed converter configuration is presented in Figure 7.35 to Figure 7.37.

To sum up, the converter will be made of combinations of modeller cells with different snubbering working at their lowest losses point. This will result in a converter with high efficiency at a wider operating range. Figure 7.33 indicates a comparison between the efficiency of a three multi-cell multi-snubber 3ϕ DAB low voltage bridge made of 4 identical cells with different snubbering.

It can be noticed from Figure 7.33 and Figure 7.34 that the converter made of cells with no snubber suffers from the highest losses at most of the loading range.

While the converter made of three heavily snubbered cells with one un-snubbered cell has the lowest losses at the high power range. This is due to the use of three heavily snubbered cells at their maximum power rating and lowest losses range.

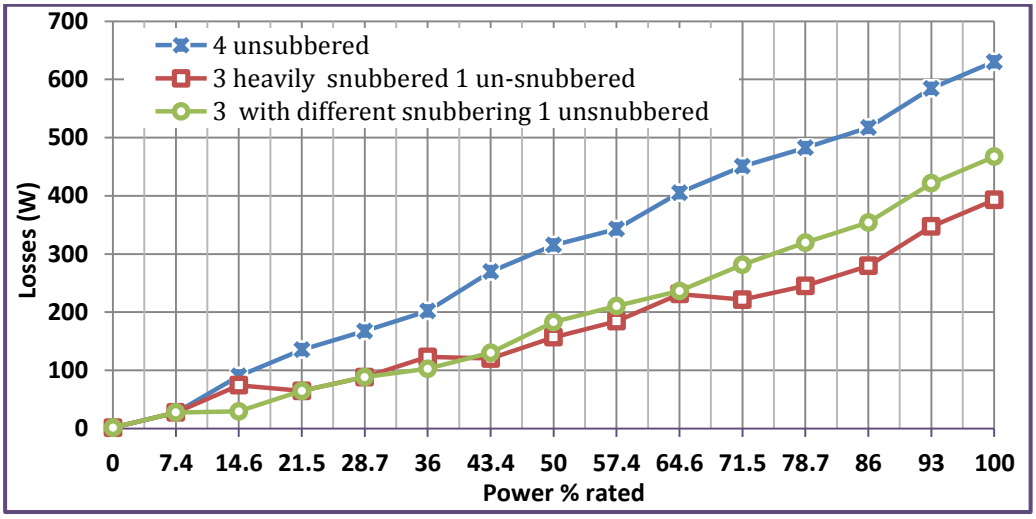


Figure 7.33 Comparison between a three multi-cell 3ϕ DAB converters low voltage bridge losses made out of 4 modeller cells with different snubbering.

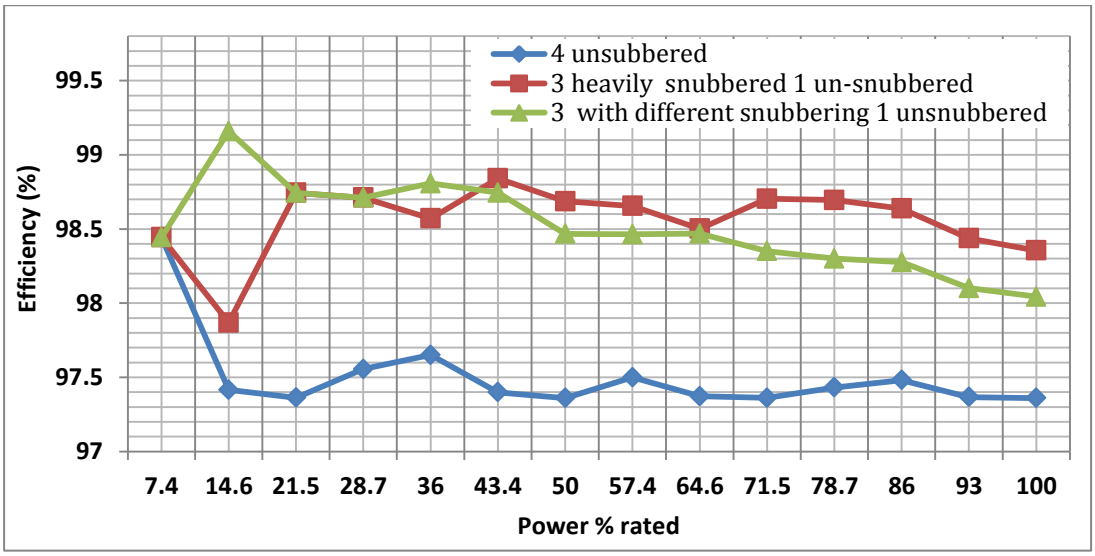


Figure 7.34 Comparison between a three multi-cell 3ϕ DAB converters low voltage bridge efficiency for a converter made out of 4 modeller cells with different snubbering.

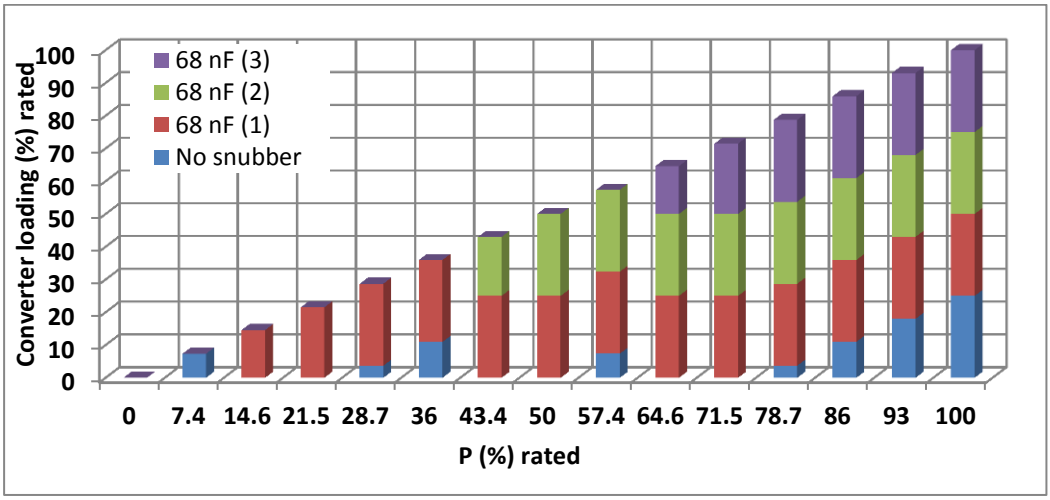


Figure 7.35 Proposed power management for a converter made of three heavily snubbered and one un-snubbered cell

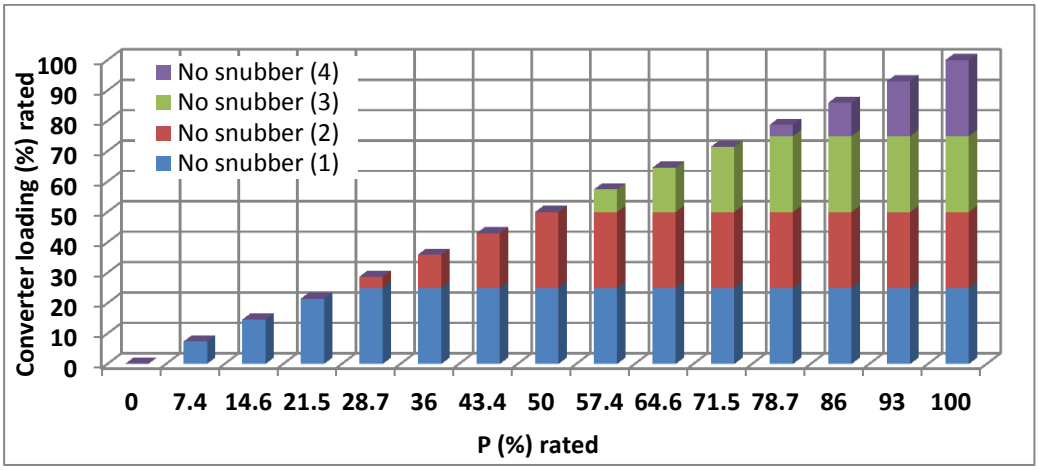


Figure 7.36 Proposed power management for the converter made of four un-snubbered cells

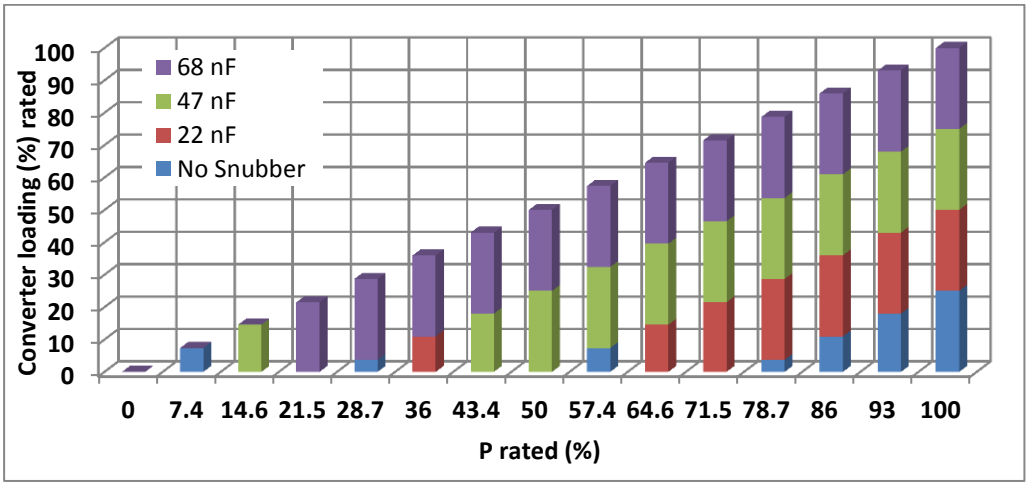


Figure 7.37 Proposed power management for a converter made of three differently snubbered cells and one un-snubbered cell

The converter made from cells with three different snubber values has the lowest losses at some of the middle range points when compared with the converter made of three heavily snubbered cells. As the cells with medium snubbering level have the lowest losses at the medium power range. This converter has higher losses at the high power range when compared to the converter made with three heavily snubbered cells.

To sum up, converters made of cells with no snubbers are likely to have more losses at most of the power range, while converters made of cells with more than one snubber value might provide slightly better performance at some loading points in the mid power range, while suffering from higher losses at the higher power range when compared to the converter made of heavily snubbered cells.

Hence, the converter made of three heavily snubbered cells and one un-snubbered cell provides the best performance at

most of the power range, and it has the best efficiency at the higher loading, while it has a lower efficiency at some points at the medium loading range when compared to the converter made of three cells with different snubbering.

In conclusion, the multi-cell multi-snubbered 3ϕ DAB converter with lower losses and high efficiency over a wide range of operation is viable and achievable if a multi-cell 3ϕ DAB converter is equipped with different snubbered cells. And each cell is used at the point where it provides its best efficiency. Thus, a converter which provides the best performance for the proposed DC/DC grid in chapter 4 can be achieved.

The proposed converter will be a modular multi-cell multi-snubbered 3ϕ DAB converter. The converter base cells will be the same while the connected snubbers and the cells power management will depend on the loading profile of the converter, which changes when the grid battery, PV or load levels are changed. Thus the only required converter change to match a change in the converter loading profile will be changing the snubbering and power management of the converter cells which is feasible even after installation if it is considered while designing the converter.

Furthermore, extra modular cells can be added if the total load is increased which waivers the need for complete converter replacements if extra power is required. Thus, the final modular multi-cell 3ϕ DAB converter can be easily adjusted to best serve each community, which reduces the total cost of

the converter and the cost of the change to DC distribution grids.

7.7 Summary

This chapter presented the steps followed to test the 3ϕ DAB converter cells under different snubbering situations. An evaluation of the proposed multi-cell multi-snubbered 3ϕ DAB was carried out.

In conclusion, a high efficiency over a wide range of loading profile for the multi-cell multi–snubbered 3ϕ DAB converter to serve the proposed DC/DC grid in chapter 4 was validated. It was noticed that it is feasible to use the same converter to serve different grid loading profiles if for example the system load has increased or the battery or PV levels in the grid were changed. This can be performed by changing the snubber values or the cells power-sharing strategy or by adding an extra cell to increase the rating of the converter. Thus the converter high efficiency can be maintained combined with the lowest cost after a change in the grid.

The following chapter will include the conclusion of this thesis combined with the suggested work to be carried out in order to continue the investigation of the proposed DC/DC grid and the multi-cell multi–snubbered 3ϕ DAB converter in this thesis.

Chapter 8

Conclusion.

8.1 Thesis Summary

AC or DC, this has been at the centre of debate since the early days of the electrical system. DC is progressing in areas such as transmission as HVDC is proven to be more economical over a long distance. This thesis proposed the use of DC voltages in the last mile of the distribution grid.

The advantages and challenges facing switching the distribution system to DC voltage were highlighted in this

thesis. A focus was given to the DC grid arrangements layouts and to a practical investigation of the proposed modular multi-cell multi-snubber three phase DAB converter to serve the chosen grid arrangement. The investigations were carried within the Libyan grid context, case study. The thesis aimed to achieve several objectives including:

The first objective of this thesis was to investigate the Libyan grid structure, loads, and generation in order to recommend a suitable method to improve its performance.

The Libyan grid is mostly a typical grid with a high number of load centres located far from generation. Also, some isolated grids exist. Its biggest loads are residential loads, where the energy is heavily used to heat water and for air-conditioning which results in high losses, voltage sags, and blackouts. Also, Libya's great solar potential has not been utilised yet. Thus a distribution system which can improve the voltage quality and help to expand the use of solar energy in Libya is needed.

The second thesis objective was, to explore the current electrical systems utilising DC voltage in order to identify the possible advantages and effects of replacing AC with DC in the future DC distribution systems.

A literature review was carried out to investigate the present usages of DC and the effects a change to DC might have on the grid. It was noticed that DC is used in many grid applications such as the International Space Station (ISS), DC shipboard systems, data centres and railway systems. Additionally, DC is used in many devices such as TVs, washing machines, LED lighting, DC inverter driven air conditioning.

Furthermore, the main distributed generation solar panel and wind turbines are either generating DC or have DC embedded inside them.

It was stated in many publications that using DC brings many advantages to grids such as better voltage quality, no reactive power and lower currents, the ability to use localised protection, higher cable transmission abilities, fewer converter stages and higher system efficiencies. These later advantages lead to higher DC system hosting capacity when compared with an AC system. Thus a DC distribution system was proposed to serve the Libyan grid due to the fact that it can accommodate PV generation and support air-conditioning load, while, improving the voltage quality and reducing the power losses.

The third thesis objective was to propose suitable DC voltage levels to serve the last mile of the distribution system.

The voltage of 325V seemed the most promising DC voltage for the low DC distribution voltage of the grid taking into account that is equal to the peak of 230AC voltage. Additionally, 1500 VDC is the highest DC or AC voltage the European Union specification allows within the low voltage grid, this was considered to be the upper voltage limit of this work.

The next objective was to investigate the possible DC distribution arrangements and to design, simulate and compare their performance based on the converter losses. This allowed identification of the chosen DC grid arrangement and converter requirements.

A study and comparison among four potential DC distribution grid layouts was carried out. The study included loads estimation, PV design, converter rating, power management and loss estimations.

The results showed that a DC grid arrangement utilising two port converters have lower total converter losses and smaller converter installed power when compared with arrangements using three port converters. Thus, two port converter topologies to serve the grid concept were proposed to be investigated afterward.

The last thesis objective was to choose, analyse, design, build and test a DC/DC converter to serve the proposed DC distribution grid layout and to further improve the chosen converter performance by building a multi-cell variant of it.

The 3ϕ DAB offers the desired DC grid requirements and thus was investigated and studied. A multi-cell multi–snubbered 3 ϕ DAB converter was proposed to further improve the converter performance under the chosen grid conditions. A converter cell was built and tested in the laboratory.

The proposed modular multi-cell multi–snubbered 3ϕ DAB converter offered low losses over a wide range of loading profiles. Furthermore, the converter performance can be easily modified to reflect a specific DC/DC grid loading profile by simply altering the snubbers attached to the cells and the power management algorithm between the cells while keeping the core modular cells the same. Extra cells can be added if higher power rating is required, which improves the converter

expandability and reduces the total cost of the proposed DC distribution system.

To conclude, DC is not an alien technology and it already has considerable use in the electrical grids A complete low voltage DC distribution grid which can be used to serve the existing inner city areas and to provide electricity to the world's yet to be electrified areas, such as in Sub-Saharan Africa, was proposed. A group of DC distribution grid layouts was proposed and studied. A DC/DC converter to serve the proposed DC grid layout was studied and practically validated.

The thesis achieved the following

8.2 Thesis achievements:

- An assessment of the present reality of the Libyan grid and the challenges facing it.
- An investigation of the present usages of DC voltage in the electrical system. A focus was given to their advantages and the voltage levels they use.
- The proposal of a novel complete DC distribution grid and suggestion of the DC voltage levels to serve it.
- An assessment of the daily electrical load profiles of the Libyan household using the CREST electrical demand model.
- The proposal of four different DC grid arrangements.

- Comparison between the different DC grid arrangements under study based on their converter losses and installed power.
- Advancements in the three phase DAB converter model and analysis and the proposal of new conduction losses model.
- The proposal of novel modeller multi-cell-multi-snubber three phase DAB converter topology.
- A Practical investigation and validation of the proposed multi-level multi-snubber three phase DAB converter.

The following futures studies are suggested to continue the investigation:

8.3 Further work

- Real time assessment of the Libyan loading profiles.
- Investigating the required control for the proposed DC grid.
- Assessment of the stability of the proposed DC grid.
- An assessment of the required converters at the entrance of the house to link it to the DC distribution grid.
- An assessment of the effect of varying the battery location on the system performance.

- Studying the effect of harmonics on the DC system and AC system in order to evaluate it is impact on the system housing capacity.
- Designing the required controller closed loop of the multi-cell multi-snubber 3ϕ DAB converter.
- Designing the required controller of the proposed DC/DC grid layout.
- Building a complete full multi-cell multi-snubber 3ϕ DAB and studying it is performance.
- Investigating the performance of the multi-cell multi-snubber 3ϕ DAB under a real power loading situation.

The war of current is not over yet, apparently, Nikola Tesla is in the lead while Thomas Edison has the upper hand.

References:

1. D.Dong, D.B., F. C. Lee,P. Mattavelli, Ac-dc Bus-interface Bi-directional Converters in Renewable Energy Systems, 2012, Faculty of the Virginia Polytechnic Institute and State University.

2. H. PANG, E.L., B.PONG, DC electrical distribution systems in buildings. 2nd International Conference on Power Electronics Systems and Applications, 2006

3. Meuser, M., H. Vennegeerts, and P. Schafer. Impact of voltage control by distributed generation on hosting capacitiy and reactive power balance in distribution grids. in Integration

of Renewables into the Distribution Grid, CIRED 2012 Workshop. 2012.

4. The Electrify Africa Act of 2015. 2015; Available from: https://www.one.org/us/policy/energize-africa/.

5. P. Salonen, T.K., P.Nuutinen, P.Peltoniemi , J.Partanen, An LVDC Distribution System Concept. NORPIE, Nordic Workshop on Power and Industrial Electronics, June 9-11,2008.

6. T.Kaipia, P.S., J.Lassila, J.Partanen, <POSSIBILITIES OF THE LOW VOLTAGE DC DISTRIBUTION SYSTEMS>. Lappeenranta University of Technology.

7. Williamson, B.J., et al. Project Edison: SMART-DC. in Innovative Smart Grid Technologies (ISGT Europe), 2011 2nd IEEE PES International Conference and Exhibition on. 2011.

8. Annual report, 2010, General Electric Company of Libya (GECOL): Tripoli Libya.

9. Sultan, S.S. and M.K. Darwish. Power quality evaluation in Libyan electrical Distribution Networks. in 2012 First International Conference on Renewable Energies and Vehicular Technology. 2012.

10. Standalone PV system for Almarhan well Village libyan office for research and development: Tripoli Libya.

11. Hybrid diesel/solar system for Misread Valley village in Libyan centre For Development, office for research and development: Tripoli Libya.

12. A.Goodland, R.J., The Urgent Transition to Environmental Sustainability, 2013, The Environmental General Authority, Tripoli: Tripoli, Libya.

13. Ali, N. and R. Ramakumar. Impact of the penetration of wind power on the Libyan power system. in Power and Energy Society General Meeting, 2012 IEEE. 2012.

14. Dr M.Ekhlat, D.I.M.S.E.N.M.K., Energy Efficiency and Renewable Energy Libya - National study, in Mediterranean and National Strategies for Sustainable Development Priority Field of Action 2: Energy and Climate Change2007, UNEP.

15. Libyan grid total load Data from the central loads control centre in libya 2012: Not published

16. F. Abograd, F.G., A.Ali, M.khalat, Y.Mansor, Study on the power consumption in the domestic loads in Libya. Energy and life magazine, 2003. 17.

17. Dr.I.Salah, D.M.K., Dr.M.Almashigery, General Libyan electrical company guide on electrification of rural areas using solar energy. Wnergy and Live, 2003(19).

18. Arbon, I.M., Baseline energy statement – energy consumption and. ATOC, 2007.

19. Wang, T.C. and J.B. Raley. Electrical power system stability assurance for the International Space Station. in Energy Conversion Engineering Conference, 1997. IECEC-97., Proceedings of the 32nd Intersociety. 1997.

20. Hart, D.S., et al. A Solid State Power Controller Module for the International Space Station EXPRESS Rack. in Energy Conversion Engineering Conference, 1997. IECEC-97., Proceedings of the 32nd Intersociety. 1997.

21. Oman, H., International Space Station power storage upgrade planned. Aerospace and Electronic Systems Magazine, IEEE, 2003. 18(5): p. 32-39.

22. Ciezki, J.G. and R.W. Ashton, Selection and stability issues associated with a navy shipboard DC zonal electric distribution system. Power Delivery, IEEE Transactions on, 2000. 15(2): p. 665-669.

23. Chen, S., et al. An Overview of the Application of DC Zonal Distribution System in Shipboard Integrated Power System. in 2012 Third International Conference on Digital Manufacturing & Automation. 2012.

24. Jonathan G. Koomey, Estimating Total Power Consumption by Servers in The U.S. and The World, 2007.

25. Mondal, S. and E. Keisling. Efficient data center design using novel modular DC UPS, server power supply with DC voltage and modular CDU cooling. in Power Electronics, Drives and Energy Systems (PEDES), 2012 IEEE International Conference on. 2012.

26. Pratt, A., P. Kumar, and T.V. Aldridge. Evaluation of 400V DC distribution in telco and data centers to improve energy efficiency. in Telecommunications Energy Conference, 2007. INTELEC 2007. 29th International. 2007.

27. Salomonsson, D., L. Soder, and A. Sannino, An Adaptive Control System for a DC Microgrid for Data Centers. Industry Applications, IEEE Transactions on, 2008. 44(6): p. 1910-1917.

28. Gonzalez, D. and F. Manzanedo. Power losses minimization in D.C. electric railways by means of traction substations coordinated voltage control. in Railway Traction Systems (RTS 2010), IET Conference on. 2010.

29. Gonzalez, D. and F. Manzanedo. Optimal design of a D.C. railway power supply system. in Electric Power Conference, 2008. EPEC 2008. IEEE Canada. 2008.

30. Sarangan, N. and Y.K. Tan. Optimal power interface topology for DC grid connected LED lighting system. in 2012 IEEE Third International Conference on Sustainable Energy Technologies (ICSET). 2012.

31. Koh, L.H., et al. An energy-efficient low voltage DC grid powered smart LED lighting system. in IECON 2011 - 37th Annual Conference on IEEE Industrial Electronics Society. 2011.

32. Shafi, M.A. and R.A. McMahon. Implementation and Verification of CFL Models for Use in Performance Analysis in High Frequency Electronic Ballasts. in 2006 3rd IET International Conference on Power Electronics, Machines and Drives - PEMD 2006. 2006.

33. Cheng, Y.K. and K.W.E. Cheng. General Study for using LED to replace traditional lighting devices. in Power Electronics

Systems and Applications, 2006. ICPESA '06. 2nd International Conference on. 2006.

34. Van der Broeck, H., G. Sauerlander, and M. Wendt. Power driver topologies and control schemes for LEDs. in Applied Power Electronics Conference, APEC 2007 - Twenty Second Annual IEEE. 2007.

35. Commission, I.E., International standard IEC 60038 standard voltages 2002: Geneva Switzerland.

36. Engelen, K., et al. The Feasibility of Small-Scale Residential DC Distribution Systems. in IEEE Industrial Electronics, IECON 2006 - 32nd Annual Conference on. 2006.

37. Shafi, M.A. and R.A. McMahon, Influence of Voltage and Frequency Dimming on Power Losses in HF Electronic Ballasts for Compact Fluorescent Lamps. IEEE Transactions on Industry Applications, 2012. 48(2): p. 839-845.

38. Anand, S. and B.G. Fernandes. Optimal voltage level for DC microgrids. in IECON 2010 - 36th Annual Conference on IEEE Industrial Electronics Society. 2010.

39. Matsumoto, A., et al. Development of 400 Vdc power distribution system and 400 Vdc output rectifier. in Telecommunications Energy Conference, 2009. INTELEC 2009. 31st International. 2009.

40. Parliament, E., Directive 2014/35/EU of the European Parliament and of the Council, 20104, Official Journal of the European Union

41. Etherden, N. and M.H.J. Bollen. Increasing the hosting capacity of distribution networks by curtailment of renewable energy resources. in PowerTech, 2011 IEEE Trondheim. 2011.

42. D.D.Konadu, Z.S.M., J.M. Allwood, K.S. Richards, G.M. Kopec , R.A. McMahon, R.A. Fenner, Not all low-carbon energy pathways are environmentally "no-regrets" options. ScienceDirect, 2015(Global Environmental Change 3): p. 379–390.

43. Masoum, M.A.S., P.S. Moses, and K.M. Smedley. Distribution transformer losses and performance in smart grids with residential Plug-In Electric Vehicles. in Innovative Smart Grid Technologies (ISGT), 2011 IEEE PES. 2011.

44. Trichakis, P., et al., Predicting the technical impacts of high levels of small-scale embedded generators on low-voltage networks. Renewable Power Generation, IET, 2008. 2(4): p. 249-262.

45. (ECI), E.C.I., Voltage Disturbances Standard EN 50160 Voltage Characteristics in Public Distribution Systems, in Power Quality Application Guide2004.

46. Chaudhary, S.K., E. Demirok, and R. Teodorescu. Distribution system augmented by DC links for increasing the hosting capacity of PV generation. in Power Electronics, Drives and Energy Systems (PEDES), 2012 IEEE International Conference on. 2012.

47. Ochoa, L., A. Keane, and G. Harrison. Minimizing the reactive support for distributed generation: Enhanced passive

operation and smart distribution networks. in Power and Energy Society General Meeting, 2012 IEEE. 2012.

48. Papadopoulos, P., et al. Distribution networks with Electric Vehicles. in Universities Power Engineering Conference (UPEC), 2009 Proceedings of the 44th International. 2009.

49. Sun, W., G.P. Harrison, and S.Z. Djokic. Incorporating harmonic limits into assessment of the hosting capacity of active networks. in Integration of Renewables into the Distribution Grid, CIRED 2012 Workshop. 2012.

50. Robinson, J., D. Jovcic, and G. Joos, Analysis and Design of an Offshore Wind Farm Using a MV DC Grid. Power Delivery, IEEE Transactions on, 2010. 25(4): p. 2164-2173.

51. Djeghader, Y., et al. Study and filtering of harmonics in a DC electrified railway system. in 2015 7th International Conference on Modelling, Identification and Control (ICMIC). 2015.

52. Antoniou, D., A. Tzimas, and S.M. Rowland. DC utilization of existing LVAC distribution cables. in 2013 IEEE Electrical Insulation Conference (EIC). 2013.

53. Design Standard of General Electricity Company of Libya, 2007, General Electricity Company of Libya.

54. I.Richardson , M.T., D. Infield, Clifford Domestic electricity use: A high-resolution energy demand model, CREST (Centre for Renewable Energy Systems Technology).

55. The United Kingdom 2000 Time Use Survey, 2003, Office for National Statistics.

56. Kersting, W., Distribution System Modeling and Analysis2001, New York: CRC Press. pp. 13-30.

57. PVSYST4. Available from: http://www.pvsyst.com/en/.

58. D. Rekioua, E.M., Optimization of Photovoltaic Power Systems2012, New York: Springer.

59. Bacha, Y.R.a.S., Power Flow Management for Grid Connected PV Systems with Batteries. transactions on sustainable energy, July 2011 p. pp. 309-320.

60. Sunny Family 2012. SMA, 2012; Available from: http://files.sma.de/dl/17333/SOLARKAT-KEN122111.pdf.

61. Lambert M. Surhone, M.T.T., Susan F. Marseken, Root Mean Square Deviation2010: Betascript Publishing.

62. De Doncker, R.W., D.M. Divan, and M.H. Kheraluwala. A three-phase soft-switched high power density DC/DC converter for high power applications. in Industry Applications Society Annual Meeting, 1988., Conference Record of the 1988 IEEE. 1988.

63. Yaqoob, M., K.H. Loo, and Y.M. Lai, Extension of Soft-Switching Region of Dual-Active-Bridge Converter by Tunable Resonant Tank. IEEE Transactions on Power Electronics, 2017. PP(99): p. 1-1.

64. Lenke, R., F. Mura, and R.W.D. Doncker. Comparison of non-resonant and super-resonant dual-active ZVS-operated high-power DC-DC converters. in 2009 13th European Conference on Power Electronics and Applications. 2009.

65. van Hoek, H., et al. Comparison of a single-phase and a three-phase dual active bridge with low-voltage, high-current output. in Renewable Energy Research and Applications (ICRERA), 2012 International Conference on. 2012.

66. van Hoek, H., M. Neubert, and R.W. De Doncker, Enhanced Modulation Strategy for a Three-Phase Dual Active Bridge—Boosting Efficiency of an Electric Vehicle Converter. Power Electronics, IEEE Transactions on, 2013. 28(12): p. 5499-5507.

67. Mustansir H. KheraIuwala, P., DeepakraJ M. Divan. HIGH POWER DENSITY DC-TO-DC CONVERTERS FOR AEROSPACE APPLICATIONDS. 1990.

68. De Doncker, R.W.A., D.M. Divan, and M.H. Kheraluwala, A three-phase soft-switched high-power-density DC/DC converter for high-power applications. Industry Applications, IEEE Transactions on, 1991. 27(1): p. 63-73.

69. Engel, S.P., et al., Comparison of the Modular Multilevel DC Converter and the Dual-Active Bridge Converter for Power Conversion in HVDC and MVDC Grids. Power Electronics, IEEE Transactions on, 2015. 30(1): p. 124-137.

70. Dušan Graovac, M.P., IGBT Power Losses Calculation Using the Data-Sheet Parameters Application Note, 2009. V 1.1,(Infineon Technologies AG).

71. Plecs User Manual 2015, Plexim GmbH.

72. Naayagi, R.T., A.J. Forsyth, and R. Shuttleworth. Performance analysis of DAB DC-DC converter under zero voltage switching. in 2011 1st International Conference on Electrical Energy Systems. 2011.

73. Diskin, E., et al. Investigating the potential to maximise wind penetration on distribution networks through active control and the implications for network users and operators. in Integration of Renewables into the Distribution Grid, CIRED 2012 Workshop. 2012.

74. Lenke, R.U., A Contribution to the Design of Isolated DC-DC Converters for Utility Applications, in Institut für Power Generation and Storage Systems2012, RWTH Aachen University.

75. Naayagi, R.T., R. Shuttleworth, and A.J. Forsyth. Investigating the effect of snubber capacitor on high power IGBT turn-off. in 2011 1st International Conference on Electrical Energy Systems. 2011.

76. De, D., et al. Achieving the desired transformer leakage inductance necessary in DC-DC converters for energy storage applications. in 6th IET International Conference on Power Electronics, Machines and Drives (PEMD 2012). 2012.

77. Litz wire gauge Available from: https://www.newenglandwire.com/default.aspx.

78. NANOPERM core specifications. Available from: http://www.magnetec.de/fileadmin/pdf/pb_kennlinien.pdf.

79. Colonel Wm.T. Mclyman, Transformer and inductor design hand book. fourth edition ed2011: CRS press.

80. W.G.Hurley, W.H.W., Transformers and Inductors for power electronics2013: Wiley.

81. Metglas® 2605SA1 & 2605HB1M Magnetic Alloy. Available from: http://www.metglas.com/products/magnetic_materials/2605sa1.asp.

82. Metglas® amorphous Alloy 2605SA1. Specifications

83. Mobarrez, M., et al. Performance and loss evaluation of a hard and soft switched 2.4 MW, 4 kV to 6 kV isolated DC-DC converter for a wind energy application. in IECON 2012 - 38th Annual Conference on IEEE Industrial Electronics Society. 2012.

84. E. K. Amankwah, A Parallel Hybrid Modular Multilevel Converter for High Voltage DC Applications, in Electrical and Electronics Engineering2013, The University of Nottingham: Nottingham, Uk

85. Rohouma, W., Design control and implementation of a four-leg matrix converter for ground power supply application,

in Electrical and Electronics Engineering2013, University of Nottingham: Nottingham UK.

86. HRO 64Zi specifications Available from: http://teledynelecroy.com/oscilloscope/oscilloscopemodel.aspx?modelid=6172.

87. CWT Ultra-mini data sheet, P.p.e. measurements, Editor.

88. Aktive Differential-Tastköpfe / Active Differential Probes TT-SI 50, TT-SI 51, TT-SI 52, T.T.p.e. GMBH, Editor.

89. TT-SI 9110 100MHz DIFFERENTIAL PROBE USER'S MANUAL, T.E. GmbH, Editor 2006.

90. Agarwal, V., Let's be accurate, What's the difference between resolution and accuracy, in New electronics 2015.

91. Dr. U. Nicolai , D.A.W., Determining switching losses of SEMIKRON IGBT modules SEMIKRON / Application Note / AN 1403 /, SEMIKRON, Editor 2014.

92. SKM 145GB066D datasheet SEMIKRON, Editor 2009.

93. Kulsangcharoen, P., et al. Experimental evaluation and efficiency optimisation of a grid-connected converter for household energy storage applications. in 7th IET International Conference on Power Electronics, Machines and Drives (PEMD 2014). 2014.

Appendices

Appendix (A) 6 the percentage of ownership and consumption of the Libyan household electrical equipment's and their consumption:

Equipment	Percentage of Holding	Day average usages hour's	Average power consumption (W)	Average yearly consumption kWh
Cooking equipment	5.22	0.3	1283	150
Fridge 1	96.5	14.4	146	796
Fridge 2	17.4	16.0	149	867

Freezer 1	40.3	12.0	147	642
Freezer 2	3.98	10.7	157	615
Washing machine	73.1	0.9	251	85
TV 1	98.8	8.0	85	249
TV 2	39.6	6.7	82	200
TV 3	8.21	6.5	87	207
Computer	3.23	3.0	207	229
Stereo type 1	60.2	4.2	25	39
Stereo type 2	7.21	3.0	25	39
Stereo type 3	0.75	2.0	25	18
Bulb -100	70.4	4.9	100	1802
Bulb-60	28.6	2.5	60	449
Bulb-40	10.7	3.7	40	783
Florescent Pulp	20.9	3.2	44	225
Iron	68.4	0.8	1009	296
Water P 1	43.8	2.0	965	693
Water P 1	1.74	0.9	745	254
Air Con 2 part 1	12.2	6.4	1901	4425
Air Con 2 part 2	3.23	9.4	1633	5582
Air Con 2 part 3	1.0	2.0	2675	1953

Air Con 2 part 4	0.5	3.8	2675	3361
Air Con 2 part 5	0.25	4.8	1400	2427
Air C 1 part 1	20.9	6.5	1690	3395
Air C 1 part 2	6.47	4.5	1876	3108
Air C 1 part 3	1.99	1.5	1400	767
Air C 1 part 4	0.5	1.5	1400	767
Air C 1 part 5	0.25	0.8	1400	387
Fan 1	46	5.3	99	96
Fan 2	8.71	4.5	94	78
Heater 1	35.8	6.1	1229	684
Heater 2	5.22	5.2	1367	646
Heater 3	1.0	8.0	500	365
Water heater 1	90.3	7.9	1203	1739
Water heater 2	20.4	7.9	1226	1774
Water heater 3	5.74	7.9	1227	1774
Water heater 4	1.49	7.9	1200	1734
Water heater 5	0.25	7.9	1200	1734

Appendix (B) The inductor current at the different zones of operation

Zone (1):

$$i(\theta) = i(0) + \frac{V_i(1+d)}{3wL}\theta \qquad for\ \ 0 \le \theta \le \phi \tag{B.1}$$

Zone (2):

$$i(\theta) = i(\phi) + \frac{V_i(1-d)}{3wL}(\theta - \phi) \qquad for\ \ \phi \le \theta \le \pi/3 \tag{B.2}$$

Zone (3):

$$i(\theta) = i(\frac{\pi}{3}) + \frac{V_i(2-d)}{3wL}(\theta - \frac{\pi}{3}) \qquad for\ \ \pi/3 \le \theta \le \phi + \pi/3 \tag{B.3}$$

Zone (4):

$$i(\theta) = i(\phi + \frac{\pi}{3}) + \frac{V_i(2-2d)}{3wL}(\theta - \phi - \frac{\pi}{3}) \quad for\ \ \phi + \pi/3 \le \theta \le 2\pi/3 \tag{B.4}$$

Zone (5):

$$i(\theta) = i(\frac{2\pi}{3}) + \frac{V_i(1-2d)}{3wL}(\theta - \frac{2\pi}{3}) \quad for\ \ 2\pi/3 \le \theta \le 2\pi/3 + \phi \tag{B.5}$$

Zone (6):

$$i(\theta) = i(\phi + \frac{2\pi}{3}) + \frac{V_i(1-d)}{3wL}(\theta - \frac{2\pi}{3} - \phi) \quad for\ \ \phi + 2\pi/3 \le \theta \le \pi \tag{B.6}$$

Appendix (C) Calculating the (I_{rms}) and the (I_{av}) for the sending bridge's IGBTs and the diodes

This appendix includes the methods used to drive the (I_{rms}) and (I_{av}) for the IGBT's and diodes of the sending bridge:

The (I_{rms}) and (I_{av}) of a waveform can be calculated using equations (C.1, C. 2):

$$I_{rms} = \sqrt{\frac{1}{2\pi}\int_{0_1}^{2\pi} I^2(\theta)d\theta} \qquad \text{(C.1)}$$

$$I_{av} = \frac{1}{2\pi}\int_{0}^{2\pi} I(\theta)d\theta \qquad \text{(C.2)}$$

Thus the current as a function of angle $i(\theta)$ for both the IGBT and the diode has to be identified:

From figure 5.6 it can be noticed that: the diode (D_1) will be conducting the current at angle range from ($0 \le \theta \le \frac{\phi}{2}$). Thus $i_{D1}(\theta)$ can be estimated using equation (C.3):

$$i_{D1}(\theta) = -\frac{V_i}{3\omega L}\left[\frac{2\pi d}{3} - d\phi - \frac{2\pi}{3}\right] - \frac{V_i(1+d)}{3wL}\theta \quad \text{For } 0 \le \theta \le \frac{\phi}{2} \qquad \text{(C.3)}$$

While ($d = 1$):

$$I_{D1}(\theta) = -\frac{V_i}{3wL}(2\theta - \phi) \text{ for } 0 \le \theta \le \frac{\phi}{2} \qquad \text{(C.4)}$$

The $IGBT_1$ conducting range can be derived from

Figure 5.5, which is ($\frac{\phi}{2} \le \theta \le \pi$). Hence the ($IGBT_1$) current wave, as a function of the angle, will be a combination of six different sections, where each section is represented by a different equation, this principle is illustrated by equation (C.5):

$$i_{IGBT1}(\theta) = \begin{matrix} \phi & \pi/3 & \phi+\pi/3 & 2\pi/3 & \phi+2\pi/3 & \pi \\ I_1\| \theta + I_2\| & \theta & + I_3\| \theta & + I_4\| \theta & + I_5\| \theta & + I_6\| \theta \\ \frac{\phi}{2} & \phi & \pi/3 & \phi+\pi/3 & 2\pi/3 & \phi+2\pi/3 \end{matrix} \qquad \text{(C.5)}$$

While ($d = 1$) the inductor current equations (B.1)-(B.6) presented in appendix (B) can be simplified to:

$$i(\theta) = i(0) + \frac{2 \times V_i}{3wL}\theta \qquad for\ \ 0 \le \theta \le \phi \qquad \text{(C.6)}$$

$$i(\theta) = i(\phi) \qquad for\ \ \phi \le \theta \le \pi/3 \qquad \text{(C.7)}$$

$$i(\theta) = i(\frac{\pi}{3}) + \frac{V_i}{3wL}(\theta - \frac{\pi}{3}) \qquad for\ \ \pi/3 \le \theta \le \phi + \pi/3 \qquad \text{(C.8)}$$

$$i(\theta) = i(\phi + \frac{\pi}{3}) \qquad for\ \ \phi + \pi/3 \le \theta \le 2\pi/3 \qquad \text{(C.9)}$$

$$i(\theta) = i(\frac{2\pi}{3}) - \frac{V_i}{3wL}(\theta - \frac{2\pi}{3}) \qquad for\ \ 2\pi/3 \le \theta \le 2\pi/3 + \phi \qquad \text{(C.10)}$$

$$i(\theta) = i(\phi + \frac{2\pi}{3}) \qquad for\ \ \phi + 2\pi/3 \le \theta \le \pi \qquad \text{(C.11)}$$

The current at zero is equal to the current at half the period $i(0) = -i(\pi)$. Thus, by solving equations (C.6, C.11), the current $i(0)$ can be estimated using equation (C.12):

$$i(0) = -\frac{\phi \times V_i}{3\omega L} \qquad \text{(C.12)}$$

Next, the currents (I_1, I_2, I_3, I_4, I_5) can be derived:

From equation (B.6), the current ($I_1(\theta)$) can be described as:

$$I_1(\theta) = i(0) + \frac{2 \times V_i}{3wL}\theta \qquad for \ \ \phi/2 \le \theta \le \phi \qquad \text{(C.13)}$$

By replacing $i(0)$ from equation (C.12) into equation (C.13), the current $I_1(\theta)$ will be the result which is represented in equation (C.14):

$$I_1(\theta) = \frac{V_i}{3wL}(2\theta - \phi) \qquad for \ \ \phi/2 \le \theta \le \phi \qquad \text{(C.14)}$$

From equation (B.6) the current $I_2(\theta)$ can be described as:

$$I_2(\theta) = i(\phi) \qquad for \ \ \phi \le \theta \le \pi/3$$

(C.15)

The current $i(\phi)$ can be calculated by substituting ($\theta = \phi$) into equation (C.14):

$$i(\phi) = \frac{V_i \phi}{3wL} \qquad \text{(C.16)}$$

From (15) and (16) the current $I_2(\theta)$ can be derived as:

$$I_2(\theta) = \frac{V_i \phi}{3wL} \qquad for\ \ \phi \le \theta \le \pi/3 \qquad \text{(C.17)}$$

From equation (C.8) the current $I_3(\theta)$ can be described as:

$$I_3(\theta) = i(\frac{\pi}{3}) + \frac{V_i}{3wL}(\theta - \frac{\pi}{3})\ \ for\ \ \pi/3 \le \theta \le \phi + \pi/3 \qquad \text{(C.18)}$$

The current $i(\frac{\pi}{3})$ can be calculated by substituting $\theta = \pi/3$ into equation (C.17):

$$i(\frac{\pi}{3}) = \frac{V_i \phi}{3wL} \qquad \text{(C.19)}$$

From (C.18) and (C.19) the current $I_3(\theta)$ can be derived as:

$$I_3(\theta) = \frac{V_i \phi}{3wL} + \frac{V_i}{3wL}(\theta - \frac{\pi}{3}) \qquad for\ \ \pi/3 \le \theta \le \phi + \pi/3 \qquad \text{(C.20)}$$

From equation (C.9) the current $I_4(\theta)$ can be described as:

$$I_4(\theta) = i(\phi + \frac{\pi}{3}) \qquad for\ \ \phi + \pi/3 \le \theta \le 2\pi/3 \qquad \text{(C.21)}$$

The current $i(\phi + \frac{\pi}{3})$ can be calculated by substituting ($\theta = \phi + \pi/3$) into equation (C.22):

$$i(\phi + \frac{\pi}{3}) = \frac{V_i \phi}{3wL} + \frac{V_i}{3wL}(\phi + \frac{\pi}{3} - \frac{\pi}{3}) \ = \ \frac{V_i \times 2\phi}{3wL} \qquad \text{(C.22)}$$

From (C.21) and (C.22) the current $I_4(\theta)$ can be derived as:

$$I_4(\theta) = \frac{V_i \times 2\phi}{3wL} \qquad for\ \ \phi + \pi/3 \le \theta \le 2\pi/3 \tag{C.23}$$

From equation (C.10) the current $I_5(\theta)$ can be described as:

$$I_5(\theta) = i(\frac{2\pi}{3}) - \frac{V_i}{3wL}(\theta - \frac{2\pi}{3}) \quad for\ \ 2\pi/3 \le \theta \le 2\pi/3 + \phi \tag{C.24}$$

The current ($i(\frac{2\pi}{3})$) can be substituting ($\theta = 2\pi/3$) into equation (C.13):

$$i(\frac{2\pi}{3}) = \frac{V_i \times 2\phi}{3wL} \tag{C.25}$$

From (C.24) and (C.25) the current ($I_5(\theta)$) can be derived as:

$$I_5(\theta) = \frac{V_i \times 2\phi}{3wL} - \frac{V_i}{3wL}(\theta - \frac{2\pi}{3}) \ for\ \ 2\pi/3 \le \theta \le 2\pi/3 + \phi \tag{C.26}$$

From equation (C.11) the current $I_6(\theta)$ can be described as:

$$I_6(\theta) = i(\phi + \frac{2\pi}{3}) \qquad for\ \phi + 2\pi/3 \le \theta \le \pi \tag{C.27}$$

The current $i(\phi + \frac{2\pi}{3})$ can be derived by substituting ($\theta = \phi + 2\pi/3$) into equation (C.26):

$$i(\phi + \frac{2\pi}{3}) = \frac{V_i \phi}{3wL} \tag{C.28}$$

From (C.27) and (C.28) the current $I_6(\theta)$ can be derived as:

$$I_6(\theta) = \frac{V_i \phi}{3wL} \qquad for\ \phi + 2\pi/3 \le \theta \le \pi \qquad \text{(C.29)}$$

After the Diode and the IGBT currents as a function of the angle are presented, the RMS and average values can be calculated:

The diode current as a function of the phase shift can be described using the equation (B.4):

$$I_{D1}(\theta) = -\frac{V_i}{3wL}(2\theta - \phi) \qquad 0 \le \theta \le \frac{\phi}{2} \qquad \text{(C.30)}$$

Thus, by using equation (C.1) and (C.3) the diode average and RMS currents can be estimated:

$$I_{D\ rms} = \sqrt{\frac{1}{2\pi}\int_0^{\phi/2} {I_{D1}}^2(\theta)d\theta} \qquad \text{(C.31)}$$

$$I_{D\ rms} = \sqrt{\frac{1}{2\pi}\int_0^{\phi/2} \left(-\frac{V_i}{3wL}(2\theta - \phi)\right)^2 d\theta} \qquad \text{(C.32)}$$

Thus:

$$I_{RMS\ D} = \frac{V_i \times \phi\sqrt{\phi}}{6 \times \omega L \times \sqrt{3 \times \pi}} \qquad \text{(C.33)}$$

$$I_{av} = \frac{1}{2\pi}\int_0^{\phi/2} I_{D1}(\theta)d\theta \qquad \text{(C.34)}$$

$$I_{av} = \frac{1}{2\pi}\int_0^{\phi/2} \left[\frac{-V_i}{3wL}(2\theta - \phi)\right]d\theta \qquad \text{(C.35)}$$

Thus:

$$I_{AV\,D} = \frac{V_i \times \phi^2}{8 \times 3\omega L \times \pi} \tag{C.36}$$

While the IGBT current wave as a function of the angle can be calculated using equations (C.5, C.15, C.17, C.20, C.21, and C.25)

$$i_{IGBT1}(\theta) = I_1 \Big\|_{\frac{\phi}{2}}^{\phi} \theta + I_2 \Big\|_{\phi}^{\pi/3} \theta + I_3 \Big\|_{\pi/3}^{\phi+\pi/3} \theta + I_4 \Big\|_{\phi+\pi/3}^{2\pi/3} \theta + I_5 \Big\|_{2\pi/3}^{\phi+2\pi/3} \theta + I_6 \Big\|_{\phi+2\pi/3}^{\pi} \theta \tag{C.37}$$

$$\begin{aligned} i_{IGBT1}(\theta) = {} & \frac{V_i}{3wL}(2\theta - \phi) \Big\|_{\frac{\phi}{2}}^{\phi} \theta + \frac{V_i\,\phi}{3wL} \Big\|_{\phi}^{\pi/3} \theta + \left[\frac{V_i\,\phi}{3wL} + \frac{V_i}{3wL}(\theta - \frac{\pi}{3}) \right] \Big\|_{\pi/3}^{\phi+\pi/3} \theta \\ & + \frac{V_i \times 2\phi}{3wL} \Big\|_{\phi+\pi/3}^{2\pi/3} \theta + \left[\frac{V_i \times 2\phi}{3wL} - \frac{V_i}{3wL}(\theta - \frac{2\pi}{3}) \right] \Big\|_{2\pi/3}^{\phi+2\pi/3} \theta \\ & + \frac{V_i\,\phi}{3wL} \Big\|_{\phi+2\pi/3}^{\pi} \theta \end{aligned} \tag{C.38}$$

$$I_{IGBT1\ rms} = \sqrt{\frac{1}{2\pi}\left[\begin{aligned} & \int_{\phi/2}^{\phi} \left(\frac{V_i}{3wL}(2\theta - \phi) \right)^2 d\theta \\ & + \int_{\phi}^{\pi/3} \left(\frac{V_i\,\phi}{3wL} \right)^2 d\theta + \int_{\pi/3}^{\phi+\pi/3} \left(\frac{V_i\,\phi}{3wL} + \frac{V_i}{3wL}(\theta - \frac{\pi}{3}) \right)^2 d\theta \\ & + \int_{\phi+2\pi/3}^{\pi} \left(\frac{V_i\,\phi}{3wL} \right)^2 d\theta + \int_{\phi+\pi/3}^{2\pi/3} \left(\frac{V_i \times 2\phi}{3wL} \right)^2 d\theta \\ & + \int_{2\pi/3}^{\phi+2\pi/3} \left(\frac{V_i \times 2\phi}{3wL} - \frac{V_i}{3wL}(\theta - \frac{2\pi}{3}) \right)^2 d\theta \end{aligned} \right]}$$

(C.39)

$$I_{RMS\ IGBT} = \frac{V_i \times \phi}{3\omega L}\sqrt{1-\frac{7\times\phi}{12\pi}} \tag{C.40}$$

$$I_{IGBT1\ av} = \frac{1}{2\pi}\left[\begin{array}{l} \int_{\phi/2}^{\phi}\left(\frac{V_i}{3wL}(2\theta-\phi)\right)\,d\theta + \int_{\phi}^{\pi/3}\left(\frac{V_i\,\phi}{3wL}\right)\,d\theta + \int_{\pi/3}^{\phi+\pi/3}\left(\frac{V_i\,\phi}{3wL}+\frac{V_i}{3wL}(\theta-\frac{\pi}{3})\right)\,d\theta \\ + \int_{\phi+\pi/3}^{2\pi/3}\left(\frac{V_i\times 2\phi}{3wL}\right)\,d\theta \\ + \int_{2\pi/3}^{\phi+2\pi/3}\left(\frac{V_i\times 2\phi}{3wL}\ -\frac{V_i}{3wL}(\theta-\frac{2\pi}{3}\right)\,d\theta + \int_{\phi+2\pi/3}^{\pi}\left(\frac{V_i\,\phi}{3wL}\right)\,d\theta \end{array}\right] \tag{C.41}$$

$$I_{AV\ IGBT} = \frac{V_i}{6\omega L\times\pi}\left(-0.75\times\phi^2+\frac{4}{3}\times\phi\times\pi\right) \tag{C.42}$$

Appendix D Analysis of three ϕ DAB converter using Thevenin's theory to estimate the turn off critical current:

This appendix includes the Using Thevenin's Theory analysis of the three ϕ DAB converter which is used to estimate the turn off critical current at which the circuit is still in ZVS the circuit in Figure 5.16 can be rearranged and presented in figure (D1).

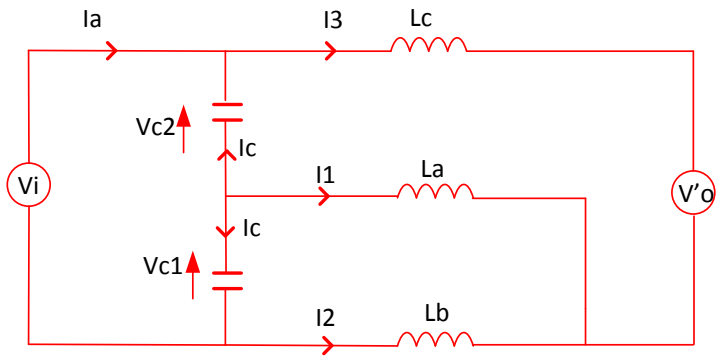


Figure (D1) the electrical circuit representing the current at the turnoff of the IGBT

The value of the currents and voltages at the moment of commutation can be presented as follow:

$$I_1(0) = I_2(0) = -I_{com} \tag{D.1}$$

$$I_3(0) = 2I_{com} \tag{D.2}$$

$$V_{C1}(0) = 0 \ , \ V_{C2}(0) = V_i \tag{D.3}$$

Using Thevenin's Theory and by removing C_1 and finding the Thevenin equivalent circuit.

- Step 1, Thevenin impedance this can be found by setting all the sources to zero while C_1 is removed

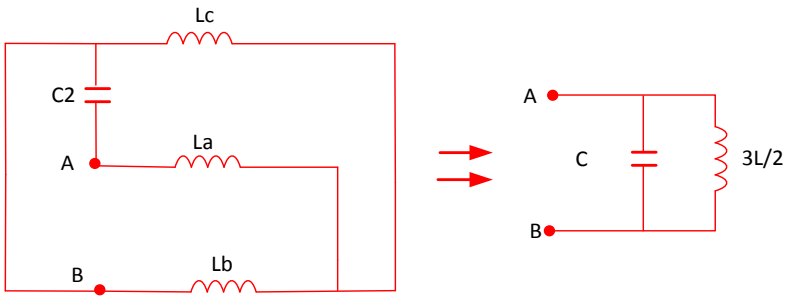


Figure (D2) The Thevenin impedance

- Step 2 is to find the Thevenin voltage.

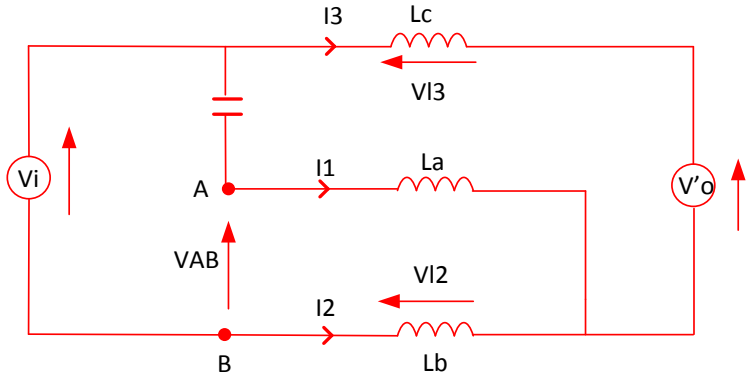


Figure (D3) the Thevenin voltage equivalent circuit

For the other loop

$V_i - V_{l3} - V_{l2} + V_{o=0}$ thus $V_{l3} = V_{l2}$

Hence $i_2 = i_3$ thus $i_1 = 0$

$$V_{AB} = 0 \qquad \text{(D.4)}$$

- Step 3 replace C_1 in the Thevenin circuit.

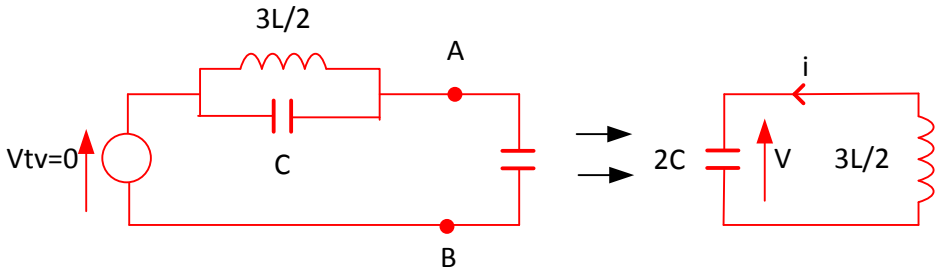


Figure (D4) the equivalent circuit at the moment of commutation

As it can be noticed from D4 at the moment of commutation there will be resonant between the equivalent inductor of $3L/2$ and the equivalent capacitor of $2C$ thus:

$$\frac{dV(0)}{dt} = \frac{I_{com}}{2} \qquad \text{(D.6)}$$

The equation (D.6) can be solved and Figure (D5) presents the snubber current and voltage after the commutation if we ignore the effect of the diode

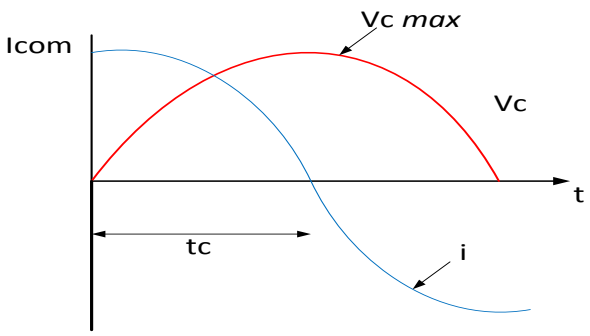


Figure (D5) the snubber voltage and current at commutation

$$V_c = V_{c\max} \sin(\omega t) \qquad \text{(D.7)}$$

$$i_c = I_{com}\cos(\omega t) \tag{D.8}$$

$$V_{c\max} = I_{com} Z_0 \tag{D.9}$$

Where

$$Z_0 = \sqrt{\frac{3L/2}{2C}} = \sqrt{\frac{3L}{4C}} \tag{D.10}$$

$$\omega = \frac{1}{\sqrt{\frac{3L}{2}\times 2C}} = \frac{1}{\sqrt{3LC}} \tag{D.11}$$

$$t_c = \frac{\pi}{2\omega} \tag{D.12}$$

The converter will be in ZVC when the $V_{c\max} = V_i$ thus

$$I_{com} = \frac{V_i}{Z_0} \tag{D.13}$$